



The project DeLIVER received funding from the European Union's Horizon 2020 research and innovation program under the Marie Skłodowska-Curie Grant Agreement No. **766181**.

Sempre.



*Ci vuole molto coraggio
per tornare indietro quando è necessario.*

Development of 3D *in vitro*
cell culture systems for
Organ-on-a-Chip and
Tissue engineering
applications

Alessandra DELLAQUILA

A dissertation submitted to
the University of Bielefeld
in partial fulfillment of the requirements
for the degree of

DOCTOR OF PHILOSOPHY

Members of the Examination Committee

Prof. Dr. Nicolas **BORGHINI**

Department of Physics, Bielefeld
University, Germany

Prof. Dr. Thomas **HUSER**

Department of Physics, Bielefeld
University, Germany

Prof. Dr. Andreas **HÜTTEN**

Department of Physics, Bielefeld
University, Germany

Dr. Teresa **SIMON-YARZA**

Laboratory for Vascular
Translational Science, Institut
National de la Santé et de la
Recherche Médicale (INSERM),
France

Supervisory Board

Prof. Dr. Thomas **HUSER**

Department of Physics, Bielefeld
University, Germany

Dr. Teresa **SIMON-YARZA**

Laboratory for Vascular
Translational Science, INSERM,
France

Prof. Dr. Didier **LETOURNEUR**

Laboratory for Vascular
Translational Science, INSERM,
France

Dr. Aurélie **VIGNE**

Elvesys Microfluidics
Innovation Center, France

Table of Contents

Ringraziamenti/ Acknowledgements	vi
List of Acronyms	x
1. Introduction	1
2. Investigation of an innovative material for Organ-on-a-Chip applications	15
2.1. Introduction to microfluidics	17
2.2. Design and Microfabrication of a novel composite Flexdym™ microfluidic device	34
2.3. Composite Flexdym™ Device Characterization	38
2.4. Results and Discussion	43
2.4.1. Composite Device Microfabrication	43
2.4.2. Material Bonding Characterization	46
2.4.3. Preliminary <i>in vitro</i> studies	54
2.4.4. Drawbacks compared to PDMS	57
2.5. Conclusions	58
3. Development of a microfluidic platform compatible with Super-Resolution optical imaging	60
3.1. The need of taking into account the imaging system	62
3.2. Design, Development and Characterization of a microfluidic device for SR-SIM	73
3.2.1. Design and microfabrication	73
3.2.2. Validation and optimization of the fabrication protocol	87

3.3. Cell Culture: use of the device for cell lines and LSECs culturing <i>in vitro</i>	95
3.3.1. Microfluidic platforms culturing	95
3.3.2. Results and Discussion	100
3.4. Validation of the microfluidic chip in a dish: testing the compatibility with SR-SIM	107
3.4.1. Microfluidic platforms culturing	107
3.4.2. Results and Discussion	110
3.5. Conclusions and perspectives	122
4. Development and characterization of polymeric scaffolds for fabrication of 3D microchanneled substrates	125
4.1. Biomaterials and fabrication strategies for tissue engineering	127
4.2. Design of biopolymeric scaffolds for vascular tissue engineering	146
4.2.1. Fabrication by templating/ crosslinking/ freeze-drying method	148
4.2.2. Optimization of standard fabrication method	154
4.2.3. Characterization of channeled scaffolds	159
4.3. Results and discussion	165
4.3.1. Standard vs optimized TCFD protocol	165
4.3.2. PUDNA scaffold characterization	176
4.4. Conclusions	189

5. Application of polymeric scaffolds to build an <i>in vitro</i> vascularized model	191
5.1. Tissue engineered models of functional endothelium	193
5.2. Endothelium formation and 3D imaging	213
5.2.1. Cell seeding strategies	214
5.2.2. Optimization of coating strategies	216
5.2.3. Evaluation of different cell culture conditions	220
5.2.4. Imaging and characterization	222
5.3. Results and Discussion	227
5.3.1. Evaluation of the cell seeding and coating methods	227
5.3.2. Evaluation of different cell culture conditions	235
5.3.3. Formation of endothelium by optimized protocol	241
5.4. Conclusions and future perspectives	256
6. General conclusion and future outlook	258
References	264
Appendix A. LIST OF DISSEMINATION ACTIONS	I
Appendix B. LIST OF SECONDMENTS IN THE DeLIVER CONSORTIUM	II
Appendix C. LIST OF CONFERENCE CONTRIBUTIONS	III
Appendix D. LIST OF PUBLICATIONS ASSOCIATED WITH THE PROJECT	IV

Ringraziamenti

Per prima cosa, vorrei ringraziare i Professori Borghini, Hütten, Huser ed il Dr. Simon-Yarza per aver accettato di far parte del mio comitato d'esame.

Un ringraziamento va ai miei responsabili accademico e istituzionale, Prof. Thomas Huser e Dr. Aurélie Vigne per la loro supervisione in questi anni. Al mio primo responsabile e buon amico, Sasha Cai Leshner-Pérez, grazie per la tua incredibile capacità di trovare l'acqua nel deserto. Il tuo supporto è stato prezioso fin dall'inizio per trovare la motivazione e la forza di continuare. Grazie a Lisa e Remis per il loro sostegno ed ai ragazzi di BlackHole Lab per il tempo passato insieme. Ad Elvsys, grazie per avermi ricordato di non giudicare un libro dalla copertina e di non lasciare mai che qualcuno ti faccia dubitare delle tue capacità.

Vorrei anche ringraziare le persone meravigliose del Consorzio DeLIVER che ho avuto la possibilità di conoscere negli anni passati, in particolare gli altri studenti, il cui supporto è stato fondamentale per continuare e concludere questo progetto. Grazie ai professori Lalor e Schermelleh per avermi accolta nei loro laboratori, è stata un'incredibile opportunità. Di tutti i ragazzi, un ringraziamento speciale va a Pantelitsa e Rita, per i bei (e brutti) viaggi ed esperimenti che abbiamo fatto insieme.

Ringrazio sinceramente il Prof. Didier Letourneur e il Dr. Teresa Simon-Yarza, che mi hanno dato la possibilità di finire questo dottorato nei laboratori di LVTS INSERM. La mia gratitudine verso di loro per avermi accolta, formata e seguita fino alla fine non ha bisogno di parole. Alla mia famiglia INSERM, Camille, Châu, Paola, Louise, Rodolphe, Cédric, Rachida, Fernanda e Soraya, grazie ragazzi per il vostro supporto e il tempo passato insieme. Questa pandemia sarebbe stata di sicuro noiosa senza di voi. A Samira e Camille va poi un grazie sentito per il loro aiuto nello sviluppo del mio progetto.

E ovviamente, niente di questo sarebbe stato possibile senza i miei amici e la mia famiglia. Ad Alex ed Emma, il mio primo nido a Parigi, per tutti i posti che abbiamo esplorato insieme. A Sara, Cristina, Tatiana e Hilaria, che sono rimaste con me, nonostante la distanza. Grazie per avermi ripetuto “dai che ce la fai” quando nemmeno io ci credevo. A tutti i nuovi amici che ho conosciuto durante questa avventura a Parigi, e ai vecchi amici, sparsi qua e là.

A Davide, per ricordarmi che non c'è luce alla fine del tunnel, perché non c'è tunnel se non quello che costruiamo noi stessi. Ad Olivia, che mi ha ricordato l'importanza di fermarsi e dare peso alle piccole cose della vita. Questo fa tutta la differenza. A Margherita, la mia prima futura nipotina, perché la vita è più forte di ogni altra cosa. Ti aspettiamo.

Grazie a mio fratello e a papà, per il grande amore e l'attenzione che mettono in ogni cosa che fanno per me. A mio fratello, per le sue teorie strampalate, che forse veniamo da due mondi diversi, ed è bello così. Ai miei genitori, per il loro sostegno incondizionato, per i tanti chilometri che hanno fatto per venire a trovarmi, per i bei momenti che abbiamo passato in questi ultimi anni. Infine, alla mia mamma, il mio specchio, il mio punto di riferimento. Nonostante avessi promesso ci saresti stata, Qualcuno ti ha riservato dei piani diversi. So che non avresti mai infranto la tua promessa. Grazie per la donna forte, indipendente, coerente, divertente, leale, incredibile che sei stata. Nonostante nulla di tutto questo possa essere insegnato né appreso, so quante cose di te mi porto dietro.

Una volta un professore mi disse che con i principi non si va da nessuna parte nella vita. Ora so che non poteva sbagliarsi di più. Il principio è l'unica cosa che conta.

Acknowledgements

Firstly, I want to thank Professors Borghini, Hütten, Huser and Dr. Simon-Yarza for accepting being the members of my examination committee.

Thanks to my academic and institutional supervisors, Prof. Thomas Huser and Dr. Aurélie Vigne for supervising my work during these years. To my former supervisor and good friend, Sasha Cai Leshere-Pérez, thank you for your amazing ability of finding water in the desert. Your help has been precious since the beginning to find the motivation and the strength to continue. Thanks to Lisa and Remis for their support and to the BlackHole Lab guys for the time spent together. To Elvsys, thanks for reminding me to don't judge a book from its cover and to never let anyone make you doubt yourself.

Also, I want to thank all the wonderful people from DeLIVER Consortium I had the chance to meet along these years, particularly, my ESR mates, whose support has been precious to continue and finish this project. Thanks to Prof. Lalor and Prof. Schermelleh for accepting me in their labs, these have been great opportunities. Of all the ESRs, my special thanks go to Pantelitsa and Rita for all the good (and bad) trips and experiments we did together.

I want to deeply thank Prof. Didier Letourneur and Dr. Teresa Simon-Yarza, who gave me the chance to finish this PhD in LVTS INSERM labs. My gratefulness to them for having accepted, trained and supervised me until the end is beyond words. To my INSERM family, Camille, Châu, Paola, Louise, Rodolphe, Cédric, Rachida, Fernanda e Soraya, thank you guys for the support and time we have spent together. Things would have been much boring without you during this pandemic. To Samira and Camille, a special thank for their help in developing my project.

And of course, none of this would have been possible without my friends and family. To Alex and Emma, my first family in Paris, for all the places we explored together. To Sara, Cristina, Tatiana and Hilaria, who have always been with me, despite the distance. Thank you for repeating me "you can do it" even when I could not believe it myself. To all the new friends I've met during this adventure in Paris, and the old ones, scattered around the world.

To Davide, for reminding me that there is no light at the end of the tunnel, as there is no tunnel except the one we build ourselves. To

Olivia, who has reminded me the importance of resting and valuing the small things in life. This makes all the difference. To Margherita, my first niece-to-be, as life is stronger than anything else. We are waiting for you.

Thanks to my brother and dad, for their great love and care they put in everything they do for me. To my brother, for his funny theories, as maybe we are from two different worlds, and that's ok. To my parents, for the genuine support they have always gave me, for the many kilometers they did to come and visit me, for the good time we had in these last years. Finally, to my mum, my mirror, my reference point. Though you promised to stay until the end, someone had different plans. I know you would have never broken your promise. Thank you for the strong, independent, coherent, fun, loyal, incredible woman you have been. Though none of this can be taught nor learnt, I know how much of you is part of me.

Once, a professor told me that with principles you don't build anything in life. Now I know he couldn't be more wrong. Principle is the only thing that matters.

List of Acronyms

AB	Antibody
ALI	Air-liquid interface
BSA	Bovine serum albumin
CMDR	Cell Mask Deep Red™
CMG	Cell Mask Green™
DAPI	4',6-diamidino-2-phenylindole, dichlorhydrate
DFD	Double freeze-drying
DI	Deionized
DMEM	Dulbecco's Modified Eagle Medium
EB	Ethylene-butylene
EC	Endothelial cell
ECM	Extracellular Matrix
FA	Formaldehyde
FBS	Fetal bovine serum
FD™	Flexdym™
FD	Freeze drying
FITC	Fluorescein isothiocyanate
FT-IR	Fourier transform infrared spectroscopy
GelMA	Gelatin Methacryloyl

HUVEC	Human umbilical vein endothelial cell
ICC	Immunocytochemistry
IM-HHSEC	Immortalized human hepatic sinusoidal endothelial cell
LSEC	Liver sinusoidal endothelial cell
LSFM	Light sheet fluorescence microscopy
MIP	Maximum intensity projection
MPM	Multiphoton microscopy
OOaC	Organ-on-a-chip
PBS	Phosphate Buffered Saline
PC	Polycarbonate
PDMS	Polydimethylsiloxane
PEEK	Polyether ether ketone
PLA	Polylactic acid
PMMA	Polymethylmethacrylate
PUDNA	Pullulan-dextran-NaCl
RT	Room temperature
SEM	Scanning electron microscopy
SFD	Single freeze-drying
SHG	Second harmonic generation
SIM	Structured illumination microscopy

SRM	Super-resolution microscopy
STMP	Sodium trimetaphosphate
sTPE	Soft thermoplastic elastomer
TE	Tissue engineering
TCFD	Templating – Cross-linking – Freeze-drying
TPEF	Two-photon excited fluorescence
TRITC	Tetramethyl rhodamine B isothiocyanate
VEGF	Vascular endothelial growth factor

1. Introduction

Biomedical engineering is nowadays a developed discipline whose aim is the application of engineering principles and know-how for addressing biology and medicine-related questions. Characterized by a multidisciplinary approach, biomedical engineering, also known as bioengineering, has exponentially evolved in the last decades and many branches have been identified, from human robotics to bioinformatics, from tissue engineering and biomaterials science to biomechanics, from clinical engineering to microfluidics [1]. Compared to conventional disciplines, bioengineering combines the knowledge from chemical, mechanical, electrical engineering and computer science with human biology and health sciences to bridge the gap between these two fields and develop new tools for human healthcare.

General Background

In the context of investigation of human pathophysiology, conventional biology methodology is still widely applied in research, analytical and medical laboratories. This approach can be found in at least two important steps of the research pipeline:

- (i) Design and development of the model: biology models are commonly first developed *in vitro*, thus in a laboratory setting, with techniques normally consisting in culturing cells on flat substrates and studying their behavior and response to applied stimuli [2,3];
- (i) Investigation of the model: after developing the *in vitro* model, many techniques are available for its investigation and one of the

most important is the use of microscopy for visualization as well as for functional and quantitative studies. Conventional optical and fluorescence methods are commonly used for imaging of *in vitro* models [4,5].

Nevertheless, bioengineering has revealed the important pitfalls and limitations of standard methodology in mimicking the complex anatomical and physiological properties of the human body. Though centuries of biology provided the basis for modern medicine, the current *in vitro* approaches have been demonstrated to be too simplistic and often limited or even inaccurate when it comes to recapitulate pathophysiological mechanisms [3,6]. Some major aspects should be taken into account: (i) The human body is a multiscale system, from both the architectural and functional point of view. As we learn since elementary school, cells make up tissues, tissues make up organs, organs make up systems. But also, the cell is not the smallest element, as it is composed of even smaller structures, as organelles and DNA. The body thus shows a hierarchical organization, from the nanoscale to the macroscale. (ii) Cells are not alone, cells are not steady: cells are surrounded by a complex three-dimensional (3D) microenvironment, composed of extracellular matrix (ECM), signaling molecules, and other cells. This creates a dynamic setting, as the microenvironment also provides the cells with specific physical, chemical, mechanical and topographical cues. (iii) Cells are inclusive: tissues and organs are composed of different cell types, each one with a specific function. Apart from the specialized cells performing the main task, called parenchymal cells,

many others are colocalized, playing equally important roles, as supplying blood or regulating the immune response.

Rationale

From this general picture, it can be seen how the conventional two-dimensional (2D) models, in which cells are cultured on flat surfaces, fail to recapitulate the complex cellular microenvironment under many aspects. Bioengineering aims therefore to develop sophisticated models to mimic the cells and tissues 3D microenvironment, the dynamic stimuli and the different tissue components in multiscale models.

Moreover, important efforts are conducted in parallel to develop innovative imaging systems to achieve two important goals: to go deeper and image phenomena at the submicron and nanoscale, and to go further and image full tissues, organs or even organisms in their entirety [7,8]. Again, this need is due to a new awareness, where researchers know that subcellular phenomena orchestrate the tissue functioning and that multiscale models can give new insights compared to single-scale models. Therefore, the engineering of new models has to be accompanied by the development and adoption of new microscopy techniques to see and unravel unknown mechanisms.

Specific background

In this thesis, the reader will encounter two of the main bioengineering approaches alternative to standard 2D *in vitro* models, namely microfluidics and tissue engineering (TE).

Microfluidics is the technology that studies and manipulates fluids at the microscale, by means of micrometric channels. Microfluidic devices are commonly produced by microfabrication techniques, as soft lithography, using polymeric materials. The most widely used material in microfluidics is polydimethylsiloxane (PDMS), a silicon-based elastomer [9]. In *in vitro* modeling, microfluidics finds an emerging place as tool to mimic the tissue microenvironment, notably by application of a flow, that mimics the blood microcirculation. The flow generates shear stress, sensed by the cells, that guides their proliferation and behavior, and that is capable of mimicking physiological as well as pathological conditions, as cancer development or cardiovascular diseases [10,11]. These microfluidic platforms have reached such a level of complexity that a new branch of microfluidics has been created in 2010, called organ-on-a-chip (OOaC) technology [12]. OOaC models commonly consist of a co-culture of parenchymal and non-parenchymal cells within microchannels, communicating with each other and exposed to the flow. Complex designs have been fabricated to introduce other components on-chip, that can apply for instance mechanical forces to mimic the lung breathing or the gut movements, or electrical stimulation for heart tissue modeling [13]. Microfluidics and OOaC technologies therefore hold great potential in mimicking the dynamic microenvironment of tissues and organs and recent efforts have been made to create connected devices to recapitulate multi-organ interaction, paving the way towards a body-on-a-chip platform [14]. This technology is particularly appealing for some specific fields,

mainly in the pharmaceutical domain: as the drug research and development is a long, expensive and time-consuming process, OOCs are now adopted to speed up the pre-clinical studies, with the final goal of eventually replacing animal models [15].

Few decades before, another field started to emerge, named tissue engineering. TE finds its main purpose in the design of tissue analogues for implantation and regeneration of a human tissue with lost or hampered functionalities [16]. TE is based on the use of biomaterials, eventually combined with cells and signaling molecules. The first goal of a biomaterial is to “fill the gap” where the tissue is missing, thus a scaffolding function. But biomaterials have evolved over time and have been engineered with the scope of providing the *in vivo*-like 3D environment discussed before, thus not only acting as physical template but also guiding the growth of new functional tissue by providing mechanical, chemical and biological cues [17]. TE is rapidly evolving and it has already seen the first application in clinics, for instance for skin and hard tissues regeneration. A plethora of biomaterials has been developed and complex physiologically relevant models have been engineered for the study of human physiology, pathology and therapeutics [18,19].

An insight into the DeLIVER project



This research was fully funded by the ITN H2020 DeLIVER project. The project, started in 2018, features nine main partners across Europe, including public universities and companies, and international collaborators.

The DeLIVER project focuses on and combines two main topics, super-resolution microscopy (SRM) and liver biology. Particularly, the liver capillaries, called sinusoids, are lined by liver sinusoidal endothelial cells (LSECs). As the primary function of the liver is the clearance of molecules, these cells present peculiar features, related to their role. In fact, they show on their membranes thousands of nanometric pores called fenestrations for blood filtration and clearing. Though biologists know of their existence because of imaging on fixed samples, little is known about their functioning, as their size is below the diffraction limit of light, thus making them impossible to be observed with conventional imaging techniques. It is in this context that the combination of biology with super-resolution imaging occurs for the development of sophisticated platforms to study cellular phenomena at the nanoscale. Therefore, the main research objectives of DeLIVER are the development of novel SRM techniques, particularly structured illumination microscopy (SIM), and open-access tool for image reconstruction and to study by SR-SIM how LSECs respond to drugs, ageing and diseased conditions.

Existing Gaps and Hypotheses

Despite the tremendous advances of the past two decades in bioengineered models, some drawbacks still need to be addressed. In the field of microfluidics, PDMS has become the material of choice for chip microfabrication due to its low cost, transparency, elasticity and accessible fabrication [20]. However, its use has revealed major limitations, notably the absorption of small molecules and the difficulty of scaling up the fabrication process to industrial settings [21]. Research groups and companies are working on alternative materials, as thermoplastics or hydrogels, to find high-throughput and versatile solutions for a fast transition of this technology towards the market.

HYPOTHESIS 1. *The use of new or different materials to PDMS, whose properties and fabrication process overcome the drawbacks of this polymer, would offer researchers an alternative for the fabrication of PDMS-free platforms and a faster scale-up of microfluidics towards the market.*

Moreover, the design of OoC platforms has been standardized over the years and the majority of the devices present a horizontal structure, composed of two layers, separated by a porous membrane [22]. Cells from different sources are cultured on the two sides of the membrane, that acts as physical support and as communicating barrier. Nevertheless, this design results extremely difficult to image with high and super-resolution imaging methods, due to the several layers and the distance of the cultured cells from its bottom.

HYPOTHESIS 2. *The redesign of conventional horizontal OOaC platforms would ensure their compatibility with SR-SIM imaging technology and open up new possibilities for super-resolution studies in dynamic microsettings.*

Regarding the SR-SIM state of the art, research still focuses on the imaging of 2D samples, as thin tissue slices or cells cultured on coverslips, that are cultured under static conditions and fixed prior to imaging [23]. However, in the context of DeLIVER, where the final goal is to image LSECs by means of SR-SIM, this experimental setup poses a major drawback: LSECs isolated and cultured *in vitro* have shown to lose their fenestrations within few hours from the isolation [24]. This phenomenon hampers a long-term study of these subcellular structures, and makes the design of dynamic experiments extremely difficult.

HYPOTHESIS 3. *Thanks to the application of physiological shear stress, cells cultured on microfluidic platforms have demonstrated to maintain a healthier phenotype and metabolism compared to cells cultured in static conditions [2]. Therefore, microfluidics has the potential to improve in vitro culture of LSECs and ensure longer maintenance of their phenotype and nanostructures.*

Nevertheless, as conventional microfluidic platforms mainly provide for cells cultured on a membrane, the recapitulation of tissue architecture becomes extremely challenging. With the objective of mimicking the liver sinusoid, then, tissue engineered biomaterials offer an interesting solution, as they can provide for complex 3D

shapes. However, most of the current TE models present organ-specific features but they are limited in providing microenvironmental cues [25]. Among them, the presence of flow plays a main role as it ensures nutrients, gas exchange and waste removal. *In vitro* vascularization of biomaterials would thus guarantee a physiologically relevant tissue assembly and growth and it has been demonstrated to enhance TE constructs integration with the host tissue and tissue regeneration *in vivo* [26].

HYPOTHESIS 4. *The use of biomaterials designed ad hoc would ensure physiological formation of endothelium compared to microfluidics and unspecific TE platforms.*

Objectives

Considering the existing gaps and the final goal of DeLIVER, the main research objectives of this thesis could be summarized as follows:

- (i) To investigate materials and fabrication processes alternative to PDMS for microfluidics and OOaC applications;
- (ii) To redesign conventional microfluidic platforms to ensure compatibility with SR-SIM imaging setup;
- (iii) To use microfluidic platforms for dynamic cellular studies and simultaneous SR-SIM imaging and for culturing of LSECs;
- (iv) To engineer and characterize tailored biomaterials for vascularization and to build a functional vascularized model *in vitro*.

Methodology

The development of research objectives was done in close collaboration with DeLIVER partners. For the first objective the study of an alternative microfluidic material to PDMS was done by testing a patented soft thermoplastic elastomer, Flexdym™ [27]. Characterized by optical transparency and elastomeric properties, as PDMS, the polymer can be easily thermomolded. We thus worked on the high-throughput and reproducible fabrication of OOaC platforms out by Flexdym™. The devices were characterized to test their stability and suitability for OOaC applications and their biocompatibility was assessed by performing *in vitro* cell culturing [28].

For the second objective, microfluidic platforms compatible with SR-SIM systems were instead produced in PDMS and glass. Stability and compatibility of the devices with SIM were investigated via a collaboration between Elvsys Microfluidic Innovation center, France and University of Oxford, UK. For the third objective, the platforms were used for *in vitro* studies with different cell sources under static and dynamic conditions and imaging evaluation was carried out by either standard or advanced microscopy techniques. Culturing and imaging of human LSECs was done in collaboration with University of Oxford, UK and University of Birmingham, UK. For the fourth objective, the design of scaffolds for vascularization was done at LVTS INSERM, France, from a material developed and patented by the laboratory [29]. The biomaterial, composed of

naturally-derived biopolymers, was engineered by micromolding of channels. The design, optimization of standard fabrication protocols, and complete characterization of the scaffold were carried out. The platform was then used for *in vitro* assembly of functional endothelium. Seeding strategies, culture parameters, coating methods were carefully investigated. Special attention was given to the analysis of imaging techniques suitable for 3D thick samples.

Main findings

For the first research line, our results showed that OOaC platforms fabricated by using Flexdym™ could be produced in less than 2.5 hours and by a parallelized process, while PDMS soft lithography normally entails up to 48 hours of process and production cannot be run in parallel. The Flexdym™ chips showed a suitability for their application as OOaC devices and *in vitro* data confirmed their biocompatibility, with high cellular viability up to one week.

For the second and third research lines, the optimization of microfluidic chips led to devices compatible with SR-SIM equipment and imaging. To the best of our knowledge, we demonstrated for the first time the flow of drugs and labeling molecules on living and fixed cells respectively during live SIM image acquisition. Results conducted with primary LSECs showed they maintained healthy morphology for several days on-chip and imaging of LSECs fenestrations on-chip was also carried out.

Finally, for the fourth research line, design and characterization of biopolymeric scaffolds revealed the possibility to create matrices

with tailored mechanical, physical and chemical properties and to obtain a specific architecture with a selective coating for enhanced vascularization.

The *in vitro* studies confirmed the assembly of functional endothelium by optimization of the cell culture parameters. Moreover, we were able to tune the formation of endothelium over time, thus creating a matrix that can be used for different TE applications. Finally, investigation of different 3D microscopy systems allowed us to define the optimal setups for imaging of complex biomaterials.

Despite the encouraging results obtained from this research, some of the hypotheses could not be investigated, as the prolonged maintenance of LSECs fenestrations under flow, or the design of more complex co-culture platforms to build a recapitulative liver tissue model. As the COVID-19 pandemic has strongly hit Europe since March 2020, physical collaborations were interrupted, as well as on site working for several months, with some restrictions still going on. As countries have made extraordinary efforts to manage the social, health and economic crisis, the fundamental role of research has been confirmed more than ever. The hope is thus that new time will be found to address these questions in a near future.

Thesis layout

The thesis is organized as follows: Chapters 2 and 3 are related to microfluidics research while Chapters 4 and 5 describe a TE vascularized model. Particularly, Chapter 2 gives a short introduction

Chapter 1. Introduction

to microfluidic and OoAC technologies and materials, then focusing on the development and characterization of platforms with Flexdym™, a material alternative to standard PDMS. Chapter 3 introduces the basic principles of SRM and liver biology and their current limitations. The topic of the chapter is the design and validation of a microfluidic platform compatible with SRM systems for imaging of subcellular structures and LSECs fenestrations. Chapter 4 details the concept of tissue engineering, biomaterials and fabrication processes and focuses on the development and characterization of prepatterned biopolymeric scaffolds. Chapter 5 follows Chapter 4 by describing the use of these scaffolds for the *in vitro* modeling and engineering of vasculature. Finally, Chapter 6 presents a general conclusion and future perspectives for further developments.

Funnily enough, I had a good time writing this thesis and now I hope you will enjoy reading it.

2. Investigation of an innovative material for Organ-on-a-Chip applications

Chapter partially based on the following works:

A.H. McMillan, E.K. Thomée, A. Dellaquila, H. Nassman, T. Segura, and S.C. Lesher-Pérez. Rapid Fabrication of Membrane-Integrated Thermoplastic Elastomer Microfluidic Devices. *Micromachines* 2020, 11, 731. <https://doi.org/10.3390/mi11080731>

Adapted with permission, copyright © 2020 by the authors

A. Dellaquila, Five Short Stories on The History of Microfluidics, Microfluidic reviews on www.elflow.com/microfluidic-reviews/general-microfluidics/history-of-microfluidics/

STATEMENT OF SIGNIFICANCE

The scale-up of microfluidic platforms for biology-related studies is still hindered by the wide use of polydimethylsiloxane (PDMS) for the devices microfabrication. PDMS suffers from several limitations, the most relevant being the slow prototyping and the absorption of small molecules, that represents a major drawback for drug research. In this chapter, a microfluidic platform fabricated with an innovative thermoplastic elastomer, Flexdym™, is proposed. The low absorption profile, the biocompatibility and the rapid and scalable fabrication process of this material offer a new alternative to conventional microfluidic platforms for cell biology applications.

2.1. Introduction to Microfluidics

The term microfluidics refers to both the science and the technology of studying and manipulating fluids at the micrometric scale [30]. By using small channels, with typical dimensions ranging from tens to hundreds of micrometers, microfluidics has represented an alternative, cost-effective and precise technology for a wide range of applications, ranging from chemical analysis to cellular biology (**Figure 2.1**) [31–34]. Its widespread use can be related to the advantages it offers when compared to research standard methodologies and models: from a technological point of view, the use of micrometric channels allows for a reduction of samples and reagents, that are often expensive or with limited availability [35]. Moreover, the possibility to integrate multiple channels on a single device, defined as parallel microfluidics, has been widely adopted for batch production of molecules, nanoparticles and drugs [36,37] or automated analyses on chip with high throughput [38–40], enabling researchers to shorten the experimental times as well as to reduce the costs. Another main advantage is the possibility to produce miniaturized systems, that are portable and can be used autonomously without the need of being in a laboratory environment and by a wide range of end users, a feature of major importance when it comes to environmental or diagnostics applications [41,42]. All these features make microfluidics particularly suitable for the production of platforms capable of scaling-up and translating a technology from laboratory to industrial settings [43,44]. From a scientific point of view, fluids at the microscale are dominated by a

laminar fluid regime, a feature that enables precise control within the channels of the fluids themselves as well as of molecules and reagents [30]. Although turbulent microfluidics can be adopted for specific applications, as fluids mixing and particles manipulation [45], the laminar flow is peculiar of microfluidics-based technologies and represents the fundamental prerequisite for many different applications, such as gradients generation, mimicry of the cellular microenvironment, analytes separation [46–48].

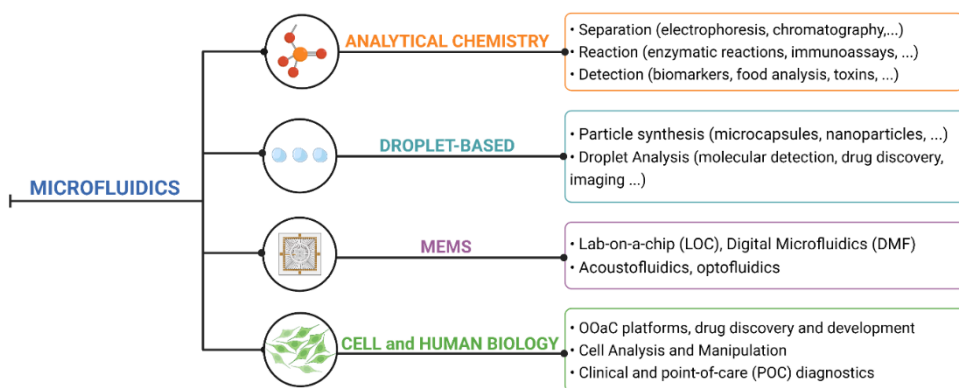


Figure 2.1. Main fields of application of microfluidics. Due to the versatility and multidisciplinary of microfluidics technology, the schematic is not exhaustive and has the objective of representing some of the major fields that have adopted it. Of note to the reader, the four main categories illustrated here (i.e., analytical chemistry, droplet microfluidics, microelectromechanical systems – MEMS- and cell and human biology) have been eventually applied interchangeably; for instance, droplet microfluidics has been used for single cell analysis and DMF has been used for development of POC diagnostics platforms. Created with BioRender.com.

Microfluidics for cell and human biology: OoAc application

In this chapter, we will focus on microfluidics for cell culture application. In the context of cellular and human biology,

microfluidic technology has emerged as an important tool to build relevant three-dimensional (3D) *in vitro* microphysiological systems for the study of human pathophysiology and for drug testing and development [49,50]. Compared to traditional *in vitro* models, since microfluidics offers the advantage of manipulating fluids at the microscale, it enables the study of cellular response to physical factors, such as shear stress or oxygen gradients, and to biochemical cues via exposure to molecules, drugs or growth factors [11,51–53]. Mechanical stretching of cells or application of pulsatile flow on-chip have been used as strategies to mimic tissue-specific mechanics such as for lung, intestine or heart [49,54]. The use of microfluidic platforms enables the development of long-term 3D cell culture systems in complex and physiological- like geometries, co-culture studies and the mimicry of the cellular-ECM interactions [55], with the main goal of creating an organ minimal functional unit that can be easily operated *in vitro* [56]. These platforms are known as organs-on-a-chips (OOaCs) and they are defined as microengineered biomimetic systems used to reconstitute living organs and tissues *in vitro* for modeling their pathophysiology [1] (**Figure 2.3A**). The first OOaC, engineered by Donald Ingber's group from Harvard university in 2010 [12], led to the development of the most used organ-on-a-chip model nowadays: they reproduced the Air-Liquid Interface (ALI) of the lung by culturing alveolar epithelial cells and human pulmonary microvascular ECs on two sides of a porous membrane in a two-channel microfluidic device. Cyclic mechanical strain was applied by introducing lateral vacuum channels, thus

mimicking physiological breathing. This simple yet functional model was used to recreate a long-term model of the ALI, showing *in vivo*-like barrier permeability, enhanced production of surfactants by the epithelium when exposed to air and endothelium alignment under mechanical stretching. Exposure to nanoparticles showed the capability and versatility of the platform to model lung physiological response to inflammatory conditions and the importance of including mechanical stimuli and vascular component to generate a physiologically relevant *in vitro* platform. This pioneering platform paved the way for the design of other many OOaC platforms, where tissue-tissue-like interfaces could be generated to simulate critical physiological barriers, such as that of the blood-brain barrier [57], liver [58] and the epithelial-endothelial membranes in the lung [12], kidney [59] and gut [60], among other human organs and tissues [61–63]. OOaCs can nowadays replicate organ-level functions and multi-organ interactions, representing a cutting-edge technology for disease modeling and drug research. Furthermore, as discussed above, the compactness of these devices and the sample parallelization lead to an overall reduction of experimental times and costs and microfluidic strategy has already shown a great potential as a tool for creating scalable, standardized, high-throughput *in vitro* models, more accessible to non-specific end-users, thus accelerating the translation towards clinical and industrial application [15,30,64].

● **FOCUS ON | Where does microfluidics come from?**

As described by George Whitesides [30,34,65], microfluidics has four parents: molecular analysis, microelectronics, national security and molecular biology.

The oldest one is considered to be molecular analysis, which includes methods such as gas-phase chromatography (GPC) or capillary electrophoresis (CE)[66,67]. These techniques, developed from the 1950s and 60s, allow for the separation of chemical compounds or biomolecules by flowing small amounts of sample in narrow tubes or capillaries, reaching high sensitivity and resolution. The most famous parent of microfluidics is microelectronics [68]: at the beginning researchers tried to directly fit fabrication methods and materials from microelectronics to microfluidics: photolithography as well as silicon and glass were the first players on microfluidics stage. Only later did microfluidics split from microelectronics and semiconductors technology by using new specific microfabrication methods and materials [69]. A lesser known but pivotal forerunner of microfluidics is military detection. Starting from 1994, the DARPA (Defense Advanced Research Projects Agency of USA) substantially contributed to the growth of microelectromechanical systems (MEMs) and the development of miniaturized and portable “laboratories on a chip” with the main goal of the detecting chemical and biological weapons. Molecular biology, and especially genomics in the 1980s, strongly contributed in microfluidics birth and evolution as its fourth “parent”. The interest of scientists in studying and sequencing nucleic acids led to the development of sequencing machines capable of working with small samples to ensure a high sensitivity read-out [66]. An example? The famous PCR (polymerase chain reaction) technique used to amplify a DNA sequence by means of heat was developed in the early 1980s by Kary Mullis. The reaction requires small amounts of liquid, usually 10-200 μ l, so precision equipment is necessary. At the beginning, due to the lack of automated equipment, the reaction was a time-consuming multi-step process that had to be performed manually. The first commercial machine, a simple thermal cycler, was developed in 1987; it made the process reliable and its small dimensions gave the possibility to miniaturize operations as well as to work outside of the lab.

From the 1950s, there was an increasing interest in designing miniaturized systems and components and researchers started to miniature sensors, transducers and other components and to then integrate them within microcomputers to obtain

portable integrated platforms that could be used as environmental or medical monitors/ measurements systems. A pioneering work was carried out by Stephen Terry from Stanford university, who in the mid-1970s produced a miniaturized gas chromatograph (GC) integrated on a silicon wafer [70]. The miniature GC was composed of gas supplier, sample injection system, a capillary column and an output miniaturized thermal conductivity detector. The injection valve and the capillary were fabricated through a micromachining technique onto a silicon wafer while integrated circuit (IC) processing methods, developed starting from late 1950s, were used for the detector microfabrication. This device was considered one of the firsts examples of “laboratory-on-a-chip”. Following in the footsteps of Terry, Andreas Manz, a Swiss researcher and analytical chemist, was one of the first to use microchip technology in the field of chemistry to shrink a laboratory to the size of a chip in the 90s [71,72]. In 1990, he published a paper in which he introduced the concept of miniaturized “total chemical analysis system”, abbreviated to “ μ -TAS”, for chemical sensing, *i.e.* a microfluidic device capable to perform all steps in an analysis [42]. He demonstrated that μ TAS allows for faster and more efficient sample separation (chromatographic or electrophoretic), shorter transport times and reduced consumption of reagents compared to chemical sensors and conventional analysis systems. Moreover, the fabrication of a multi-channel device allowed experiments to be run in parallel. Thus, in 1993, he created a μ TAS on a glass chip that could perform capillary electrophoresis of amino acids in few seconds [72]. The results demonstrated the possibility of creating a miniaturized laboratory-on-a-chip that could be used for complex analyses.

The development of techniques capable of patterning small structures was fundamental in microelectronics as well as optoelectronics; starting from the 1960s, the most used approach to fabricate integrated circuits and other micro-components was photolithography [69]. The name indicates a range of different techniques that provides for the transfer of a pattern through a light source (UV, X-ray, ...) from a photomask to a photoresist on a solid substrate.

Photolithography was invented in the early 1950s, when the U.S. National Bureau

of Standards (NBS, then US Army Diamond Ordnance Fuze Laboratory, DOFL) promoted a program to develop new methods to obtain small electronic circuits that could be easily integrated into military proximity fuzes [73]. From 1952, Jay Lathrop and James R. Nall started using photoresists to pattern germanium. They were able to project light through a specially modified microscope that led to germanium transistors that could be easily incorporated into miniaturized hybrid transistor-to-ceramic circuits. Lathrop and Nall wrote a paper and patented their discovery in 1958-1959, coining the word *photolithography*. Lathrop himself declared: “*The operation actually involved etching, not lithography. However, photolithography sounded higher tech to us than photoetching ... and this misnomer has been used ever since*”. Lathrop and Nall were not the only researchers who worked on this topic. From 1955, Andrus Jules and Walter L. Bond at Bell Laboratories also developed etching (photoengraving) techniques for producing patterns on silicon semiconductors by using oxide layers, an invention patented in 1964 (US Grant US3122817A). However, photolithography turned out to be a difficult process when working with non-semiconductors materials, such as glass and polymers, and from the late 1980s new non-lithographic microfabrication processes started being developed. Researchers were looking for a cheap technology, capable of patterning 3D structures (also on nonplanar surfaces), to control the surface chemistry, that could be used on a wider range of materials, and thus able to overcome the drawbacks of photolithography. And so, soft-lithography was born. The main difference when compared to photolithography was that an elastomeric mold could be used to transfer the pattern instead of a rigid photomask and that a wide range of materials (organic and biological molecules, polymers, etc.) could be directly patterned. Some of the most known soft lithography techniques like replica molding (REM), microtransfer molding (μ T), microcontact printing (μ CT) and micromolding in capillaries (MIMIC) became very successful microfabrication techniques in microfluidics.

The first microfluidic devices were usually made of silicon and glass since the fabrication techniques derived from microelectronics were well known [34]. However, these materials had some issues: silicon is expensive and cannot be coupled to optical microscopy because of its opaqueness while both silicon and glass have low gas permeability, which make them inappropriate for microfluidics applied to biology. Other materials were then investigated for potential use in microfluidic platforms. Researchers were looking for alternative compounds that could be optically transparent, easy to process, flexible and cheap compared to previous ones. Organic polymers seemed to be a good option and in the late 1990s G. Whitesides group of Harvard university introduced a new concept of low-cost microfluidics by using poly(dimethylsiloxane), known as PDMS, as new material for microchips rapid prototyping (Figure 2.2).

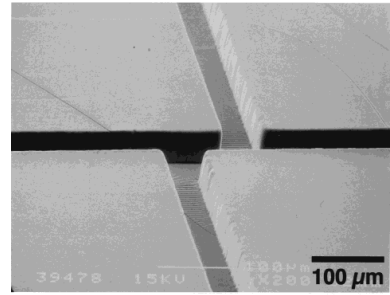


Figure 2.2. Scanning Electron Microscopy (SEM) of the channels of the first PDMS microfluidic device fabricated by replica molding by Whitesides group from Harvard University in 1998. Adapted with permission from D.C. Duffy *et al.*, Rapid prototyping of microfluidic systems in poly (dimethylsiloxane). *Anal. Chem.* 70 (1998) 4974–4984. Copyright 1998, American Chemical Society [20].

The need for alternative materials to PDMS

Although microfluidic devices have been commonly fabricated using silicon [4] and glass [5] via photolithography techniques adopted from microelectronics (See *FOCUS ON / Where does microfluidics come from?*), polydimethylsiloxane (PDMS) is currently the most widely used material for microfluidic devices fabrication since G. Whitesides' group introduced its soft lithography microfabrication in 1998 [20,74]. Its use as standard material for microfluidics is due to

its favourable chemical and physical properties of high optical clarity, its biocompatibility and easy handling due to its elasticity and stiffness (tensile modulus of ~1–3 MPa [75–77]). Furthermore, PDMS microfabrication could be achieved at relatively low cost and little required expertise as compared to traditional materials, such as glass or silicon. PDMS suffers, however, from a number of drawbacks, notably (i) small molecule absorption, (ii) hydrophobic recovery and (iii) transferability of fabrication. Absorption of small hydrophobic molecules into the bulk of the material [78] is problematic in applications that involve soluble factors, as drugs and dyes [79,80], where essential concentrations can be altered and experimental outcomes changed. This severely hinders the utility of PDMS for drug screening, a key area of therapeutic research and development that OOaCs can address. Fast hydrophobic recovery after surface hydrophilization is due to mobile polymer chains [81] and limits the shelf-life of PDMS devices post-fabrication, imposing the devices use within hours of their preparation for effective surface treatments and channel filling. Finally, the poor transferability of fabrication, from small to large-scale, limits PDMS translation into industrial implementation. While PDMS allows relatively facile fabrication of microfluidic devices when compared to glass or silicon-based microdevices [82], its multi-step process results to be difficult to transfer to large industrial-scales [83]. Because of these drawbacks, microfluidic models developed in research using PDMS must thus be reimaged with different materials when aiming to large-scale implementation.

Alternative materials for device fabrication

Alternative materials to PDMS for OOaC application have thus been proposed in the last years and can be categorized as (i) thermoplastics, (ii) elastomers, (iii) hydrogels, (iv) paper-based, (v) resins and (vi) inorganic materials (glass and silicon) [21,84] (**Figure 2.3B**).

Hard thermoplastics are low-cost materials normally produced by melt-processing with high-throughput techniques, as injection molding and hot embossing, or by computer numerically controlled (CNC) micromilling [39–43]. Polystyrene (PS), polycarbonate (PC), polymethylmethacrylate (PMMA) and cyclic olefin homopolymers and copolymers (COPs and COCs) have been used recently for the fabrication of different OOaC devices. PMMA platforms are generally fabricated by CNC micromilling starting from polymer sheets, that are then bonded by thermal or solvent-assisted techniques: complex PMMA-based models, such as skin-on-chip or lung airway system, have been successfully developed, thus offering alternative platforms that overcome the PDMS drawbacks in drug-related studies (Sriram- Humayun) [85,86]. Thanks to its gas impermeability properties, PC has been chosen as fabrication material for microfluidic platforms that require a precise control of the oxygen concentration, as in the work from Shah *et al.*, who designed a PC chip for mimicking the interface between human gastrointestinal tissue and microbiome [87]. Alternatively, COC thermoplastics have been used [58] and devices made of this material are already available on the market, as for the COC-TOPAS[®] chips

produced by microfluidic ChipShop. Comparison studies of different materials for microfluidics have shown that PC and COC show the highest gas permeability and chemical resistance to organic solvents when compared to other thermoplastics and standard PDMS as well as low adsorption of small molecules and high biocompatibility [88].

Thermoplastics, however, have high stiffnesses (tensile moduli of ~1–4 GPa [44]), that make them difficult to be processed at small scales, with subsequent need for expensive molds and process-intensive bonding and interfacing to fluidic setups, that make their use difficult to a wide range of end users.

Elastomers alternative to PDMS have been used in some studies, offering the advantage of higher flexibility compared to hard thermoplastics, tunable mechanical properties and low absorption profiles. Although their use remains relatively limited, polymers such as poly(octamethylene maleate (anhydride) citrate) (POMaC) or tetrafluoroethylenepropylene (FEPM) have been investigated for fabrication of OOaCs. For instance, POMaC has been used by Zhang *et al.* to fabricate vascularized cardiac and hepatic constructs: using layer-by-layer manufacturing, they stacked 25 μm thick POMaC layers patterned by UV photolithography [89,90]. The presence of microholes and nanopores in the scaffold walls ensured physiological-like mass transport and cell migration. The use of a photo-crosslinkable hydrogel provided for tunable stiffness, thus creating an anisotropic construct that closely mimics the myocardium mechanical properties.

Paper, resins and inorganic materials have been adopted as well for fabrication of microfluidic devices for cell culture but some major drawbacks, as the opaqueness of paper and silicon and the expensive complex fabrication of glass, silicon and resins limits their application and scalability when thinking of a translation of the technology [21].

On the contrary, hydrogels have been widely investigated in the last years and the recent combination with tissue engineering approaches, notably bioprinting, and biomaterials has accelerated the transition from non-biomimetic materials such as glass, silicon and PDMS to 3D ECM-like hydrogel-based microfluidic platforms. Many examples can be found in the literature and hydrogels such as Gelatin Methacryloyl (GelMA) [91,92], poly(ethylene glycol) (PEG) [93], gelatin [94], fibrin [95], collagen [96,97] or even decellularized extracellular matrix (ECM) [98], eventually incorporating cells, have been bioprinted, molded or photopatterned for the production of OOaC models [99]. With the main advantages of tunable mechanical properties, optical transparency and properties that mimic the cellular microenvironment, hydrogels represent a valuable alternative to PDMS-based devices. However, they suffer from some limitations, as the need to embed them in rigid frames for manipulation and flow, the reduced resolution and the difficulty in scaling up the fabrication protocols.

Alternatively, the introduction of a class of materials known as soft thermoplastic elastomers (sTPE) for microfluidics has provided for a unique combination of the rapid and high-throughput processing of

thermoplastics with the flexible and easy handling of elastomers like PDMS [100–103]. Styrene-ethylenebutylene-styrene (SEBS) copolymer pellets have been injection molded and extruded and used in absorption tests and for cell culture studies in the form of a membrane-based standard OOaC platform made entirely of SEBS. Results showed lower absorption profiles when compared to PDMS and alveolar epithelial cell adhesion with no need for surface activation [104]. The commercially-available sTPE Flexdym™ (FD™) has been shown to have advantageous material properties for its use as a microfluidic device substrate [27]. It is a soft and flexible styrenic block co-polymer (tensile modulus of ~1 MPa), biocompatible and optically transparent. It can be rapidly hot embossed with high resolution within minutes using microfluidic molds, that are simple and low-cost as compared to the hard thermoplastics molds. Thanks to its hard and soft block co-polymeric structure, FD™ has adhesive and cohesive bonding properties to allow for facile and spontaneous sealing of microfluidic devices after molding without the need for additional adhesives or surface treatment. Indeed, FD™ has been described as a “slow” adhesive polymer foil and has been shown to create reversible bonds with itself and other polymer surfaces, which can be strengthened at high temperatures [27,105]. The sTPE has additionally demonstrated more stable hydrophilization with plasma treatment and lower absorption of small hydrophobic molecules as compared to PDMS [27]. FD™ offers as well the transferability of fabrication that both PDMS and hard thermoplastics lack; it permits rapid and accessible fabrication

in research laboratory settings, while providing a feasible scope for scaling up to industrial production.

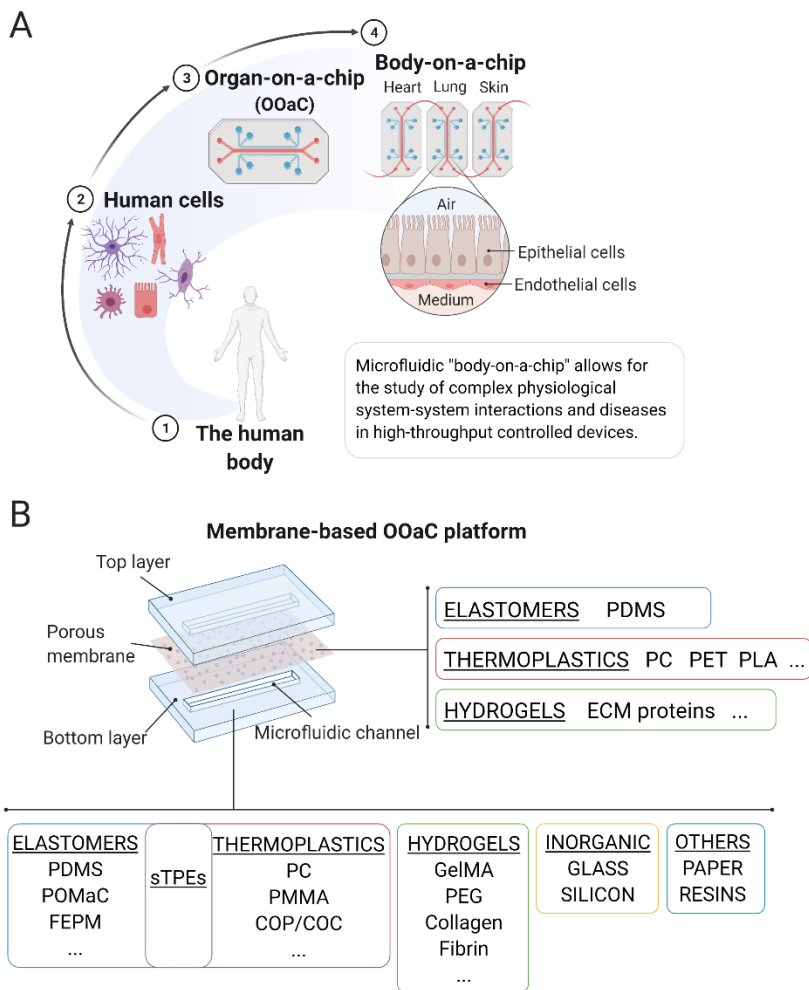


Figure 2.3. OOaC technology and its materials. (A) From the human body to the body-on-chip. (B) Schematic of a membrane-based OOaC platform and materials commonly used for the fabrication of the microfluidic substrate and membrane. Soft thermoplastic elastomers (sTPEs) have been represented at the intersection between elastomeric polymers and hard thermoplastics. Created with BioRender.com.

Alternative materials for membrane fabrication

Since the choice of the materials used to create a microfluidic device is critical to its ultimate function, a given material should be evaluated from two perspectives—its material properties and its fabrication process. The latter becomes particularly influential when complex device geometries are desired. The porous membrane-integrated microfluidic devices, widely used for OOaC design are such an example. The use of thin, porous membranes as a cell culture substrate has shown great value for studying cell-cell signaling, cell filtration and cell migration, in both static [106–108] and more recapitulative dynamic microfluidic models [109–111]. At the forefront of membrane-based cell culture is OOaC technology, whose standard design consists of two adjacent compartments separated by a porous membrane.

Also concerning the materials used for the membrane fabrication in the standard OOaC design, PDMS has been the top choice material. Although protocols for large-scale production of PDMS membranes have been proposed [112], the fabrication of thin, porous PDMS membranes is time-consuming and intricate and often based on custom-made protocols, that vary among different laboratories [113–115], further hindering the reproducible high-throughput production of PDMS membrane-based platforms. In this context, the utilization of commercially available track-etched porous polymeric membranes, biocompatible and available in a range of material compositions, thicknesses and porosities represents an alternative to the custom fabrication of PDMS membranes commonly used [116,117]. Thus, different materials have been adopted as alternative

to PDMS membranes, notably Polyethylene terephthalate (PET) [58] and PC [85,118]. Hydrogels have been used as well as supporting materials and integrated in several commercially available devices [86].

Track-etched membranes reflect one aspect of a growing interest in thermoplastic microfluidic devices, which is not only related to the material property concerns around PDMS but also leverages the wealth of industrial processing for high throughput manufacturing [119].

Rationale and objectives

Microfluidics represents an innovative tool for recapitulating complex intercellular interactions and for mimicking microenvironmental cues, as circulation and mechanical stress. Nevertheless, a wide application and scale up towards industrial settings is still hampered by the materials used for the devices microfabrication. Particularly, polydimethylsiloxane, most widely used in microfluidic applications, poses some constraints in biology studies due to the absorption of hydrophobic molecules and studies on alternative materials have been extensively carried out. Two of the most promising classes of materials, thermoplastics and hydrogels, show however some limitations, notably the high stiffness and the difficult scale-up, respectively. An interesting solution is the adoption of a new class of thermoplastics, called soft thermoplastic elastomers, that show elastic properties compared to thermoplastics and easy scalability compared to hydrogels.

The chapter presents the fabrication of a composite microfluidic device made of sTPE Flexdym™ and a commercially available porous polycarbonate membrane designed for use as a membrane-integrated cell culture platform. The first objective was the development of a rapid and scalable fabrication protocol, that could be also adopted for complex devices, with clear advantages compared to PDMS in terms of timing, throughput and reproducibility. As the material is relatively new, we thus tested the device and studied its properties to assess its potential application in OOaC technology. We thus characterized the bonding integrity that can be achieved with an automated setup as well as the flow characteristics in devices representing typical microfluidic cell culture geometries. Finally, preliminary *in vitro* studies were conducted to

evaluate the biocompatibility of Flexdym™ composite devices. Sustained cell adhesion and culturing was possible inside the devices, giving a proof-of-concept for a facile, robust and scalable microfluidic platform for OOaC applications.

2.2. Design and Microfabrication of a novel composite

Flexdym™ microfluidic device

Mold Fabrication

Microfluidic molds were fabricated using Ordyl® SY 300 dry film negative photoresist (55 μm thickness, ElgaEurope s.r.l., Milan, Italy) on 75 mm x 50 mm borosilicate glass slides (Corning Inc., Corning, NY, USA). After cleaning with acetone and isopropanol and dehydration of the glass slide on a hotplate (Thermo Fisher Scientific, Waltham, MA, US) for 5 min at 150 °C, two sheets of photoresist were laminated onto the slide using a thermal laminator (325R6, FalconK, France) at 120 °C. Using an exposure masking UV LED lamp (UV-KUB 2, Kloé, Montpellier, France), the photoresist was then exposed to UV light (365 nm, 23.3 mW/cm²), for 7 s with a film photomask of the desired pattern (Selba S.A., Versoix, Switzerland) and subsequently developed with a solvent developer (Ordyl® SY Developer, ElgaEurope s.r.l., Milan, Italy) for 10 min to remove unexposed surfaces of the photoresist. Finally, the mold was hard baked for 30 min at 120 °C on a hotplate. This mold can be used for both sTPE hot embossing as well as PDMS soft lithography. Molds with thicker features can be achieved by laminating

successive layers of the photoresist before the exposure masking step.

Hot Embossing

Extruded sheets of FDTM polymer (Eden Microfluidics SAS, Paris, France) of 1.3 mm thickness each were cut with scissors to fit the size of the glass mold and cleaned with tape to remove any large dust particles (**Figure 2.4A**). They were then manually placed into contact with the photoresist features on the mold, ensuring good contact and minimal air bubbles between the FDTM sheet and the mold. A clean, blank glass slide was then similarly pressed into contact with the other side of the FDTM sheet and the entire assembly (mold- FDTM - glass slide) was placed in a vacuum-assisted heat press (Sublym100TM, Eden Microfluidics SAS, Paris, France) between two aluminum plates. The assembly was subjected to an isothermal hot embossing cycle of 2 min at 150 °C and 0.7 bar of pressure, corresponding to approximately 6.5 bar of pressure on the stacked assembly. Spacers of 2.3 mm thickness were placed in between the aluminum plates to achieve a final FDTM thickness of 1.1 mm (**Figure 2.4B**). The assembly was then removed from the heat press and the hot embossed FDTM layer separated from the other layers using isopropanol. Four holes were punched in one FDTM sheet with a steel hole punch at the appropriate port locations and the resulting micropatterned FDTM layer was cut with scissors to the desired size before microfluidic device assembly (**Figure 2.4C**).

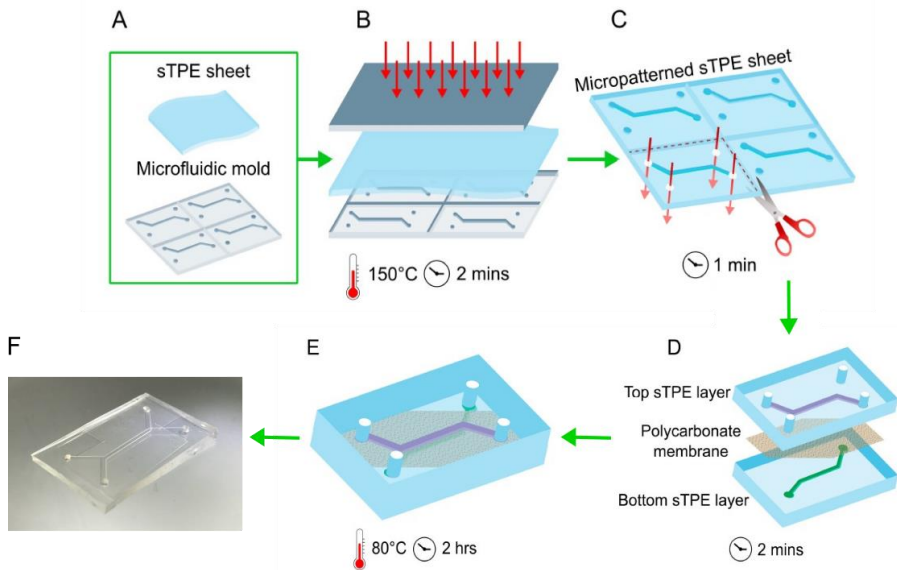


Figure 2.4. Schematic of the fabrication of the composite FD™ membrane-integrated cell culture microfluidic device. (A) a pre-extruded Flexdym™ sTPE sheet and a microfluidic mold. Fabrication consists of (B) a 150 °C hot embossing cycle of the sTPE sheet atop a microfluidic mold, (C) cutting of the micropatterned sTPE to appropriate device size and punching access holes, (D) layering of the micropatterned sTPE layers with an off-the-shelf porous polycarbonate membrane and (E) baking at 80 °C to achieve device bonding resulting from the mobility of the intrinsically adhesive “soft” block polymer chains. The durations of each fabrication step are included. (F) Photograph of the finale device. Platforms with this configuration used for cell culture contained channels of cross section 800 μm x 110 μm (width x height) and 27 mm length.

Device Assembly and Bonding

The FD™-PC-FD™ composite device was fabricated by layering a porous track-etched PC membrane (2 μm pores, 5.6% porosity, 23 μm thickness, Isopore™, Merck KGaA, Darmstadt, Germany) in conformal contact with the micropatterned side of the FD™ sheet, applying pressure with tweezers to ensure contact and avoid air bubbles. Light,

reversible adhesion occurred immediately between the PC membrane and the sTPE sheet. The PC membrane was manually placed with tweezers on the sTPE layer such that it covered the entirety of the channel and its two access holes (top layer in **Figure 2.4D**) but left the remaining two holes unobstructed for access to the channel on the second sTPE layer (bottom layer in **Figure 2.4D**). The second micropatterned sheet of FDTM, with no holes punched, was then similarly layered manually with tweezers atop the PC membrane with the aid of a stereoscope to ensure proper channel alignment. The two central channels were in direct superposition and the second channel ports aligned with the access holes punched in the first sTPE layer. The light adhesion that occurs immediately upon placement of the second sTPE layer could be easily reversed, allowing for any poor alignment to easily be corrected. The device was then inverted such that the sTPE layer with access holes was on top (**Figure 2.4E**). This configuration represents a three-layer, two-channel device, with channel geometries on both sides of the membrane. Alternatively, the second FDTM sheet can be devoid of features in order to create a single-channel device; this variation will be discussed in further detail below in **Section 2.3**. Conical FDTM connectors (Eden Microfluidics SAS, Paris, France) were fixed atop the device ports to interface with microfluidic tubing by first placing the connector on a silicon wafer on a hotplate at 150 °C for 10 s to achieve a smooth, flat surface, then immediately transferring it in contact with the FDTM substrate at the desired port location. This final assembly step can vary depending on the desired method of device interfacing and

connection (such as compression or adhesive-based connectors). The FDTM-PC-FDTM microfluidic device was then baked in a forced convection oven (DKN612C, Yamato Scientific Co. Ltd., Tokyo, Japan) at 80 °C for 2 h to increase the bonding between the three layers (**Figure 2.4E**). Thanks to the intrinsic adhesive characteristics of FDTM, described in **Section 2.1**, there was no need for plasma activation or adhesives. The entire device fabrication process is summarized in Figure 1 and Figure S1 shows more detailed step-by-step images of the fabrication process. The same protocol can be followed to fabricate single or multi-channeled devices made entirely of FDTM, without the addition of the PC membrane, such as the devices for delamination testing, as detailed further in **Section 2.3**.

2.3. Composite FlexdymTM Device Characterization

Delamination Device

The integrity of bonding between FDTM and the PC membrane as well as between FDTM and FDTM substrates was evaluated by using a device with two disconnected channels separated by varying gap distances (**Figure 2.5A**). A FDTM-PC-FDTM device (containing one micropatterned FDTM sheet and one plain FDTM sheet, separated by a PC membrane) was fabricated with a channel-gap design. When pressure was applied to the input, no fluid could flow except in cases where delamination across the gap occurred and allowed for the passage of fluid from the input to the output channel (**Figure 2.5B-C**).

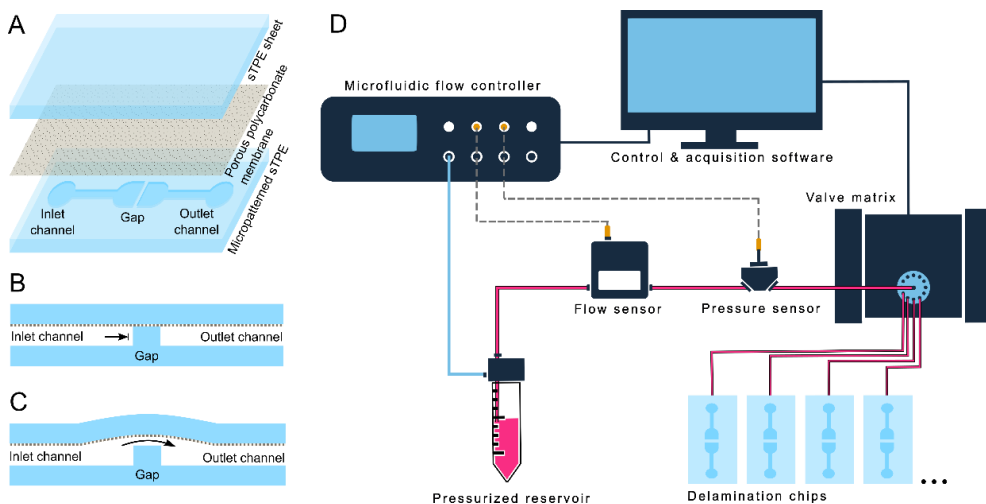


Figure 2.5. Delamination testing setup. (A) Expanded view of the FDTM-PC-FDTM microfluidic chip design for delamination tests, consisting of two disconnected channels separated by a gap of varying distances. The inlet channel is increasingly pressurized, with no flow until the delamination of the PC membrane from the FDTM gap structure occurs, at which point fluid crosses the gap into the outlet channel. (B) And (C) respectively show cross sections of the gap portion of the device before and after delamination. (D) Schematic of the automated delamination testing setup utilizing flow and pressure sensors and a valve matrix in series with a water-filled reservoir pressurized by a pressure controller. Continuous data logging and sensor feedback allowed the sequential automated testing of the pressure capacities of up to 10 microfluidic devices.

Automated Delamination Testing

FDTM-PC delamination devices were tested with a microfluidic setup (Figure 2.5D) consisting of an OB1[®] MK3+ pressure controller (0–2000 ± 0.1 mbar), thermal flow sensor (MFS3, -0–80 μL/min ± 5% m.v.) and capillary pressure sensor (MPS3, -1000–2000 ± 6 mbar), where pressure was applied from the pressure controller and transmitted to the device via water in a reservoir and polytetrafluoroethylene (PTFE) microfluidic tubing (all microfluidic equipment from Elveflow[®], Elvesys SAS, Paris, France).

Delamination devices were connected ensuring that no bubbles were present in the microfluidic system. A stepwise pressure profile between 0 and 2000 mbar gauge pressure, with 50 mbar steps of 30 s each, was executed using the Elveflow[®] Smart Interface software. The pressure controller interface logged the in-line flow and pressure sensor data and was programmed to stop the pressure sequence if a leak was detected. The leak was indicated by a sudden increase to a non-zero flow rate and drop in pressure at the device inlet. A valve multiplexer (MUX Distributor) allowed for the sequential testing of up to ten devices in a single program execution. This synchronized logging of data from both the sensors as well as the pressure controller itself offered redundancy to reduce erroneous results and allowed for the precise confirmation of the moment and pressure at which delamination between the FD[™] and PC occurred. By using a single software interface for both data logging and equipment control, feedback loops could be straightforwardly implemented to cut a testing cycle short as soon as a delamination event was detected and subsequently switch devices. Delamination devices with gap distances between 100 and 1000 μm were tested to evaluate the effect of the bonding distance on the resulting FD[™]-PC bond strength ($n = 5$ per gap distance). Delamination tests were repeated on a set of devices lacking PC membranes useful as control, for comparison of FD[™]-PC bond strength to FD[™]-FD[™] self-bonding. To simulate long-term cell culture and repetitive use, the stability of device bonding was investigated over time: pressure delamination tests were conducted on devices of 400 μm gap distance at different

time points after fabrication (1, 7 and 14 days post fabrication). Devices were aged at either room temperature or in an incubator (Model H2200-H, Benchmark Scientific Inc., Sayreville, NJ, USA) at 37 °C and high humidity rate to simulate cell culture conditions. Device stability under long term pressure conditions was tested with devices in the same delamination setup both with static and cyclic pressures to evaluate the device robustness and durability. Static tests were conducted by pressurizing the devices to 500 mbar for a period of 10 h (n = 5) and cyclic tests by subjecting devices to 10,000 cycles of 0 to 500 mbar pressure at 0.2 Hz (n = 5).

Flow Evaluation

Flow tests were conducted on FDTM-PC devices consisting of a single channel of 27 mm length, 55 μm height and varying width (200, 400, 800 μm) atop a PC membrane and second sheet of un-patterned FDTM. The microfluidic circuit consisted of (i) approximately 50 cm of 0.8 mm inner-diameter (ID) PTFE tubing; (ii) a flow sensor with a quartz capillary of 430 μm ID and 3 cm in length (MFS3, -80–80 μL/min ± 5% m.v.); (iii) a capillary pressure sensor with an effective ID of 0.8 mm and length of 8 mm (MPS3, -1000–2000 ± 6 mbar); (iv) the microfluidic channel; and (v) a 5 cm section of polyether ether ketone (PEEK) tubing of 120 μm ID. The PEEK tubing was inserted into the microfluidic circuit downstream from the chip for added microfluidic resistance to simulate additional components in the system. Pressure and flow rate data were collected across the microfluidic setup (n = 3 devices per channel size) and corresponding fluid shear stresses experienced on the PC membrane

surface were calculated to provide an evaluation of the fluid mechanical conditions achievable within the pressure range that the composite devices can withstand.

In vitro evaluation

Three-layer devices (**Figure 2.4E**) were fabricated to have two chambers separated by a PC membrane, with each chamber having a cross section of 800 μm x 110 μm (width x height) and 27 mm length. The devices were UV-sterilized and pre-treated with plasma (BD-20AC laboratory corona treater, Electro-Technic Products, Chicago, IL, US) for 10 s to increase hydrophilicity of the membranes. A coating of the inner surfaces with 10 $\mu\text{g}/\text{mL}$ fibronectin (MilliporeSigma, Burlington, MA, USA) was done by incubation for 1 h at 37 $^{\circ}\text{C}$. The devices were then flushed with 1X phosphate buffered saline (PBS) supplemented with 1% penicillin/streptomycin (Gibco®, Thermo Fisher Scientific). The upper channel was loaded by pipette with 7 μL of human dermal fibroblasts (HDFs) (ATCC, Manassas, VA, USA) at a concentration of 2×10^5 cells/mL in Dulbecco's Modified Eagle Medium (DMEM) (high glucose, GlutaMAX™ supplement, Thermo Fisher Scientific, Waltham, MA, USA) supplemented with 10% FBS (Corning Inc., Corning, NY, USA) and 1% penicillin/streptomycin. Cells were initially cultured for 12 h atop the PC membrane prior to exchanging media by flow to remove non-adhered cells. After 48 h of culturing, cells were stained with Calcein AM (Sigma-Aldrich, St. Louis, MO, USA) at 4 μM for 20 min. Cells were imaged after Calcein AM treatment to verify their viability and distribution in devices (Zeiss

Observer Z1, Carl Zeiss AG, Oberkochen, Germany). Imaging was similarly repeated at 7 days after seeding. Cell fixing and staining with Alexa Fluor™ 488 Phalloidin (Thermo Fisher Scientific, Waltham, MA, USA) and DAPI (Sigma-Aldrich, St. Louis, MO, USA) was done after 7 days of culturing. Briefly, cells were washed with PBS, treated with 4% paraformaldehyde (PFA) for 15 min at room temperature and then washed three times with PBS. Cells were then permeabilized with 0.3% Triton-X (Sigma-Aldrich, St. Louis, MO, USA) in PBS. Incubation with 488 Phalloidin and DAPI at 0.66 μM and 1 $\mu\text{g/mL}$, respectively, in PBS for 30 min was performed prior to imaging (Nikon C2 Confocal, Nikon, Tokyo, Japan).

2.4. Results and Discussion

2.4.1. Composite Device Microfabrication

FD™ sheets were patterned with microfluidic channels in 2 min via vacuum-assisted isothermal hot embossing. This molding technique is highly compatible with the already existing soft lithography expertise, as there is no need for a specific master mold; molds that are commonly used for PDMS micropatterning, namely those derived from SU-8, epoxy and dry film photoresists (such as the Ordyl® mold used in this work) can also be used for sTPE hot embossing [27]. Hot embossing was followed by punching of ports then layering of subsequent PC and FD™ sheets in conformal contact. The soft, flexible properties of FD™ allowed for facile punching and readily achievable conformal contact, which can be

both reproducibly done in a matter of minutes (depending on the complexity of multi-layer devices requiring alignment), with little training.

The co-polymeric properties of FDTM allow for a reversible bond to be formed, thus avoiding the necessity of using adhesives or plasma activation of surfaces, commonly needed with polymeric microfluidic device sealing. This bonding results from macromolecular motion of the sTPE's ethylene-butylene (EB) soft polymer portion. The EB block possesses a negative glass transition temperature, allowing polymer chain mobility that can be promoted at elevated temperatures to facilitate spontaneous bonding with itself and other materials [105,120]. Full material and microstructure deformation is inhibited, however, by the PS hard block portion of FDTM, whose glass transition temperature remains above the baking temperature. The baking at 80°C for 2 h was the most time-consuming step in the fabrication process, however, baking time and temperature could be modified depending on the bonding strength required for specific device applications. From start to finish, the fabrication protocol resulted in devices ready to be used in under 2.5 h. This represents a significant improvement on the production time of a comparable three-layer PDMS porous membrane device; the time saving is multiplied when a high number of devices needs to be fabricated, considering that the same master mold can be used to fabricate multiple devices in parallel after any 2 minutes of hot embossing. PDMS, on the other hand, relies on relatively slow curing, demanding a single mold be in use until its curing, typically

requiring between 1 to 4 h with baking or 48 h at room temperature [9,77].

The Isopore™ membranes used in this study represent a readily available and inexpensive option compared to the largely used custom-made membranes and similar PC membranes have been effectively used in microfluidic cell culture studies and for OOaC applications [57,85,118,121,122]. The membranes are structurally robust, not requiring special handling techniques and their interaction with FD™ does not affect its spontaneous sealing property, allowing easy interfacing of composite layers. Thin porous membranes in literature, central to barrier model platforms, are often made of PDMS, requiring diverse and often complicated processes that limit their accessibility, reproducibility and scalability. Instead, the PC membrane in combination with extruded FD™ sheets, which can similarly be stored and employed off-the-shelf, allows for rapid full-device fabrication with minimal time investment and planning. However, the mechanical properties of PC would suggest difficulty in elastically stretch the membrane: this presents a limitation when cellular mechanical stimuli are of greater significance, such as when modelling breathing or peristalsis in lung and gut-on-a-chip systems respectively, and more elastic materials would be desirable [12,123,124]. Another potential drawback of these track-etched membranes is their micro-scale thickness, which can limit bright field imaging and cell-cell juxtacrine signaling [116,125,126]. More recent advances in ultra-thin nano-scale membranes have shown improved optical clarity, permeability and cell contact [127] but they

have yet to be made readily available for widespread implementation.

The fabrication of these composite devices represents a highly accessible and transferrable process. It leverages the elastomeric properties of sTPE materials for facile and inexpensive production at small lab-scales that shares equipment and know-how from soft lithography techniques, while being higher throughput than PDMS production. The thermoplastic nature of FDTM and the simplicity of fabrication steps gives scope for the scaling up of the developed fabrication protocol. Injection molding or roll to roll hot embossing can be envisioned for the fabrication of large quantities of highly reproducible devices: this transferability from lab to industrial-scale is in sharp contrast to both PDMS and hard thermoplastic microfluidics.

2.4.2. Material Bonding Characterization

Automated Delamination Testing

We developed an automated pressure testing setup to characterize the bonding strength between FDTM and PC membranes in a robust and precise manner. The developed setup allowed the sequential burst testing of up to ten samples with no user monitoring, regulated by feedback from continuous logging of pressure and flow rate data. By varying the gap distance of the delamination device, the bonding characteristics of small features inherent to microfluidics could be investigated. This is significant in understanding the minimum feature sizes attainable with given materials in cases where, for

example, thin channel walls or micro pillars are desired. A method of effectively sealing a microfluidic device is an integral part of its design and implementation and remains a continual challenge faced by the microfluidics community in the evaluation of new materials [128]. Standardized leak/burst testing thus becomes imperative in assessing sealing techniques. Accordingly, while no standardized method specific to microfluidic applications exists, a wide variety of bond testing techniques have been used. This includes flow rate-based evaluation in flow-through channels and the pressurization of closed channel structures, both of which often rely on optical detection of leaks [129–134]. In comparison to the automated system developed here, these existing methods remain low-throughput and, since they examine the leaking of a device from the channel structure toward the exterior of the device, often representing millimeters or centimeters of bonding distance, they often lead to inaccurate or misleading data. In this work, we thus proposed a reproducible technique for bonding test that is both more representative in a microfluidic context and higher-throughput than existing methods, two fundamental aspects in the development and evaluation of new materials for microfluidic devices.

Flexdym™ - Polycarbonate Bonding Strength

To evaluate the integrity of the FD™-PC bond, we carried out delamination testing to assess the suitability of the composite FD™-PC devices for cell culture applications. More specifically, by using the gap-channel delamination device, we investigated the minimum bonding distance that could be attained with the fabrication protocol

developed. Results from delamination tests showed a linear increase of the pressure capacity from 529 ± 318 mbar with a gap distance of $100 \mu\text{m}$ to 1802 ± 186 mbar with a gap distance of $1000 \mu\text{m}$ (noting that a maximum testing pressure of 2000 mbar was used, which, accounting for some pressure drop between the pressure controller and the devices, corresponded to a maximum pressure of ~ 1880 measured at the devices) (**Figure 2.6A**). In comparison, the control group (FDTM-FDTM devices) showed an overall increase in pressure capacity to ~ 1500 mbar and above at all gap distances. At gap distances of $300 \mu\text{m}$ and above the pressure capacity consistently corresponds with the bulk pressure capacity found by Lachaux *et al.* using a similar bonding protocol [27]. It is critical to note that also at FDTM-FDTM gap distances of 100 and $200 \mu\text{m}$, the data showed increased variability. This might be due to a limitation of the manual process using tweezers when the device design presents small features or to faulty glass mold patterns. One potential way to minimize this variation would be through the use of microscope-assisted or automated procedures when creating conformal contact but this would require more time invested per device. Minor spontaneous resealing of gap devices was observed after delamination occurred and device pressurization was released, without an additional baking step.

The higher pressure capacity of FDTM-FDTM devices as compared to FDTM-PC devices was likely due to a high self-bonding capability of FDTM, as the bonding mechanism of such styrenic block copolymers relies on the mobility of EB polymer chains at the interface of the

two surfaces in contact [120]. Since the PC does not contain the same EB blocks, it follows a weaker interaction with FDTM. Furthermore, PC has a higher glass transition temperature of ~150 °C that is not reached in the bonding procedure, which could result in reduced interaction due to polymer chain immobility.

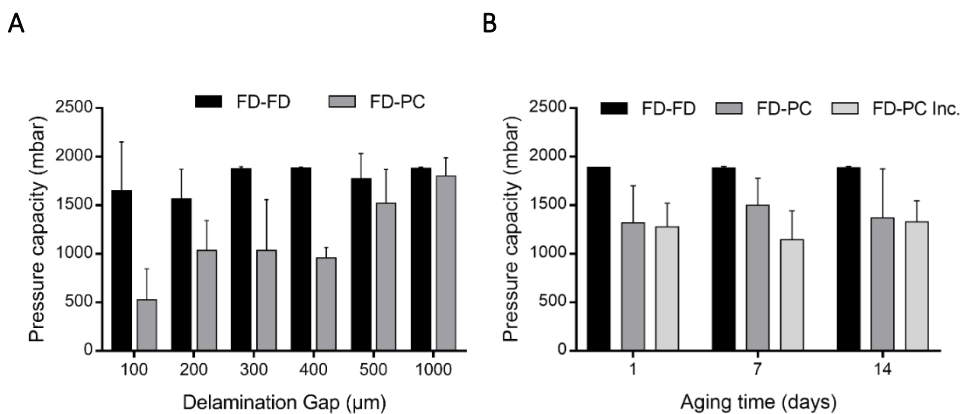


Figure 2.6. Evaluation of FD devices bonding strength. (A) FDTM-PC and FDTM-FDTM pressure capacities (mbar) were evaluated via delamination testing of devices with gap distances from 100 to 1000 µm. FDTM-PC devices show reduced bonding strength compared to FDTM-FDTM bonding but reliably withstand pressures of 500 mbar at gap distances of 200 µm and above. (B) Pressure capacities of FDTM-FDTM and FDTM-PC devices (400 µm gap distance) at 1, 7 and 14 days after fabrication (aging time). An additional set of FDTM-PC devices was aged in high humidity, 37 °C incubation (FDTM-PC Inc.). n = 5 devices per dataset, data shown as mean ± SD.

The FDTM-FDTM bonding could be facilitated as well by the FDTM elastomeric properties while for FDTM-PC surfaces there was a discrepancy of flexibility, that likely caused lesser contact. Any unreliable contact would be accentuated at smaller scales and is indeed evident in the variability of FDTM-PC bonding at smaller gap distances, as well as in that of FDTM-FDTM. Nevertheless, at a

bonding distance of 1 mm, a distance that typically defines the material bond that seals a channel from its external environment, FDTM-PC devices withstood maximum testing pressures and, for gap distances of 200 μm and above, pressures of 500 mbar and greater, that are generally sufficient for cell culture applications. The suitability of FDTM-PC device capacities in the context of their use for cell culture is discussed further in **Section 2.4.3**. While PDMS membrane-integrated cell culture systems have not expressly characterized the bond strength, most platforms of this type utilize oxygen plasma bonding between the PDMS slabs and the PDMS membrane [60,113,115]. Thus, the closest analog to FDTM-PC delamination data may be found in burst testing conducted in PDMS-PDMS plasma bonded systems. Plasma-treated PDMS-PDMS systems have been reported ranging from approximately 0.7 to 4 bar, being highly dependent on oxygen plasma parameters [133,134]. In contrast, PDMS-PDMS sealing based only on conformal contact (without plasma surface activation) has been shown to leak at pressures above \sim 400 mbar [135]. Additionally, PDMS devices that use thermoplastic membranes, in a similar “sandwiched” configuration, primarily use a PDMS glue/mortar method [129] or chemical surface modification for covalent bonding [136]. These methods result in crosslinked or covalent bonds with maximum burst pressures of 1–1.2 bar for PDMS mortar and \sim 2 bar for chemical bonding. Thus, we demonstrated the validity of the bonding strength data obtained for both FDTM-FDTM and FDTM-PC devices, with results

comparable or higher to those found in literature for PDMS-based microfluidic devices.

To investigate any bonding degradation that could occur resulting from the increased temperature and humidity conditions over time, a complementary set of delamination tests were performed: devices of 400 μm gap distance were used and tested with and without incubation at 37 °C and high humidity to mimic to cell culture conditions for up to 14 days (**Figure 2.6B**). 400 μm devices were chosen, as they were found to be the largest gap size that consistently delaminated within the test pressure range. After 14 days in incubation conditions, FDTM-PC devices withstood pressures of 1274 ± 225 mbar, as compared to FDTM-PC devices tested one day after fabrication, which withstood pressures of 1280 ± 241 mbar and 1319 ± 382 mbar, with and without incubation conditions, respectively. Kruskal-Wallis non-parametric test ($p < 0.05$) was performed separately on FDTM-PC and FDTM-PC with incubation groups to compare the pressure capacities over time (1, 7 and 14 days). Results revealed no significant difference in the integrity of the FDTM-PC bond over time and under exposure to cell culture conditions ($p=0.69$ and 0.43 for FDTM-PC and PD-PC Inc. respectively), indicating the suitability of such devices for long term cell culture studies.

Continuous fluidic perfusion of cells for transport of nutrients, waste and soluble factors is one of the main advantages of microfluidic platforms for cellular biology [137]. To evaluate the quality of bonding of the composite devices and their longevity for cell culture, we investigated the bonding behavior of FDTM-PC under constant

pressure for extended time periods (500 mbar for 10 h) or under cyclic pressures (0 to 500 mbar, 0.2 Hz, 10,000 cycles). Devices of 400 μm gap distance showed no delamination resulting from constant or cyclic pressurization, demonstrating robust and reproducible performance under realistic working conditions.

Flow-Pressure Correlation

The influence of shear stress on cells is a significant factor that must be considered when recapitulating *in vivo* conditions inside of a microfluidic device. It has been shown to have a major impact on cell differentiation and function, such as drug metabolism and cytokine secretion [138,139]. Thus, the ability to implement and control the appropriate shear stresses on a cell population should be evaluated during the design and fabrication stages of a device development. Here, flow tests of FDTM-PC composite devices were conducted to understand the flow rates and calculate the shear stresses attainable inside of our devices, as a contextualization of the device pressure capacity results obtained through delamination testing. A design consisting of a simple channel of varying widths atop a PC membrane was used as a model to represent geometries and flow characteristics typical of barrier model cell culture chambers in literature, in which there is no flow across the membrane, most notably models developed by Harvard University's Wyss Institute [59,124,140].

Figure 2.7A shows the linear relationships between the pressure measured at the inlet of the device and the flow rates in our

microfluidic setup and **Figure 2.7B** shows the corresponding shear stresses imposed on the surface of the membrane, as determined by the following equation describing the wall shear stresses τ_w of laminar Newtonian fluids in a closed rectangular geometry (**Equation 2.1**):

$$\tau_w = \frac{6\mu Q}{b \cdot h^2} \quad (2.1)$$

where μ is the dynamic viscosity of water (8.90×10^{-4} Pa·s at 25 °C), Q is the fluid flow rate, b is the channel width and h is the channel height [141]. This approximation of wall shear stress assumes parabolic Poiseuille flow in the microchannel, useful for estimating wall shear stresses in rectangular channels when flow is along the length of the channel and $w > h$. Depending on the channel dimensions used, flow rates of up to ~ 150 $\mu\text{L}/\text{min}$ and shear stresses of up to ~ 140 dyne/cm^2 could be achieved by applying 500 mbar or less of pressure to the composite devices. The results show the devices give ample range of control over fluid conditions and are suitable to generate shear stresses for typical *in vivo*-like cell culture conditions, which are normally below 25 dyne/cm^2 [142]. The relatively low pressures required for such applications indicate that the FDTM-PC bonding strength would be sufficient for cell culture applications, even with the presence of small features.

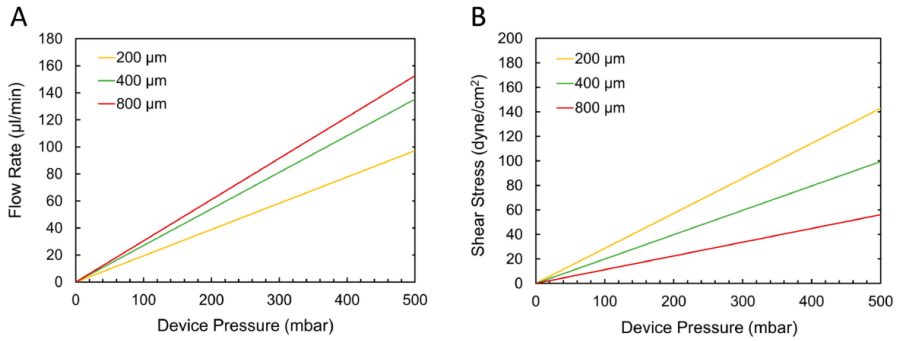


Figure 2.7. Flow-pressure correlation and shear stress graphs of FD™-PC devices. (A) Flow-pressure correlation in FD™-PC devices from tests measuring the flow rate in a straight microfluidic channel (of width 200, 400 or 800 µm) and the corresponding pressure at the channel inlet. Within 500 mbar of pressure applied at the device, flow rates of up to approximately 150 µL/min can be reached. **(B)** Wall shear stresses that can be achieved in each of the example devices, as calculated from the flow rate data in **(A)**, depending on the pressure applied. Shear stresses of up to approximately 140 dyne/cm² can be generated with pressures of 500 mbar and below. It must be noted that these relationships are dependent on the microfluidic resistance of the entire microfluidic system, which will inevitably vary from experiment to experiment, depending on the type and amount of devices, instruments and tubing that are being used. The introduction of a section of high-resistance PEEK tubing in the experimental flow setup downstream from the FD™-PC devices served to simulate additional resistance that may exist in a setup and thus provide a conservative estimate of what pressures would be required to achieve a given flow rate. These results provide an aid in translating the pressure-based delamination findings into a more practically useful context (many microfluidic cell culture experiments depend on defining fluid flow rates or shear stresses rather than pressures) in order to assist potential users in understanding the capabilities of these devices.

2.4.3. Preliminary *in vitro* studies

sTPE microfluidic devices have been used previously for cell culture in microfluidics [102,105], however, there has been limited published data associated with FD™ and its implementation in cell culture systems. To our knowledge, two different FD™ formulations

have been previously reported in only two instances with cell culture work—(i) a moldable film formulation of FDTM, similar to the one used in this study, and (ii) a spin-coating formulation named FlexdymSC. The first showed cultured yeast cells while demonstrating reduced absorption of a chemical division inhibitor due to FDTM's material properties [27] and FlexdymSC was shown to sustain culture of endothelial progenitor cells over four days [143]. Due to the limited published literature on culturing cells within FDTM microfluidic devices, we evaluated the possibility to maintain cultured cells within a FDTM composite device for longer time. To this end, we cultured HDFs within our FDTM-PC-FDTM microfluidic devices for up to 7 days, with cells being seeded on the top of the PC membrane in the devices' upper channels. Results from Calcein AM labeling showed high cellular viability, as checked at day 2 and 7 after seeding (**Figure 2.8A-B**). Moreover, sustained cell adhesion and spread morphologies were observed at day 7, after fixation and staining with phalloidin for visualization of actin filaments (**Figure 2.8C**). The thickness and porosity of the PC membranes resulted in some difficulty in observing the cells under bright field illumination while it did not pose a problem for fluorescent imaging. Although perfusion has been shown to prime and stimulate more uniform cell alignment, proliferation and confluency throughout the microfluidic device, here we focused on verifying the material and device configuration suitability for sustained cell culture over multiple days. This was particularly significant as sTPE materials similar to FDTM are known to have one to two orders of magnitude lower oxygen

permeability than that of PDMS [144,145]. Our results suggest that under static culturing with media exchanges every other day cells maintained good adhesion with spread morphologies over 7 days within the composite devices without the need for more frequent perfusion. These preliminary data confirm the potential use of this material and device configuration for barrier-like cell culture systems.

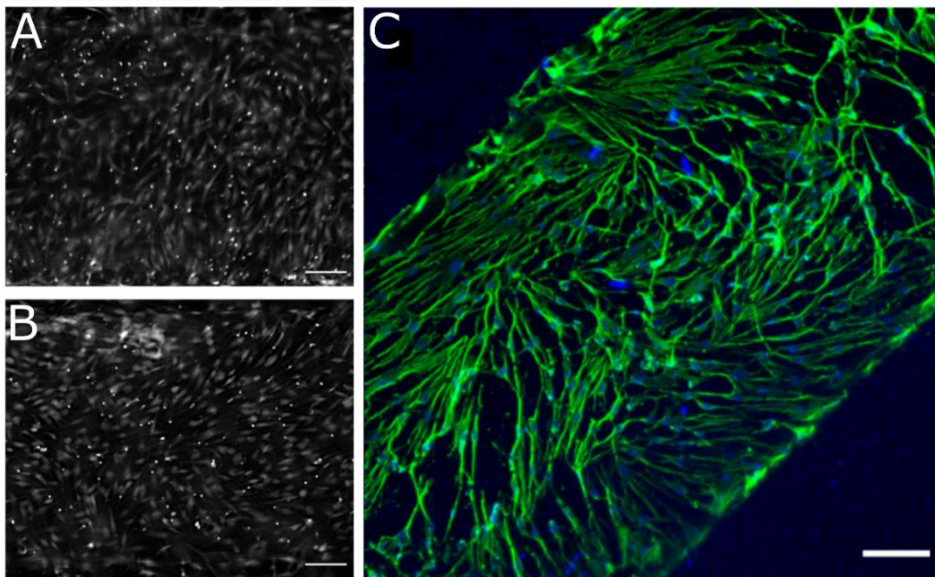


Figure 2.8. Human dermal fibroblasts cultured in FDTM-PC-FDTM devices. Widefield fluorescence micrograph of HDFs cultured in the top layer channel on the polycarbonate membrane. Cells were stained with Calcein AM in the device and imaged at day 2 (A) and 7 (B). (C) HDFs were cultured for 7 days prior to being fixed and stained with 488-Alexa FluorTM 488 Phalloidin (staining for F-actin, green) and DAPI (nuclear, blue) and imaged by confocal microscopy: they presented a primarily spindle geometry, commonly seen at high confluency. Scale bars = 150 μm .

2.4.4. Drawbacks Compared to PDMS

When compared to three-layer, membrane-integrated PDMS microfluidic devices, our composite sTPE system presents a few notable drawbacks. (i) The PC membranes have higher thickness and stiffness in comparison to porous PDMS membranes in the literature [116,125]. The more significant thickness of the thermoplastic membranes and their material properties reduces optical clarity, notably for bright field observation. Additionally, the medium diffusion and cell-cell interaction, from one side of the membrane to the other, are reduced due to the increased distance [126]. Furthermore, the non-elastomeric properties of the PC membrane prohibit membrane stretching for mechanical stimuli of cells, typical of certain OOaC devices [12,124]. (ii) Micropatterned sTPE sheets, in this and previous studies, are rather thin substrates, measuring ~1 mm in thickness, which can introduce complications when interfacing microfluidic tubing with the device, requiring an additional connector solution. While numerous connector solutions exist, such as the conical sTPE connectors used in this work, this represents an additional fabrication step to use the sTPE device in a microfluidic setup. PDMS devices, on the other hand, can simply be fabricated with tunable thickness to interface tubing directly into an access port. (iii) Styrenic block copolymer sTPE materials, like Flexdym™, are known to have significantly lower oxygen permeability than PDMS [144,145]. While this did not pose problems for culturing cells in this work, it could potentially represent a major drawback in certain geometries or flow regimes,

requiring the user to incorporate specific gas control protocols to maintain appropriate oxygen levels inside the device.

2.5. Conclusions

In this chapter, a brief introduction to microfluidic technology and its main applications has been presented. Focusing on microfluidics for cell biology and specifically organ-on-a-chip, we have provided an overview of the features and weaknesses of the most common material used for devices microfabrication, polydimethylsiloxane. Alternative materials for the production of membrane-based microfluidic platforms have been discussed as well. In this context, we have proposed an innovative soft thermoplastic elastomer, Flexdym™, for a rapid and scalable fabrication of membrane-based chips for OOaC applications. Using Flexdym™ and a commercially available porous polycarbonate membrane, we have developed a composite microfluidic platform that can be fabricated in under 2.5 h with rapid hot embossing and facile self-sealing. The microfluidic device consisted of a membrane-separated chamber, similar to the geometries of OOaC devices in literature. The bonding strength of the devices was evaluated by testing the pressure withstood between the FD™ substrate and the PC membrane. An automated pressure delamination system was designed to reproducibly test microfluidic material bonding in a high-throughput manner. FD™-PC bond strength reliably withstood pressures of 500 mbar at bonding distances of 200 μm and greater, demonstrating the suitability of our device for cell culture applications, further highlighted by confirming no degradation of bonding strength in cell culture-like conditions and

long-term pressurization. Finally, preliminary *in vitro* experiments performed by culturing human dermal fibroblasts within the composite devices showed good cell adhesion and a maintained culture over one week, demonstrating their potential to be used for more complex OOaC models. The promise that microfluidic cell culture technology offers in the advancement of *in vitro* platforms for drug testing and disease modelling has been tempered by the drawbacks of PDMS and the subsequent need for novel material solutions [146]. Our work introduces an innovative microfluidic platform composed of alternative materials that can be fabricated with a fast, easy and high-throughput process and with proven efficacy for microfluidic biology applications.

3. Development of a microfluidic platform compatible with Super-Resolution optical imaging

Results concerning use of primary liver cells and super resolution imaging acquisition and processing presented in this chapter have been obtained in collaboration with P. Papakyriacou (Dr. P. Lalor's Group), Centre for Liver Research and NIHR Biomedical Research Unit, University of Birmingham, UK and A.R. Faria (Dr. L. Schermelleh's Group), Department of Biochemistry, University of Oxford, UK.

STATEMENT OF SIGNIFICANCE

Although super-resolution (SR) microscopy techniques can unravel subcellular and biomolecular mechanisms in an unprecedented way, studies are still limited to imaging of two-dimensional substrates, such as cells cultured on a dish or tissue sections. In this chapter, the fabrication and validation of a microfluidic platform for cell culture compatible with SR microscopy is presented. The capability of imaging living cells cultured on-chip at the submicron scale provides a new tool for biological in vitro studies while recapitulating in vivo-like dynamic processes, such as microcirculation.

3.1. The need to take into account the imaging system

Going beyond the diffraction limit

By going beyond the diffraction resolution limit of light, Super-Resolution microscopy (SRM) techniques represent nowadays a cutting-edge tool to investigate and discover subcellular and molecular dynamic processes [147–149]. Indeed, imaging of cellular structures at the nanoscale in the past has been normally implemented by electron microscopy (EM) methods, as scanning (SEM) or transmission (TEM), that, suffer however from important limitations, notably the need to work with fixed specimens under static conditions [150]. On the other side, conventional optical imaging techniques have been largely adopted for studying living samples under spatio-temporal dynamic conditions but are limited to a lateral resolution of 200 μm (for oil immersion lenses in the blue light) due to light diffraction [151]. A variety of fluorescent-based SRM approaches exists nowadays, with differences mainly depending on the physical principle used for the specimen excitation and the emission detection [5,147,152]. Briefly, the SRM techniques have been classified into diffraction-unlimited, also known as nanoscopy techniques, and diffraction-limited methods. The diffraction-unlimited methods rely on the on-off switching or modulation of fluorophores to discern close molecules: the diffraction limit can be then overpassed by the ability of exciting and detecting separately adjacent fluorophores, that would be otherwise detected as a single spot by conventional optical microscopy. In this

category, two classes are distinguished, namely targeted and stochastic nanoscopy. Stimulated emission depletion (STED) and reversible saturable optical linear fluorescence transitions (RESOLFT) microscopy are the two main targeted methods and rely on the direct focusing of light to achieve the on-off fluorophore switching [153]. Otherwise, single molecules can be excited by random (stochastic) switching, a concept named single-molecule localization microscopy (SMLM). In this category, photo-activated localization microscopy (PALM) and stochastic optical reconstruction microscopy (STORM) are the most known techniques, whose widespread investigation is related to the use of wide-field illumination, thus low-cost setups could be easily built. Although theoretically unlimited resolution can be achieved by these methods, empirical limitations restrain *de facto* the resolution to tens of nanometers. Moreover, some features as small fields of view and long acquisition times represent important drawbacks for cell biology applications. Diffraction-unlimited SRM methods have been applied to biology for studies on three different scales: investigation of single molecules, protein clusters, as lipid rafts, focal adhesions or neuronal synapses, and supramolecular intercellular structures, as cytoskeleton, mitochondria and DNA have been conducted by both targeted and stochastic SRM [147,154–158].

On the other side, diffraction-limited microscopy normally enables only a 2-fold improvement of the diffraction limit but faster acquisitions and no need for high light intensities make these techniques particularly suitable for live cell imaging of dynamic

processes with reduced phototoxicity. For instance, AiryScan uses a detector array rather than a single detector typical of confocal microscopes, allowing for faster acquisition and reduced signal-to-noise ratios [159]. By generating thin light sheets, lattice light-sheet (LLS) microscopy allows for reduced photodamage and fast 3D scanning and has been successfully used for whole living cells and even embryos imaging [160,161]. However, both these techniques suffer from relatively reduced increase of the resolution and LLS requires specific costly equipments and samples clarification. Thus, an interesting alternative is represented by structured illumination microscopy (SIM), that will be the focus of this section.

SIM is a wide-field deconvolution approach that relies on periodic interference patterns to illuminate the sample [162–165]. Resolution in conventional microscopy is determined by the diffraction limit, which depends on the objective numerical aperture (NA) and the light wavelength (λ). In the reciprocal (frequency) space, the resolution in two dimensions is described by a circular observable region in which the diameter is determined by the maximum (cut-off) frequency (thus, maximum resolution) corresponding to the diffraction limit itself ($2NA/\lambda$) (**Figure 3.1**, conventional microscopy) and determined by the optical transfer function (OTF). The idea behind SR-SIM is to collect information outside the circular observable region so as to increase the resolution in the real space. This has been implemented by exploiting the Moiré effect: when overlapping two periodic patterns, a coarser interference pattern,

called Moiré fringe, is obtained. Here, one pattern corresponds to the illumination pattern used for the imaging and practically generated by a phase grating while the second one is the sample, that contains unknown distribution of fluorophores. When switching to the reciprocal space, the circular observable region of typical conventional microscopy will thus contain new frequency components with a displacement corresponding to the Moiré fringes in the real space. Thus, after acquisition of the raw data, the super-resolved image is reconstructed by separating and deconvolving the frequency contributions to create new observable regions. By combining different phases and orientations of the illumination patterns, information on an observable region twice bigger compared to the original one can be collected, thus increasing twice the spatial lateral resolution of the reconstructed image (**Figure 3.1**).

Analogously, the resolution can be improved in 3D by creating interference patterns in both lateral and axial directions; in this case, the observable region will have a torus-like shape and the resolution can be improved by adding the new frequency contributions from both the dimensions, thus implementing 3D SIM. With this technique, a lateral resolution of ~ 120 nm and an axial resolution of ~ 300 nm have been achieved, doubling the diffraction limits [166,167]. Compared to other SRM methods, SIM offers the advantage of using low light intensities (few W/cm^2 compared to tens or hundreds of MW/cm^2 of STED [167]) and the possibility to do multicolor imaging without the need for specific fluorophores, as switchable fluorophores required for SMLM techniques [168].

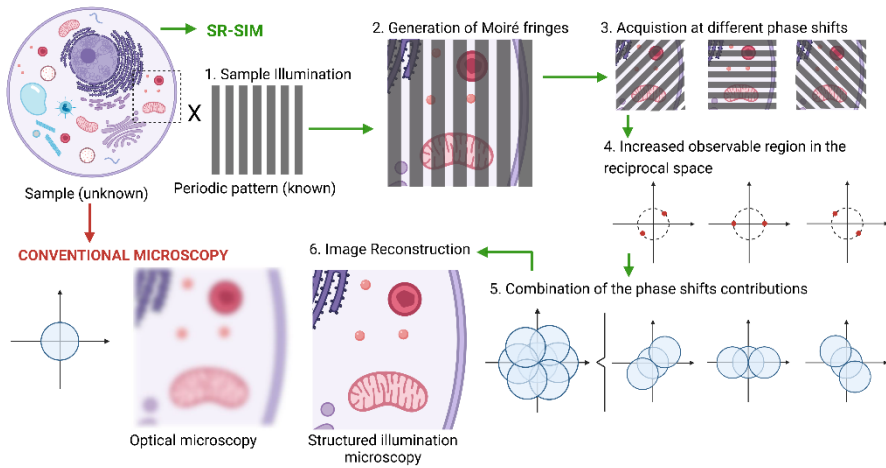


Figure 3.1. Schematic of SIM working principle for enhanced lateral resolution.
Created with biorender.com.

In the last decade, many different SIM-based methodologies have been engineered, all relying on patterned illumination, notably to further improve the spatial and temporal resolution capabilities. Techniques as non-linear SIM [169–171] and point or multi-point SIM [172] and combination of SIM with other microscopy and SRM approaches [165,173–175] have been described in detail elsewhere.

Despite SR-SIM has been widely used for the study of fixed specimens due to limited capabilities of commercially available setups [165], the recent advancements on the development of setups with increased temporal resolution have pushed this technology to be increasingly adopted for live cell studies [7,176,177]. Already in 2011, M Gustafsson’s group demonstrated the capability of imaging living cells by 3D SIM, thus overcoming some of the major drawbacks of other SRM techniques, such as photobleaching and photodamage, limited field of view (STED) or limited speed

(SMLM). They imaged microtubules of living *Drosophila* S2 cells and mitochondria of HeLa cells over hundreds of time points, demonstrating high lateral and axial resolutions (120 and 360 nm respectively) and the possibility to study mitochondria dynamics with a speed of 0.12 $\mu\text{m/s}$ and with low dye bleaching [167]. The data acquisition and pattern switching was however hindered by the use of electron-multiplying charge-coupled device (EMCCD) camera due to the long exposure time. The year after, they reported time-lapse dual color imaging of microtubules and mitochondria of living HeLa cells and cytosol and actin filaments of neurons with a temporal resolution of 8.5 s, that could be achieved by using a complementary metal-oxide semiconductor (sCMOS) camera [178]. Recently, studies conducted on living human bone osteosarcoma cells by 3D SIM were used to investigate the role of actin and myosin filaments during cellular movement [179]. Therefore, SR-SIM holds great potential for the analysis and discovery of dynamic subcellular processes at the nanoscale, that have been unresolvable so far by conventional microscopy.

In the frame of DeLIVER project, special focus has been paid on studying the liver sinusoidal endothelial cells (LSECs). Although hepatic models have deeply investigated the function of hepatocytes, the liver parenchymal cells, often at the expense of the other cell types, the fundamental role of LSECs in liver pathophysiology is today well known [180–182]. LSECs compose the endothelium of the liver capillaries, called sinusoids, and they play an active role in liver homeostasis, blood flow regulation and filtration of metabolites

as well as in liver diseases, such as chronic and acute liver diseases and cancer [181]. Compared to other endothelial cells, as in the lungs, brain and skeletal muscles, that form a continuous endothelium [183,184], liver sinusoids are a discontinuous endothelium, characterized by intercellular gaps, with LSECs lacking basement membrane and presenting open nanometric pores called fenestrations or *fenestrae*, features intrinsically related to their filtration and transportation functions [185–187]. The *fenestrae* are dynamic structures, eventually organized in sieve plates, involved in the filtration and transfer of molecules and the maintenance of hepatocytes and other non-parenchymal cells under homeostasis [188]. In fact, in pathological conditions, when exposed to certain drugs or during aging, LSECs have been proven to undergo important morphological and physiological changes, the major one being their capillarization, *i.e.*, the loss of fenestrations and formation of basement membrane, with consequent hepatic impairment [24,189–192]. First observed in rat livers by electron microscopy [193,194], their nanoscopic size (50-200 nm) make SRM techniques particularly suitable for their investigation [188]. 3D-SIM and STORM, eventually combined, have been used to investigate the LSECs morphology and organization within the surrounding microenvironment [23,174,191] and their response to different drugs [195], leading to novel findings as the distribution of sieve plates in between membrane lipid rafts [196]. Recently, STED imaging of dedifferentiated LSECs showed the intact capability of LSECs to re-form fenestrae [197]. However, all these studies are limited by the

use of rodent cells and imaging after fixation. An interesting work has recently reported the use of atomic force microscopy (AFM) [198], also previously adopted [199], for the investigation of living LSECs fenestrae dynamics, eventually after exposure to drugs, with high resolution and fast acquisition, though also performed on murine specimens. Furthermore, AFM has some drawbacks, as limited axial resolution and risk to damage the samples, that fluorescence microscopy could overcome. Another important drawback to these studies is that loss of fenestrations has been demonstrated to occur *in vitro* after few hours from the isolation and plating of primary LSECs in 2D cell culture plates, with dedifferentiation and apoptosis within 48 hours [186,200], a phenomenon that limits a longer-term study of these structures dynamics. In this context, microfluidics has been shown to be a powerful tool for maintenance of cellular phenotypes and functions over prolonged periods due to the recapitulation of microenvironmental cues [201,202]. To decipher the complex dynamic subcellular structures of LSECs, further studies should therefore focus on the use of human cell sources and studies on live specimens, ideally in a dynamic microenvironment.

Combination of microfluidic platforms and SR microscopy for dynamic studies

Despite the relevance of the results obtained so far by using SRM, the choice of cellular model is equally significant and, as discussed in the previous chapters, the use of fixed samples and 2D cellular substrates represents a major limitation. Thus, although still limited

examples have been reported in literature, researchers have started engineering microfluidic devices compatible with SRM. Microfluidic platforms have been developed for the immobilization and study of mammalian cells and bacteria by SMLM [203]. Cattoni *et al.* proposed a simple microfluidic chamber composed of a parafilm mask with channels of 130 μm sealed between a glass coverslip for imaging and a glass slide for stability [204]. The chamber was used to immobilize bacteria cells to different coatings, offering the advantage that the seeding, washing and staining could be done on-chip by flowing the products of interest. 3D-SIM was used to confirm cells flatness while bacteria growth and division were studied by PALM imaging in time-lapse experiments. The data collected allowed for automatic sorting and classification of different bacteria populations based on proteins distribution and DNA localization within the cells. Recently, a PDMS microfluidic device was used for on-chip culture and labeling of living mammalian cells from monkey and coupled to STORM SR imaging for study of mitochondrial dynamics [205]. STORM has also been used for the study of cilia dynamics: a PDMS device was used to culture and perfuse mouse kidney cells under different shear stress conditions and imaging by STORM revealed the effect of mechanical cues on cilia morphology and proteins localization. Although the work proposed on-chip fixation, the actual super-resolution studies were performed on fixed and labeled cells only after the detachment of the microfluidic chamber, thus limiting the potential of the platform [206]. In another example, STED imaging was performed on human

umbilical vein endothelial cells (HUVECs) cultured within a PDMS microfluidic device to study the features of the glycocalyx layer under flow [207]. Despite these recent advances, microfluidic platforms for human biology, as OOaCs, have not been coupled yet with SRM. Furthermore, although SIM shows advantages compared to other SR methods, as high acquisition speed and low cellular photodamage, it has been rarely used for imaging of processes on dynamic platforms [204].

Rationale and objectives

Structured illumination microscopy focuses nowadays on imaging samples under static conditions. The rationale behind Chapter 3 is thus to design and develop a microfluidic platform compatible with SR-SIM equipments to provide an alternative dynamic in vitro model for the culturing and super-resolution imaging of cells and subcellular structures. The final goal in the context of DeLIVER project was the SIM imaging of endothelial cells from liver, whose peculiar features, as membrane fenestrations, and functioning are of great interest to unravel hepatic physiopathology.

In this chapter, we first present the investigation of different materials, notably thermoplastics and elastomers, for building the microfluidic devices. We thus focus on the design of a PDMS microfluidic platform and its implementation to ensure the compatibility with SR-SIM. The design of the devices has been optimized considering both its physicochemical and geometrical features as well as its biocompatibility as in vitro platform. Important parameters as device dimensions, bonding strength and channels geometry have been evaluated and discussed. The platform has been used for in vitro culturing of human and mammalian cell lines and primary cells. Surface coating, seeding strategies, cell densities and culturing under flow have been optimized depending on the cell sources to enable long-term viability. Staining procedures for imaging with conventional and super-resolution microscopes have been addressed. Combination with SR has allowed us to perform on-chip imaging of subcellular structures on living cells, on-chip labeling and to study the real-time response of cells to drug flow. Culturing and imaging on-chip of primary LSECs and their fenestrations has also been demonstrated.

3.2. Design, Development and Characterization of a microfluidic device for SR-SIM

3.2.1. Design and microfabrication

The use of SRM imaging techniques poses intrinsic constraints to the design of microfluidic platforms. Due to the need of minimizing refractive index mismatches to prevent optical aberrations and to the relatively limited imaging depth compared to conventional light microscopy techniques [152], the use of standard membrane-based microfluidic models is practically unfeasible. To ensure compatibility with SR systems, cells should be cultured in a 2.5D system, meaning they can be encased in a microfluidic platform but the bottom layer of the device should be a glass coverslip. Thus, typical OOaC platforms should be re-designed to take into account these requirements. The integration of membranes also represents an issue for imaging of cells, especially the ones cultured on the top side, which are the furthest from the microscope objective. Thus, conventional membrane-based horizontal models, in which the membrane is sandwiched between the channels, should be rethought “vertically”. Here, a simple microfluidic chip composed of a single patterned PDMS layer sealed to a glass coverslip has been proposed. Cells were cultured in monolayers on the coverslip (bottom layer) in presence of an optimized coating and consequently imaged by SR-SIM (**Figure 3.2A**).

Chapter 3. Development of a microfluidic platform compatible with Super-Resolution imaging

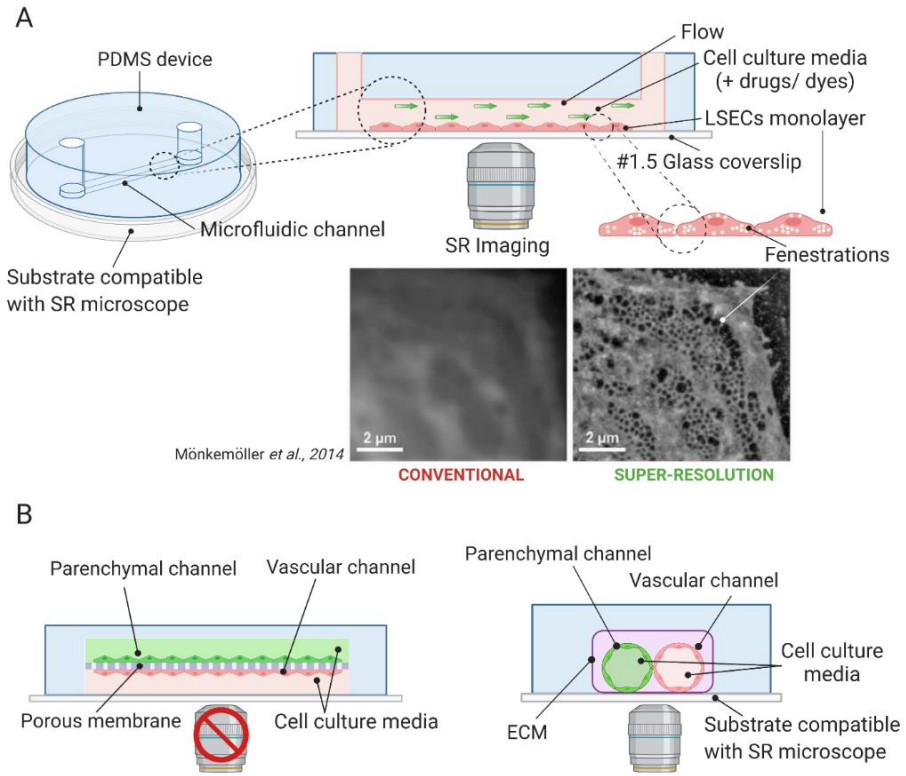


Figure 3.2. Conceptualization of microfluidic platforms compatible with super-resolution microscopy. (A) Design of the platform presented here: the micropatterned PDMS with the channel structures is sealed to a glass coverslip where cells are cultured. In the frame of DeLIVER project, LSECs have been cultured for SR imaging of their fenestrations. The microscope images shown in the pictures display fenestrations with conventional widefield microscopy (left) and resolved by STORM (right). Scale bar 2 μm . Adapted with permission from Mönkemöller et al. 2014. (B) Conventional OOaC platforms present a membrane-based design, in which the parenchymal and vascular cells are cultured on the opposite sides of a horizontal membrane, sandwiched between the channel substrates (left, lateral view). The design is not compatible with SRM. A vertical rather than horizontal design should thus be envisioned for engineering complex models compatible with SR imaging: a possible configuration is represented by the encapsulation of perfusable cellularized channels within an ECM matrix on a glass coverslip (right). Created with Biorender.com.

Besides the model proposed here, the advances in biological polymer sciences and technologies as 3D bioprinting can be successfully adapted for building “vertical” complex microfluidic platforms compatible with SRM [208]. The basic idea consists in printing confined hydrogels, eventually encapsulating cells and containing perfusable microchannels on a 2D substrate (a glass coverslip for SR applications). This way, the parenchymal and vascular interfaces can be bioprinted side by side, with subsequent removal of the horizontal membrane. An interesting example has been reported by the team of J A Lewis, who 3D printed a kidney tissue model composed of a perfusable vascularized proximal tubule [94,209]. The microfluidic device frame was composed of a printed silicon gasket on a glass slide. The microfluidic model was engineered by an ECM layer composed of gelatin and fibrin and of two convoluted microfluidic channels, one for the epithelium and one for the endothelium, fabricated by 3D bioprinted fugitive Pluronic ink. After the dissolution of the fugitive ink at 4°C, the two adjacent microfluidic channels could be perfused and seeded with proximal tubule epithelial cells and glomerular vascular endothelial cells respectively. They confirmed the expression of renal and endothelial markers under physiological conditions and assessed the selective reabsorption mechanisms of albumin and glucose with cross-talk between endothelial and epithelial channels. Impaired mechanisms as hyperglycemia were also mimicked on-chip, demonstrating the ability of the platform to recapitulate both physiological and pathological conditions. This tissue engineering

approach offers the advantages of printing tubular structures with complex geometries and of designing more physiologically relevant model by inclusion of ECM and 3D cellular organization into channels. However, the main drawback was the need of seeding cells after bioprinting and bioprinting using cell-integrated bioinks should be envisioned [210]. **Figure 3.2** shows the schematic of the microfluidic platform compatible with SRM proposed here and a possible optimized configuration for building complex “vertical” microfluidic-based tissue models for SR imaging.

In terms of choice of the materials, Chapter 2 describes the major benefits that can be obtained by using materials alternative to polydimethylsiloxane (PDMS), commonly used for microfluidic devices fabrication. We thus firstly investigated the possibility of using the thermoplastic elastomer previously described, Flexdym™ (FD™), for the fabrication of microfluidic platforms compatible with SRM. To overcome one of the main limitations of FD™, its intrinsic thinness, we present in the next section a protocol for the fabrication of thick FD™ substrates: since the raw material comes in form of sheets (nominal thickness of 1.3 mm), that become even thinner once they are heat-pressed, the final layer thickness is ~1 mm [28]. This introduces complications for tubing connection to the device, requiring additional fabrication steps for the insertion of external connectors for interfacing with the flow system. Furthermore, it is important that the connectors remain stable over time and under multiple tubing insertions, without detaching, a requirement that often involves the use of glues for their maintenance in place. A

modified protocol allowed us for the production of thick patterned FDTM substrates but several other issues, further detailed in the chapter, led us to exclude this alternative material for SRM imaging, finally using standard PDMS for the microfabrication.

Fabrication of thick FlexdymTM substrates for microfluidics

Due to the advantages of thermoplastic elastomers in comparison to PDMS, preliminary experiments were carried out to define a protocol for the production of thick FlexdymTM substrates in order to obtain compact devices with no need for external connectors. Two different protocols were investigated, as reported in **Table 3.1**. Briefly, the first protocol was maintained similar to single FDTM micropatterning by hot embossing (see Chapter 2) while the second protocol added a previous melting of overlaid FDTM sheets on a hotplate followed by hot embossing.

Table 3.1. Fabrication protocols proposed for thick FlexdymTM substrates.

PROTOCOL 1 (Hot embossing)

- i. A vacuum-assisted heat press (Sublym100TM, Eden Microfluidics SAS, Paris, France) is heated at 170°C and spacers are properly chosen to obtain the desired final FDTM thickness;
- ii. Extruded FDTM sheets (Eden Microfluidics SAS, Paris, France) are cut at the desired size and cleaned with tape to eliminate any dust;
- iii. Several (2 to 3) FDTM sheet are stacked together by placing them in conformal contact and positioned in between two glass slides
- iv. FDTM sheet are then hot embossed at 170°C for 2 minutes;
- v. FDTM sheets are separated from the glass slides using isopropanol.

PROTOCOL 2 (Melting + Hot embossing)

- i. A metal case is placed on a hotplate at 220°C;
-

-
- ii. FDTM sheets are cut with scissors to fit the mold and cleaned with tape;
 - iii. Several FDTM sheets (basing on the thickness desired) are stacked together and placed within the pre-heated metallic mold on the hotplate;
 - iv. A flat tool (ex: glass slide) is used to press carefully the FDTM sheets during the melting process to reduce the presence of air bubbles;
 - v. After 30 minutes, the mold is removed from the hotplate and the FDTM substrate let to cool down;
 - vi. Steps (i, iv-v) of Protocol 1 are performed for the hot embossing procedure.
-

Results from protocol 1 showed that the hot embossing only was not sufficient to achieve uniform bonding of the FDTM layers (**Figure 3.3A and B**), that resulted partially melted with uneven melting over the length and loss of flatness of the entire substrate. The introduction of a first hotplate step induced FDTM to become more opaque and to lose partially its stickiness and self-bonding properties. Although experiments were performed by stacking up to three layers of FDTM and obtaining substrates with a final thickness of ~ 4 mm, air bubbles were visible between the layers due to the difficulty of removing them during the melting process because pressing the FDTM caused partial loss of structure and flatness. On the other side, single FDTM sheets resulted to be completely melted together, with the cross-section resulting to be a homogeneous thick FDTM sheet (**Figure 3.3C and D**). Therefore, the hotplate step was followed by hot embossing using the same parameters as in protocol 1. Results showed that after the heat press step, FDTM partially recovered its transparency and adhesive properties. Different spacers thicknesses were tested, particularly with spacers higher than the

glass-FDTM-glass substrate or shorter. In the first condition (**Figure 3.3E**), FDTM experienced vacuum but not pressure from the metal plates. The final substrate resulted to partially recover its transparency and adhesiveness with no reduction of thickness compared to the hotplate step. In the second condition (**Figure 3.3F**), FDTM experienced vacuum and pressure, resulting in total recovery of transparency and adhesiveness. However, a thickness decrease occurred and the air bubbles encased within the FDTM layers during the hotplate step spread uniformly between the layers, hindering the final applicability of the FDTM substrate.

Chapter 3. Development of a microfluidic platform compatible with Super-Resolution imaging

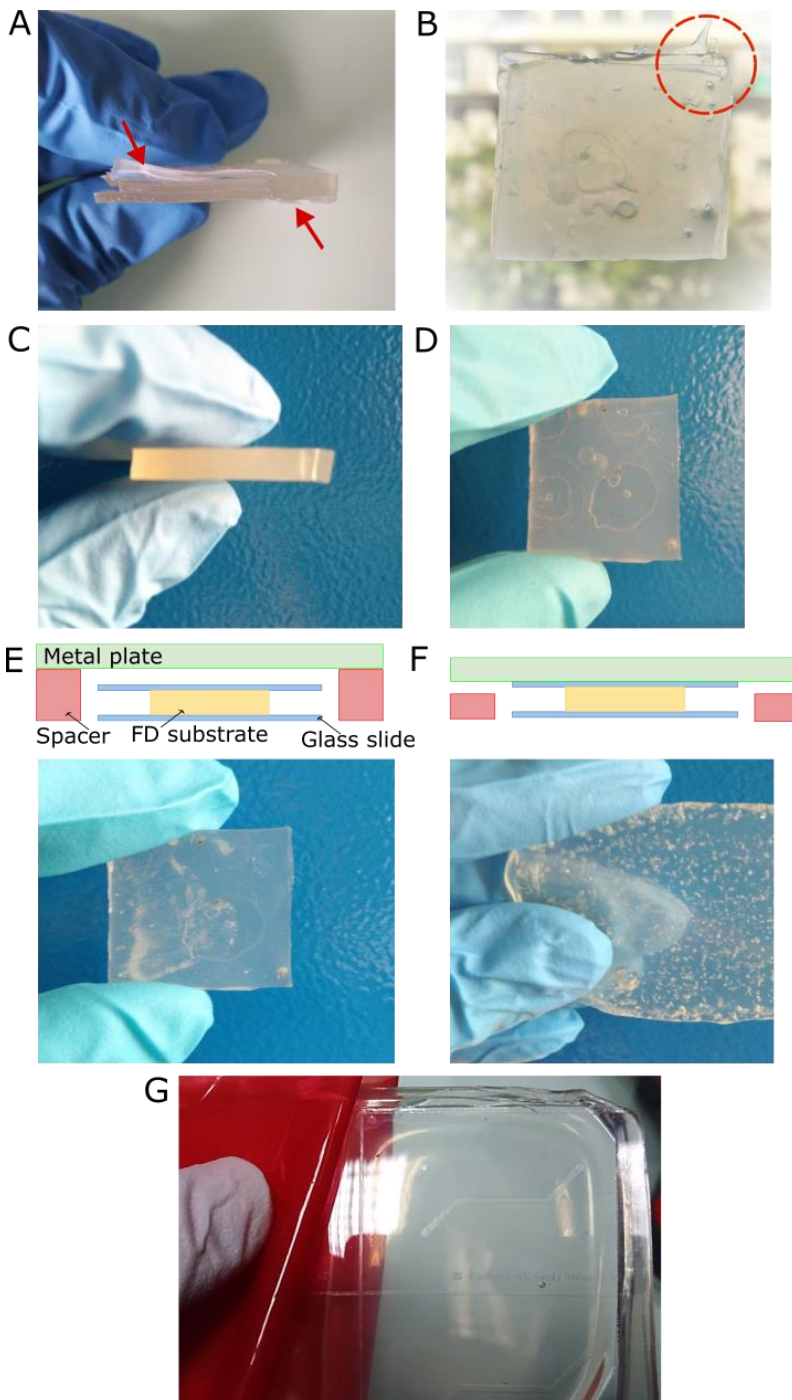


Figure 3.3. Fabrication of thick FDTM substrates. (A, B) Protocol 1 (side and top view respectively): simple hot embossing resulted in partially and heterogeneous melted FDTM layers (red arrows and circle in A and B respectively). (C-F) Protocol 2. (C, D) Melting (hotplate) step (side and top view respectively): the addition of an initial melting step leads to homogeneous bonding of the FDTM layers (C) but incorporation of air should be carefully avoided (D). (E, F) Hot embossing after melting by using taller (E) or shorter (F) spacers. (G) Patterned thick FDTM for microfluidic applications optimized by our group.

Preliminary data reported here showed the feasibility of fabricating thick FDTM substrates by overlaying of thin FDTM sheets. A simple hot embossing resulted to be ineffective for the optimal melting of the layers. The combination of an initial hotplate step followed by hot embossing (protocol 2) resulted to be the most effective process: the layers were firstly homogeneously melted at 220°C for 30 minutes while the hot embossing allowed for recovery of FDTM adhesiveness and transparency. For spacers higher than the glass-FDTM-glass substrate, the vacuum resulted not sufficient to change the FDTM opaqueness due to the lack of pressure applied. Therefore, spacers shorter than the substrate should be used: however, particular attention should be paid in avoiding the air encapsulation during the melting of the layers and spacers thickness should be designed carefully to prevent an excessive flattening of FDTM during the hot embossing, with consequent thickness reduction. Protocol 2 has been further optimized by our group (work unpublished, **Figure 3.3G**), demonstrating the possibility to produce thick FDTM, that can be directly micropatterned after melting by replacing the bottom glass slide with a microfluidic mold. However, the process resulted to be more time consuming compared to standard one layer FDTM

fabrication due to the 30 minutes melting step, hindering the rapid prototyping benefits typical of thermoplastics.

Although the feasibility of fabricating thick FDTM substrates by stacking and heat-pressing several FDTM sheets together has been demonstrated, the process resulted to be not straightforward and issues, as formation of air bubbles between the layers, increased opacity of the material over repeated hot embossing steps and decrease of adhesive properties, led us to exclude this option. In contrast, PDMS thickness can be easily tuned by pouring different amounts of polymer on the mold. Moreover, as previously shown, FDTM presents some other important drawbacks. The second major drawback is the difficulty of bonding FDTM to glass: even if this thermoplastic shows excellent self-bonding properties, with no need for extra functionalization steps, its bonding to glass resulted challenging and preliminary experiments performed at either room or at higher temperature showed the contact between the two materials without formation of a stable covalent bonding, leading ultimately to leaky devices. On the contrary, although requiring an extra fabrication step, PDMS can be covalently bonded to glass via simple surface plasma activation. Furthermore, in the device shown in Chapter 2, another limitation was represented by the use of a relatively thick (23 μm) porous polycarbonate membrane, that decreases the optical clarity, hampering the use of the device for SRM. Due to these limitations, that should be addressed in detail to improve the versatility and applicability of thermoelastomers, PDMS was thus chosen for the design of microfluidic platforms for SRM.

Switching to PDMS: design and microfabrication of microfluidic devices compatible with SIM

The siloxanes, the macromolecules that compose the backbone of PDMS, were firstly characterized by the English chemist Frederick Stanley Kipping in 1927. Considered as one of the founding fathers of silicon chemistry, he started studying the materials which are now globally known as silicones from 1899 and coined the term *silicone* in 1904. In 1943 the Dow-Corning Corporation was established as a joint venture between Corning Glass and Dow Chemicals and it became the first silicones manufacturer, following Kipping's method [20]. PDMS is the material of choice for soft lithography and microfabrication of microfluidic platforms for cell biology [9,35]. Because of its transparency, elastomeric mechanical properties, reduced cost and facile fabrication, it has been widely preferred to glass and silicon for fabrication of microfluidic devices. Because of its non-cytotoxicity, biocompatibility and permeability to gases, it has been largely used for fabrication of OOaCs [211,212]. Considering the drawbacks of FDTM in its use for building devices compatible with SRM, we decided to adopt PDMS for the development of these platforms.

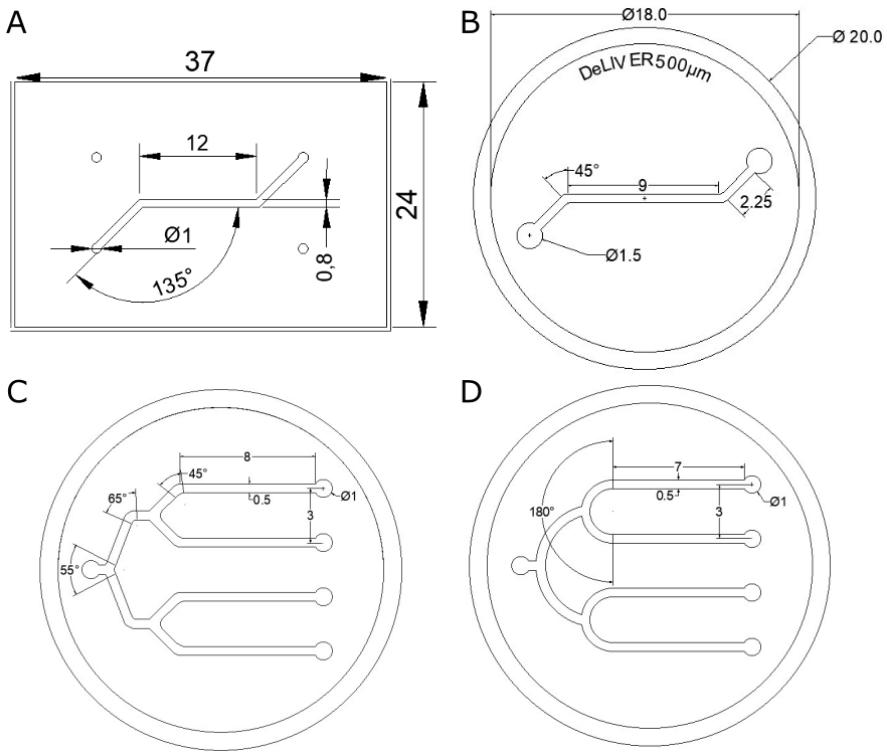


Figure 3.4. CAD designs of microfluidic devices developed for SRM studies.

Design and fabrication of the microfluidic mold

Microfluidic molds were fabricated with a similar protocol as the one described in Chapter 2 (**Figure 3.5B**). 75 x 50 x 1 mm (L x W x H) borosilicate glass slides (Corning Inc., Corning, NY, USA) were cleaned with acetone and isopropanol and dehydrated on a hotplate (Thermo Fisher Scientific, Waltham, MA, US) for 20-25 minutes at 120 °C. For a single layer photoresist mold, one sheet of Ordyl® SY 300 dry film negative photoresist (55 µm thickness, ElgaEurope s.r.l., Milan, Italy) was laminated onto the slide using a thermal laminator (325R6, FalconK, France) at 120 °C and roller speed 4. Using an

exposure masking UV LED lamp (UV-KUB 2, Kloé, Montpellier, France) the photoresist was then exposed to UV light (365 nm, 23.3 mW cm⁻²), for 7 seconds with a film photomask (Selba S.A., Versoix, Switzerland) and the micropatterned slide was subsequently put on the hotplate for 5 minutes at 120°C. After 15 minutes in the dark, the photoresist was developed with a solvent blend (Ordyl® SY 300 Developer, ElgaEurope s.r.l., Milan, Italy) for 5 minutes to remove unexposed sections of the photoresist and washed with IPA to remove any debris.

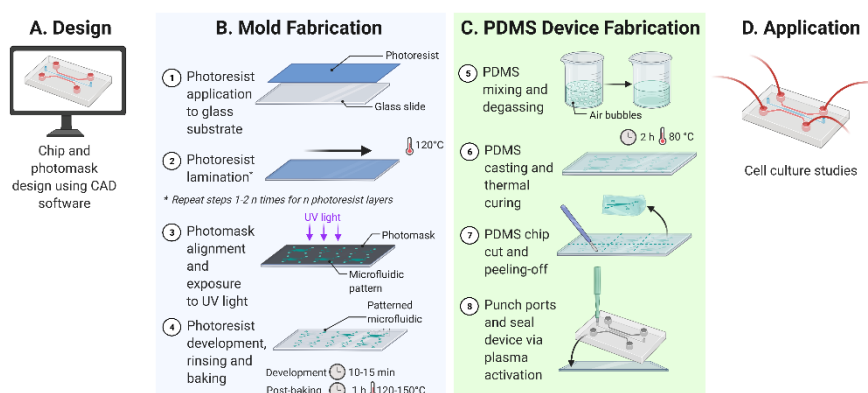


Figure 3.5. Schematic of the PDMS device fabrication workflow. (A) The first step consists in the design and printing of the photomask with the desired microfluidic pattern. (B) Steps 1-4 show the fabrication of patterned glass mold using a dry pattern photoresist. (C) Steps 5-8 represent the microfabrication of PDMS chips via replica molding before the final application (D). Created with BioRender.com.

The mold fabrication process was finished with a hard bake of 1 hour at 150 °C on a hotplate. For a multilayer photoresist mold, Ordyl sheets were laminated in sequence at 120°C and speed 4 with a cooling step of 2 minutes in between each lamination and consequently placed on a hotplate at 120°C for a minimum of 5

minutes. The UV exposure times were adapted accordingly to the number of laminated layers, being 2 s, 6 s and 11 s for one, two or three Ordyl layers respectively. After a baking step of 5 minutes on the hotplate, the micropatterns were developed in a time depending on their features, ranging from 5 to 15 minutes and hard baked for 1 hour at 120°C.

PDMS devices microfabrication

The microfluidic devices were fabricated by PDMS soft lithography (Sylgard 184, Dow Corning Corporation, Michigan, USA) by mixing manually the liquid silicone base and the curing agent completely with a ratio 10:1 (w/w) for 10 minutes. The mixture was degassed then in a vacuum chamber for 30 minutes to remove any air bubble and poured over the master mold containing the negative replica of the channel. After a second step of degassing, the samples were fully cured in oven at 80°C for 2 hours for PDMS polymerization and subsequently cooled at room temperature. The cured PDMS slab was peeled off from the mold by carefully cutting its edges with a razor blade and the single devices were consequently separated. The inlet and outlet ports of the channels were punched to create holes of 1.5 mm of diameter by using a biopsy punch and the micropatterned PDMS was then cleaned with tape to remove any debris or dust particle. A glass coversheet (No. 1.5H, Marienfeld Superior, Lauda-Königshofen, Germany) was cleaned with EtOH 70% and let dry before placing it and the PDMS (with the channel structures facing upwards) in a plasma system (PDC-002, Harrick Plasma, Ithaca, NY,

USA) for air plasma activation (200 mTorr, 30W, 2 minutes). The bonding process was performed by placing the two layers in conformal contact after the plasma treatment to ensure irreversible bonding (**Figure 3.5C**). Devices with different designs and channel dimensions have been fabricated (**Figure 3.4**), with nominal heights corresponding to single, double or triple Ordyl mold (55 to 165 μm), widths ranging between 100 and 800 μm and lengths of the central device area of about 10 mm.

3.2.2. Validation and optimization of the fabrication protocol

Exclusion of the PC membrane from the microfluidic platform design

Initial fabrication of the devices included a porous track-etched polycarbonate membrane (2 μm pores, 5.6% porosity, 23 μm thickness, Isopore™, Merck KGaA, Darmstadt, Germany), that was sandwiched between the bottom glass slide and the PDMS layer during the plasma bonding process. This design was implemented to evaluate the possibility of keeping a microfluidic device structure resembling common membrane-based OOaC platforms. The compatibility of PDMS chips (single channel design, cross section 800 x 155 μm , W x H) including the PC membrane with SRM was tested in collaboration with the Physics and Biology Departments, Bielefeld University, Germany. The devices were used for culturing Human Embryonic Kidney (HEK-293) cells on top of the PC membrane: a cellular density of 4×10^6 cells/mL in Dulbecco's Modified Eagle Medium (DMEM) was used for the seeding, after

sterilization in autoclave and coating of the channels of collagen type I from rat tail for 1 hour at 37°C. After culturing overnight, devices were imaged by using a high-resolution widefield DeltaVision Elite microscope (Ge Healthcare, Bio-Science, Pittsburgh, USA). Data showed cellular spread morphology and viability, although the imaging was severely impaired by the presence of porous PC membrane (**Figure 3.6**). These results led us to exclude the possibility of including a porous membrane in SRM studies, that was removed in the following experiments.

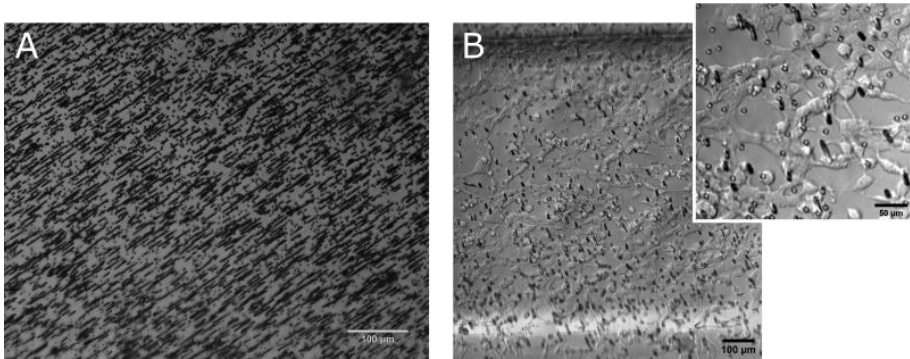


Figure 3.6. Study on the compatibility of PDMS-PC-glass devices with SRM. (A) High-resolution image of the porous PC membrane: the pores and patterns are clearly visible (20X magnification objective, scale bar: 100 μm). (B) HEK cells cultured overnight within the PDMS device (the channel edges are visible, scale bar 100 μm): the PC membrane pattern resulted to disturb the imaging process (inset, scale bar 50 μm).

PDMS-glass bonding characterization and optimization

To test the efficacy of PDMS bonding to thin glass coverslips, burst pressure experiments have been performed in order to evaluate the maximum pressure capacities of the devices before undergoing delamination, with consequent leaking from the channels. A standard

microfabrication process was performed for the fabrication of chips with $W \times H$ of $800 \mu\text{m} \times 55 \mu\text{m}$. Only the inlet of the channel was punched and sealed to the glass bottom layer so as to create a dead-end channel for the delamination tests. Devices were either bonded to #1.5 glass coverslips or 1 mm thick microscope glass slides, used as control group ($n=3$ for each condition). Burst pressure experiments were performed with an OB1 pressure controller, imposing a ramp pressure function from 0 to 2 bar, with a burst time of 10 minutes and acquisition frequency of 0.1 Hz. Tests were run by flowing colored water under an optical microscope equipped with a machine vision camera (PL-D725, Pixelink®, Ottawa, Canada) for visual inspection of the devices. Results showed that the bonding between PDMS and #1.5 coverslip was relatively weak, with a maximum pressure withstood of $725 \text{ mbar} \pm 74 \text{ mbar}$ but with leaks spreading from the inlet areas for 2 devices out of 3. On the contrary, PDMS devices bonded to the 1 mm thick slides did not show any leak during the experiments, however the data trend was highly scattered with an average value of burst pressure of $825 \text{ mbar} \pm 106 \text{ mbar}$ (Figure 3.7, left panel). Therefore, results highlighted the unstable bonding behavior of the PDMS-glass systems and the need for further optimization of the microfabrication protocol. Although this conclusion can be drawn regardless of the glass substrate, the ineffective bonding protocol was mainly critical for the bonding with thin coverslip due to delamination and leaking of the devices.

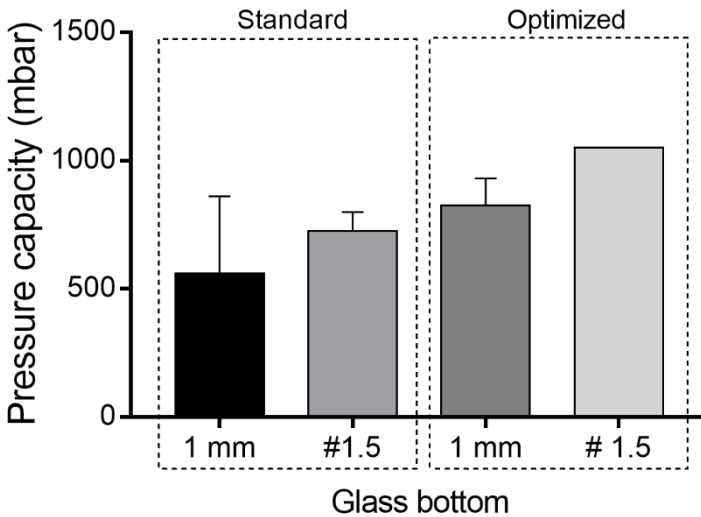


Figure 3.7. PDMS-glass bonding evaluation by burst pressure testing.

The bonding protocol was then modified by including two additional steps before and after the plasma activation: firstly, the glass coverslip/slide were cleaned with IPA and clean room tissues and dehydrated on a hotplate (120°C for 20-30 minutes). The bonding was performed by holding the vacuum (0.5 Torr) for one minute before switching on the plasma. The plasma bonding was then followed by a post-baking in oven (120°C for 2h) to further improve the bonding strength.

Burst pressure experiments were repeated under the same testing conditions and results showed that the PDMS-#1.5 coverslip system could withstand pressures above 1 bar while the PDMS-1 mm slide systems withstood an average burst pressure of 825 mbar \pm 106 mbar, higher compared to the standard bonding protocol and with more uniform data distribution (Figure 3.7, right panel).

Furthermore, none of the devices leaked from the edges/inlet ports of the channel structure. Pressure delamination tests performed on the devices with maximum pressure tested of 2 bar confirmed the capability of the devices produced by optimized bonding protocol to withstand the high pressure rates with no delamination occurring at the inlet port nor along the channel (**Figure 3.8**). As already discussed in Chapter 2, the pressures tested followed a precautionary approach, meaning that the devices were tested under “extreme” pressure conditions compared to standard pressures applied to flow OoCs devices, where few tens of mbar are usually applied.

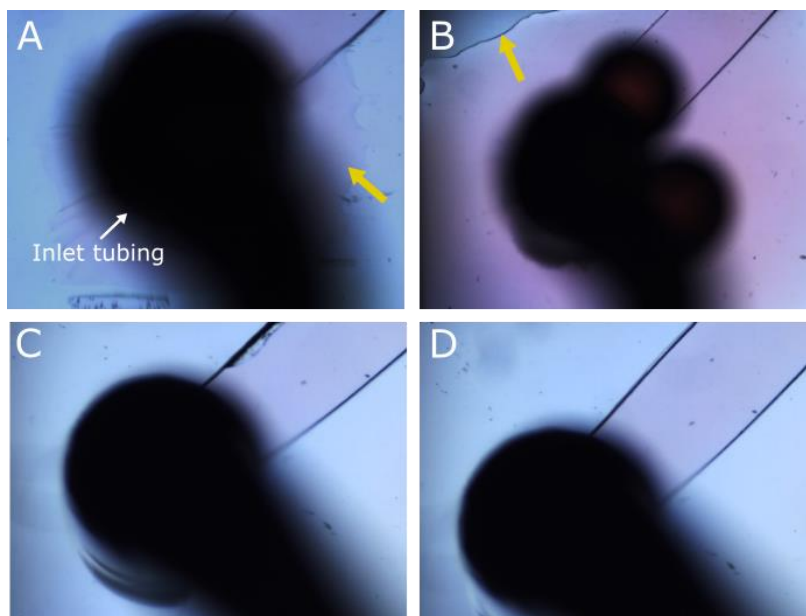


Figure 3.8 Optimization of the PDMS-glass bonding protocol. (A, B) Standard bonding protocol: tests performed at increasing pressure resulted in delamination of the devices (detected at the inlet area) at 1 bar (A) with significant progress of the meniscus at 2 bar (B). Yellow arrows indicate the meniscus movement while the black shades represent the inlet tubing. (C, D) Optimized bonding protocol: devices could withstand the testing pressures (1 bar- C and 2 bar -D) without any delamination occurring.

Design optimization to fit the SR-SIM stage: the concept of microfluidic chip in a dish

The device structure was optimized at different stages of the project to ensure its compatibility with the SRM stage while maintaining a simple microfabrication process. Initial devices were fabricated by bonding of the PDMS layer to rectangular #1.5 glass coverslips (No. 0107242, Marienfeld Superior, Lauda-Königshofen, Germany) with a dimension of 24x60 mm, bigger than the micropatterned PDMS. This led to difficult handling of the devices, with easy breaking of the glass substrate during manipulation and transport. Following optimization was carried out by fitting the PDMS chip onto rectangular 22x32 mm coverslips (#1.5, Menzel Gläser, Hessen, Germany) and cutting the PDMS in the shape of slightly larger rectangles, with a dimension of approximately 24x37 mm (**Figure 3.4A**) to solve the issue of the glass bottom fragility. However, the rectangular device resulted to be not compatible with the available SR-SIM stages: its size smaller than stage represented a major drawback in device stability during imaging and mapping as well as during the flow of the device on stage. Rather than modifying the device structure, we firstly decided to create a portable case compatible with the SR-SIM stage dimensions to hold the device in place. The case was designed in Autodesk Fusion 360 with a dimension of 75 x 25 x 2 mm and an internal frame or wings with a thickness of 0.5 mm were included for the microfluidic device support. The case was micromilled from polystyrene using a 1/32 flat milling tip (CNC milling machine, Bantam Tools, NY, USA). While

making the chip dimensions compatible with the SR-SIM stage dimensions, the case did not ensure the needed stability of the device and the presence of the wings to fit the device added an important thickness of 500 μm that could represent an eventual problem while working with the objective and focusing.

Therefore, a final device structure was proposed to fit the circular SR-SIM stage: to avoid any additional fabrication steps, the design of the microfluidic platform was adapted to fit the observational area (diameter of 21 mm) of a 35 mm imaging plastic dish with #1.5 glass bottom (170 $\mu\text{m} \pm 5 \mu\text{m}$ D 263 M Schott glass, Cat. No. 81158, ibidi GmbH, Gräfelfing, Germany) (Figure 3.4B-D) compatible for SR imaging. Novel photomasks and molds were produced to have a circular PDMS layer with a diameter of ~ 20 mm for fitting the glass observational area. The channels dimensions were scaled down accordingly, with a channel length of 9 mm and channel widths ranging from 250 to 750 μm and up to 6 patterns could be fit on a single 75x25 mm glass mold, compared to the 4 rectangular patterns previously used. The microfabrication protocol was slightly modified by modification of the device cutting and assembling steps. Rather than using manual cutting of the PDMS edges by razor blade, the PDMS layer was punched by using an 18 mm steel round hole punch to obtain sharp edges and ensure optimal bonding and precise diameter. Furthermore, the optimized bonding protocol for PDMS optimal adhesion to glass coverslips was no longer applicable. In fact, the optimized protocol provided for a glass coverslip dehydration step at 120°C and a post-baking of the assembled device.

However, these temperatures were not available for the PDMS-plastic dish system because the chamber could withstand a maximum temperature of 80°C due to the presence of the plastic frame. Although a good sealing after plasma bonding with a post-baking at lower temperatures (45°C) was verified, the devices were manipulated carefully to prevent any delamination to occur. The platform structure improvement ensured (i) compactness and facile transport of the device, (ii) size compatibility with SR common stages without the need for further device modification, (iii) facile localization of the channels with SIM and (iv) stability of the device during the flowing and acquisition processes.

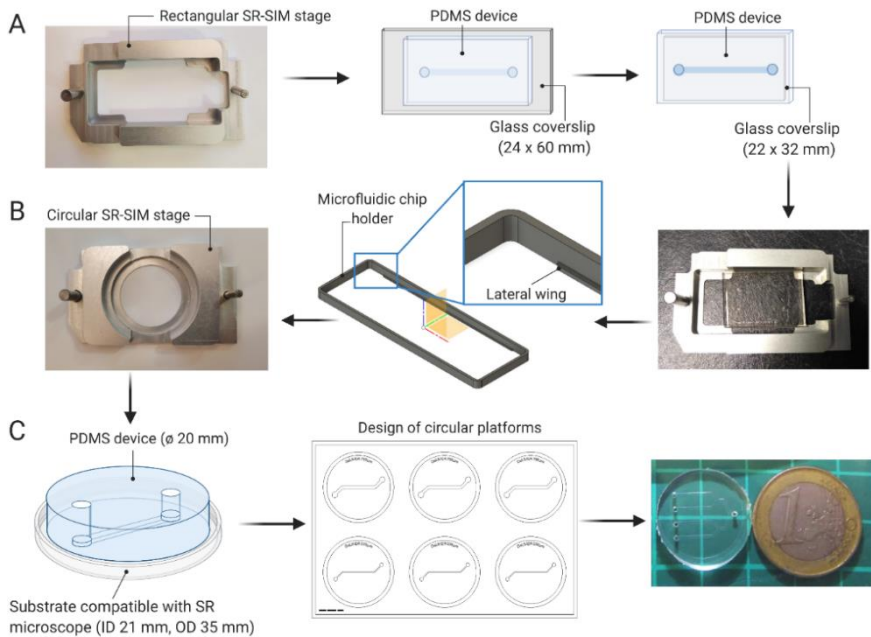


Figure 3.9. Workflow of the optimization steps of a microfluidic platform compatible with SRM stages. (A) The first designed focused on the development of standard rectangular PDMS platforms that could be easily handled. However, it was difficult to fit the

devices on the rectangular SIM stage and further studies were conducted for the fabrication of custom-made chip holders (B). Finally, to reduce the fabrication time and adopt a more universal solution the design focused on circular PDMS devices that could be easily fitted in commercially available plastic dishes (C) and that could be adapted to circular SIM stages. The final devices resulted to be highly compact, with the PDMS layer being smaller than a 1 € coin, showing improved stability of the device- SIM stage system. Created with BioRender.com.

3.3. Cell Culture: use of the device for cell lines and LSECs culturing *in vitro*

3.3.1. Microfluidic platform culturing

To evaluate the suitability of optimized microfluidic devices for *in vitro* cell studies, the platforms were cultured with human cell lines and primary cells. Experiments with human cell lines were performed at Elvys Microfluidic Innovation Center, Paris, France. Experiments with primary human LSECs were performed in the framework of DeLIVER project at the Centre for Liver Research and NIHR Biomedical Research Unit, University of Birmingham, UK.

Isolation of human liver sinusoidal endothelial cells

Liver sinusoidal endothelial cells were isolated from human adult donor tumor distal livers according to established protocols from Liver Research Laboratories in Birmingham [213–215]. Briefly, liver tissue slices were diced in small pieces with a sterile surgical scalpel and digested with collagenase at 37°C for 30 minutes to remove any extracellular matrix component. Tissue was then strained through a mesh filter to remove any clump and washed several times with PBS to remove collagenase. Several steps of centrifugation in PBS at

2000 rpm for 5 minutes were done to obtain a single pellet of unsorted cells from the digested tissue. Isolation of the non-parenchymal cells fraction was performed by placing 3 mL of cell suspension on a Percoll gradient (top: 3 ml of 33% Percoll and bottom: 3 ml of 77% Percoll, both diluted in PBS 1X). After centrifugation for 25 minutes at 2000 rpm with no brakes, the nonparenchymal fraction at the interface of the Percoll gradient was separated from the supernatant and hepatocytes fraction, resuspended in PBS and centrifuged at 2000 rpm for 5 minutes. Isolation of LSECs was performed by positive immunomagnetic selection using CD31-coated magnetic beads. Briefly, cells were firstly incubated with HEA-125 mouse antibody at 37°C for 30 minutes to select epithelial cell adhesion molecule (EPCAM-1)-positive cells. Cells were incubated in ice cold PBS containing goat anti-mouse magnetic Dynabeads® at 4°C for 30 minutes and placed in a magnet for 2 minutes to isolate the epithelial fraction. The supernatant containing endothelial cells was incubated in CD31-coated magnetic Dynabeads® at 4°C for 30 minutes and placed in a magnet for 2 minutes three times for selective isolation. Finally, isolated LSECs were resuspended in cell culture media in a vessel and incubated at 37°C for cell culture.

Cell culture

Human embryonic kidney (HEK) 293 (CRL-1573™, ATCC®, VA, USA) and human epithelial cervical carcinoma HeLa cells (CCL-2™, ATCC®) were cultured in tissue culture flasks in DMEM (High

Glucose with stable Glutamine and Sodium Piruvate, L0103-500, Dutscher, Bernolsheim, France) supplemented with 10% Fetal Bovine Serum (FBS, P30-3306, Pan Biotech GmbH, Aidenbach, Germany) and 1% penicillin/streptomycin (10000 U/mL and 10 mg/mL respectively, P06-07100, Pan Biotech). Isolated LSECs were cultured in collagen-coated T-25 cell culture flasks in human endothelium serum-free medium with 10% human serum, 10 ng/ml vascular endothelial growth factor (VEGF) and 10 ng/ml HGF (R&D Systems, Abingdon, UK). Cells were incubated in a humidified incubator at 37°C and 5% CO₂ atmosphere and the culture medium was changed every 2 days until reaching about 80% of confluency.

Culturing of Microfluidic Platforms

Microfluidic devices previously fabricated were sterilized by flowing the channels with 100 µL of EtOH 70 % for a minimum of 10 mins or by autoclave. The channels were then washed twice with Dulbecco's Phosphate Buffered Saline w/o Calcium w/o Magnesium (DPBS, L0615-500, Dutscher) for 5 minutes, complete culture medium and with DPBS again. A solution of collagen type I from rat tail (354236, Corning, NY, USA) with concentrations varying between 25 and 100 µg/mL was prepared by diluting the collagen in DPBS and consequently mixing. The devices were coated by pipetting carefully the collagen to avoid any air bubble formation and propagation within the channel and incubated at 37°C for 1 hour or at 4°C overnight. After rinsing the culture dishes with DPBS, cells were detached with 1 mL of Trypsin 0.05% EDTA 0.02% in PBS (P10-

023100, Pan Biotech) by placing them 2 minutes in incubator at 37°C. Cells were then centrifuged and resuspended in DMEM at the final concentration, with a minimum concentration of 1×10^6 cells/mL. Microfluidic devices were removed from the incubator and the coated channels washed once with sterile DPBS to remove any excess of coating protein and verify the absence of clogs. Cell seeding was performed manually by gently flowing ~30 μ L of cell suspension within the inlet with a micropipette. When the liquid reached the outlet, the outlet port was partially closed to induce the cells to stop flowing towards the end of the channel and exiting the device. Once the cells were stabilized within the central area of the device, two drops of cell culture medium were placed on the ports to prevent ant evaporation and drying and the platforms were put in the incubator for 1 hour to ensure primary adhesion. After visual inspection to confirm the adhesion, the devices were incubated overnight by placing micropipette tips filled with medium within the ports. The day after, the devices ports were cleaned carefully with a small tip to remove any floating cell and prevent their flow within the channel. Culture medium was changed into fresh DMEM every other day.

Staining and imaging

Live cell imaging was performed by incubating the cells with the following fluorescent dyes: Hoechst for DNA staining (1 μ g/mL, 33258, Biotium, CA, USA), Calcein AM (2 μ M, 354216, Corning, NY, USA) and propidium iodide (PI, 50 μ g/mL, 40016, Biotium,

CA, USA) for live/dead fluorescent assays. Cells were incubated for incubated at RT for 7 minutes with Hoechst, followed by 30 minutes incubation with Calcein AM and 10 minutes incubation with PI. Each step was followed by DPBS flushing of the channels. Fluorescent samples were imaged using an upright optical microscope (Leica Microsystems Inc., Wetzlar, Germany) equipped with a Pixelink® PL-D725MU-T camera (Pixelink, Ottawa, Canada). For cell studies, samples were washed with DPBS and fixed by either methanol or formaldehyde (FA). For methanol fixation, 50 µL of ice-cold 100% methanol were flown in the channels and the devices kept for 15 minutes at -20°C. For FA fixation, 50 µL of 3.7% FA were flown in the channels and the devices kept for 10 minutes at RT. After fixation, the samples were washed three times with 100 µL of DPBS for 5 minutes. The devices fixed with FA were consequently permeabilized by Triton™ X-100 (3402130090, Sigma-Aldrich, MO, USA) diluted at 0.2 % in DPBS for 10 minutes at room temperature. LSECs were stained with Cell Mask Deep Red™ Plasma Membrane Stain (CMDR, C10046, Invitrogen Life Technologies, CA, USA) at a final concentration of 4 µg/mL and DAPI (A4099, PanReac AppliChem GmbH, Darmstadt, Germany) at a final concentration of 5 µg/mL for 7-10 minutes at RT. Channels were subsequently washed and filled with DPBS or a solution of VECTASHIELD® antifade mounting media (Vector Laboratories, Inc., CA, USA) and PBS (ratio 1:1 v/v) and the devices kept at 4°C. Imaging was performed by confocal microscopy (LSM 780, Zeiss, Oberkochen,

Germany). Image analysis and post-processing were performed using Fiji software (ImageJ, [216]).

3.3.2. Results and Discussion

Seeding of human cell lines within microfluidic devices

Initial cell culturing experiments were conducted by seeding HEK293 within rectangular PDMS microfluidic devices composed of microfluidic channel with cross section of $800\ \mu\text{m} \times 55\ \mu\text{m}$ and two ports, 1 inlet and 1 outlet, with a diameter of 1.5 mm. Preliminary results showed however a suboptimal adhesion of cells to the glass bottom during flowing of the devices for media replacement or staining. These results led us to investigate the use of different collagen coating concentrations to evaluate the possibility to enhance cellular adhesion with increasing collagen densities. Collagen type 1 from rat tail was used for coating of the channels at concentrations of 25, 45 and $100\ \mu\text{g/mL}$. Results showed that cells seeded in devices coated with low and intermediate collagen concentrations showed higher cellular adhesion, spread morphology and uniform distribution compared to cells seeded onto highly concentrated collagen. At $100\ \mu\text{g/mL}$ collagen resulted to enhance cell adhesion in 2D wells but it caused formation of aggregates within the devices chip due to higher viscosity of the coating, resulting in uneven cellular spreading and distribution (**Figure 3.10, A-C**). On the other side, a higher coating concentration enabled cells to better adhere to the substrate over time (**Figure 3.10D**) while low collagen densities resulted in cells assuming a spherical shape and

eventually detaching after few days of culture. Nevertheless, the prolonged exposure to flow during cell culturing and more significantly during the multistep staining process caused complete cell detachment and formation of cell clusters even at higher coating densities (**Figure 3.10E**), leading to significant drawbacks for the study of HEK 293 in a dynamic microenvironment.

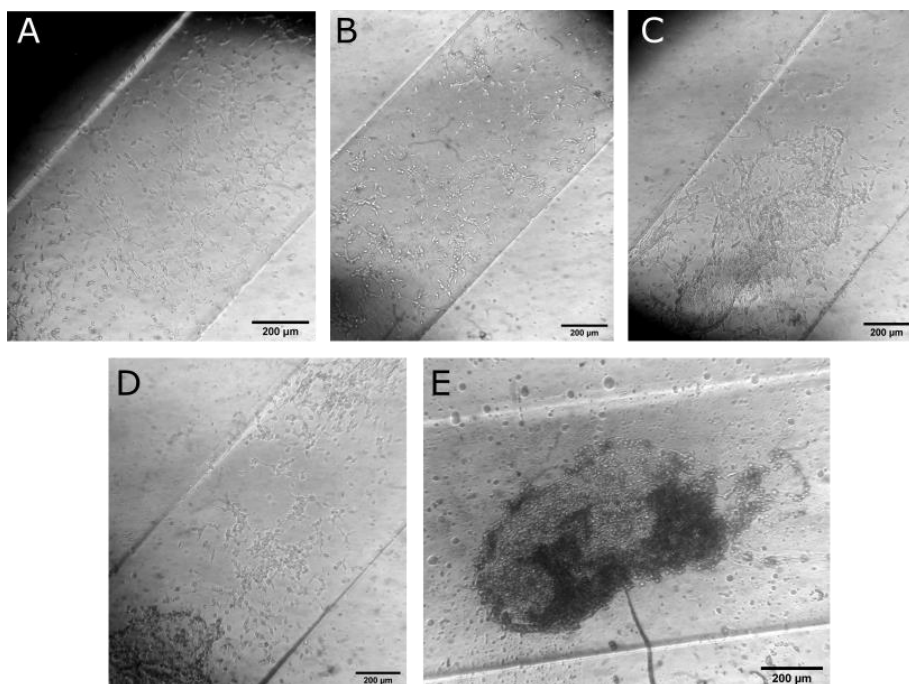


Figure 3.10. HEK293 cells culturing within the microfluidic devices. (A-C) Testing of the optimal collagen coating concentration: brightfield images show HEK293 cells cultured within the devices coated with 25 (A), 45 (B) and 100 (C) µg/mL of collagen after 4 days from the seeding. (D-E) Prolonged flow of the devices caused the cells to become round and progressively detach; a higher collagen concentration of 100 µg/mL enabled higher cellular adhesion after 1 week (D), however the multistep staining protocol determined cells detachment already after the fixation procedure (E). Scalebar 200 µm.

This behavior can be reconducted to the semi adherent nature of HEK293 cell line [217,218]. Originally obtained from an embryo kidney as adherent cell line, numerous cell lines were subsequently modified for growth in suspension, making them suitable for production of recombinant proteins and viral vectors in bioreactors [218,219]. Mechanical characterization of HEK293 cells has shown a low surface stiffness when cells are adherent due to immature actin scaffolding, which increases when cells are suspended [217]. The results shown by HEK293 to easily detach from the substrate and form cell clusters can thus be attributed to their tendency to grow in suspension. Because of these unique features, HEK293 cells have been rarely adopted for the modeling of kidney by means of OOaC platforms [220]. Following studies were thus focused on the use of HeLa cell line. Obtained from human cervical adenocarcinoma, HeLa cells are an immortalized tumor cell line that has been widely used as cancer model *in vitro*. HeLa cells have been adopted as well to build microfluidic platforms for the mimicry and investigation of cancer microenvironment and development mechanisms [221–223] as well as for tumor cells detection and capture on-chip [224]. HeLa cells were cultured within the devices under passive flow as previously described by using a 25 $\mu\text{g}/\text{mL}$ collagen coating and a cell concentration ranging from 4×10^6 to 6×10^6 cells/mL. Visual inspection of the channels confirmed cellular adhesion, spreading and proliferation, with cells showing a typical soft-irregular morphology.

Live/dead assays were performed by live cell staining with Calcein AM and propidium iodide at different time points and up to 10 days of culture (**Figure 3.11**), a time scale analogous to that of many OOaC platforms [22,225,226]. The cells resulted to be well adherent during the washing and the staining protocol, also at high pressures. Results showed high cellular viability up to 10 days under passive flow and cells tended to show higher apoptosis rates when forming clusters (**Figure 3.11C**), probably due to insufficient nutrients exchange. The distribution was mainly characterized by monolayers formation, confirming the suitability of the seeding and culturing protocol, though cells tended to grow on different planes over time, as underlined by the fluorescent intensity variations. Further experiments should be performed under active flow conditions, in comparison to passive flow: deciding the physiological flow rate would be essential to ensure optimal cellular viability over time as well as healthy morphology and functionality.

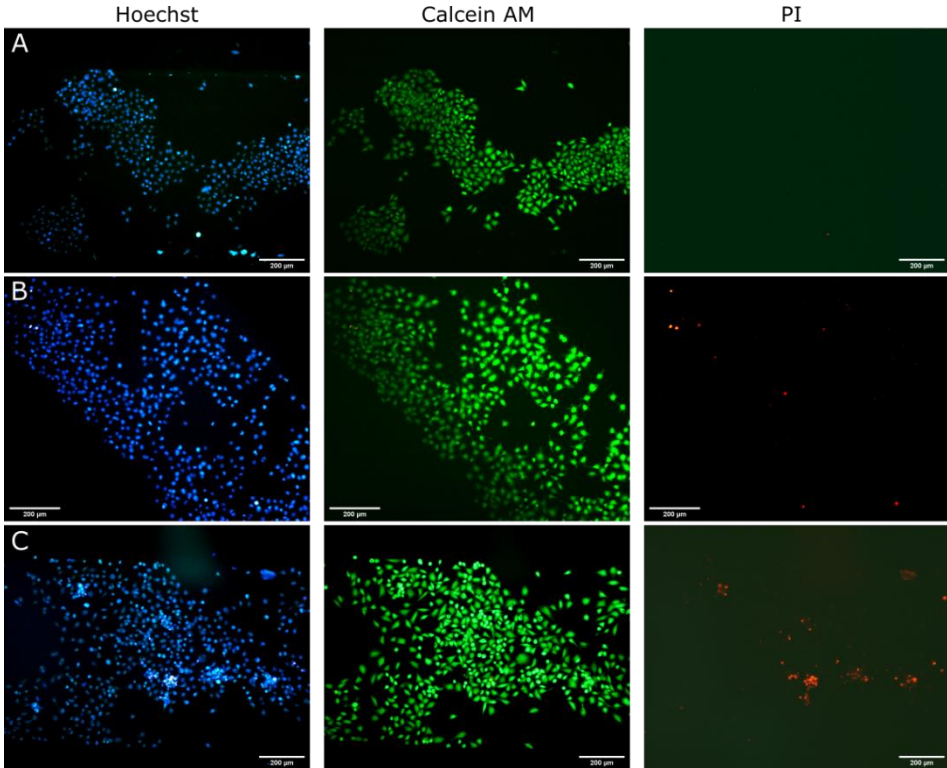


Figure 3.11. HeLa cells culturing within the microfluidic devices. Fluorescent live/dead assays were conducted at day 3 (A), 7 (B) and 10 (C) from seeding. Each picture shows staining with Hoechst for nuclei, Calcein AM for cell membrane and PI for dead cells respectively. Scalebar 200 μm.

Seeding of human primary LSECs within microfluidic devices

Rectangular PDMS microfluidic devices composed of microfluidic channel with cross section of 800 μm x 55 μm and two ports, 1 inlet and 1 outlet, with a diameter of 1.5 mm were used. LSECs from tumor distal (p.2) were seeded with a concentration $> 2 \times 10^6$ cells/mL in the devices previously sterilized by autoclave and coated with collagen at a concentration of 25 μg/mL. Cells were flowed in the channels and incubated for 15 min to ensure a primary adhesion prior

to add the cell culture media. Once adherent and homogeneously distributed, cells were fixed, permeabilized and stained with CMDR and DAPI. CMDR was chosen for membrane staining accordingly to previous published works on SIM imaging of LSECs [23,227]. Results showed a uniform cell distribution over the channels length, with fast primary adhesion after two hours from the seeding and maintenance of healthy phenotype up to 48 hours under passive flow. Confocal images confirmed the formation of homogeneous cellular monolayers, with effective nucleus and membrane staining protocols (**Figure 3.12**). These results are significant when the goal is recapitulating the tissue functions *in vitro*, as for OOaC models. In fact, nowadays the fabrication of liver and liver sinusoid models does not rely on the use of primary human cells, a drawback that hinders the physiological relevance of these platforms. In the past years, research has moved from platforms including hepatocytes only [228,229] to more complex models based on co-culture of hepatocytes with nonparenchymal liver cells, isolated from rodents [230,231]. However, the majority of the liver platforms is still based on the use of human cell lines, as HUVECs and EA.hy926 endothelial cells as model of LSECs [58,202,230,232]. Few examples have been reported on use of human primary liver cells due to limited samples availability and laborious isolation protocols [233,234]. Furthermore, the culture *in vitro* of human primary LSECs is challenging due to rapid dedifferentiation and loss of fenestrations after isolation [180]. Although we could not prove the maintenance of fenestrations over time, microfluidics offers the

advantage of mimicking physiological dynamic cues *in vitro* compared to traditional 2D static cell culture and our findings suggest the achievability of models built from tissue-specific human primary cells. The imaging of these samples by SR-SIM was in fact hindered by the chips design and the difficult coupling with the microscope stage, as discussed in **Section 3.2.2**. The new design with circular PDMS devices was then implemented before further super-resolution studies.

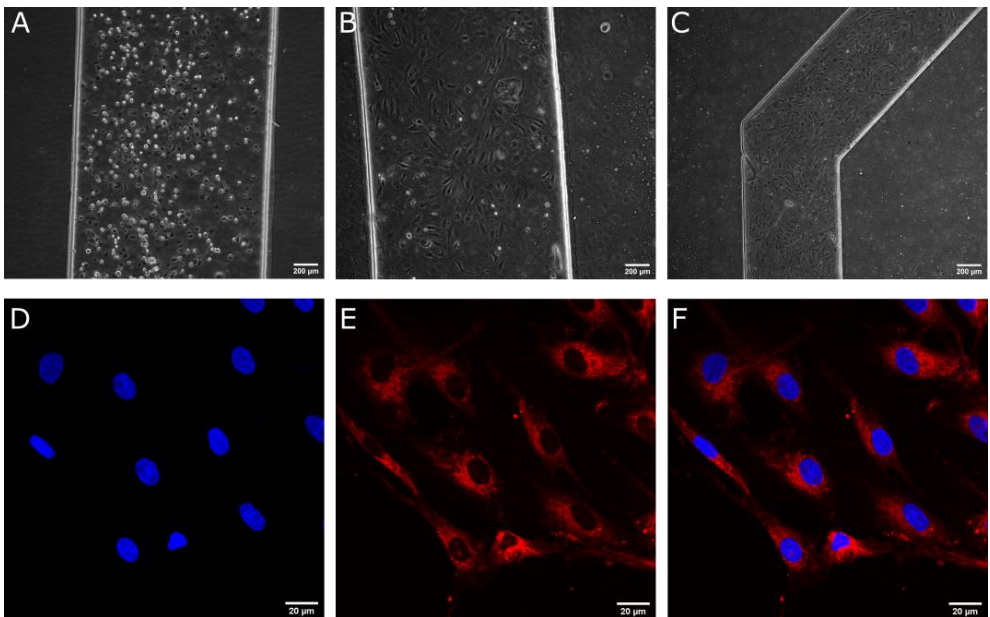


Figure 3.12. Primary human LSECs culturing within the microfluidic devices. (A-C) Phase contrast images of LSECs cultured within the channels at day 0 (A), 1 (B) and 2 (C) respectively. Scalebar 200 µm. (D-E) Confocal images of primary human LSECs after fixation and staining at day 2. (D) Nuclear staining with DAPI, (E) Membrane staining with CMDR and (F) merge. Scalebar 20 µm.

3.4. Validation of the microfluidic chip in a dish: testing the compatibility with SR-SIM

To evaluate the compatibility of the microfluidic devices in a dish with SR-SIM microscopy, the platforms were used for the culture of cell lines, well known for their stability and easy to use, primary endothelial cell line (HUVEC) as LSECs model, and LSECs in order to build step-by-step a more representative and complex model for the study of liver sinusoidal endothelial cells. The SR-SIM imaging was performed by comparing the different cell sources with either fixed or living cells and under static as well as flow (dynamic) conditions. Culture of primary human LSECs was performed at the Centre for Liver Research and NIHR Biomedical Research Unit, University of Birmingham, UK. Experiments were performed in the framework of DeLIVER project at the Department of Biochemistry, University of Oxford, UK. The authors gratefully acknowledge the Micron Advanced Bioimaging Unit (supported by Wellcome Strategic Awards 091911/B/10/Z and 107457/Z/15/Z) for their support and assistance in this work.

3.4.1. Microfluidic platforms culturing

Cell culture and culturing of microfluidic platforms

Mouse mammary epithelial cells C127 and primary Human Umbilical Vein Endothelial Cells from single donor (HUVECs, C-12200, PromoCell, Heidelberg, Germany) were cultured in tissue culture flasks in DMEM (high glucose, GlutaMAX™ Supplement, pyruvate, 31966021, Gibco™, Thermo Fisher Scientific, MA, USA)

supplemented with 10% FBS (F7524, Sigma-Aldrich) and 1% penicillin/streptomycin (P4333, Sigma-Aldrich) and Endothelial Cell Growth Medium (C-22010, Promocell) respectively. Isolated human LSECs were cultured as described in **Section 3.3.1**. Cryopreserved Sprague Dawley (SD) rat LSECs from the animal research facility at UiT - The Arctic University of Norway were thawed and cultured in RPMI-1640 cell culture medium supplemented with 20 mM sodium bicarbonate (R8758, Sigma-Aldrich), and allowed to attach for 3 h to fibronectin pre-coated devices (concentration of 200 $\mu\text{g}/\text{mL}$, [235]). Cells were incubated in a humidified incubator at 37°C and 5% CO₂ atmosphere and the culture medium was changed every other day until ready for imaging.

Microfluidic devices in a dish with either single or multichannel design, channel height of 55 μm and channel widths of 500 μm were sterilized with EtOH 70% for 10 minutes and washed as previously described with Phosphate Buffered Saline (PBS, 10010015, Gibco). Some of the devices were coated with collagen (C3867, Sigma-Aldrich) with initial concentration of 40 $\mu\text{g}/\text{mL}$, eventually increased up to 100 $\mu\text{g}/\text{mL}$ to enhance cellular adhesion. Cells were detached as previously described and eventually stained with CellMask™ Green Plasma Membrane Stain (CMG, C37608, Invitrogen) with a ratio 4:1 (v/v) before seeding within the devices as per protocol.

Staining, cell treatment and imaging

Live cell staining was performed by incubating the cells with 1X CMG (dilution 1:1000 in warm cell culture media, as per

manufacturer protocols) for 30 minutes at 37°C. Live cell studies of actin depolymerization were performed by exposing fluorescent cells to Cytochalasin D (2 μ M, C2618, Sigma-Aldrich) for 30 minutes. After washing with PBS, cells were fixed with 3.7% FA for 10 minutes at RT and washed three times with PBS for 5 minutes. Staining for actin filaments was done by flowing the channels with Alexa Fluor™ 594 Phalloidin (0.66 μ M, A12381, Invitrogen) for 20 minutes at RT.

Flow experiments were performed by using a syringe pump system (Standard Infuse/ Withdraw Pump 11 Pico Plus Elite Programmable Syringe Pump, Harvard Apparatus, MA, USA) and imposing a flow rate of 30-100 μ l/min. The pump was placed in the SIM microscope cage on a dedicated stage (Figure 3). The setup (syringe, tubing, chip, outlet tubing, chip stage) was mounted outside and then put in place.

Widefield microscopy acquisitions were performed with DeltaVision Core Zippy microscope, equipped with a cooled CCD camera for data collection. Standard filter set was used for FITC channel with wavelength/bandwidth of 475/28 nm for excitation and 525/48 for emission. Super-resolution structured illumination microscopy (SR-SIM) was used to acquire images of cell lines and LSECs inside of microfluidic devices. The commercial equipment OMX V3 Blaze system (Applied Precision, GE Healthcare Life Sciences, NJ, USA) using an UPLSAPO 60X/1.42NA oil immersion objective lens (Olympus, Tokyo, Japan) and Edge sCMOS cameras (PCO AG, Kelheim, Germany) was used for SIM acquisitions. The field of view

(FOV) of the microscope was 512x512 pixels, with 1 pixel corresponding to 82 nm, so an area of approximately 40x40 μm was displayed. For fixed cells, the full thickness of the sample was considered (approximately 6-10 μm for the nuclei and 1-3 μm for the membrane area). Acquisitions on living samples were done on a thinner layer (ca. 750 nm) to image the cell membrane, with a number of sections of 7 (minimum number to have reconstruction) in order to avoid bleaching and disturb the cell. Reconstructions were performed with SoftWoRx software. Before the imaging, the device coverslip bottoms were cleaned carefully with EtOH 70% and methanol and mounted on the circular stage.

3.4.2. Results and Discussion

After validation of the microfluidic platform for long-term *in vitro* cell culture and culturing of primary LSECs, the design was further optimized to be compatible with the SR-SIM microscope stage. Because of the chip mounted within the ibidi plastic dish, there was no longer the issue of device dimensions and it was easy to localize the channel and consequently the cells, placed in the center area of the platform bottom layer. Experiments were performed in this phase to evaluate the potential combination of dynamic systems with super-resolution imaging. Specifically, tests were conducted to investigate the following aspects: (i) influence of the collagen coating on SIM imaging (light scattering, reconstruction artifacts); (ii) influence of flow on SIM imaging; (iii) feasibility of real-time imaging of the

cellular response to flow of molecules; (iv) possibility to perform staining protocols on-chip.

SIM in static conditions: adherence of cells and influence of collagen

The collagen coating was used to reproduce the seeding conditions of human LSECs, as previously reported [180,213]. Murine C127 cells, HUVECs and human LSECs isolated from nonalcoholic steatohepatitis (NASH, p.3) and alcoholic liver disease (ALD, p.6) were cultured within the devices either coated with collagen type I or non-coated and imaged under static conditions by widefield and SIM microscopy techniques. Results showed that when the staining of CMG was performed after the seeding by flowing the channels, C127 resulted to be more adherent compared to HUVECs (**Figure 3.13**, left panels). Further experiments showed that to minimize the risk of detachment, the staining protocols on HUVECs should be run on chip after at least 48h from the seeding. We thus decided to pre-stain the cells before the devices seeding, that resulted in suitable fluorescence intensity.

Widefield images of fixed human LSECs showed a good distribution of cells along the channel length (**Figure 3.13C**, left panel). Interestingly, we noticed that NASH LSECs, seeded at lower concentration, showed good adhesion overnight and higher resistance to flow compared to ALD LSECs. From previous data collected from primary human LSECs, we believe that the behavior can be attributed to the cells passage number. The seeding concentration

might also affect the adhesion and high seeding concentrations (as in the case of ALD LSECs) might not be ideal for HSECs. However, staining of NASH LSECs resulted to be ineffective and further imaging was performed on fixed endothelial cells from ALD. **Figure 3.13C** shows the pseudo-widefield image of and ALD liver sinusoidal endothelial cell fixed after 1 day and the same image after SIM reconstruction.

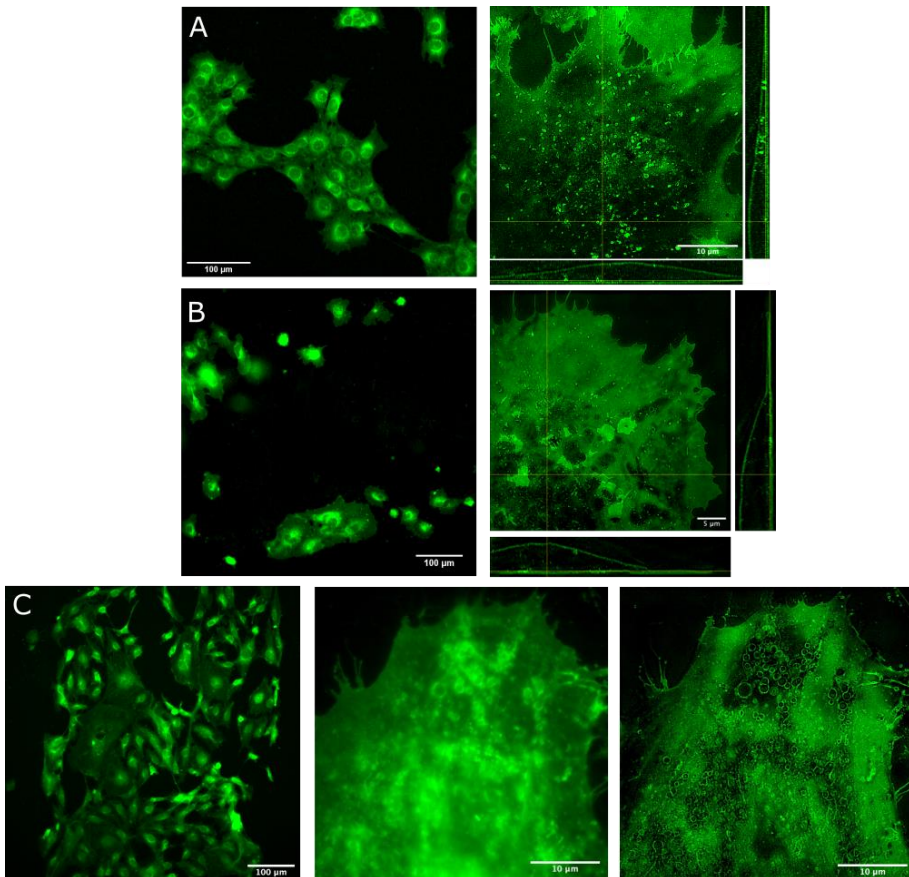


Figure 3.13. Widefield and SR-SIM images of cell lines and primary human LSECs within the microfluidic devices. Widefield images were taken after 24h seeding on cells cultured in collagen coated devices, fixed and stained with CMG (left panels): (A) C127

cells; (B) HUVECs and (C) LSECs from ALD, p.6. Scalebar 100 μm . (A, B, right panel) SR-SIM images of C127 and HUVECs were acquired on live cells pre-stained with CMG at day 3. Images show the orthogonal views (XZ and YZ cross sections). (C, centre and right panel) SR-SIM images of ALD LSECs were acquired on fixed cells stained with CMG at day 1. Centre panel shows the pseudo-widefield image before reconstruction and right panel shows the reconstructed SIM image.

Static SIM acquisitions of live HUVECs and C127 were initially performed without CO₂ chamber, resulting in modification of cell microenvironment pH, with consequent cellular contraction and morphological alteration (data not shown) [236]. The maintenance of physiological pH was firstly ensured by adding 20 μM HEPES buffer to the cell culture media and subsequently using a temperature and CO₂ controlled chamber on the SIM stage for live-cell experiments. The results showed both C127 and HUVECs looked healthy and well adherent during live acquisition (**Figure 3.13A-B**, right panels) and the presence of the collagen did not interfere with the imaging process, validating the use of this ECM protein as coating matrix, as commonly used for culturing human LSECs on 2D substrates, while previous SIM studies on LSECs from animal sources were normally performed on fibronectin coated substrates, as described later [23,174]. The entire cell thickness could be imaged with reduced photodamage and orthogonal views showed the presence of intracellular structures, confirming the possibility to image subcellular components at various imaging depths.

SIM in dynamic conditions: imaging stability under flow

For the flow experiment coated devices seeded with C127 cells pre-stained with CMG were used. Preliminary tests were run to evaluate

the stability of the system (pump, tubing and device, **Figure 3.14**). The syringe pump was firstly run with no load to evaluate if it induced vibrations that could potentially disturb the acquisition. After mounting the pump with the syringe and connect the tubes to the chip ports, we focused on a cell in the device and then started the flow. Results demonstrated that, while the running of the pump system without load does not disturb the imaging process, starting the flow after focusing on the region of interest led the samples to be out of focus and/or the chip to slightly move. Therefore, to minimize any movement and sample displacement, the protocol adopted for imaging under flow consisted in firstly connecting the pump to the device via the tubing, starting the flow and closing the microscope cage, and secondly identifying a region of interest and starting the imaging acquisition. Experiments performed by flowing PBS for 10 minutes on fixed C127 cells at a flow rate of 45 $\mu\text{L}/\text{min}$ confirmed the absence of any cell movements nor detachment.

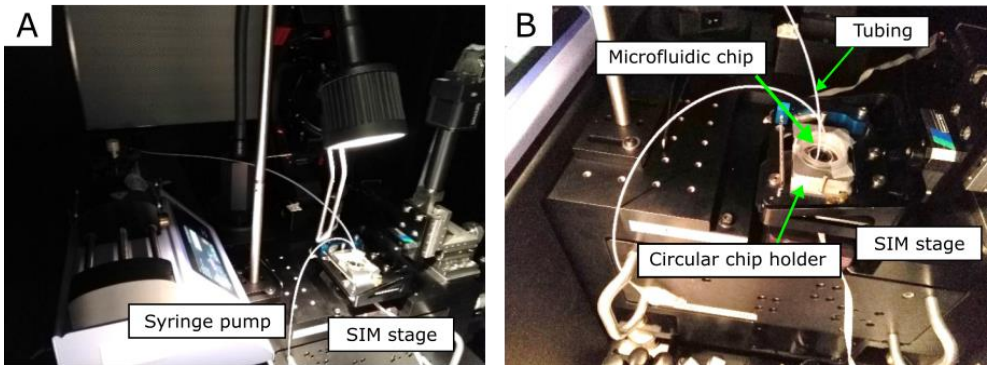


Figure 3.14. Microfluidic setup on the SIM microscope stage. (A) Syringe pump placed in the SIM microscope connected to the device and (B) device mounted on the SIM stage (on the circular chip holder) connected to the tubing.

SIM in dynamic conditions: real-time imaging of cell response to molecules

The main objective of this study was to evaluate the possibility of performing real-time super-resolution imaging of cells exposed to flow of molecules, such as fluorescent dyes for staining on-chip or drugs. Here, we performed two sets of experiments: staining on-chip of fixed C127 CMG-labeled cells with Alexa Fluor™ 594 Phalloidin and treatment of live C127 CMG-labeled cells with cytochalasin D, known to be a strong actin depolymerizing toxin [195].

Real-time imaging of actin filaments staining was performed by perfusing the channels over a 20 minutes acquisition time-lapse. The data showed an increase of the red channel intensity, however with important photobleaching of CMG and phalloidin dyes after the first 10 minutes of exposure (**Figure 3.15D**). These findings are in line with previously reported results, in which long-term SIM acquisition of mitochondrial dynamics on a time frame of 13.5 minutes could be performed with reduced fluorescence loss [237]. Nevertheless, the addition of antifading agents, that has been successfully proposed to prevent and reduce fluorescent dyes photobleaching in SMLM studies, could represent a valid strategy to further implement long-term experiments [237,238]. An interesting finding was the instant labeling of actin filaments just after the exposure to phalloidin, while standard staining protocols normally suggest an incubation time of tens of minutes. Therefore, these data underline the need for taking into account the temporal resolution when studying dynamic phenomena at the nanoscale [239,240]. Although numerous works

have reported SR imaging on live cells, the labeling of specimens is commonly performed before the imaging [237,241,242].

Interestingly, a recent work reported an automated platform for serial labeling of cells during STORM imaging for multiplexed proteins localization, however the time frames were not shown [243]. Thus, our experimental setup can be used to evaluate real-time effect of dyes on the samples of interest, either living or fixed, by performing real-time staining on-chip [244]. This application could lead to optimization of incubation times, with consequent improvement of signal to noise ratios during acquisitions as well as labeling-related cellular responses, such as effect of permeabilization, interaction among dyes, unspecific binding. Further, the use of parallel microfluidic devices composed of channel arrays would enable automated complex operations on-chip, as testing and screening molecules by exposure to different conditions on the same device [245]. These features result of particular interest when studying the dynamics of subcellular components and, since their investigation by SR depends on the use of fluorescent probes, real-time labeling coupled with SR has the potential to disclose drawbacks and develop novel techniques for studies at the cellular micro and nanoscales.

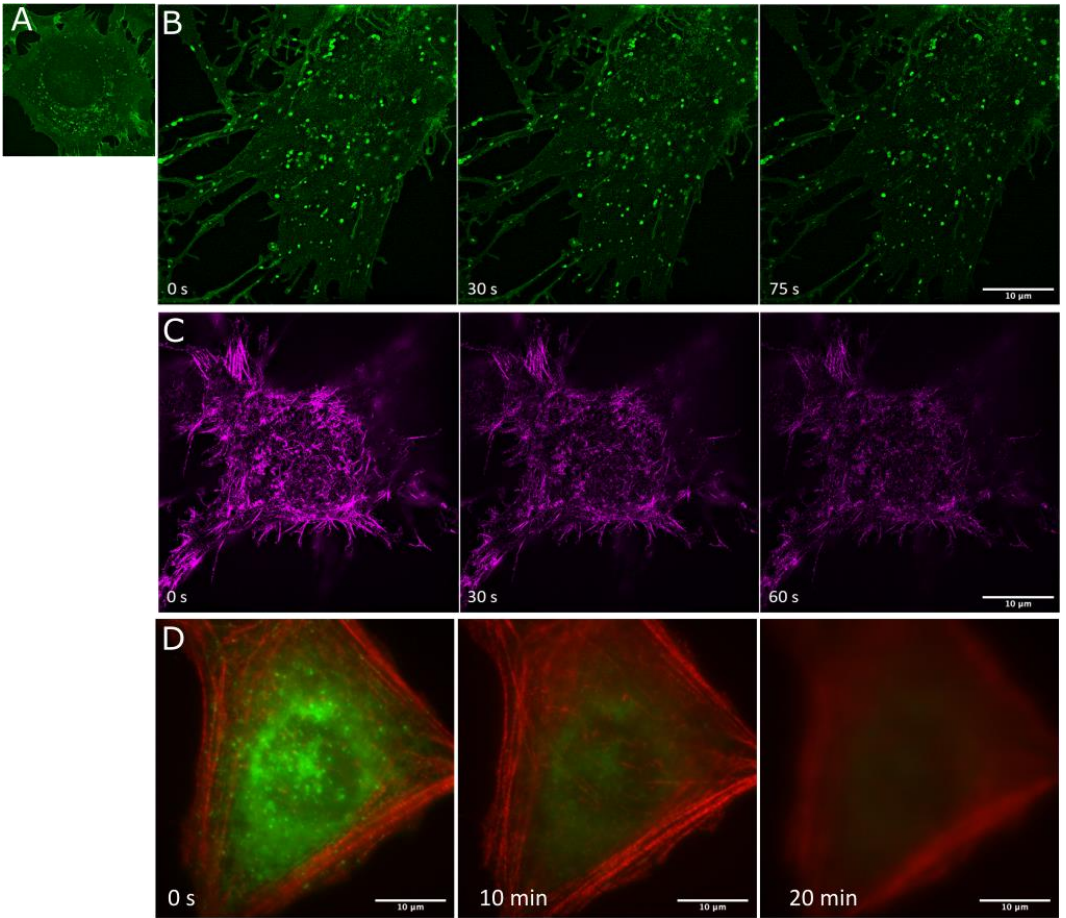


Figure 3.15. SIM imaging during dynamic experiments on-chip. (A) SIM image of live C127 seeded on a chip at day 3 before treatment. (B) Time-lapse acquisition of live C127 during flow of Cytochalasin D. (C) Time-lapse acquisition of real-time phalloidin staining of fixed C127 after treatment with Cytochalasin D. (D) Long-term time-lapse acquisition of real-time phalloidin staining of fixed C127 without treatment. Images correspond to the Maximum Intensity Projection (MIP) of 7 slices (thickness of ~750 nm). Scalebar 10 µm.

The dynamic setup was used to investigate the effect of drugs on the cell membrane of live cells. Cytochalasin D was flowed in devices seeded with C127 CMG-labeled cells at day 3, with treatment parameters chosen accordingly to previously reported studies [197].

Cytochalasin D is a toxin extracted from the fungus *Zygosporium mansonii* that inhibits actin polymerization and elongation by binding to actin filaments, causing a change in cell membrane morphology [246,247] and its effect on LSECs fenestration dynamics has been widely investigated [195,197]. The devices were placed in the SIM incubator chamber (CO₂, T=37°C) and images of CMG-stained cells were taken before starting the flow (**Figure 3.15A**). Then, the drug was perfused with the syringe pump system with time-lapse acquisition of live cell for 1.5 minutes. After the treatment, the chip was washed with DMEM and fixed with 3.7% FA for 10 min. After washing with PBS, cells were stained with Alexa Fluor™ 594 Phalloidin to confirm the action of cytochalasin D on the actin filaments. Results showed that exposure to cytochalasin D caused substantial changes in the plasma membrane morphology and cellular retraction, with formation of thin branches of the cytoplasmic area, as previously shown [248] (**Figure 3.15B**). Staining of actin filaments after cell treatment and fixation revealed a limited interaction of phalloidin with the actin due to the depolymerization effect of cytochalasin D. Moreover, during acquisition it resulted difficult to focus because of cells round shape and movement, with eventual detachment from the substrate (**Figure 3.15C**). Nevertheless, these results demonstrated the feasible combination of super-resolution imaging with microfluidic platforms for dynamic studies on living cells, showing the potential of microfluidics in providing a controlled microenvironment for investigation of nanoscopic events.

Main drawbacks of SR-SIM imaging

Despite the encouraging results discussed in this chapter, some major issues were observed during SIM acquisition, notably (i) cellular photodamage, (ii) fluorophore photobleaching over prolonged exposure and (iii) sample drifting (**Figure 3.16**). To reduce photodamage and bleaching, careful calibration of acquisition parameters, as laser power, time of exposure or dynamic range, should be done [152,249]. The drawback of sample drifting was instead due to the combination of SIM with a dynamic platform rather 2D specimens. The drift could be either due to movement or vibrations of the microfluidic device on the stage or to cell displacement under flow. We have reported here a strategy to minimize any movement or vibration of the chip by optimization of the setup implementation and connection and acquisitions done with the optimized protocol on live and fixed cells did not present any artifact caused by the drifting. In case of cells or particles movement during the flow, which could cause issues as out of focus, blur and reconstruction artifacts, optimizations can be done during the sample preparation by carefully choosing the coating concentration and cell density as well as during dynamic experiments by balancing the flow parameters. Though SR-SIM microscopy combined with dynamic models for live cell imaging is still in its infancy, several requirements need to be fulfilled and setup development and acquisition criteria designed carefully for optimal imaging.

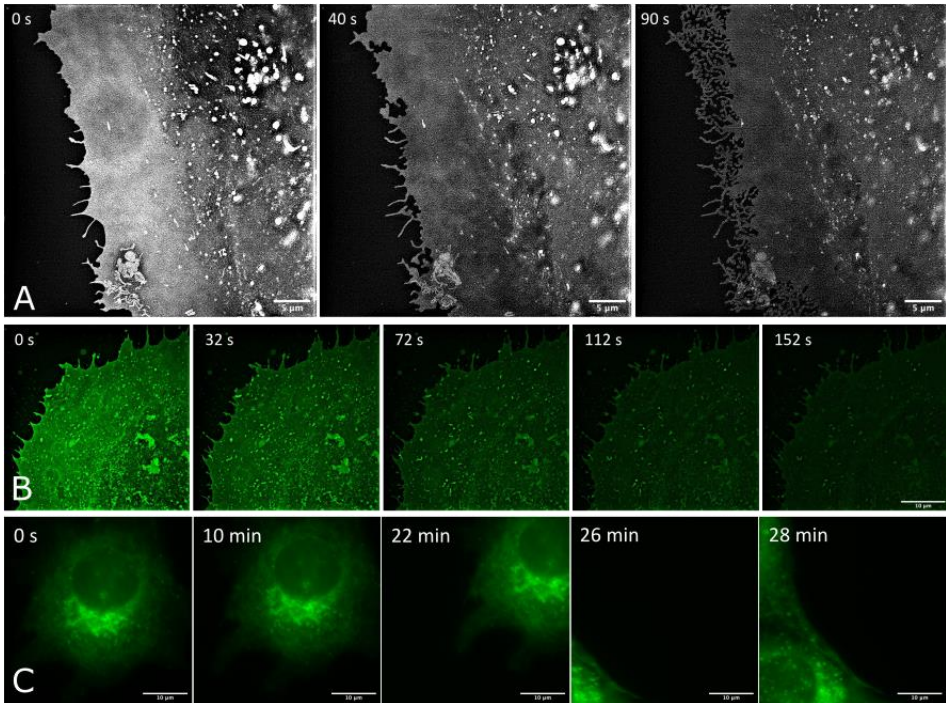


Figure 3.16. Main drawbacks related to SIM imaging on-chip. (A) Membrane retraction of live HUVECs (day 1) during time-lapse acquisition. Scalebar 5 μm . (B) Bleaching of the membrane dye during time-lapse acquisition of live HUVECs (MIP). Scalebar 10 μm . (C) C127 cell drifting over time during active flow of the channels using a syringe pump. Scalebar 10 μm .

Imaging of rat LSECs fenestrations cultured in a microfluidic platform

Finally, culturing of rat LSECs was performed on-chip for imaging of fenestrations. Cryopreserved rat LSECs were thawed and cultured directly on fibronectin pre-coated microfluidic chips. A protocol for cryopreservation and thawing of rat LSECs with maintenance of phenotype and fenestrations was followed here [235]. Cells were fixed after 3 hours from plating and stained with CMG.

Reconstructed SIM images acquired under static conditions showed the presence fenestrations and their organization in sieve plates, as previously reported (**Figure 3.17**). Measurement of the fenestrations size was done in Fiji ($n > 200$) from SIM reconstructed images and results showed an average diameter of $164 \text{ nm} \pm 46 \text{ nm}$, in line with the values found in literature [174,235].

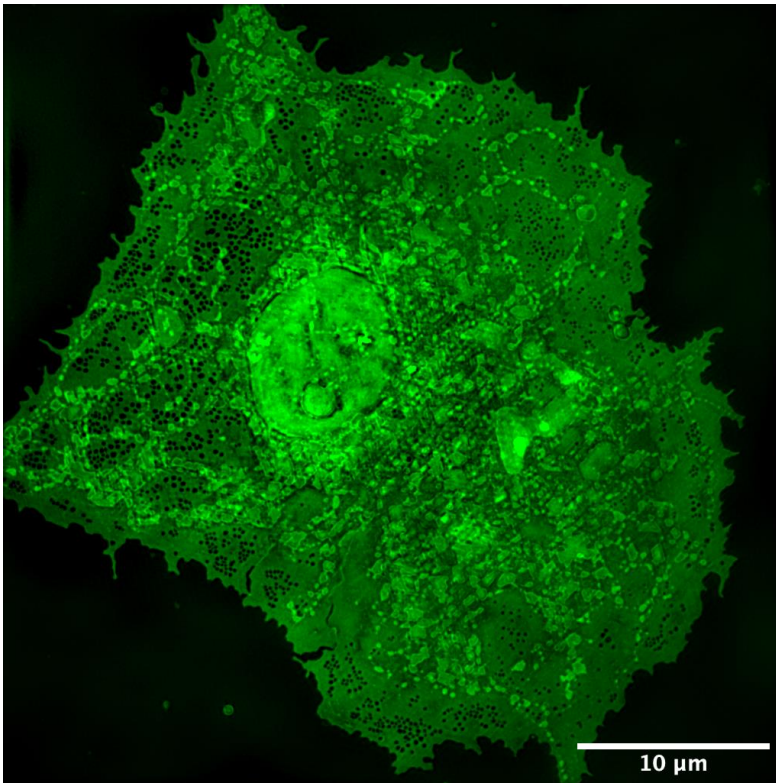


Figure 3.17. SIM image of fenestrations in rat LSECs. The image is the MIP of a 200 nm-thick slice of the cell. Scalebar 10 μm .

These preliminary results confirmed the possibility to seed primary LSECs on a microfluidic device and perform the staining protocol on-chip without cell damage or detachment. Nevertheless, time

frames for observation of fenestrations remain limited to few hours after cellular adhesion. More investigation should thus be carried out to study fenestrations and their dynamics on live cells and to prolong the maintenance of fenestrations over longer periods of time by exposure of cell to physiological stimuli, such as shear stress.

Overall, results confirmed the compatibility of our microfluidic platforms in a dish with the SR-SIM microscopy system and the possibility to use the setup in dynamic condition to perfuse either fixed or live cells with dyes or drugs. We demonstrated that this platform can be conveniently used to investigate, compare and optimize staining protocols with SR-SIM and to investigate real time cellular response to molecules. To the best of our knowledge, these are the first images of super-resolved human and animal LSECs cultured on a microfluidic device. Despite several improvements, such as dynamic flow conditions and longer culture and observation time, could be implemented, these results open up new possibilities for the study of subcellular structures and processes in more physiologically relevant models.

3.5. Conclusions and perspectives

Here, the fabrication and validation of a microfluidic device compatible with SR-SIM imaging setup was present as well as its use as *in vitro* system for on-chip imaging of the cellular micro and sub-microenvironment. We have firstly illustrated the main super-resolution imaging techniques, with a focus on structured illumination microscopy and its relevance on investigation of liver

sinusoidal endothelial cells. Current pitfalls and the combination with microfluidic platforms have been described. We have then presented the design of a microfluidic device compatible with SR-SIM and discussed the need for rethinking common organ-on-a-chip models, shifting from sandwich-based to vertical designs. After proposing a solution for optimal use of thermoplastic materials, we have chosen PMDS for the device development. Device design, fabrication and optimization steps have been described: drawbacks, as suboptimal bonding and incompatibility with SIM stage, have been addressed and led us to develop a microfluidic device in a dish. The devices were used for the culture of cell lines, known for their stability and easy to use, and primary cells, with the final goal of investigating the liver sinusoid microenvironment. *In vitro* studies with HeLa cell line confirmed the efficacy of the chips for long term cell culture and culturing of human primary LSECs on chip demonstrated maintenance of healthy phenotype up to 2 days. The SR-SIM imaging was performed to investigate cellular response to flow of dyes and drugs and image LSECs fenestrations. Drawbacks as fluorophores bleaching and drifting have been discussed. Results confirmed the compatibility of the devices with the SR-SIM system and the possibility to use the setup under perfusion during real time imaging acquisition. This study shows that the combination of SR imaging with dynamic *in vitro* systems enables a deep investigation of sub-cellular processes while mimicking more physiologically relevant conditions compared to 2D *in vitro* models.

As depicted in this chapter, engineering of cellular microenvironment using biomaterials is fundamental to build relevant complex three-dimensional models and Chapter 4 will thus focus on use of tissue engineering approaches to build a vascularized model resembling the liver sinusoid.

4. Development and
characterization of
polymeric scaffolds for
fabrication of 3D
microchanneled substrates

STATEMENT OF SIGNIFICANCE

Although capable of mimicking physiological shear stress and mechanical cues, conventional microfluidic-based models for biology are limited by 2D distribution of cells on flat substrates and lack of microenvironmental architecture. In this context, tissue engineered models show the great advantage of using biomaterials mimicking the ECM as cellular scaffolds. Therefore, this approach offers the possibility to recapitulate the cellular 3D microenvironment. This chapter focuses on the optimization and characterization of 3D channeled polymeric scaffolds to build a vascularized *in vitro* model.

4.1. Biomaterials and fabrications strategies for tissue engineering

Introduction to TE and its application

In 1993, R Langer and JP Vacanti firstly defined tissue engineering (TE) as “an interdisciplinary field that applies the principles of engineering and life sciences toward the development of biological substitutes that restore, maintain, or improve tissue function or a whole organ” [250]. Commonly related to regenerative medicine, TE has the main goal of recreating *in vitro* functional constructs that can repair or regenerate a living tissue once implanted *in vivo*. Originated in the ‘80s with the first attempts of engineering artificial skin [251,252], the development of tissue engineered analogues comes the need to face a shortage of donors for tissues and organs transplantation, which represents nowadays a severe healthcare issue in the public and medical community [253]. The final goal of TE would thus be the use of autologous cells from the patient for the formation *in vitro* of functional “personalized” tissue, which could be then implanted to restore the lost functions, also avoiding the risk of rejection that occurs when using xenogeneic or allogenic sources [16,254,255]. TE approaches are based on the combination of cells, biomaterials and cues for the development of tissue analogues and their principles have been extensively reviewed elsewhere [17,251,256] (**Figure 4.1**). As discussed above, cells are ideally isolated from the patient’s tissues (autologous source), although the majority of TE constructs in research rely on extensive use of

heterologous sources or cell lines. In the past decades, many research lines have focused on the use of stem cells in TE, that offer the main advantages of self-renewal ability and programmable differentiation [257,258]. The main factor that distinguishes TE from cell therapy techniques is however the use of biomaterials: in TE, biomaterials are one of the main characters and are used as substrates to seed and grow cells. Though at the beginning the initial goal was mainly to provide mechanical stability to the cells and create inert self-standing constructs with 3D architecture [251,252,259], the field of biomaterials has evolved far beyond its starting point and biomaterials with bioactive properties, tunable mechanics, programmable features and complex biomimicry of the cellular microenvironment are now available [260–262].

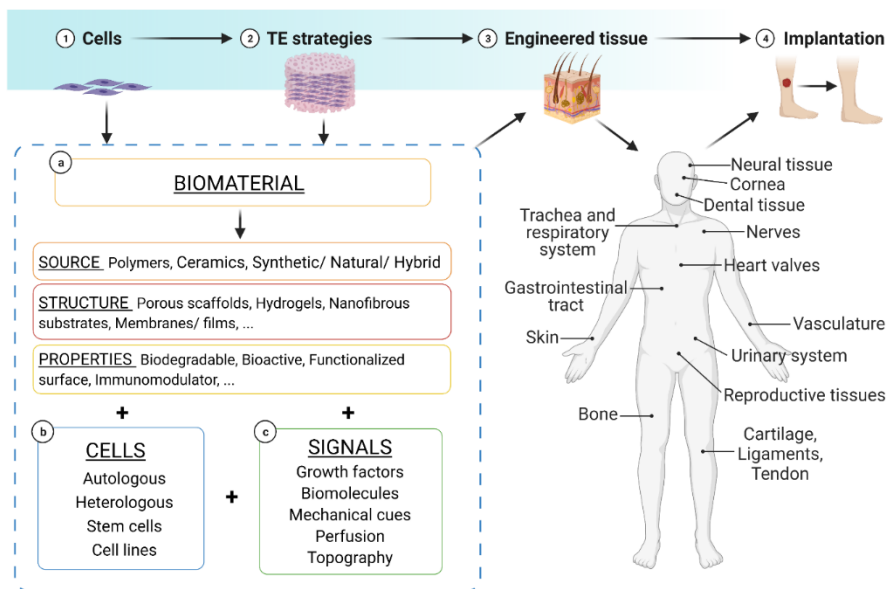


Figure 4.1. Tissue engineering principles. Starting from a cell source (ideally, from the patient), the goal of TE is to create functional tissues *in vitro* for implantation and restoration of

damaged and non-functional tissue (top). The combination of biomaterials, cells and signals represents the baseline of TE approaches (bottom left) and many engineered tissue constructs have been now developed (bottom right). Created with Biorender.com.

Biomaterials are engineered mainly depending on their ultimate function and here we give a brief overview. Comprehensive works can be found elsewhere [260,263]. In terms of the material source, biomaterials can be generally classified into natural, synthetic and hybrid [264]. Natural and natural-derived biomaterials are commonly based on the use of extracellular matrix (ECM) components, as collagen, gelatin or elastin, or on natural polysaccharidic biopolymers, such as chitosan, agarose or alginate, extracted from crustaceans or algae [265]. Synthetic biomaterials are produced artificially and commonly classified into polymers and ceramics. Polymers such as poly(glycolic acid) (PGA), poly(lactic acid) (PLA) or polycaprolactone (PCL) have been widely used for the synthesis of biomaterials, mainly for soft tissue engineered tissues, while ceramics, as calcium phosphates and bioactive glasses, have found their main application in hard tissues regeneration. Based on the form, biomaterials can be shaped with specific micro and macroarchitectures depending on the final application: porous scaffolds, injectable hydrogels, nanofibrous meshes, multi-layered membranes are the most common forms, and specific fabrication methods have been developed to obtain the desired topography, 3D architecture and structure. Thirdly, based on the properties, biomaterials have been designed *ad-hoc* to be biodegradable, bioresorbable, or bioactive, for controlled adhesion or proliferation, controlled release of biomolecules, or even immunomodulation,

showing anti-inflammatory and antimicrobial properties [261,266,267]. Finally, signals represent the third component of TE: normally referring to growth factors and soluble molecules that can guide and enhance tissue regeneration [251,261], this category includes other fundamental signals as the presence of perfusion and mechanical cues, achieved for instance by culturing in bioreactors, and surface nanotopography.

Fundamental parameters for the design of TE scaffolds

The main objective of a scaffold designed for *in vivo* implantation is to give mechanical support to the cells and to provide them with a 3D environment that guides their growth and arrangement into functional tissue. During *in vitro* culturing and consequent implantation *in vivo*, the scaffold functions are progressively replaced by the ECM produced by the cells, both from the substitute and the host tissue. Therefore, after the regeneration has occurred, the scaffold becomes unnecessary and this explains the importance of using biodegradable or bioresorbable biomaterials in TE. In this paragraph we briefly describe the main design parameters to consider when developing novel TE constructs. They can be categorized into five main classes, notably (i) mass transport properties, intrinsically related to the scaffold's microarchitecture, (ii) physicochemical properties, (iii) mechanical properties, (iv) electrical properties and (v) time-related properties [268] (**Table 4.1**).

Table 4.1. Classification of scaffold properties and requirements for TE applications.

Scaffold property	Design features
Mass transport	<ul style="list-style-type: none">• Pore architecture• Pore size• Porosity degree• Pores interconnectivity• Surface area• Vascularization
Physicochemical properties	<ul style="list-style-type: none">• Surface chemistry• Topography• Geometry
Mechanical properties	<ul style="list-style-type: none">• Match tissue mechanics at the macroscale• Micromechanics• Mechanical stability over time
Electrical properties	<ul style="list-style-type: none">• Electrical conductivity• Tissue contractility
Time-related properties	<ul style="list-style-type: none">• Scaffold degradation• Stability• Controlled release of biomolecules

The transport of oxygen, cell culture media and nutrients is a fundamental feature to ensure proper cellular behavior and proliferation within a seeded scaffold. When considering porous substrates, adequate porosity is the key parameter to allow for proper transport. The pores architecture and size influence the cells penetration within the scaffold, their adhesion and growth. For the majority of TE applications, pores with sizes lower than 100 μm normally hinder optimal cell seeding, however for some tissues, such as skin or nerves smaller pore diameters have been found to be more effective. To obtain good proliferation, fluid and gases exchange and facilitate anastomosis and vascularization *in vivo*, the porosity degree (i.e., the ratio between the mass and the voids) required is generally very high, about 90%, and pores should show a high degree of interconnectivity to make the scaffold more permissive, rather than a

closed porosity. However, porosity needs to be carefully engineered since highly porous structures are generally characterized by low stability and stiffness, that could lead to a collapse over time. Also, the porosity degree is inversely proportional to the surface area available for cell colonization. Techniques as electrospinning, that lead to formation of constructs with micro and nanofibrous architecture, offer the advantage of highly increasing the surface-to-volume ratios. Importantly, pore size and porosity measurements are normally conducted via image analysis on dry samples after their fabrication. However, porous scaffolds undergo structural changes once they are seeded with cells because of the transition from a dry to a wet state. Parameters as the swelling ratio should thus be taken into account during scaffold characterization. When looking at human physiology, cells benefit from optimal transport because they are located no further than 200 μm from a capillary or blood vessel. Thus, despite the porosity, the design of thick functional TE constructs has demonstrated to be extremely challenging without the presence of a vascular network and perfusion. Though the majority of the models normally rely on vascularization of the scaffold after implantation, there is an increasing interest in pre-vascularization methods *in vitro* to obtain more physiological models and ensure long-term viability of the engineered tissue.

Physicochemical properties also influence cellular behavior. For instance, the use of natural polymers derived from the native ECM as biomaterials ensures a better mimicry of the cellular microenvironment, thus a better response of the cells. Especially

when fabricating composite scaffolds, performing surface modifications or loading biomolecules, the chemical composition should be investigated to validate the fabrication method and quantify the components. Physical features such as surface roughness and topography should be analyzed as they have been shown to influence cell adhesion, orientation and differentiation. Furthermore, the constructs geometry should be taken into account to recapitulate the tissue architectural and anatomical features, as we will discuss later.

At the macroscale, the bulk mechanical properties of the scaffold should ideally match the mechanics of the native tissue at the macroscale. Particularly important for tissues that bear important loads, as bone, the stiffness of the implanted biomaterial should not show any mechanical mismatch with the host tissue to avoid formation of fibrotic interfaces and impaired regeneration. At the microscale *in vitro*, substrates with different stiffnesses have shown to have a fundamental role on cell differentiation because of cellular mechanosensing properties, with scaffolds showing lower stiffness guiding stem cells to differentiate into soft tissue cells compared to stiffer ones [269,270]. Electrical properties result to be fundamental for the regeneration of tissues such as cardiac, nervous and muscular tissues. In this regard, conductive biomaterials, as conductive polymers (polyaniline, polypyrrol, ...), carbon-based and gold-based nanomaterials, have been widely investigated. Moreover, the control and tuning of perfusion, mechanical and electrical properties of the scaffold can be implemented also by use of external systems, as

bioreactors. Finally, the study of time-related properties ensures the proper behavior of the scaffold during *in vitro* phase and after implantation. Degradation tests of the constructs *in vitro* by either physiological or enzymatic methods allows researchers to estimate their durability and stability while experiments *in vivo* enable to tailor the degradation rate of the constructs to match the remodeling rate of the host tissue. It is also important to evaluate the cytotoxicity of the scaffold byproducts during degradation *in situ* and the excretion pathways to confirm their biodegradability and reduce the immune response from the host body. In case of scaffolds loaded with growth factors, biomolecules or drugs, release kinetics and rates should be assessed to ensure a controlled and gradual effect. During the scaffold degradation, other properties also undergo changes and therefore, investigation over time of the mechanical properties and stability should be conducted to prevent collapse before tissue regeneration.

Fabrication strategies for polymeric biomaterials

TE constructs are produced starting from the raw biomaterials by means of a fabrication strategy [271]. A plethora of fabrication methods has been engineered in the past decades and the choice of the suitable process depends on the type of biomaterial and the form and features the construct needs to have. For simplicity, here we have divided the fabrication strategies based on the final biomaterial structure, i.e., porous or fibrous scaffolds and hydrogels (**Table 4.2**) and we will briefly discuss the most relevant techniques for the

purpose of this chapter, focusing on porous scaffolds [272], though many others have been engineered and combination of techniques has also been investigated [273,274].

Table 4.2. Classification of the main fabrication strategies used in TE. The methods have been classified based on the final biomaterial structure (i.e., Porous, fibrous scaffold or hydrogel). For porous scaffolds, SCPL, TIPS, gas foaming, emulsification/freeze-drying and electrospinning are considered conventional fabrication approaches.

		Biomaterial structure		
		Porous scaffolds [19,271,274–277]	Fibrous scaffolds [278]	Hydrogels [275,279–281]
Fabrication strategy [272]	Conventional	<ul style="list-style-type: none"> • Solvent casting and particulate leaching (SCPL) • Phase separation/thermally induced phase separation (TIPS) • Gas foaming • Emulsification and freeze-drying 	<ul style="list-style-type: none"> • Nonwoven fiber bonding • Textile methods (knitting, weaving, braiding) • Melt and wet spinning 	<ul style="list-style-type: none"> • Physical gelation (electrostatic, hydrophobic interactions, ...) • Chemical crosslinking (photopolymerization, ...) • Microfabrication (photolithography, microcontact printing, ...)
			<ul style="list-style-type: none"> • Electrospinning 	
		<ul style="list-style-type: none"> • Rapid prototyping/ Solid Freeform Fabrication (SFF) (Inkjet, extrusion and laser-assisted bioprinting, stereolithography, ...) 		

Biofabrication techniques for tissue engineering and regenerative medicine have been commonly classified into top-down and bottom-up basing on the fabrication approach [278,282]: the top-down approach consists in the fabrication of constructs with relevant morphological, physical and chemical properties that are subsequently seeded with cells to build *in vitro* tissues or to be implanted *in vivo*. The top-down category includes the conventional biofabrication strategies for porous scaffolds: solvent casting,

particle leaching, freeze drying, phase separation, gas foaming and electrospinning [18,278,283]. On the other hand, the bottom-up approach consists in creating multicellular biological building blocks, that are subsequently assembled to form a larger functional construct [284]; the main bottom-up approach is rapid prototyping. Because of its modularity, the bottom-up approach represents a valid alternative to conventional biofabrication strategies.

One of the first methods developed for the fabrication of porous scaffolds is solvent casting and particulate leaching (SCPL), that consists in casting a polymeric biomaterial, previously dissolved in an organic solvent and mixed with a porogen agent, and consequently remove the solvent and leach the porogen to get a porous structure. Salt and sugar granules as well as beads have been used as porogen agents, with their size and concentration determining the scaffold microarchitecture. SCPL has proved to create highly porous scaffolds (porosity > 90%), with a pore size normally ranging between 100 and 500 μm . Widely used for fabrication of scaffolds for hard tissues regeneration (bone and cartilage) [285], the technique has evolved to avoid the use of organic solvents [277] and to produce multi-layered scaffolds with specific shapes (e.g., tubular) for applications as vascular TE [286]. Phase separation relies on the formation of a polymer-rich and a polymer-lean phase. Briefly, the polymer is dissolved in a solvent (normally naphthalene, phenol or dioxane) and quenched below the solvent melting point to have liquid phase separation and remove the solvent by sublimation. The use of low temperatures allows for

incorporation of bioactive molecules and the method has often been used combined with other strategies, as spinning and bioprinting [276]. Nevertheless, phase separation is hindered by low resolutions achievable and limited choice of materials, namely thermoplastics, such as PMMA. To overcome the use of organic solvents, alternative techniques were developed. In gas foaming methods, porosity is created by the use of gaseous porogen agents, originated during polymer crosslinking or by the nucleation of gas bubbles when the biomaterial is exposed to pressure or temperature [287]. Despite high degree of porosity, the technique is often limited by closed porosity and impossibility to control pores interconnectivity. In emulsification and freeze-drying (FD) processes, the dissolved polymer mixture is freeze-dried and the sublimation of the solvent leads to scaffolds with high porosity and interconnected pores. Interestingly, this technique allows for production of scaffolds characterized by both micro (15-35 μm) and macropores (hundreds of μm), generated respectively by the solvent and the ice crystals sublimation [276,288]. By optimizing the emulsion reagents and the freeze-drying parameters, constructs with tunable architectural properties, such as multi-layered and anisotropic scaffolds, have been produced [288–291]. FD has in fact been widely used in TE research, especially for bone [292,293], skin [290,294], neural [295] and cardiovascular [296–298] tissue substitutes. One of the main advantages of FD technology is the possibility to use a variety of polymers: FD has been used for fabrication of porous constructs from both natural and synthetic biomaterials, as well as composite

blends and ceramics. PLA and PGA-based polymers as well as polyurethanes (PUs) and poly(vinyl)alcohol (PVA) have been adopted as synthetic polymers mainly for soft tissues regeneration. Among the natural polymers, collagen, gelatin, hyaluronic acid, silk and cellulose have often been chosen. Combination of polymers with hydroxyapatite nanoparticles and other calcium phosphate ceramic phases has led to production of substrates for hard tissues regeneration. Fabrication of layered constructs has also been achieved by freeze-drying technology, with each layer showing different material composition so as to mimic the physiological tissues interfaces: the main applications were production of graded scaffolds for osteochondral regeneration [291] and wound healing. Several studies have also shown the feasibility of incorporating biomolecules, such as growth factors for enhanced tissue regeneration or silver nanoparticles to achieve antimicrobial features [299,300]. The main disadvantage of this technique is the long fabrication time, especially during primary drying, since long steps are normally selected to avoid any structural damage [288].

Alternatively, scaffolds with controlled geometry and hierarchical organization have been created by self-assembly organization of polymers or peptides [275,301]. Electrospinning consists in the fabrication (spinning) of nano and microporous scaffolds from a polymeric solution by electrostatic charge, that generates a jet when the applied voltage overcomes the surface tension of the liquid droplet [302,303]. During the spinning process, the solvent evaporation causes the fiber solidification and accumulation on a

collector. The fibrous and porous architecture created by electrospinning mimics the *in vivo* ECM nano-environment, that has been shown to have a fundamental role in regulating cellular phenotype, adhesion and organization [304]. Moreover, the versatility of this technique enables the fibers to be functionalized or grafted with molecules, peptides, drugs or growth factors to promote cell adhesion and specific functions, such as endothelialization and antithrombogenic properties [305]. Electrospun scaffolds have been manufactured with a variety of natural and synthetic polymers and their combination in blends leads to devices with physiologically relevant mechanical behavior while promoting cell adhesion and proliferation thanks to the large surface-to-volume ratio [302,306]. Electrospinning has been used in bone, skin, heart, liver, ligament and kidney TE and it finds its main application in tissue repair and regeneration, as wound healing and dressing [307], osteochondral implants [308] and tissue engineered vascular grafts (TEVGs) [302]. However, it shows several limitations as (i) low production rate, (ii) pore size and fibers density that hinders cell infiltration and (iii) 2D thin shape at the macroscopic scale [305,309]. Some drawbacks have been addressed, for instance cell infiltration can be increased by surface treatments or by coupling with other techniques to enhance macro-porosity [310] and thick scaffolds can be engineered by multilayered electrospinning [311]. Nevertheless, top-down techniques often lack of versatility and precise control over the scaffold properties (mainly mechanical) and cellular organization, with difficult scale-up and reproducibility [312,313], making them

less effective for the manufacturing of 3D highly organized tissue constructs. Rapid prototyping, also known as solid freeform fabrication (SFF), represents nowadays the cutting-edge bottom-up technology for fabrication of engineered tissues. Particularly, 3D-bioprinting uses biomaterials, eventually combined with cells and molecules, as bioinks, that are assembled in a layer-by-layer fashion by means of additive manufacturing techniques starting from 3D CAD models [271,278]. This strategy has been widely adopted for the fabrication of different biomaterials structures, as porous scaffolds and hydrogels. For description of bioprinting methods and their application in TE, we refer the reader to existing reviews [312,314–316]. Compared to traditional top-down techniques, bioprinting shows rapid and reproducible fabrication, possibility to print multiple materials with complex geometries, ability to directly print cells and biomolecules with precise spatial organization and to create heterogeneous scaffolds with gradual compositions [280].

Patterned constructs and scaffolds with complex geometries for specific applications

Scaffold geometry plays a fundamental role in guiding cellular adhesion, proliferation, differentiation and production of functional tissue [317]. Recently, the influence on cellular behavior of macro, micro and nanoscale features, such as pore geometry, size and distribution, curvature, surface topography and roughness, and substrate stiffness has been widely investigated [318]. At the macroscale, the majority of porous scaffolds produced by

conventional fabrication methods possess a cylindrical or cubical shape due to the molds commonly used to pour the polymer solution. However, when it comes to recapitulate the features of specific tissues, it is important to underline the need for complex geometrical shapes. Particularly, regeneration of tubular tissues, such as vascular networks, trachea, intestines, urethra and nerves, will require scaffolds with pipe-like structures. For membrane-like tissues, as the skin, the use of multi-layered membranous constructs would be more appropriate. For rope-like tissues, as skeletal muscles and tendons, fibrous scaffolds should be preferred, and so on. At the microscale, porous scaffolds present highly interconnected porosity for cellular penetration and proliferation, without however necessarily showing an architectural similarity with the native tissues. At the nanoscale, then, tuning the nanotopography, nano surface chemistry and mechanics becomes extremely challenging. In this paragraph, we briefly discuss the importance of designing scaffolds with relevant architecture, with reference to fabrication methods for tubular and microchanneled scaffolds.

The design of tubular structures is a key prerequisite to provide cells with geometrically-relevant templates for *in vitro* generation of vascular networks [26,319]. The patterning of tubular constructs for vascular TE has been achieved by different approaches, notably: (i) subtractive and sacrificial molding; (ii) layer-by-layer assembly and (iii) direct fabrication.

Subtractive and sacrificial molding are methods widely used to engineer scaffolds containing either simple or complex channel

networks. The techniques usually consist in using a solid material (mold) of the shape of the channels embedded within a polymer solution, that is the scaffold biomaterial. After the polymer crosslinking, the mold is either mechanically removed when structures as needles or fibers are used (subtractive molding) or dissolved when a polymer template, as gelatin and alginate, is used (sacrificial molding) [320]. Many works have adopted these techniques for the fabrication of hierarchical scaffolds containing microchannels and the use of bioprinting to deposit the sacrificial template has allowed researchers to develop constructs with complex network geometries, resembling the physiological tissue [321,322].

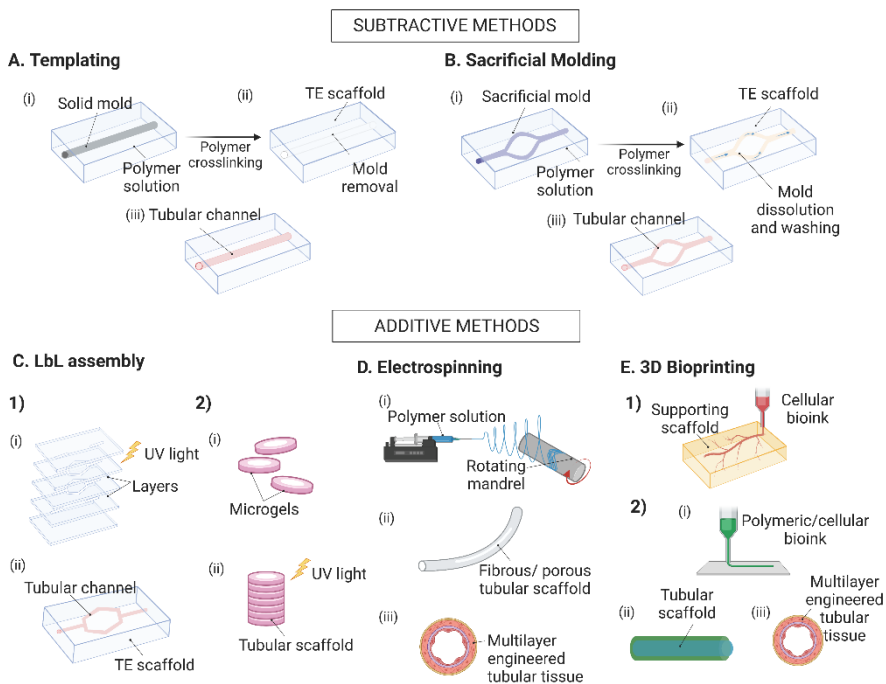


Figure 4.2. Fabrication strategies for tubular TE. (A) Templating by means of solid molds, as fibers or needles. **(B)** Templating by means of sacrificial polymers, dissolved after polymeric scaffold crosslinking. **(C)** Layer-by-layer assembly can be done by stacking of

polymer sheets to obtain a construct containing channels (1) or by stacking of ring-like microgels to obtain a tubular scaffold (2). **(D)** Electrospinning to obtain tubular scaffolds, eventually multilayered. **(E)** 3D bioprinting can be performed by direct patterning of cells-containing bioinks in complex geometries (1) or by coaxial bioprinting of multilayered tubular substrates (2). Created with Biorender.com.

On the other side, layer-by-layer assembly is an additive strategy that consists in sequentially aligning and stacking scaffolds components (planar sheets, cylindrical rings, ...) to form a tubular structure or a bulk scaffold containing channels. Poly(ethylene glycol)- diacrylate (PEGDA) ring-like microgels were assembled and crosslinked by UV photopolymerization to form perfusable 3D hierarchical constructs [323] while, in another work, assembly of patterned poly(octamethylene maleate (anhydride) citrate) (POMaC) sheets by UV photopolymerization was used to fabricate a perfusable scaffold containing complex branched microchannels that could directly anastomosed *in vivo* [90].

Thirdly, direct fabrication of tubular structures has been mainly achieved by electrospinning and rapid prototyping techniques. Tubular scaffolds have been electrospun by using rotating mandrels [302] or combination with electrospraying to create highly cellularized constructs and multilayer core-shell constructs resembling the blood vessels structure have been manufactured by coaxial electrospinning [324–327]. For instance, bilayer tubular scaffolds of PCL/collagen blend have been engineered by co-electrospinning over a rotating mandrel [328]. The different porosity of the two layers led to optimal seeding of the outer layer with smooth muscle cells and of the inner layer with endothelial cells.

Multilayered scaffolds with aligned microfibers produced by electrospinning of rotating mandrels have also been engineered for other applications, as for tendons and ligaments TE [318].

Fabrication of multilayer channels for urothelial and vascular TE has also been achieved by coaxial bioprinting of gelatin methacryloyl (GelMA) blends [329,330]. Alternatively, complex microvasculature architectures have been fabricated *in vitro* by direct endothelium micropatterning via 3D-bioprinting. [331] However, examples of conventional methods for the fabrication of complex geometries have also been reported. In a recent work, bundles of porous microchannel scaffolds were produced for spinal cord nerve regeneration [332]. Salt leaching was used in combination with fuse printing to create tubular porous structures. Sodium chloride was used as porogen agent and mixed with PCL. The mixture was firstly shaped into thin films and then rolled around sacrificial polystyrene rods, etched to form hollow structures. The PCL/NaCl hollow tubes were consequently thermally extruded through a printing nozzle to obtain fused microchannels and the salt leached to create the scaffolds porosity. With this technique, tubular and bifurcated scaffolds could be fabricated, with a single fiber inner diameter of 50 - 3000 μm , a wall thickness of 20-1000 μm and tens of meters in length. *In vitro* culture of dorsal root ganglia (DRG) for mimicry of peripheral nerves confirmed a significantly higher neurites outgrowth compared to cells cultured on films, confirming the importance of scaffold geometry in guiding nerve cells growth and expansion.

Rationale and objectives

Tissue engineering holds great promise for the regeneration of functional tissues and organs. Based on the use of biomaterials, TE has rapidly evolved in the past decades and a plethora of materials and processes has been developed for specific applications. The design of biomaterials, often in the form of porous scaffolds, needs to meet specific requirements on a multiscale level. Important features, as mechanical and physicochemical properties, biocompatibility and degradation need careful investigation to assess the suitability of the constructs *in vitro* and after implantation. Moreover, complex architectures mimicking the native tissue are often required. The rationale behind Chapter 4 is to design, develop and characterize patterned scaffolds capable of guiding vascularization, with a final goal in the context of DeLIVER project of adopting these platforms for *in vitro* engineering of liver sinusoids.

The chapter focuses on the study of polymeric scaffolds of natural origin produced via a combination of subtractive molding and freeze-drying technologies. After presenting the current methods adopted for the fabrication of these biomaterials and their patterning, we focus on the optimization of the fabrication process for further implementation. Particular interest is given to the design of thin samples that could be easily imaged with conventional confocal technology and to obtain a selective coating of the patterns for guided cell adhesion and proliferation. Evaluation of the constructs from a physical, chemical and mechanical point of view is described and results from different scaffolds formulations compared. Validation of the optimized fabrication processes is done by samples analysis and by using different imaging techniques, including SHG and SEM analyses.

4.2. Design of biopolymeric scaffolds for vascular tissue engineering

As discussed in **Section 4.1**, the use of natural polymers offers advantages as resemblance with native ECM components and architecture, biocompatibility, biodegradation with formation of non-toxic debris, easy manufacturing processes [264]. Here, a pullulan-based scaffold formulation has been proposed. Pullulan is a natural polysaccharide derived from the yeast *Aureobasidium pullulans*, a ubiquitous fungal organism. The commercial manufacturing of this polymer in form of powder is usually done by starch fermentation and purification and some properties of the final product such as molecular weight can be tuned based on manufacturing parameters. Pullulan is a linear and unbranched polysaccharide composed of maltotriose units linked via a α -1,6-glycosidic bonds. Because of its hydrophilicity and biocompatibility, it has been widely used in pharmaceutical and food industry, mainly in form of films [333,334]. However, its favorable properties have been investigated also for production of biomaterials for TE, drug delivery, medical imaging and plasma-substitute applications [335,336]. Pullulan has been used alone in form of hydrogel for vascular TE [337] or more often in combination with other polymers, such as dextran, collagen and chitosan, or functionalized with bioactive molecules for enhanced biomaterial formulations [335]. Its main applications can be found in wound healing and dressing, for instance coupled to antibacterial agents, bone regeneration, functionalized with nano-hydroxyapatite, and vascular TE, conjugated with heparin. Moreover, thanks to its

facile handling and processing, it has been fabricated in form of hydrogels, porous and nanofibrous scaffolds, and membranes [293,335,336]. Especially to enhance cellular adhesion, pullulan has been conjugated here to dextran, following a protocol patented by INSERM laboratories [338]. Dextran is another linear polysaccharide mainly produced from *Leconostoc mesenteroides* bacteria from fermentation in sucrose-containing media [339]. The polymer is mainly composed of $\alpha(1,6)$ -linked glucosyl residues, with few branching chains. Initially formulated as plasma substitute, its use has been subsequently extended to production of gels for molecular purification, drug delivery, as an agent for treatment of vascular diseases as thrombosis thanks to its anticoagulant properties, as well as for eye care and cosmetics [339]. Because of its cytocompatibility, biodegradability and stability properties, its use as biomaterial has been proven effective for vascular, bone, cartilage and skin TE [340,341]. In this work, a pullulan/dextran (PUDNA) polysaccharidic porous scaffold was fabricated by subtractive templating for formation of inner tubular microchannels using a crosslinking/ freeze-drying fabrication method (TCFD method).

The experiments presented in this chapter were conducted at INSERM U1148, Université de Paris, FR. Imaging was performed at the Plateforme d'imagerie photonique IMA'CRI, Faculté de médecine site Bichat, Paris, FR.

4.2.1. Fabrication by templating/ crosslinking/ freeze-drying method

Mold and fabrication setup preparation

PUDNA scaffolds containing channels were fabricated by a sacrificial molding subtractive strategy. Suture monofilaments were used as channel templates (PROLENE™ 7/0 dec. 0,5 3/8c polypropylene monofilament, ETHICON Inc., NJ, USA) (**Figure 4.3A**). For this purpose, the filaments needed to be tied around a supporting structure to keep them in place while pouring the hydrogel solution.

A special mold composed of pillars was designed in AutoDesk Fusion 360 and 3D printed by using an Ultimaker S3 printer (Cubeek3D, France) in polylactic acid (PLA) (**Figure 4.3B and C**). Printing parameters and monitoring were done using Ultimaker Cura software. Layer height of 0.2 mm, printing speed of 70 mm/s and printing temperature of 205°C were set for PLA extrusion.

After the suture filaments were wrapped around the pillars (**Figure 4.3D**), the fabrication setup was assembled by placing a thick glass slide on the bottom and then stacking a spacer (thin plastic frame), previously 3D printed or cut to fit the glass slide size. For large hydrogel slabs production, glass slides of 75x95x1 mm were used while for small hydrogel slabs, glass coverslips with a size of 25x75x1 mm were chosen.

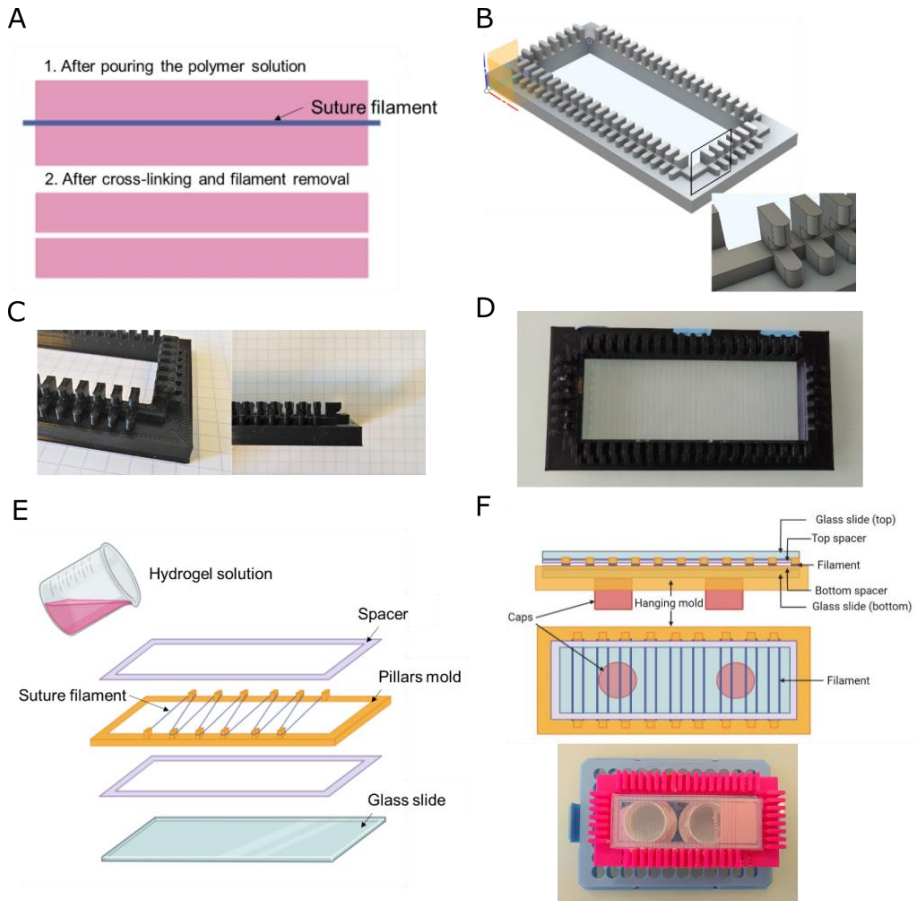


Figure 4.3. Mold and fabrication setup for patterned PUDNA scaffolds. (A) Schematic of the fabrication process (hydrogel side view): the suture filament is enclosed within the PUDNA solution after pouring (1) and the empty channel is obtained after removal of the filament when the hydrogel is crosslinked. (B) CAD design of the pillar mold and detail of the pillars structure (inset). (C) Image of the 3D printed PLA mold (left) and side view of the mold with pillars profile (right). (D) Image of the pillar mold assembled with suture monofilaments. (E) The fabrication setup consisted of a pillar mold where suture filaments are embedded and two spacers that determine the hydrogel thickness. (F) Schematic of side and top view of the assembled components (top) and picture of the top view (bottom): the caps that keep the mold suspended are visible on the bottom.

The spacer had multiple functions, particularly (i) confining the gel before its crosslinking, (ii) defining the hydrogel thickness once cut and (iii) hold the filaments. Different spacer materials and thicknesses were tested, as discussed in **Section 4.2.2**. The pillar mold with the filaments assembled was then placed at the top of the bottom spacer, followed by the second spacer. A top glass slide was placed after pouring the hydrogel solution. The whole setup was kept lifted by caps placed below the bottom glass slide to ensure the contact between the filaments and the spacers (**Figure 4.3E-F**).

Hydrogel solution preparation

Hydrogels were prepared from a solution of the polysaccharides pullulan (75% w/w, Mw = 200 kDa, Hayashibara) and dextran (25% w/w, Mw= 500 kDa, Pharmacosmos) mixed with sodium chloride (NaCl, Mw=58.44, Fisher Chemical) as porogen agent, with a protocol previously described [29]. The acronym PUDNA derives from these three main reagents (PULLulan, Dextran and NaCl). Briefly, 9 g of pullulan powder, 3 g of dextran powder and 14 g of NaCl were weighted separately and thoroughly mixed with a spatula before adding 40 mL of distilled water. A small spatula of Fluorescein isothiocyanate Dextran (FITC-Dextran 500 kDa, TdB Consultancy AB, Uppsala, Sweden), corresponding to 5-10 mg of the powder was eventually added to the solution for visualization of the scaffold structure under fluorescent microscope. The mixture was then placed on a magnetic stirrer and mixed at RT and 400-450 rpm for about 1 hour to ensure proper homogenization. During mixing, eventual salt clumps were manually broken up to have a uniform

solution. After mixing, the solution turned completely transparent. The solution was then left for 24h at RT to eliminate the air bubbles (**Figure 4.4A**).

Scaffold fabrication - Standard protocol

The scaffolds fabrication was done by crosslinking/ freeze-drying method (**Figure 4.4B**). The hydrogels were prepared first by following the protocol patented from INSERM [338]. Briefly, 10 g of PUDNA solution previously prepared and degassed were weighted at RT. 1 mL of NaOH 10 M was added to the solution for activation of the -OH chains. The mixture was then stirred at 200 rpm at RT for about 15 minutes until the color turned yellowish. In parallel, a solution of 3% w/v sodium trimetaphosphate (STMP, $\text{Na}_3\text{O}_9\text{P}_3$, Sigma Aldrich) was prepared by dissolving 300 mg of STMP salt in 1 mL of distilled water and placed on a tube rotator for salt dissolution. The STMP solution was used as chemical crosslinker agent for the hydrogel formation.

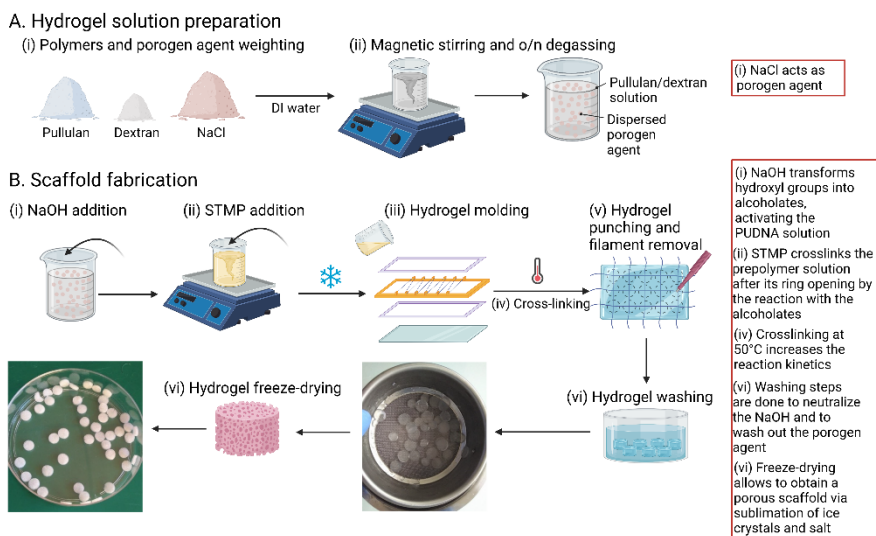


Figure 4.4. Schematic of PUDNA scaffold fabrication. (A) Preparation of the hydrogel solution and (B) PUDNA scaffold fabrication. The red rectangles indicate the chemical role of the reagents and chemophysical reactions occurring during the process. Created with Biorender.com.

After homogenization of PUDNA with the NaOH, the solution was placed in ice to slow down the crosslinking and the STMP was added while increasing the stirring up to 400 rpm. After ca. 1 minute, the stirrer was stopped and the gel poured over the fabrication setup previously described and the second glass slide placed over the top spacer to allow the gel confinement within the two plates and molding with the desired thickness. Silicon spacers with a nominal thickness of 0.35 mm were used. The setup was then placed in an oven at 50°C for 20 minutes for hydrogel complete crosslinking. After 20 minutes, the mold was removed by cutting the suture filament edges and the glass slides were separated from the crosslinked gel, that was consequently placed in a 10X PBS bath for

10 minutes. This step enables a primary swelling of the hydrogels, thus facilitating the filaments removal while preventing channels damage. The hydrogel slab was then moved to a rigid support (e.g., a glass substrate) and each filament removed by pulling them off, eventually with the help of a surgical needle holder. While removing the filament, the hydrogels were punched in correspondence of the empty channel by using a 5 mm puncher. The hydrogels were then placed in a 10X PBS bath under slight mechanical agitation for at least 1h to ensure neutralization of the NaOH. After checking the bath pH was neutral by either digital pH Meter or pH test strips, the samples were placed in a distilled water bath overnight under agitation (changed regularly every one hour for the first three hours minimum). This step allowed the removal of the porogen agent, that was verified by checking the gels conductivity and changing the DI bath until a conductivity $< 5\text{-}10\ \mu\text{S}/\text{cm}$ was reached (conductivity meter 145A+, Thermo Scientific Orion). Then, the hydrogels were placed in a 0.025% w/v NaCl bath under agitation until the equilibrium conductivity $< 500\ \mu\text{S}/\text{cm}$ was obtained. Gels were placed in 100x15 cm polystyrene Petri dish (Falcon, Corning) (about 30-40 gels per Petri) covered with a thin layer of 0.025% w/v NaCl solution and freeze-dried by loading the samples at 15°C. A standard freeze-drying protocol was performed as follows:

Table 4.3. Parameters used for the standard freeze-drying cycle. T= temperature, t= time, P= pressure.

1) Freezing					
T1	-20°C	t1	5h50min		
T2	-20°C	t2	1h30min		
2) Primary freeze-drying					
T1	-5°C	t1	2h10min	P1	0.05 mbar
T2	-5°C	t2	8h	P2	0.05 mbar
T3	10°C	t3	1h15min	P3	0.05 mbar
T4	10°C	t4	2h	P4	0.05 mbar
3) Secondary freeze-drying					
T1	30°C	t1	1h	P1	0.001 mbar

A freezing speed of 0.1°C/min was set until reaching -20°C and maintained for 90 minutes. Primary freeze-drying was done with a vacuum of 0.05 mbar and with increasing temperature from -20°C to 10°C by imposing a step function and freeze-drying speeds of 0.1°C/min (from -20°C to -5°C) and 0.2°C/min (from -5°C to 10°C). Finally, a fast secondary freeze-drying was performed at 0.001 mbar of pressure and 0.33°C/min of speed until reaching a temperature above RT.

4.2.2. Optimization of standard fabrication method

Optimization of scaffold thickness

Production of thin scaffolds was carried out by testing thinner spacers compared to the silicon ones used for the standard fabrication protocol. Different materials were evaluated and their properties (namely, thickness, stiffness and handling) were considered during the optimization steps (**Table 4.4**). Chemical paper and Parafilm®

were finally chosen for optimized production. The materials were manually cut by using a razor blade with a dimension fitting the glass slide's size in order to produce frames with an average frame width of 5 mm for large glass slides and 3 mm for glass coverslips. Standard scaffold fabrication protocol was followed by including the novel precut spacers within the setup.

Table 4.4. Specifications of the different spacers tested for the fabrication of thin hydrogels.

Material	Thickness (mm)	Aspect	Easy to handle
Silicon spacer	0.35	Semi rigid	YES
SEFAR NITEX 03-5/1	0.07	Soft	NO
SEFAR NITEX 03-10/2	0.03	Soft	NO
Chemical paper	0.23	Rigid, it deforms when wet	YES
Colored tape	0.12	Rigid, sticky	YES
Parafilm [®]	0.12	Semi-rigid, sticky	YES

Optimization of freeze-drying protocol for thin gels

Thin gels produced by changing the spacers thickness were freeze-dried by a modified freeze-drying protocol by loading the samples at 5°C (**Table 4.5**). A fast freezing speed of 0.5°C/min was set until reaching -30°C and maintained for 2.5 h. Primary freeze drying was performed at 0.05 mbar and temperature increasing from -30°C to 10°C under step function, with freeze-drying rates of 0.1°C/min for both the steps (from -30°C to -5°C and from -5°C to 10°C, respectively). Secondary freeze-drying parameters were kept unchanged compared to standard protocol.

Table 4.5. Parameters used for the standard freeze-drying cycle.

1) Freezing					
T1	-30°C	t1	1h10min		
T2	-30°C	t2	2h30min		
2) Primary freeze-drying					
T1	-30°C	t1	2h	P1	0.05 mBar
T2	-5°C	t2	4h10min	P2	0.05 mBar
T3	-5°C	t3	8h	P3	0.05 mBar
T4	10°C	t4	2h30min	P4	0.05 mBar
T5	10°C	t5	1h	P5	0.05 mBar
3) Secondary freeze-drying					
T1	30°C	t1	1h	P1	0.001 mBar

Selective coating of microchannels in PUDNA constructs

Collagen is the most abundant ECM protein and collagen-based biomaterials have been widely produced and investigated for TE applications due to the resemblance with native ECM [342]. Here, we used collagen as protein to coat PUDNA constructs in order to promote cellular adhesion and increase the physiological relevance of the matrices.

Two different approaches were proposed, namely pre-coating and post-coating strategies (**Figure 4.5**). In pre-coating strategies, PUDNA gels were coated before their use for *in vitro* experiments. Coating procedure could be performed by following two different approaches:

- A. Single freeze-drying approach: the PUDNA hydrogels were coated with a collagen solution after the washing step with DI

water. The gels were then freeze-dried and subsequently used for cell seeding;

- B. Double freeze-drying approach: PUDNA scaffolds were fabricated following standard fabrication protocol. After freeze-drying, the scaffolds were coated with the collagen solution and freeze-dried a second time before cell seeding.

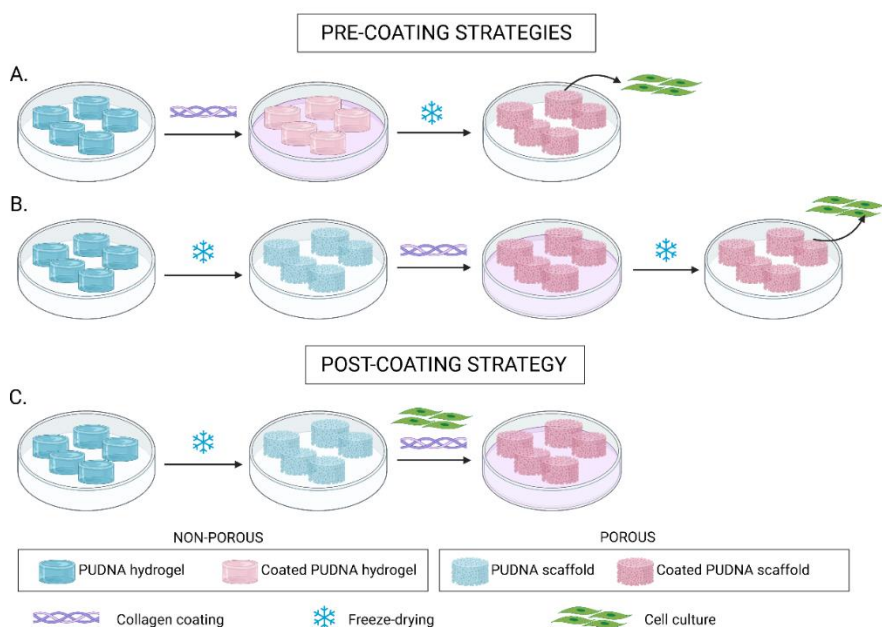


Figure 4.5. Coating strategies for PUDNA constructs. (A, B) Pre-coating strategies: PUDNA constructs are coated when either in form of non-porous hydrogels (A) or porous scaffolds (B) and then freeze-dried. (C) Post-coating of PUDNA scaffolds during cell seeding step. Created with Biorender.com.

The major difference between the two approaches was the final coating protein localization and distribution. Particularly, when the coating was done before freeze-drying, the PUDNA was still in form of hydrogel, thus not showing any porosity. This feature ensured the

collagen penetration within the molded microchannels and its deposition on the surfaces and edges. Therefore, this process allowed us to obtain a selective coating of the inner features. On the other side, collagen coating performed after freeze-drying would be uniformly distributed within the scaffold pores since it was performed when PUDNA was in a porous (scaffold) form. Similar to double freeze-drying pre-coating, the post-coating of porous PUDNA scaffolds was done during the phase of cell seeding, by mixing the protein solution directly with the cells. The protocol and results will be described in detail in Chapter 5. Although coating of pores could be useful for some TE applications, such as bone or skin regeneration, where homogeneous layers of tissue need to be engineered, our main goal was to permit selective cellular adhesion within the microchannels. Therefore, a single freeze-drying pre-coating strategy was chosen.

Soluble collagen type I from bovine corium (initial concentration 6 mg/mL, Collagen Solutions, Glasgow, UK) was diluted in 0.01 N HCl to obtain a collagen solution with final concentration of 1 mg/mL. After overnight DI washing of PUDNA hydrogels and when a conductivity $< 10 \mu\text{S}/\text{cm}$ was obtained, hydrogels were removed from the bath and slightly blotted with tissue paper to remove the excess of water. Then, they were placed in a sterile 15 mL syringe without needle whose end was closed with a three-way valve. Collagen solution was added and the syringe closed with its plunger. About 3 mL of solution were used to coat 15 gels. The solution was flushed back and forth for 5 minutes with the valve slightly opened

to ensure proper penetration within the microchannels without breaking the gels under high vacuum. The gels with the excess of solution were placed flat in a Petri dish and left at least 2 hours at RT with no agitation to allow for collagen deposition. After 2 hours, the excess was removed and samples washed once with PBS 1X for 5 minutes and once with PBS 0.1X for 5 minutes under mild agitation to allow for collagen neutralization. Coated hydrogels were then freeze-dried with a thin layer of PBS 0.1X with optimized freeze-drying cycle.

4.2.3. Characterization of channeled scaffolds

Morphological characterization

Scaffolds fabricated by addition of FITC-Dextran were visualized using a confocal microscope (LSM780, Zeiss, Oberkochen, Germany) with a 488 nm excitation argon laser (Excitation/emission 495/517 nm for FITC) and 10X objective (C-Apochromat 10x/0.45, Zeiss). Scaffolds were immersed overnight in PBS 1X prior to imaging. Scanning electron microscopy (SEM, JSM-IT100 InTouchScope™, JEOL Ltd., Tokio, Japan) was used for imaging of scaffolds topography and internal structure. Samples were either imaged at the top and bottom surfaces or cut in cross-section and then glued to a sample holder. Low vacuum condition (40 Pa), 10-kV acceleration voltage and backscattered electron detection (AsB) were used for imaging. Imaging of collagen coating was performed by confocal imaging of Sirius red-stained samples and multiphoton (MP)-induced second harmonic generation (SHG, TCS SP8, Leica

Microsystems, Wetzlar, Germany). For Sirius red staining, freeze-dried scaffolds were immersed in the dye for 30 minutes at RT without agitation. Then, samples were washed extensively under agitation with PBS 1X until the control (non-coated PUDNA) turned white (overnight at 4°C), thus confirming proper rinsing and remove of unbonded stain. For SHG, the MP was equipped with a 405/10 nm bandpass filter for collagen imaging. Samples were prepared by overnight immersion in PBS 1X and they were mounted on a circular plastic Petri dish and embedded in Aquasonic 100 ultrasound transmission gel (No. 01-08, Parker Laboratories, Inc., NJ, USA) to reduce light scattering. A 25X water immersion objective (HCX IRAPO, L25x/0.95, Leica) and excitation at 810 nm were used for image acquisition.

Physical characterization

As described in **Section 4.1**, the physical characterization of constructs for TE is fundamental prior to *in vitro* studies to evaluate their suitability for eventual *in vivo* implantation. Among a plethora of properties that can be evaluated depending on the final application, we have focused here on evaluation of short-term physical properties of PUDNA scaffolds, namely porosity and swelling behavior.

Porosity of freeze-dried scaffolds was evaluated by water squeezing method, as previously reported [343]. Tests were carried out by soaking the specimens (n=5 per each scaffold formulation) in PBS 1X for 2 hours under mechanical shaking. After 2 hours, the sample

was weighted after removing the excess of liquid (M_{swollen}) and after squeezing the liquid with the help of tissue paper by gentle pressing with a spatula to avoid breaking the gels (M_{squeezed}) in order to calculate the macropores volume occupied by the PBS.

The percentage porosity, representing the volume of macropores within the scaffold, was calculated as follows:

$$\text{Porosity (\%)} = 100 \cdot \frac{M_{\text{swollen}} - M_{\text{squeezed}}}{M_{\text{swollen}}}$$

For swelling measurements, specimens were placed in oven at 50°C overnight to remove humidity excess before the experiments.

Swelling tests were performed by soaking the specimens in PBS 1X and incubating them at 37°C. At each time point ($t=x$), the sample was weighted after removing the excess of liquid ($M_s^{t=x}$, expressed in mg). The swelling ratio was calculated as follows:

$$\text{Swelling Ratio} = \frac{M_s^{t=x} - M_d}{M_d},$$

where M_d indicates the initial weight of the specimen in dry state.

The swelling ratio was determined for $t = 0, 0.5, 1, 2, 6, 24, 48, 72$ h and 1 week. Two different PUDNA batches ($n=5$) were evaluated.

Chemical characterization

Chemical characterization of PUDNA hydrogels was carried out by spectroscopy and elemental analyses. PUDNA functional groups and the presence of collagen coating were investigated by Fourier transform infrared spectroscopy (FT-IR, Nicolet AVATAR 370, Thermo Fisher Scientific). Before the tests, the samples were placed

in oven at 50°C overnight to remove humidity excess. For the pellet preparation, 10 mg of sample powder were mixed with 190 mg of potassium bromide anhydrous (KBr) and then pressed at 6000 psi for ten minutes. The reading of the absorption spectra was done with OMNIC software in the infrared range $400\text{ cm}^{-1} - 4000\text{ cm}^{-1}$, with 32 cm^{-1} of resolution. Three different set of samples were analyzed: (i) freeze-dried 1 mg/mL bovine collagen powder (positive control); (ii) freeze-dried PUDNA scaffolds (negative control); and (iii) freeze-dried PUDNA scaffolds coated with 1 mg/mL bovine collagen.

Elemental analysis of the nitrogen content was done at the BioCIS – UMR 8076, Service Chromato-Masse Microanalyse, Faculté de Pharmacie, Université Paris- Saclay (vario EL cube, Elementar). Briefly, 1 mg of dry specimen was weighted at least twice in tin vials. The tin vials were consequently warmed at 900°C under oxygenated atmosphere for combustion of the specimens and the gases reduced on copper. The H_2O , CO_2 , N_2 and SO_2 were consequently collected and quantified via Helium chromatography for calculation of the mass percentage of C, H, N and S respectively. Three set of samples were analyzed ($n \geq 3$ for each formulation): (i) two different batches of freeze-dried PUDNA (non coated, negative control); (ii) freeze-dried 1 mg/mL PUDNA scaffolds coated with 1 mg/mL bovine collagen (PUDNA SFD); (iii) PUDNA scaffolds coated with 1 mg/mL rat tail collagen after double freeze-drying (PUDNA DFD).

Mechanical characterization

The Young's modulus of immersed coated and uncoated PUDNA gels was studied by nanoindentation (PIUMA Nanoindenter, Optics11Life, Amsterdam, Netherlands). The equipment was connected to a Dino-Lite digital microscope to allow the proper placement of the probe on the scaffold surface. A spherical probe with 0.45 N/m of stiffness and a tip radius of 103.5 μm was used. Samples were hydrated in PBS 1X for different time points and the tests were performed in immersion at RT in nanoindentation control mode. Each specimen ($n \geq 3$ for each formulation and time point) was analyzed by a matrix scan of 3x3 points with displacements Δx and Δy of 25 μm), with a total of 9 measurements per sample. The Young's modulus was calculated using the Hertzian model, with 3000 μm of maximum indentation depth and a Poisson's ratio of 0.5. The data analysis was performed using DataViewer V2.4 software and GraphPad Prism 7 was used for statistical analysis.

Optimization of scaffolds preparation for nanoindentation

The standard technique to avoid the floating of the samples consists of using a melted agarose stand on which the samples is glued (**Figure 4.6A**).

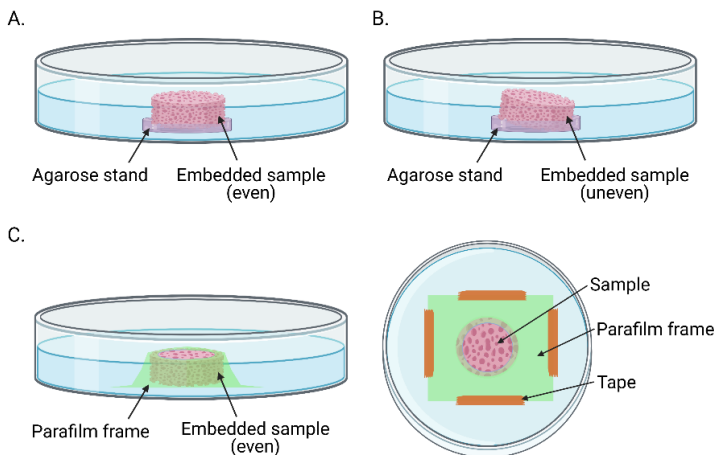


Figure 4.6. Optimization of scaffold preparation for nanoindentation tests. a. Standard agarose embedding of the sample, example of even sample surface. b. Standard agarose embedding of the sample, example of uneven sample surface. c. Optimized sample preparation consists in using a parafilm frame (left: side view, right: top view). Created with Biorender.com.

Here, a solution of 6% agarose (UltraPure™ Agarose, 15510-027, Gibco™, Thermo Fisher Scientific, MA, USA) in distilled water was heated in a microwave for 1 minute and then a small drop of the melted solution was poured onto a Petri dish and the scaffold was placed on the agarose while still viscous [344]. After the agarose solidification, the sample remained glued to the stand and could be submerged by the media for the tests. However, the technique was

mainly limited by the difficulty of spreading a layer of agarose with uniform thickness and placing the sample manually to have a flat surface, with the consequence of having uneven sample position, that hampered the mechanical tests (**Figure 4.6B**). To overcome this drawback, samples were prepared by cutting 3x3 cm parafilm pieces and punching them in the middle with a 5 mm puncher. The samples were then placed in the center of the Petri dish and layered with the parafilm frame, after making sure the hole was matching the sample surface. The medium was added after taping the parafilm to the Petri dish to avoid any floating of the scaffolds during the tests (**Figure 4.6C**).

4.3. Results and discussion

4.3.1. Standard vs optimized TCFD protocol

Optimization of hydrogel thickness

For the standard fabrication process, two silicon spacers with a nominal thickness of 0.35 mm were used. Due to hydrogel swelling during the washing steps, the final thickness of dry freeze-dried scaffolds resulted to be $1.45 \text{ mm} \pm 0.235 \text{ mm}$ ($n=10$), thus about twice thicker than the nominal spacers thickness. Since the channels were placed in the middle of the matrix, the use of thick scaffolds (with thickness increasing after hydration) hampered optimal imaging of the scaffold's depth by optical and confocal microscopy.

To overcome this drawback and fabricate thinner gels, the fabrication setup was modified and optimized. Though the hydrogels thickness could be modulated by changing the fabrication protocol, notably the

washing solutions and timing, here we decided to modify the spacers, whose thickness determines the nominal thickness of the hydrogels and the freeze-dried scaffolds (**Table 4.4**). Despite a wider choice of thicknesses, the SEFAR NITEX, a nylon woven filtration tissue, was excluded due to difficulty in handling and keeping the spacers in place during the hydrogel fabrication. Among the thinner materials tested, chemical paper and Parafilm[®] were selected because stiffer and easier to handle while, although very thin, colored tape was excluded to avoid release of glue and dye during the process. Parafilm[®] also presented the advantage of being sticky so the spacer could easily adhere to the glass slide during the molding process and remain in place.

Results from the fabrication process by using Parafilm[®] spacers showed the crosslinked gel were extremely thin and the bathing step before punching easily caused the thin gel layer to break (**Figure 4.7A**). Gels after the final washing steps resulted to be easily breakable and difficult to manipulate but they remained intact and thin (**Figure 4.7B**). However, the main drawback in producing thin scaffolds was the freeze-drying process with standard protocol, during which, after one hour of freezing, the gels resulted to be dried and shrunk (**Figure 4.7C**). On the contrary, the fabrication performed with chemical paper (nominal thickness of 0.23 mm) as spacer material showed that the paper deformed easily and often broke once wet, but the hydrogel slab was easy to manipulate and easy to cut. **Figure 4.7E** shows freeze-dried scaffolds produced by using chemical paper: in this case, the standard freeze-drying

protocol was effective. Intact scaffolds with a thickness of $0.71 \text{ mm} \pm 0.077 \text{ mm}$ ($n=10$) could be fabricated, thus reducing the initial thickness by one-half.

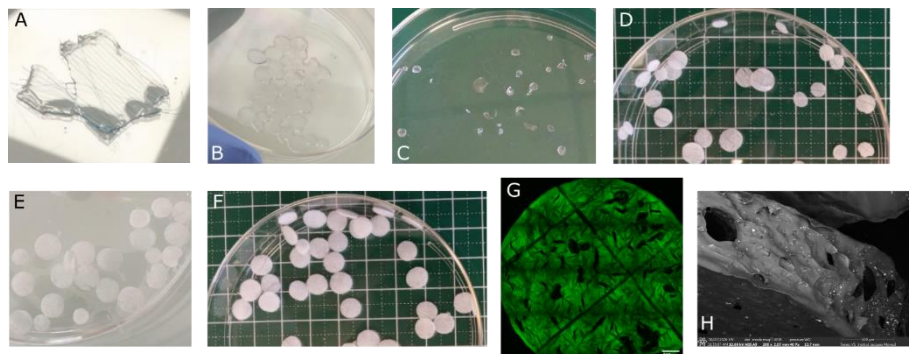


Figure 4.7. Comparison of hydrogels produced by using different spacer materials. Top (A-D): images of the fabrication process with Parafilm® spacers. (A) Molding, (B) washing, (C) freeze-drying with standard cycle and (D) freeze-drying with optimized cycle. Bottom (E-F). Image of scaffolds produced with chemical paper spacers. (E) freeze-drying with standard cycle, (F) freeze-drying with optimized cycle, (G) confocal image (Tile scan 4X4, 10 % overlap) and (H) SEM image of the channels within scaffolds produced with chemical paper spacer (top and side view respectively) with optimized freeze-drying. Scalebar 500 μm .

Confocal analysis of FITC-Dextran modified PUDNA hydrogels produced by using 0.23 mm thick spacers confirmed that the channels within the scaffold could be easily identified and visualized and SEM images of the cross-section confirmed the channels were embedded within the matrix (**Figure 4.7G** and **H**).

Optimization of freeze-drying protocol for thin gels

Freeze-drying technology is based on three main steps, notably freezing, primary and secondary drying. During the freezing step, the samples were loaded and cooled down by mechanical refrigeration to

a temperature lower than the triple point of the hydrogel. Large and thin containers were chosen to ensure optimal sublimation and temperature transmission to the samples. Calibration of freezing parameters is the most critical step to have proper freeze-drying. During primary freeze-drying, the sublimation of water in form of ice crystals occurs under vacuum. Then, secondary drying is performed to have final solvent evaporation with increase of temperature up to RT and further pressure decrease [288,345]. Figure 4.7A shows the typical FD graph obtained from standard cycle for thick samples, where the green and black curves represent the probes temperature, i.e., the products temperature. It can be noted the occurrence of the two main steps of the FD process, displayed as positive and negative peaks (yellow and purple circles) and corresponding to the water crystallization during the freezing and to water sublimation during primary drying, respectively. As it can be seen in **Figure 4.8B**, these steps did not occur during FD of thin samples with standard FD protocol.

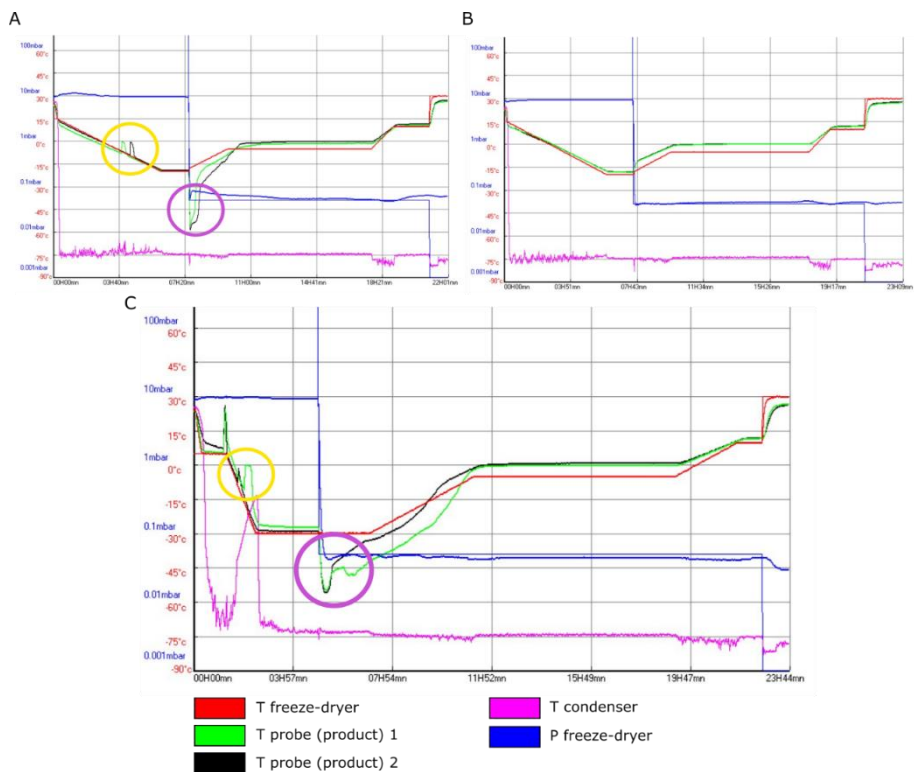


Figure 4.8. Freeze-drying curves from standard and optimized protocols. (A) Standard freeze-drying curve for thick hydrogel formulation. **(B)** Standard freeze-drying results to be ineffective for thin samples. **(C)** Optimized freeze-drying for thin samples.

We believe that this behavior might be due to suboptimal freezing temperature and rate. Cooling down at -20°C resulted to be not sufficient to attain the triple point, resulting in scaffolds undergoing melting rather than sublimation during the drying phases. In fact, the final products appeared to be transparent, with no porosity and important structure shrinkage and collapse. Moreover, the use of high freezing rates has shown to form small and numerous ice crystals, with consequent modification of final scaffold porosity and architecture, notably leading to reduced pore size and overall

porosity. This strategy could thus prevent the formation of big crystals, that could cause structure collapse during drying. Although the formulation of thick and thin scaffold was the same, the hydrogels thickness caused an important difference in temperature transfer and freezing process. In fact, the cycle resulted to be effective for thick and intermediate samples (from silicon and chemical paper, respectively) while a further decrease of thickness resulted in ineffective FD. For production of thin samples, we have thus decided to optimize several parameters for both freezing and primary drying, notably freezing temperature and slope and drying slopes. Freezing temperature was modified from -20°C to -30°C and, although ΔT was kept constant at 35°C , loading temperature of the samples was switched from 15°C to 5°C , increasing the freezing rate from 0.1 to $0.5^{\circ}\text{C}/\text{min}$. thus, also the time of freezing was much shorter for the optimized protocol. Figure 4.7C shows the modified cycle curves for thin samples: the water nucleation peaks appear in the graph after about 2h while with standard protocol the phenomenon occurred after ca. 4h, confirming the proper response of the samples to higher freezing rates and water crystallization. Moreover, scaffold shrinkage and collapse were prevented during primary drying by keeping a constant low drying rate of $0.1^{\circ}\text{C}/\text{min}$ during the whole phase while pressure was kept at 0.05 mbar as per standard protocol. Finally, pressure was further decreased to 0.001 mbar during fast secondary drying for 1h, as lower pressures ensure higher sublimation rate, thus reducing the moisture content [345]. Results showed the optimized protocol was effective for freeze-

drying of thin scaffolds produced by using chemical paper and Parafilm[®] spacers, with formation of pores and maintenance of scaffold shape and stability (**Figure 4.7D**). Scaffold thickness measurements conducted on dry specimens after freeze-drying were performed by using an electronic caliper ($n \geq 10$). Thickness measurements showed that optimized FD cycle led to a scaffold thickness (reported as mean \pm SD) of 0.81 ± 0.12 mm and 0.33 ± 0.073 mm for chemical paper and Parafilm[®] spacers respectively (**Figure 4.9**). For the thinnest scaffolds produced using Parafilm[®], the thickness resulted more than four times reduced compared to initial silicon spacer values (1.45 ± 0.24 mm). These results confirmed the possibility to freeze-dry thin scaffolds by properly modifying the process parameters without hampering their structural properties and stability.

Although useful for some membrane-based applications, the use of thin gels containing channels was however hampered by the channels localization. In fact, in thin scaffolds produced from Parafilm[®], most of the channels resulted to be on the surface of the constructs rather than placed within the middle of the gel. This was due to the slight displacement of suture filaments under the hydrogel weight during the pouring and molding steps, with consequent formation of open channel geometries. Therefore, scaffolds produced by using intermediate spacers thicknesses (0.2-0.25 mm, as for chemical paper) were preferred and freeze-dried by optimized cycle.

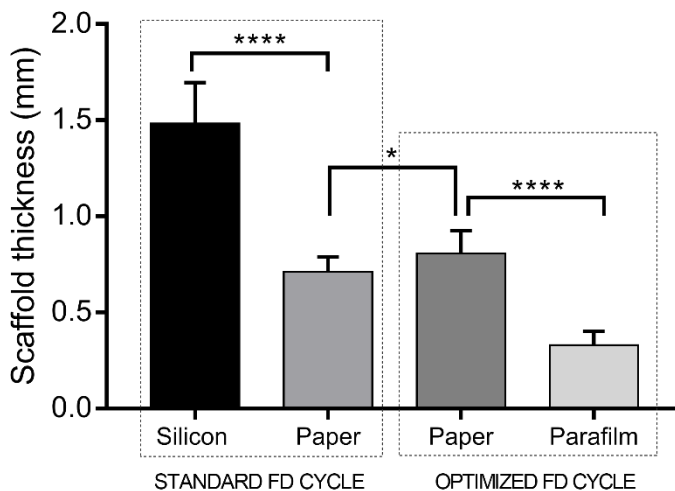


Figure 4.9. Comparison of scaffolds thickness obtained with different freeze-drying (FD) cycles for silicon, paper and parafilm spacers. Statistical analysis between 2 groups performed with unpaired t-test, *: p-value<0.05, ****: p-value<0.0001.

Selective collagen coating

Selective collagen coating within the molded microchannels was achieved by deposition of bovine collagen with concentration of 1 mg/mL and subsequent neutralization by PBS at pH 7.4 in non-porous PUDNA hydrogels prior to freeze-drying. The neutralization step normally entails a self-assembly process of collagen monomers in organized fibrils [342]. After freeze-drying, the surface of coated scaffolds appeared to be more compact and covered with a white layer, indicating occurred collagen deposition (**Figure 4.10A**). The influence of collagen in the physicochemical and mechanical properties was also assessed, as discussed in **Section 4.3.2**.

Detection of selective collagen coating within the microchannels was performed by either fluorescent imaging of Sirius red or by second

harmonic generation (SHG). Sirius red is an azo staining molecule widely used in histochemical staining and quantification of collagen by brightfield imaging, fluorescence or polarization techniques [297,346]. Sirius red staining was performed on both non-coated PUDNA scaffolds, as negative control, and collagen-coated specimens, where PUDNA was additioned with FITC-dextran for channels visualization. After rinsing of the dye, the non-coated samples turned the original color while coated PUDNA scaffolds retained the red coloration. Fluorescent imaging confirmed the presence of collagen distribution along the microchannels for coated scaffolds compared to the negative control (**Figure 4.10B and C**). The absence of collagen staining outside the channels confirmed the selective coating of PUDNA inner structures. Further investigation of the collagen structure was carried out by SHG analysis. SHG is a powerful imaging technique for studying collagen distribution and organization in native tissues as well as in engineered constructs and it has been applied to study cancer development and tissue repair, phenomena in which the ECM remodeling plays a fundamental role [347–349]. Based on multiphoton microscopy principles, SHG is a label-free nonlinear method based on the second-order polarization of materials: by using near-infrared excitation lasers, SHG is a coherent technique, meaning the signal depends on the orientation and order of the molecular and supramolecular structures compared to the laser directionality. Therefore, to generate a second harmonic signal, highly organized hierarchical harmonophores are required. Apart from collagen type I and II, SHG has been used successfully

only to image a reduced number of biological structures, such as myosin and microtubules [350,351]. The main advantages of SHG compared to other imaging techniques are that no staining is needed for visualization of collagen, with consequent no phototoxicity and bleaching, the capability of imaging thick samples due to intrinsic optical sectioning and increased resolution.

Images of the PUDNA scaffolds in wet state were taken under tile scan and z-stack modes, with tiles overlap of 10% and 5 μm -thick slices. Results showed a uniform distribution over the entire channel length and formation of a thin collagen coating within the prepatterned microchannels (**Figure 4.10D-F**). However, no fibrillar distribution was noted and collagen was mainly deposited in the form of small aggregates. This result could be related to the fact the collagen was deposited onto the hydrogel structure with no formation of a covalent bonding with the PUDNA due to the absence of functional surface groups. Also, deposition and neutralization at 4°C could prevent collagen dissolution. However, we believe that the final collagen form was mainly due to the collagen source. In fact, a soluble collagen formulation rather than a fibrillar one was chosen, thus the self-assembly of collagen fibrils could be hampered as coating with alternative sources of fibrillar type I collagen performed by our group have shown formation of organized collagen fibers on the surface of the devices (data not shown). Future improvements of the coating strategy might thus consider the use of fibrillar collagenic sources and evaluate their impact on the final coating form and on cellular response and interaction with the biomaterial. Nevertheless,

our results showed homogeneous distribution over channels with several mm length and *in vitro* tests further confirmed the successful coating activity, as will be presented in Chapter 5.

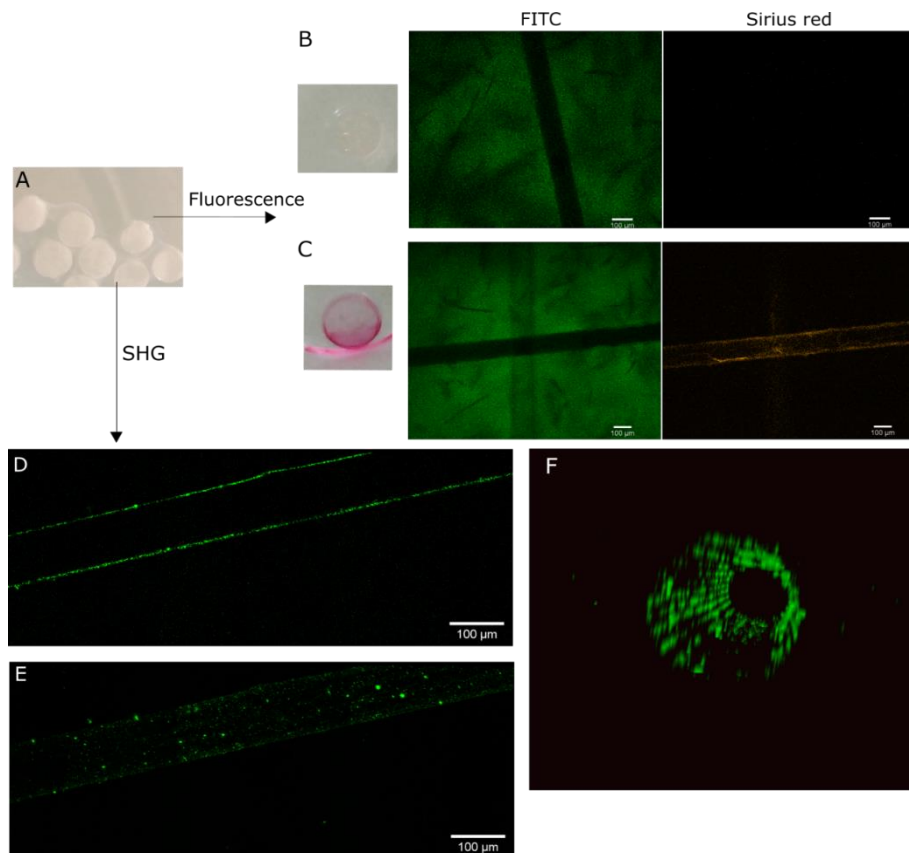


Figure 4.10. Fluorescent and SHG imaging of selective collagen coating. (A) Coated PUDNA scaffolds after freeze-drying. (B, C) Fluorescent imaging. Scaffold coloration after the last washing from Sirius red (left) and confocal imaging of FITC scaffold (green, center) and Sirius red (red, right) for control and coated PUDNA, respectively. (D-F) SHG imaging: (D) channel cross-section shows the presence of a thin and homogeneous distribution of collagen along the channel walls, (E) maximum intensity projection of the channel coating and (F) 3D rendering of collagen distribution within the channel. Scalebar 100 μm .

4.3.2. PUDNA scaffold characterization

Physical properties

a. Porosity

Porosity is an essential parameter of constructs for TE since the pore micro and microarchitecture, alignment, volume, interconnection, shape and roughness determine cellular adhesion, orientation, proliferation and behavior. Porosity calculation can be done by several methods [352]. Particularly, SEM image analysis has been widely used for estimation of porosity but critical aspects as sample sectioning, long post-processing time and operator intervariability hamper the establishment of reliable protocols. Here, we used water squeezing method to estimate the volume occupied by the macropores, as previously reported in literature [343]. The technique is based on the assumption that the physiological medium (PBS, in this case) that can be squeezed out from the construct corresponds the volume occupied by the macropores. Although other techniques, as microcomputed tomography, allow for a more accurate estimation, water squeezing offers the advantage of fast sample preparation and data analysis and results conducted by different operators showed low variability. PUDNA scaffolds produced with different formulations were analyzed, notably: (i) PUDNA fabricated by standard fabrication protocol, comparing different batches for assessment of porosity reproducibility; (ii) PUDNA with different crosslinking degrees (from 100 to 500 mg of STMP); (iii) PUDNA with varying concentration of NH_2 (from 25 to 100%) and (iv)

collagen coated PUDNA produced by optimized fabrication protocol. Data from classical PUDNA formulations showed average porosity values ranging from 30% to 40% depending on the batch. However, no statistically significant differences were found, confirming the reproducibility of PUDNA physical properties as well as the accuracy of porosity estimation by water squeezing (**Figure 4.11A**). Moreover, results are in line with previously reported data for the same biomaterials in the wet state [353]. Variation of porosity at different crosslinking degrees was also studied in a first stage to evaluate the suitable amount of STMP crosslinker for scaffold fabrication. As expected, higher porosity rates were found for low and intermediate crosslinker quantities (from 100 to 300 mg) while porosity tended to drastically decrease for increased amounts of crosslinker (**Figure 4.11B**). The behavior can be attributed to an increase of the crosslinking extent with increasing STMP concentration, as previously reported by Lack et al. [354]. Though high porosity is commonly preferred for TE applications and the use of 1% (w/w) STMP led to a porosity of almost 70%, these scaffolds presented impaired stability and difficult crosslinking due to the low crosslinker amount and 3% (w/w) STMP was chosen for the fabrication. Also, formulation of hydrogels including diethylaminoethyl-dextran hydrochloride (DEAE-Dextran) were initially investigated, by partial or complete substitution of dextran in different percentages (from 25 to 100%). DEAE-dextran is in fact a positively charged dextran formulation and its content of polycations and ammine groups favor cellular adhesion [355]. Also in this case,

several batches were evaluated. Although inter-batch variability was noted, (**Figure 4.11C**), the trend was similar among the different batches, with increasing porosity up to 36 and 38% for scaffolds containing 75 and 100% DEAE-dextran respectively. The results were however lower compared to not charged dextran and scaffolds produced with DEAE-dextran resulted opaque and sticky due to its formulation, with subsequent imaging and handling drawbacks. Finally, a standard dextran formulation was chosen for PUDNA fabrication. Three batches of collagen coated PUDNA scaffolds produced by optimized freeze-drying were finally tested. Data showed porosity percentages of 32.98 ± 0.37 , 32.15 ± 1.36 and 32.13 ± 4.90 for batches 1,2 and 3 respectively, with no statistically significant differences among the different batches (**Figure 4.11D**). The lower porosity percentage compared to standard protocols can be related to lower freezing temperature and increased freezing speed adopted for the optimized freeze-drying cycle, that have been demonstrated to cause reduction of scaffold porosity, as detailed above.

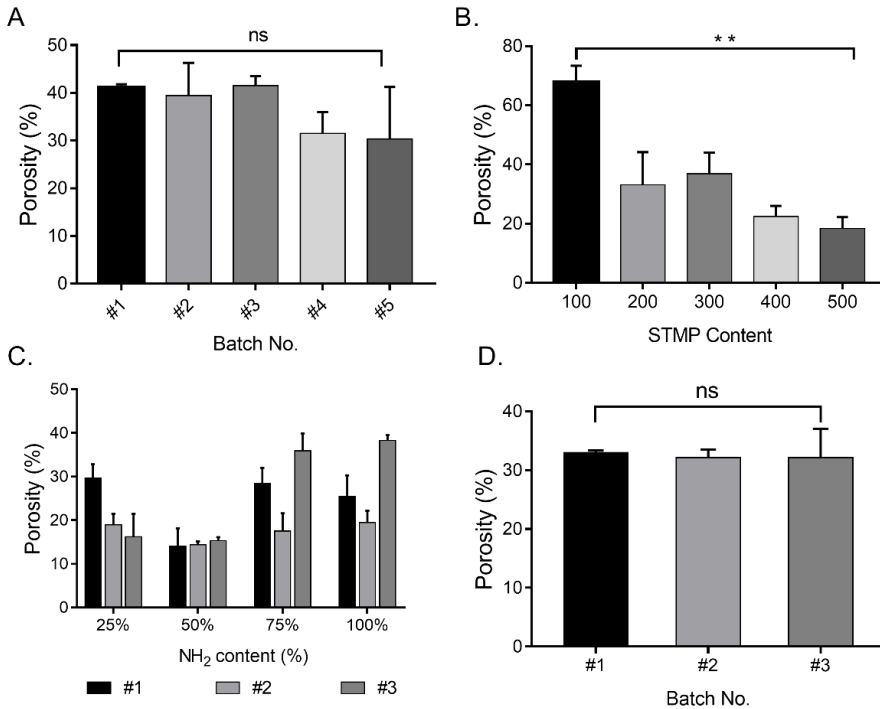


Figure 4.11. Porosity data obtained by water squeezing method. (A) Five different PUDNA batches, fabricated with standard fabrication and FD protocol. Porosity inter-batch variations resulted to be not statistically significant ($p < 0.05$, Kruskal-Wallis test). **(B)** Porosity variation based on STMP content (from 100 to 500 mg): the variation over the 5 concentrations tested resulted to be statistically significant (**, Kruskal-Wallis analysis), with p -value=0.0185. **(C)** Porosity variation based on NH_2 content, for three different batches. **(D)** Porosity variation for three different batches of PUDNA coated with 1 mg/mL collagen, single freeze-drying. Porosity inter-batch variations resulted to be not statistically significant ($p < 0.05$, Kruskal-Wallis test).

b. Swelling

Swelling indicates the capability of the scaffold to absorb a liquid and it influences the scaffold chemical, physical and mechanical properties before and after implantation and, thus, the cellular

response. For *in vitro* studies, the swelling ratio provides information about the scaffold efficiency in absorbing cell culture media, fundamental for cell seeding.

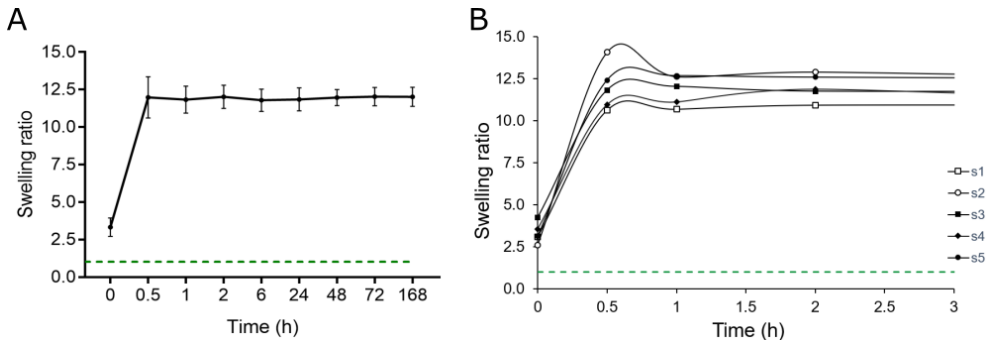


Figure 4.12. Swelling ratio of PUDNA hydrogels over a 7 days study. (A) Swelling trend between 0 and 168 hours, reported as average value \pm SD. **(B)** Initial scaffold settling curves reported for 5 samples in the first 3 hours of test. The baseline at 1 (no swelling) has been reported as reference (green dotted line in both the graphs).

Results from swelling tests showed that the maximum water uptake, with a swelling ratio varying from 10 to 14 depending on the sample and average of 11.98 ± 1.37 , occurred already 30 minutes after the initial incubation (**Figure 4.12**). This initial burst trend has been previously shown in porous scaffolds swelling and can be reconducted to immediate water uptake and scaffold structure settling before reaching a plateau. The swelling stabilized over time after the first 2 hours and remained constant during 1 week of testing, with final swelling ratios between 11 and 12.5m with a mean value of 12.02 ± 0.64 . Values are coherent with previously reported data for PUDNA constructs [356]. These data indicate the constructs have the capability to rapidly absorb medium after hydration, confirming their suitability for *in vitro* studies, during which cellular adhesion on

a substrate normally occurs in the first 30 minutes after seeding, as well as for *in vivo* implantation. Moreover, swelling of the construct is an important parameter to know in order to adapt the scaffold final size to the host defect area. The preservation of a similar swelling ratio over time for each gel indicated that the saturation point of the water uptake capability was reached and that the scaffold stability over time under hydration was maintained, without substantial weight loss.

Chemical properties

Fourier Transform Infrared spectroscopy (FT-IR) was utilized to detect the functional groups of PUDNA scaffolds and the eventual presence of collagenic units after the coating. To this aim, FT-IR spectra of bovine collagen, PUDNA produced by standard fabrication protocol and coated PUDNA were collected and investigated (**Figure 4.13**). Typical collagen peaks were visible in the bovine collagen FT-IR spectrum. Particularly, the collagen protein structure is characterized by the presence of amide I, II and III bands, 1650 cm^{-1} , 1550 cm^{-1} and 1230 cm^{-1} , respectively. Moreover the amide A broad band, representing NH stretching and located at ($3360\text{--}3320\text{ cm}^{-1}$) for bovine-derived collagen could also be observed [357–360].

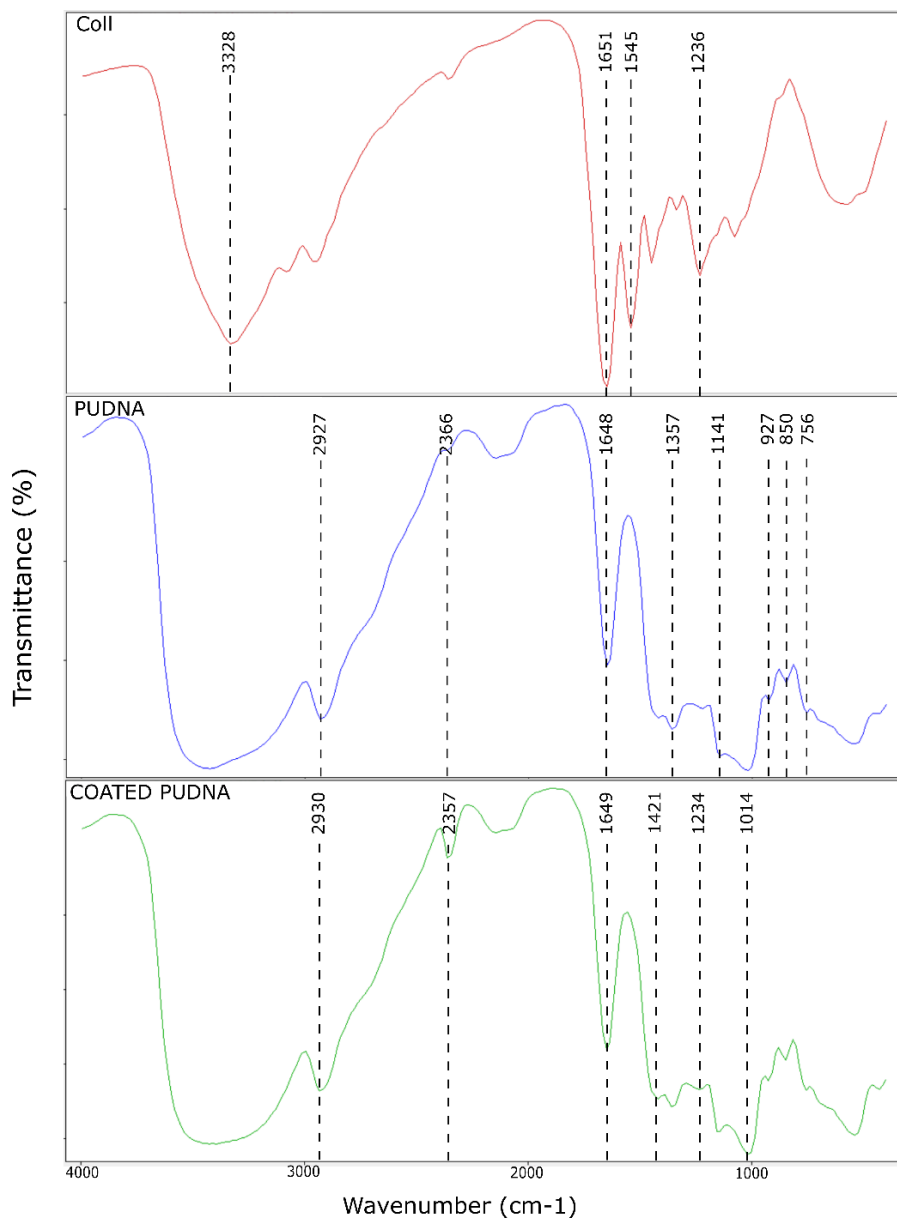


Figure 4.13. FT-IR spectra of PUdNA and coated PUdNA. (A) FT-IR spectrum of lyophilized bovine collagen, concentration of 1 mg/mL. (B) FT-IR spectrum of bare PUdNA and (C) FT-IR spectrum of PUdNA coated with 1 mg/mL bovine collagen.

For both the PUDNA spectra (coated and uncoated), a broader band could be observed in the 3000-3600 cm^{-1} , compared to the collagen spectrum. This feature can be ascribed to the OH stretching mode typical of water, confirming the trend of PUDNA biomaterial to easily absorb and retain water, as typical of hydrogels [361].

Uncoated PUDNA spectrum peaks showed a carbon-hydrogen (C-H) stretching bond at 2927 cm^{-1} and stretching vibration of -O-C-O- group at 1648 cm^{-1} . Peaks at 1357 cm^{-1} and 1141 cm^{-1} could be assigned to -C-O-H- bend and -C-O-C- stretch respectively. The absorption band at 850 cm^{-1} also appeared, corresponding to the typical pullulan glucose units while peaks at about 750 cm^{-1} and 930 cm^{-1} could be ascribed to the α -(1,4)- glycosidic bond and α -(1,6) units [335,362]. For collagen-coated PUDNA scaffolds, the band at 3300 cm^{-1} became even broader due to interaction between amide A band of collagen with the PUDNA hydroxyl components. Peaks at 1421 cm^{-1} and 1234 cm^{-1} could be ascribed respectively to interaction of the scaffold with amide II and III of collagen. Finally, the band of PUDNA at 1141 cm^{-1} shifted and increased in intensity and the band at 1014 cm^{-1} was ascribed to C₆-OH bond stretching vibrations [362,363]. Nevertheless, analyses on FT-IR data were difficult due to the small amount of collagen within the PUDNA formulation and to the absence of literature. Though the presence of collagen was confirmed by other methods, further FT-IR analyses on PUDNA scaffolds containing higher amounts of the protein should be conducted in the future.

To further evaluate the presence of collagen within the coated PUDNA hydrogels, elemental analysis studies were conducted for nitrogen quantification. Bare PUDNA formulations were compared to collagen coated scaffolds produced by either single or double freeze-drying. Results showed that nitrogen content was respectively $0.035\% \pm 0.028$ and $0.04\% \pm 0.027$ for PUDNA and single FD coated PUDNA, meaning no collagen could be detected in coated formulation (**Figure 4.14**). Double FD method gave a higher nitrogen content, of $0.095\% \pm 0.021$, however with no significant statistically difference compared to the other samples. This result can be reconducted to the difference in the coating area when performing single and double freeze-drying. In fact, during single freeze-drying, the gel is coated when its structure is not porous, thus the collagen coating results to adhere mainly to the empty channel and the gel surfaces. On the other hand, during double freeze-drying protocol, the collagen is performed on porous scaffolds, thus meaning collagen can penetrate within the pores in addition to external surfaces and internal patterns. This could explain the increase of nitrogen amount in double freeze-dried scaffolds. Also, since with double freeze-drying protocol the scaffold is coated starting from a dry state, this could ensure a higher uptake of the collagen protein. However, due to the small quantity of collagen retained during the coating, its presence was assessed by other techniques, mainly imaging of collagen structure, mechanical characterization (**Figure 4.10** and **4.15**, respectively) and *in vitro* cellular adhesion, discussed in Chapter 5.

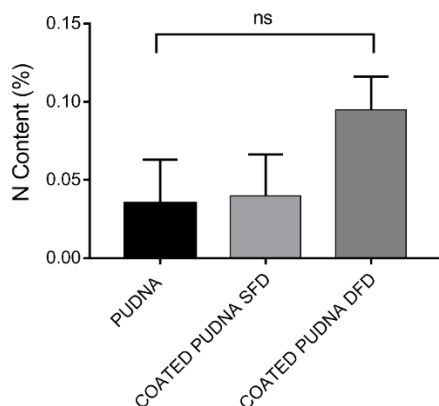


Figure 4.14. Nitrogen content of PUDNA and PUDNA-coated scaffolds. column bar graphs for PUDNA non coated, PUDNA coated and single freeze-dried (SFD) and PUDNA coated and double freeze-dried (DFD) show the nitrogen content (Mean \pm SD). Statistics were performed with Kruskal-Wallis test for three groups comparison and Kolmogorov-Smirnoff tests for each two groups comparisons (p-value < 0.05). Not statistically significant differences were found.

Mechanical properties

Mechanical tests were performed by nanoindentation of samples in a wet state, after hydration in PBS 1X. The Young's modulus was calculated by using Hertzian contact model, commonly adopted for soft biomaterials [364–366]. Hertz model is based on the assumption that the material behaves as a purely linear elastic and the ratio between the stress and strain is calculated by fitting the loading indentation curve (**Figure 4.15A**). The model can be used for a spherical tip when the indentation depth is smaller than its radius [367], prerequisites that were satisfied in the experimental setup used. PUDNA scaffolds produced by either standard protocol and after collagen coating followed by single freeze-drying were analyzed.

Results showed that the Young's modulus of bare PUDNA was of $16.04 \text{ kPa} \pm 2.76 \text{ kPa}$ while collagen-coated scaffolds showed a higher value, of $19.51 \text{ kPa} \pm 4.27 \text{ kPa}$ (**Figure 4.15C**).

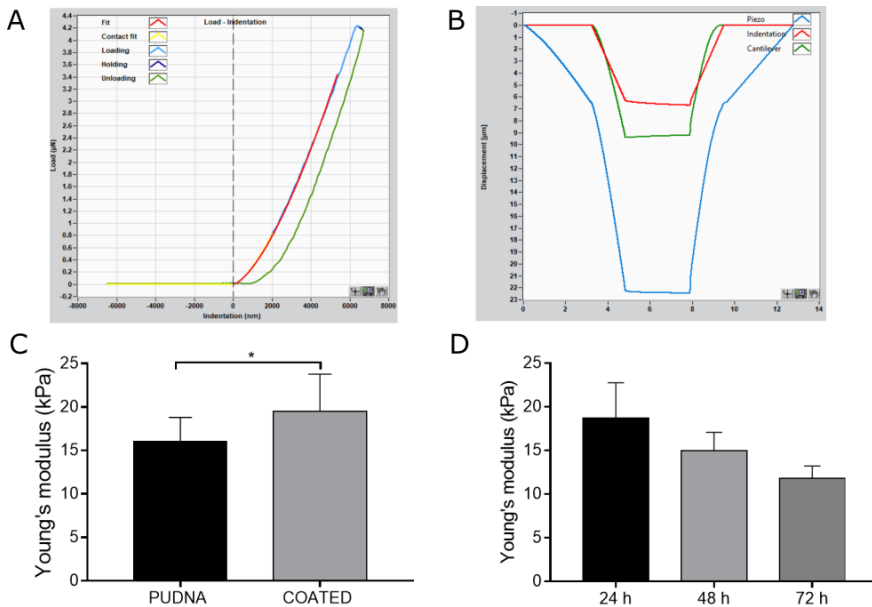


Figure 4.15. Mechanical characterization of PUDNA scaffolds. (A) Typical load curve for hydrated PUDNA scaffolds: the Young's modulus is calculated from the fit of the loading curve (red line). (B) Typical indentation curve showing the cantilever displacement and the indentation depth. (C) Young's modulus of non-coated and coated PUDNA scaffolds (Mean \pm SD, p-value of 0.0105 calculated with unpaired t test with Welch's correction). (D) Variation of PUDNA coated Young's moduli within the first 72 hours of hydration.

Different mechanical properties have been reported for pullulan-based scaffolds in literature, depending on the application and on which other materials it was combined with. For instance, pullulan-based hydrogels engineered for wound healing showed a tensile strength ranging between 0.3 and 1 MPa based on the crosslinker

[368]. In another study, electrospun scaffolds composed of STMP-crosslinked pullulan and cellulose acetate were investigated for bone TE application [369]. The elastic modulus from compression tests of the formulation containing the highest pullulan amount (80%) was of about 3 MPa, from tensile tests was of 5 MPa while tensile strength was of 0.34 MPa. Scaffolds composed of oxidized pullulan and crosslinked collagen showed a tensile strength between 0.1 and 0.2 MPa while compression tests of methacrylated pullulan crosslinked by PEGDA and produced by 3D printing for culturing of stem cells revealed an elastic modulus between 1.5 and 2.5 kPa depending on the crosslinker concentration [370,371]. Interestingly, PUDNA gels produced by using NaCl as porogen agent and used for 3D culture of hepatic organoids were characterized by bulk dynamic mechanical analysis (DMA) and resulted in a storage modulus of 5 kPa [356].

Young's modulus of pure collagenic scaffolds is below 1 kPa [372,373], although values can vary depending on the crosslinking method, while a tensile modulus of 50 kPa has been reported for crosslinked and freeze-dried bovine collagen scaffolds [374]. Moreover, at the nanoscale level, collagen fibrils have a modulus of several GPa [342,375]. In general, results for stiffness values obtained with nanoscopic techniques, as atomic force microscopy and nanoindentation, show much higher values due to the intrinsic difference of materials response at small scales compared to bulk characterization [376]. Highly organized hierarchical structures as collagen also show higher stiffness at the nanoscale compared to other ECM components, as elastin or fibronectin. This can thus

explain the increase of Young's modulus in our coated PUDNA gels at the surface compared to bare PUDNA. Assuming a selective collagen coating of single freeze-dried PUDNA scaffolds, as verified by SHG analysis, the value of elastic modulus found at the surface can be considered representative of the channels mechanical properties, where cells would adhere. These findings about the stiffness of the substrates at the nanoscale are useful to evaluate their suitability for cellular adhesion and response to local mechanical cues.

Although many soft tissues have been reported to have a Young's modulus below 10 kPa (for instance, 1-3 kPa for the brain, about 4 kPa for liver and kidney), many tissues show a stiffness of tens of kPa, such as the cardiac muscle, the spleen or the thyroid [377]. To make a comparison, polystyrene dishes normally used for 2D cell culture have an elastic modulus of about 1 GPa [378], thus 6 order of magnitude higher than PUDNA. However, a comparison becomes difficult as most of the data reported in literature for tissue were obtained from macroscale investigations.

We also studied the evolution of mechanical stiffness up to 3 days of immersion in PBS for collagen coated scaffolds. In contrast to swelling data, that stabilized within the first hours of immersion, Young's modulus of hydrated samples continued to decrease over time, being $14.99 \text{ kPa} \pm 2.07 \text{ kPa}$ and $11.77 \text{ kPa} \pm 1.45 \text{ kPa}$ after 48 and 72 hours respectively (**Figure 4.15D**). This discrepancy compared to swelling trend can be explained referring to the different scale the two tests refer to. For swelling tests, the sample at the

macroscopic scale is analyzed and the ratio is calculated from a difference in weight. Thus, at the macroscale, no significant differences are noted over time. Nanoindentation works rather at the nanoscale, investigating the first few microns of the scaffold's surface. Therefore, variations that are not observed for bulk evaluation become evident at smaller spatial scales, although other techniques are available for bulk characterization of mechanical properties, such as tensile and compression tests, as previously discussed [379]. Though nanoindentation results are not necessarily representative of the bulk properties, as seen in [356], it is interesting to note the decrease of stiffness during the first days, probably due to continuous settling of the hydrated scaffold at the nanoscopic level rather than to degradation, a property that should be taken into account when studying the matrix-cellular interactions. Further studies should be conducted to homogenize and correlate results derived from mechanical analyses at different scales and to evaluate the long-term variation of the scaffolds mechanical properties *in vitro*.

4.4. Conclusions

Here, the fabrication and optimization of porous biopolymeric scaffolds patterned with tubular microchannels was presented. We have firstly introduced the concept of tissue engineering and discussed the types of biomaterials available, their properties and the main fabrication strategies for porous constructs. We have thus focused on patterning techniques for scaffolds with specific

applications. Then, we have presented the design of a porous pullulan-based (PUDNA) scaffold patterned by means of subtractive templating. A custom-made molding setup was designed and engineered. Optimization of standard fabrication protocols was proposed, with a focus on production of thin scaffolds for optimized imaging and selective collagen coating for cellular adhesion within the microchannels. Complete characterization of the final constructs was also presented and discussed, with main interest to short-term evaluation. In this context, morphological, physical, chemical and mechanical studies were conducted and different scaffold formulations compared, mainly to evaluate the successful optimization in comparison to standard production methodology. Results showed the possibility to produce thin constructs by modification of freeze-drying parameters and to selectively coat the inner scaffold surfaces. Physical studies revealed good degrees of porosity and swelling and, although addition of small amounts of collagen did not induce an evident chemical modification with the methods proposed here, its presence was confirmed by imaging techniques and mechanical tests. Stiffness at nanoscale was investigated by nanoindentation and results compared to current literature. After validation of the constructs for their use as TE substrates, Chapter 5 will focus on their use *in vitro* for building of a vascularized model.

5. Application of polymeric scaffolds to build an *in vitro* vascularized model

The introduction to this chapter is partially based on the following work:

A. Dellaquila, C. Le Bao, T. Simon-Yarza, and D. Letourneur. In Vitro Strategies to Vascularize 3D Physiologically Relevant Models. *Advanced Science*, 2021. DOI: [10.1002/advs.202100798](https://doi.org/10.1002/advs.202100798).

Adapted with permission, Copyright © 2021 by the Authors.

STATEMENT OF SIGNIFICANCE

Cells in human tissues have been demonstrated to be located within 200 μm from the blood vessels to ensure proper nutrients supply, gas exchange and wastes removal. The design and fabrication of constructs for tissue engineering applications should thus take into account this fundamental physiological feature and integrate vascular networks *in vitro*. Although avascular matrices are generally vascularized by the host tissue after implantation *in vivo*, prevascularized models offer several advantages and reduce the risk of failure. This chapter describes the use of 3D patterned polymeric scaffolds as substrates for *in vitro* engineering of functional vascular microchannels.

5.1. Tissue engineered models of functional endothelium

In physiological conditions, the tissues of the human body are vascularized thanks to an abundant network of blood vessels, known as the vascular network. Human vasculature has essential biological functions, such as nutrients and gas exchange, metabolic waste removal and homeostasis maintenance[380,381]. Its role is fundamental at the macro as well as at the microscale, where a diffusion limit of oxygen and nutrients has been reported to be around 200 μm , meaning that the cells located farther from a capillary undergo hypoxia and apoptosis [26,382]. Thus, vascularization plays a pivotal role in achieving physiologically relevant tissue and organ substitutes for tissue engineering and regenerative medicine applications. Despite the unprecedented advancements of tissue engineering in the last decades, the integration of a functional vascular network in tissue constructs prior to implantation still represents a challenge that hampers an efficient and fast scale-up towards the clinical application.

The majority of current approaches in regenerative medicine still relies on implantation of constructs and subsequent *in vivo* vascularization from the host tissue; they can be classified as post-vascularization strategies (**Figure 5.1A**). The scaffold can be implanted either directly after the manufacturing process, as acellular, or after seeding with relevant parenchymal cells for the tissue that needs to be regenerated and their culturing *in vitro*. In the first case, although the scaffold can be bioactive, thus loaded with vascular growth factors or molecules to induce vascularization, it

does not include any cell type, thus not providing any biological cue. This often leads to suboptimal scaffold integration and degradation, with preferential formation of scar tissue at the interface (tissue repair) rather than functional regeneration of the host tissue [383]. However, they are available off-shelf, with commercial products already on the market, and they have low immunogenicity. On the other side, the use of cellularized scaffolds built with relevant cell types has shown advantages in terms of tissue regeneration due to the active interaction between the implanted cells and the injured area [384]. Nevertheless, the host tissue takes a relatively long time to vascularize the implanted construct, thus meaning that cells within the scaffolds would lack nutrients and perfusion especially in the inner matrix area. This would eventually lead to formation of a necrotic core that would hamper the proper scaffold functioning over time. This drawback becomes particularly relevant for thick cellularized constructs, as the angiogenesis *in vivo* would take longer.

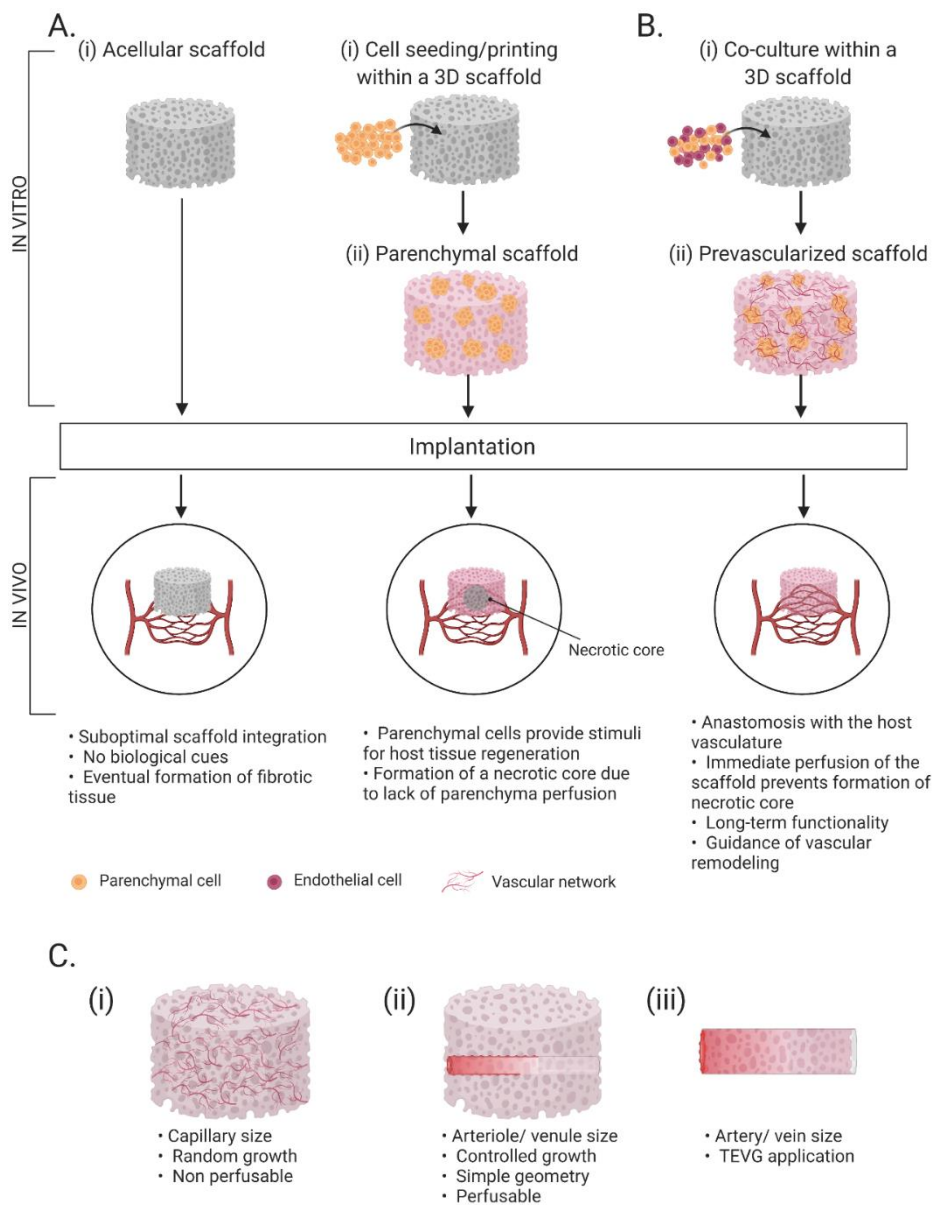


Figure 5.1. Vascularization strategies in TE. (A) Post-vascularization strategies can involve the direct implantation of acellular constructs (left) or cellularized constructs containing parenchymal cells (right). (B) Pre-vascularization approach is based on integration of vascular cells during the *in vitro* culturing for formation of a vascular network

prior to implantation. (C) Prevascularization approaches by conventional fabrication methods: (i) spontaneous network assembly; (ii) prepatterning of microchannels within the scaffold; (iii) formation of large tubular scaffolds for TEVG applications. Created with Biorender.com.

Therefore, in bioengineered models, the presence of vasculature would ensure the proper exchanges, preventing cellular death in constructs thicker than 200 μm and contribute in mimicking the tissue physiology and cell microenvironmental cues. Overall, a functional capillary network would allow for a long-term maintenance of the construct in terms of viability, morphology and functionality. Furthermore, organ-specific vasculature has shown to strongly affect the behavior of the parenchymal cells and to drive organ-related biological events [385]. Vasculature plays a key role also in many diseases, such as cancer metastasis, atherosclerosis or tumor angiogenesis [386]. For *in vitro* studies, the use of prevascularized models could give more realistic insights of human response to drug testing, toxicology assays or in pathological models [387]. In regenerative medicine, the implantation of prevascularized constructs compared to constructs that spontaneously vascularize *in situ* would enhance the grafting to the host tissue and fasten its regeneration. Moreover, although the successful implantation of thin constructs like skin has been reported, the formation of abundant and functional vascular network is a key prerequisite for the generation of thick and metabolically active organs, such as liver, heart, or kidney [381] (**Figure 5.1B**). In fact, the host vasculature needs time to integrate and vascularize the implanted tissue and the use of avascular scaffolds is inefficient due to the impossibility to be

instantly perfused. The implantation of prevascularized scaffolds would thus represent one of the most favorable strategies for regenerative medicine purposes.

Many efforts have been conducted over the past years to build three-dimensional (3D) physiologically relevant models that could fully recapitulate the tissues and organs functioning. As depicted in Chapter 4, TE has thus developed a plethora of 3D cell culture constructs, that have proven to be more physiologically relevant compared to traditional 2D cell culture, providing accurate results in biological studies, such as *in vivo*-like cell viability, morphology, differentiation, and proliferation, as well as cellular response to stimuli, protein synthesis, and drug metabolism [388]. In recent decades, researchers have thus moved from culturing of single cell types on flat and rigid substrates, to the co-culture of cells, first in 2D (i.e., Transwell[®] systems) and later in 3D, with the introduction of spheroids and organoids models. Complex physiological conditions, such as blood flow, oxygen gradients or mechanical stimuli, can be mimicked nowadays by using microfluidic devices. In parallel, new biomaterials have been developed to mimic the cell niche by means of 3D scaffolds with tunable physical-chemical and mechanical properties [353,356,389]. Recently, these *in vitro* models have often adopted the emerging strategy of 3D bioprinting to engineer more complex systems, eventually replacing the conventional fabrication methods. The synergistic use of these technologies would allow for a precise control of the cell culture conditions and the microenvironment and it would represent a key strategy to engineer

biostructures that mirror human tissues and organs while ensuring high throughput, fundamental for their translation towards their application in industrial and clinical settings. Nevertheless, lacking or inefficient perfusion and vascularization remains one of the main limitations of tissue engineered constructs as the need for vascularization exists from the moment the tissue-engineered constructs are assembled *in vitro*, to the moment when they are implanted in a patient [390].

Physiological properties of the vascular network

The vasculature is a network of blood vessels consisting of the arterial system, the venous system, and the microcirculation (**Figure 5.2**). The arterial system, composed of arteries and arterioles, distributes oxygenated blood from the lungs while the venous system, composed of veins and venules, returns low oxygenated blood to the heart. Separating these two systems is the microcirculation, where nutrients and cellular wastes exchange is carried out by the capillaries. The distinct anatomy and size of the blood vessels are dictated by the different physiological functions they play. To withstand high blood pressures and shear stress, the larger vessels, namely arteries and veins, are composed of three layers. The external layer, called tunica adventitia, is mainly composed of collagen and nerve fibers, with a protective and support function. The middle layer, tunica media, is composed of smooth muscle cells (SMCs) and elastic connective tissue, responsible for vasodilation and vasocontraction. The inner layer, tunica intima, is the lumen wall, lined with endothelial cells (ECs) and surrounded by

a thin basement membrane, a 40-120 nm thick membrane mainly composed of collagen type IV, laminin and other glycoproteins and proteoglycans [320,391]. The arteries and veins are large diameter vessels, ranging from 25 mm for the aorta and about 2 mm for the pulmonary veins to hundreds of micrometers for the smallest arteries and veins. While moving down into the vascular tree, the blood pressure decreases and less elasticity is needed: that is why arterioles, with a size of 10-100 μm , are composed of the tunica media and intima only and the capillaries (less than 5 μm) are composed of a single ECs monolayer. At the tissue level, the anatomy is extremely complex: in healthy conditions, the capillary density is about 300-400 capillaries/ mm^3 in skeletal muscles and above 2000 capillaries/ mm^3 in myocardium, brain, liver and kidney [392]. Furthermore, the surrounding parenchymal tissues are composed of cells at high concentration, of about 10^5 cells/ mm^3 [97,393]. Due to its direct contact with blood, the endothelium participates in numerous physiological functions including selective barrier membrane, thrombosis prevention, blood pressure regulation, and angiogenesis. Although ECs in different regions of the body fulfil similar physiological demands, heterogeneity in their morphology, function, gene expression, and antigen composition has been reported [183,184]. Specifically, the morphology of the endothelium varies to adapt to the specific functions of their underlying tissue, as described in Chapter 3 (**Figure 5.2B**).

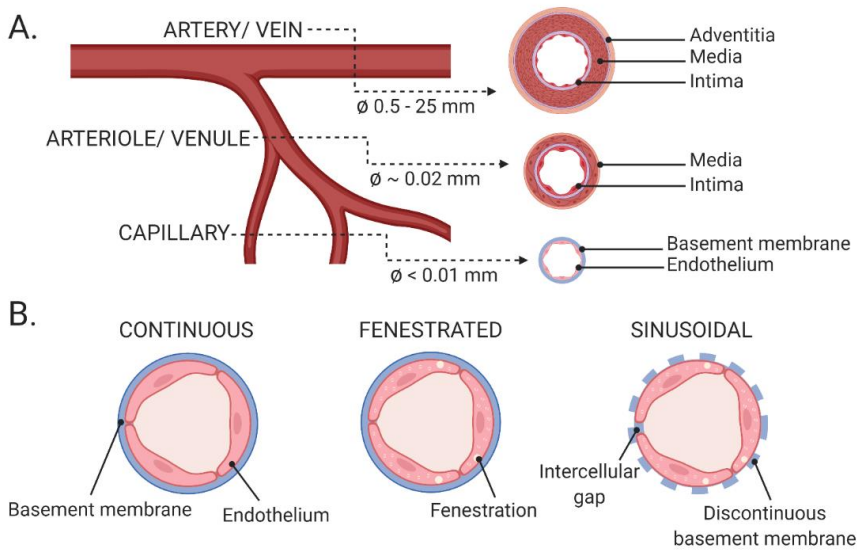


Figure 5.2. Physiological properties of the vascular network. (A) Anatomical properties and dimensions of the human vasculature. **(B)** Phenotypic heterogeneity of organ-specific endothelium. Adapted with permission from [394].

Requirements for the fabrication of engineered vascularized tissues

Based on the morphological and physiological aspects illustrated so far, the engineering of functional vascularized constructs should fulfill several parameters, summarized in **Table 5.1**.

Table 5.1. Design parameters for engineering vascular network in TE models.

Requirements	Features	Properties
Morphology	Circular cross-section [395–397]	<ul style="list-style-type: none"> • Homogeneous cell seeding • Physiological shear stress
	Multilayer structure	<ul style="list-style-type: none"> • Inclusion of other cellular components to mimic tunica media and adventitia in big vessels

	Endothelium specificity [398]	<ul style="list-style-type: none"> • Mimicry of specific ECs functionality and interaction with the parenchyma
Architecture	Branched and multiscale [26]	<ul style="list-style-type: none"> • Mimic blood flow from macro to microscale • Large vessels for anastomosis in vivo
	Capillary and tissue density	<ul style="list-style-type: none"> • Proper tissue functioning and mass transfer
Microenvironment	Integration of ECM components [399–403]	<ul style="list-style-type: none"> • Mimicry of basement membrane for cellular support and guidance
	Integration of cues [377,404–407]	<ul style="list-style-type: none"> • Recapitulation of blood flow • Mechanical stiffness of the substrate to reproduce the parenchyma

Prevascularization strategies for physiologically relevant 3D models

TE prevascularization strategies can be classified into microfluidic technology, 3D co-culture models, namely spheroids and organoids, and 3D scaffolds. It is worth highlighting that some of these approaches are used also as fabrication strategies for other models; in particular, bioprinting is currently used for engineering microfluidic platforms and 3D cell cultures and microfluidic devices have been used for culturing and vascularizing spheroids and organoids, leading to the raising of a new category of hybrid vascularization techniques. The fabrication methods, their features, main advantages and disadvantages are summarized in **Table 5.2**.

3D scaffolds will be the main focus of this chapter and, as already illustrated in Chapter 4, the fabrication strategies can be classified into conventional methods and 3D bioprinting. We refer the reader to the article [394] for a full overview of these methods.

Prevascularized 3D scaffolds by conventional and 3D bioprinting strategies

Fabrication of prevascularized constructs can be achieved by scaffold-based or scaffold-free strategies [408]. TE generally relies on scaffold-based approaches, where the scaffold is used as template to mechanically support and guide the growth of the vascular network. These fabrication methods are described in detail in Chapter 4. The *in vitro* model is built in a second step, after seeding of the matrices with cells. Scaffold-based approach thus involve a multistep production, with long and eventually laborious operations. However, thanks to the advances in the manufacturing methods and a wide choice of biomaterials, it offers high tunability over the scaffold properties, with consequent possibility to control cellular behavior. On the other side, scaffold-free approaches rely on assembly of biological building blocks into relevant structures. Though scaffold-free approaches normally refer to the 3D cell culture technology, they have been achieved lately by bioprinting techniques, that have been successfully used for direct printing of cells into organized 3D tubular structures. The scaffold-free approach shows the advantage that the cell seeding step is not needed, thus reducing the fabrication timing. However, it suffers from important limitations, as limited mechanical properties and resolution, difficulty in incorporation of

molecules and time needed for constructs stabilization prior to implantation [329,409].

Among the conventional fabrication methods for 3D patterned porous scaffolds (see Chapter 4), freeze-drying and electrospinning are the most widely used. Recent interesting works have been reported about fabrication of vascularized constructs *in vitro* by freeze-drying, achieved either within the porous matrix or by integration of microchannels (**Figure 5.1C**). For instance, freeze-dried RGD-modified alginate scaffolds were used to fabricate a complex pathological model mimicking the breast tumor microenvironment by integration of vascular and parenchymal cells [410]. Here, the vascular network was created by spontaneous assembly of endothelial cells within the porous scaffold. In another work, spontaneous assembly of endothelial cells and myoblasts into muscle bundles and vascular tubules respectively was achieved by using microgrooved freeze-dried collagenic scaffolds [411]. The strategy is limited however by the difficulty of spatially controlling the vascular growth and building endothelialized perfusable lumens, hampering the recapitulation of physiologically relevant vasculature.

Complex matrices were obtained by combination with other technologies, as electrospinning or cell sheet engineering. Particularly, electrospun TE models for vascularization are normally produced in two different forms, i.e., tubular scaffolds or nano/microfibrous mats. Tubular scaffolds, fabricated by collecting the fibers onto rotating mandrels, find their main application in TEVG since their diameter is generally in the mm range. The main

advantage is that they show a multiscale architecture, that favors cellular alignment at the microscale due to fibers orientation and guides blood vessel regeneration at the macroscale due to resemblance with the native geometry [302,412]. For smaller vessels and capillaries, electrospun scaffolds in the form of oriented mats are generally used.

Table 5.2. Fabrication strategies for each vascularized 3D model, comparison of their properties and main applications. **SL** Soft lithography; **T** Templating; **B** Bioprinting; **EB** Extrusion based; **DB** Droplet based; **LAB** Laser assisted; **CM** conventional fabrication methods; **Vat-P** Vat photopolymerization. Adapted with permission from [394].

Vascularized 3D model

	Microfluidic – based	3D cell culture	3D scaffold
Fabrication strategy	<ul style="list-style-type: none"> • Soft lithography • Templating • Bioprinting 	<ul style="list-style-type: none"> • ECM scaffolding • Hanging drop • Low adherent plate • Bioreactor-based 	<ul style="list-style-type: none"> • Magnetic levitation • Micropatterning • Microfluidics • Bioprinting
Vessel geometry	<ul style="list-style-type: none"> • Rectangular cross-section (SL) • Straight circular channels (T) • Branched microvasculature (T, B) 	<ul style="list-style-type: none"> • Capillary-like structures <i>in vitro</i> 	<ul style="list-style-type: none"> • Simple geometries (CM) • Tubular interconnected channels (B)
Vessel dimension	<ul style="list-style-type: none"> • Tens-hundreds of μm ($> 30 \mu\text{m}$) 	<ul style="list-style-type: none"> • Tens-hundreds of μm 	<ul style="list-style-type: none"> • Tens of μm (Vat-P) • Hundreds of μm (CM, EB, DB) • Tens-hundreds of μm (LAB)
Microenvironment	<ul style="list-style-type: none"> • Possibility to integrate ECM proteins and growth factors 	<ul style="list-style-type: none"> • Cell-cell interactions • Possibility to integrate ECM proteins and growth factors 	<ul style="list-style-type: none"> • Possibility to integrate ECM proteins and growth factors and to print multiple cell types
Advantages	<ul style="list-style-type: none"> • Physiological shear stress • <i>In vivo</i>-like cues (oxygen gradient, mechanical stimuli, ...) • Modular and multi-organ platforms • Integration of sensors 	<ul style="list-style-type: none"> • Scalable to various cell culture platforms • Patient specific • Vascular network mimicking <i>in vivo</i> complexity and architecture 	<ul style="list-style-type: none"> • Versatile method (CM) • Fast method • Multiple cell/materials (CM, EB) • Thick constructs (CM, EB) • Low cost (E, DB, Vat-P)
Disadvantages	<ul style="list-style-type: none"> • Use of non-biomimetic polymers (SL) • Expensive equipment for fabrication • Multi-step production • Need for external pumps 	<ul style="list-style-type: none"> • Limited diffusion and nutrient transport as size increases • Difficult to manipulate • Need for a large number of cells to generate substantial quantity of tissue 	<ul style="list-style-type: none"> • Low reproducibility (CM) • Low resolution (CM, EB) • Cell sedimentation (EB) • Bioink printability limits mechanical properties (EB) • High cost (LAB)

In a recent work, electrospun fibrin scaffolds were used for skeletal muscle TE [384]. Fibrin was spun in the form of microfibers bundle to mimic the skeletal muscle architecture and the construct used *in vitro* for culturing of C2C12 muscle cells and HUVECs mixed with adipose-derived stem cells (ASCs) for the vascular component. The work showed the formation of functional contractile myotubes *in vitro* and results *in vivo* indicated that C2C12-seeded scaffolds led to a muscle regeneration compared to acellular constructs and the implantation of pre-vascularized scaffold enabled direct anastomosis with the host tissue and perfusion. However, the presence of ASCs *in vivo* caused the formation of a wide collagen boundary and reduced scaffold degradation and integration. In an interesting work, a 3D vascularized liver scaffold was produced by using PCL membranes [413]. Using a wet spinning method, membranes containing hollow fibers (diameter of 1 mm) were fabricated for the culturing of human hepatocytes in the extraluminal compartments and HUVECs within the channels. The samples were subject to perfusion at 0.5 mL/min in a custom-made bioreactor and cultured up to 18 days. Results showed formation of a functional hepatic module, with endothelial cells forming complete vessels and expressing CD31 and hepatocytes showing active metabolism, with synthesis of albumin and production of urea, and drugs excretion. Moreover, an increased metabolism of the liver parenchyma was noted in prevascularized constructs compared to hepatocytes monocultures.

As previously discussed, 3D bioprinting is nowadays the most used technology for fabrication of prevascularized constructs thanks to the great versatility of the fabrication techniques and materials, the possibility to create and control complex geometries and finely tune the scaffold parameters (**Table 5.2**). Because of the complexity of the topic and the extensive research that has been done, we refer the reader to comprehensive reviews [278,283,414,415]. Here, we discuss some representative examples to illustrate the potential of this technology for prevascularized TE. Among the different bioprinting techniques, extrusion-based bioprinting is the most used as it offers the possibility to print materials with a wide range of viscosity, attain high cellular concentrations and thick constructs [416]. This method consists in the extrusion of bioinks through nozzles via a pneumatic system controlled by a computer for precise path printing. The technology has been widely used for sacrificial templating of vascular structures. In the work by Noor *et al.*, thick perfusable cardiac patches for personalized medicine were 3D printed by extrusion sacrificial technique. The authors used decellularized human omental tissue to produce a thermoresponsive hydrogel. Using CT anatomical images of the patient and computational simulations of oxygen diffusion, the vascular network was designed. Omentum hydrogel mixed with cardiomyocytes was printed to form the parenchymal tissue while printing of gelatin mixed with endothelial cells and fibroblasts according to the designed network was done to form physiological vasculature in between the omentum matrix. After printing, the construct was

incubated at 37°C for crosslinking and dissolution of the gelatin, used as sacrificial material for the vessels formation. This way, thick vascularized constructs of 7 x 7 x 7 mm could be engineered. *In vitro* and *in vivo* studies confirmed the formation of vascular channels of about 300 µm in diameter, with fibroblasts exhibiting a lumen supporting function, and of cardiac tissue. The authors also showed the fabrication of human hearts at the small scale (20 x 14 mm). Another interesting extrusion-based bioprinting technology for creating vascularized constructs is coaxial bioprinting: by using coaxial nozzles, the method allows for deposition of multimaterial structures in a concentric geometry [417]. Shao *et al.* have produced thick vascularized tissue constructs at the cm scale by coaxial bioprinting of cell-laden GelMA and gelatin bioinks [418]. The self-standing scaffold was produced by printing of GelMA mixed with parenchymal cells from the outer coaxial nozzle, followed by polymer photocrosslinking. The vasculature was fabricated by extrusion of endothelial cells-laden gelatin from the inner nozzle and consequent gelatin dissolution, leading to channels of 200-1000 µm in diameter. The method shows the advantage of single-step fabrication by means of coaxial printing and production of solid macroscale constructs with controlled architecture at the microscale. Although this work reported the engineering of vasculature composed of a single endothelial layer, complex multilayer constructs mimicking the anatomy of bigger vessels have been already manufactured [329].

Furthermore, in recent years the combination of 3D scaffold fabrication technologies with the other vascularization approaches, as microfluidics and spheroids/organoids technology, has opened up the possibility to manufacture even more complex vascularized models, create physiologically relevant microenvironment and produce high throughput and standardized platforms, as presented in numerous works [356,405,419–423].

Nevertheless, several limitations still need to be addressed. Among the main drawbacks, we can find:

(i) Pre patterning of relatively large vessels (hundreds of microns): most of the models fail to recapitulate the capillary scale. In this context, the 3D geometrical complexity and the dimensions of the microcirculatory system can be more easily replicated with self-vascularization strategies compared to prevascularization techniques due to the spontaneous assembly of ECs, with sprouts diameters often below 30 μm [424,425]. However, this technique is not reproducible and it takes a longer time for the vasculature to be functional and perfusable. Current bioprinting strategies have shown the capability to 3D print complex vascular geometries [90,94], as well as dense tissue constructs [426], that could not be achieved otherwise. However, vessels size is still restricted by the resolution limit of many fabrication techniques and relatively few works have obtained capillary-like diameters, mainly by laser-based strategies, which have proved effective to create multi-scale vascular networks with capillaries of less than 10 μm [210,427].

(ii) Extensive use of cell lines and particularly HUVECs for endothelium modeling due to easy handling, reliability in long-term culture and affordable costs. Even though this common feature can be convenient when comparing results from different studies, it hampers the study of tissue-specific mechanisms at the vascular interface and the clinical translation. Tissue specific human-derived primary endothelial cells represent a more valid source, however, access to human tissue and isolation protocols are often difficult and laborious operations [233]. For this reason, many studies are still based on animal cell sources, which once again impede data and system scalability towards “human-sized” models. Stem cell biology might be an alternative to address the current limitations and develop platforms for personalized medicine. Hence, vascular models using endothelial cells derived from multipotent or pluripotent stem cell sources have been already successfully engineered [146,428].

(iii) Short term evaluation *in vitro* (normally below 21 days); in the case of 3D scaffolds, the long-term evaluation of their stability is fundamental for their *in vivo* application while, for 3D cell culture and microfluidics, the establishment of long-term models would ensure more accurate pathology-related and drug testing studies [202,429,430].

(iv) Incorporation of biochemical and mechanical stimuli. Although achieved by microfluidics-based strategies and the great potential of 3D cell culture models to recapitulate both geometrical complexity and the *in vivo* microenvironment thanks to their unique feature to

self-organize, yet engineering models that fully recapitulate the microenvironmental physiological cues is still a challenge [97,210].

(v) Incorporation of the lymphatic system must also be considered to create more comprehensive microcirculatory models [431,432]. This network plays a fundamental role in tissue fluid homeostasis, immune cells trafficking, and actively participates in cardiovascular pathophysiology, cancer metastases and several diseases progression [433–435].

(vi) Automation represents another key requirement in the development of reliable and high throughput platforms and, although sophisticated devices for automated manipulation, testing and analysis on-chip have been recently developed [436,437], most of the works do not consider this feature. In parallel, the further integration of sensors for *in situ* monitoring of construct performances would speed up the automation, scalability and readouts of these models, while boosting their value in both academic and industrial setups [22,438–440].

Rationale and objectives

Vascularization of 3D models represents a major challenge of tissue engineering and a key prerequisite for their clinical and industrial application. The use of prevascularized models could solve some of the actual limitations, such as suboptimal integration of the bioconstructs within the host tissue, and would provide more *in vivo*-like perfusable tissue and organ-specific platforms. In the last decade, the fabrication of vascularized physiologically relevant 3D constructs has been attempted by numerous tissue engineering strategies, that can be classified in microfluidic technology, 3D co-culture models, and 3D scaffolds, obtained by either conventional methods or biofabrication.

In this chapter, the *in vitro* vascularization of prepatterned biopolymeric porous scaffolds is presented. After physicochemical and mechanical characterization of PUDNA scaffolds, presented in Chapter 4, we focus here on the evaluation of engineering strategies and their optimization for building an endothelium model. We firstly focus on different cell seeding strategies to obtain uniform cellular distribution, initially by post-coating of the scaffolds with ECM proteins. We thus introduce the use of pre-coating of PUDNA hydrogels to evaluate the possibility of creating a selective pattern coating with collagen. The endothelium design also entails the evaluation of different cell culture aspects, notably the choice of the endothelial cells source and the microenvironmental conditions. We thus discuss how different experimental parameters determine the growth and assembly of endothelium over time. The labeling procedures for 3D matrices are also detailed, as optimization is needed compared to standard 2D staining protocols used in biology. The use and comparison of different imaging techniques is also described, in order to evaluate the suitable

method for simple and effective imaging of thick cellularized constructs. An outlook of the project and possible future directions are also discussed for further implementation of the vascularized model presented here.

5.2. Endothelium formation and 3D imaging

PUDNA prepatterned scaffolds containing circular microchannels were used as template for seeding of endothelial cells and spontaneous formation of organized endothelium mimicking the capillaries anatomy and physiology. The engineering of endothelium was carried out in a multistep process, that involved the evaluation and optimization of different parameters: (i) strategy for optimal penetration and seeding of endothelial cells within the microchannels; (ii) strategy for optimal coating of the scaffold patterns with ECM proteins; (iii) formation of endothelium by seeding with different endothelial cell sources; (iv) influence of cell seeding concentration on the final endothelium architecture and on the timing for spontaneous assembly; (v) influence of environmental parameters, as composition of cell culture milieu.

Results were evaluated by imaging of fixed and labeled scaffolds at specific time points. Due to the nontrivial influence of the thick porous PUDNA matrix on 3D imaging of the inner features, particular attention was given on optimization of staining protocols and on testing of different 3D imaging systems and methods (**Figure 5.3**).

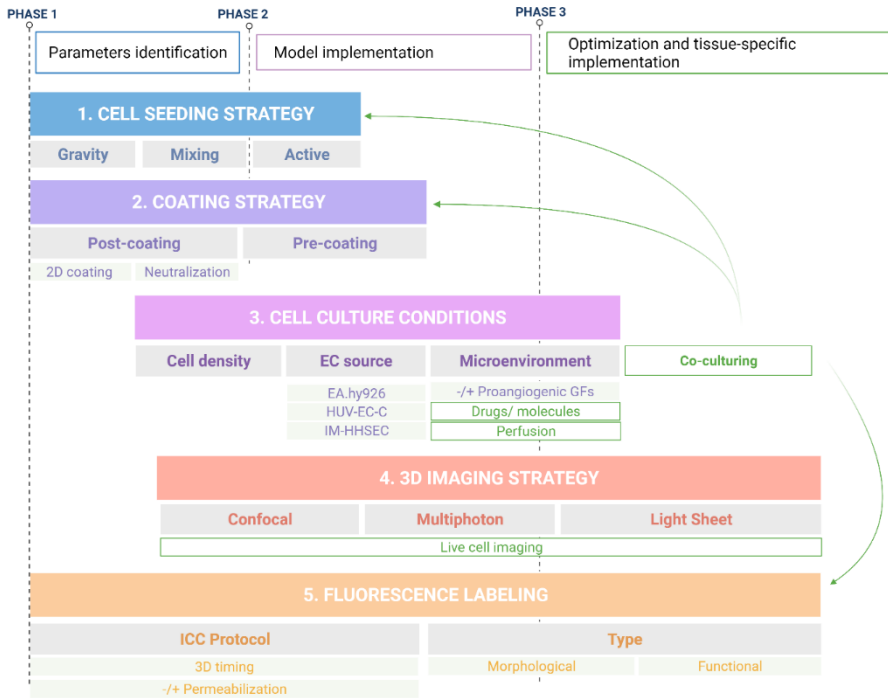


Figure 5.3. Flowchart of experimental conditions for engineering the endothelium. The process has been divided into 3 main phases (1-3), corresponding to the identification of the important parameters, creation of the endothelium model and further development, respectively. The third phase has been partially started while the next possible steps are illustrated as white boxes in a green frame. As example, introduction of co-culture would modify not only the cell culture conditions (as medium composition, choice of cell sources, ...), but also the seeding method (order and timing of the seeding), the coating (if specific proteins are needed or should be avoided), as well as the labeling (green arrows). Created with BioRender.com

5.2.1. Cell seeding strategies

Evaluation of different seeding strategies was carried out to find the optimal method for seeding endothelial cells within the channels. Several strategies were tested, as described below:

- i. Gravity (or drop) seeding: often used in literature for the seeding of porous matrices, it consists in pipetting a drop of cell suspension on the scaffold top surface. The seeding occurs through wetting of the scaffold, with cellular penetration within the pores driven by gravity, and consequent adhesion. Although simple, this method might lead to inhomogeneous cellular distribution and cellular adhesion within the channels located in the middle of the matrix results difficult. Even if optimization can be done, for instance by flipping the gels to have similar distribution on both sides, this strategy normally shows low efficacy for seeding of patterned scaffolds.
- ii. Active (or syringe) seeding: the gels and the cell suspension are loaded in a 10 mL syringe with closed end. Generally, 1 mL of suspension was used for up to 15 scaffolds, depending on their size). The cell suspension was pumped back and forth with the syringe for several minutes. The advantage of this method is the use of homogeneous mixing and vacuum pressure for homogeneous and active cellular penetration within the scaffolds. On the other hand, the application of pressure might cause scaffolds damage and eventually breakage.
- iii. Mixing (or vial) seeding: the cell suspension and the hydrogel are placed in a vial and the suspension pipetted back and forth for several minutes. The same cell suspension and scaffolds quantities as for the active seeding are used. The main

advantage is the homogeneous cellular penetration within the pores but the lack of active pressure ensures a gentler seeding compared to the active seeding strategy.

After optimization of the coating approach, a gentle active seeding resulted to be the most effective due to the application of pressure that eases cell infiltration within the microchannels. In a late stage of the project, active seeding was thus preferred and further seeding techniques were evaluated and compared:

- iv. **Single vs double active seeding:** in single active seeding, the syringe method is performed as previously described. In double active seeding, the syringe method was performed once and the scaffolds incubated for 30-45 minutes to enable primary cellular deposition and adhesion. Then, scaffolds were placed again within the syringe and the process repeated a second time with fresh cell suspension. Scaffolds were incubated for a minimum of one hour before adding culture medium in the wells.

5.2.2. Optimization of coating strategies

PUDNA scaffolds were coated with different proteins to enhance cellular adhesion and formation of organized luminal endothelium within the micropatterned PUDNA matrices. Partially discussed in Chapter 4, the final goal of the coating was to obtain a homogeneous and distributed layer of ECM proteins within the microchannels in order to ensure selective adhesion of cells within the patterns and to reduce or prevent deposition of cells within the pores, with

consequent formation of clusters. Initial experiments involved the use of post-coating strategies, in which porous PUDNA scaffolds after freeze-drying were coated by mixing with a protein solution, normally incorporating the cell suspension, to have a single step coating-seeding procedure. We firstly tried to obtain homogeneous coatings by using either gelatin or collagen at dilutions typically used for 2D coating of culture vessels, as reported in conventional biology protocols. Based on the results, we then decided to implement 3D coatings by gelation of collagen at higher concentrations. Finally, we report the adoption of pre-coating of non-porous PUDNA hydrogels prior to freeze-drying as optimal approach.

2D coatings evaluation

Gelatin type B from bovine skin (G1393, 2% solution, Sigma-Aldrich, MO, USA), collagen type I from rat tail tendon (354249, Corning, NY, USA) and collagen type I from bovine corium (Collagen Solutions, Glasgow, UK) were used for the PUDNA scaffolds coating, by both pre and post-coating strategies (see Chapter 4). EA.hy926 human somatic endothelial cells from hybrid tissue (CRL-2922™, ATCC®, VA, USA) were cultured in DMEM, low glucose, GlutaMAX™ (21885025, Gibco™, Thermo Fisher Scientific, MA, USA) supplemented with 10% FBS (35-079-CV, Corning) and 1% antibiotic-antimycotic (15240062, Gibco™) in T75 flasks, as per standard culture protocols.

In preliminary experiments, collagen type I from rat tail and gelatin were tested to evaluate the optimal coating/cell suspension ratio for

post-coating strategy. Protein dilutions typical of 2D coatings were used, according to the literature. Briefly, dry scaffolds were sterilized by placing them under UV light for 1 hour. Cells with confluency of about 80% were detached from the culture vessel by using 2 mL of 0.05% Trypsin-EDTA (15400054, Gibco™) diluted in DPBS 1X (14190144, Gibco™), after washing the vessel once with 5 mL of DPBS to remove serum and debris. Cells were placed in incubator at 37°C for 5 minutes for detachment, then resuspended in cell culture medium and centrifuged at 200 g for 5 minutes. Supernatant was removed and cells resuspended for counting. A final concentration of 5×10^6 cells/mL was used. Collagen with concentration of 25 µg/mL and gelatin 0.2% were mixed with the cell suspension at different ratios (cell suspension: coating, v/v, from 1:1 to 20:1) and scaffolds seeded by mixing. Scaffolds were placed in a 24 multiwell plate and incubated for at least 1 hour at 37°C for primary adhesion. Then, 1 mL of medium per well was added for cellular nutriment. Culture medium was changed into fresh DMEM every 3 days. The collagen/gelatin coating mixing was also compared to pre-coating strategies, in which porous scaffolds were incubated over the weekend with collagen 25 µg/mL or gelatin 0.2 % before cell seeding. No second freeze-drying was performed in this case after the coating.

Post-coating: collagen neutralization strategies and variation of collagen concentration

Coatings at concentrations higher than 0.1 mg/mL were done by gelling collagen type I from rat tail via neutralization process. Two different neutralization strategies were tested, either by following the manufacturer's instructions (NaOH neutralization) or by HEPES neutralization. In the first case, a collagen gel was formed by firstly mixing PBS 10X with ice-cold water and 1N NaOH and consequently adding collagen to obtain a final collagen concentration of 300 µg/mL. HEPES neutralization was performed by dissolving in DI water NaOH, NaHCO₃ and HEPES buffer with mass ratio (1:6:8, w/w). The solution was kept under magnetic stirring for 10 minutes at RT to dissolve the salts and sterile filtered by using a 0.2 µm filter under a cell culture hood. Neutralization was done in ice by adding the collagen solution to the buffer, with a volume ratio depending on the initial collagen concentration and calibrated to obtain a neutral pH of 7.2-7.4 and determined in preliminary tests. Solution was gelled as per NaOH protocol.

Seeding of the scaffolds was done by testing two different approaches: in the first approach, the PUDNA scaffold was firstly soaked in the cell suspension and then the neutralized collagen was added. In the second approach, the cell suspension was added to the ice-cold neutralized collagen and then the ice-cold scaffolds seeded by mixing method. The second method was chosen as most effective (data not shown), although the procedure needed to be executed rapidly to avoid prolonged exposure of cells to low temperatures,

necessary to prevent collagen gelation during the seeding. Gelation occurred by placing the seeded scaffolds in incubator at 37°C for 30 minutes. Based on the results, HEPES neutralization strategy was further investigated and different collagen concentrations (1 to 10 mg/mL) were tested in order to identify the optimal coating concentration.

Pre-coating strategy

After evaluation of post-coating strategies by direct mixing of cell suspension with the coating protein, coating of the microchannels was optimized by pre-coating of PUDNA hydrogels with collagen after the rinsing steps and subsequent freeze-drying. Pre-coating was chosen to obtain selective coating of the microchannels as the protein deposition occurs when the PUDNA is in form of hydrogel, thus presenting no porosity. Briefly, the coating was realized by exposure of the hydrogels to a solution of 1 mg/mL collagen from bovine corium (Collagen Solutions, Glasgow, UK), diluted in 0.01 N HCl and consequent neutralization in PBS 1X and 0.1X. Detailed description of the process is given in **Section 4.2.2**.

5.2.3. Evaluation of different cell culture conditions

Organized and functional endothelium was engineered by seeding PUDNA scaffolds with endothelial cells and letting them proliferate and self-assemble within the prepatterned microchannels by using the polymeric scaffolds as template. The presence of selective coating was fundamental for optimal primary adhesion within the channels. After optimization of the coating strategies, experiments

were conducted to evaluate (i) different endothelial cell sources, (ii) different cellular concentration and (iii) different cell culture nutrients, notably by comparing the presence to the absence of growth factors.

Different endothelial cell from established lines or primary sources were tested. Preliminary studies were conducted by using the somatic hybrid endothelial cell line EA.hy926, as previously illustrated. Cells were cultured in standard DMEM 1X. To build a more relevant model, we then tested the human cell line HUV-EC-C [HUVEC] from umbilical vein/vascular endothelium (CRL-1730™, ATCC®, VA, USA). Scaffolds seeded with HUV-EC-C were either cultured in DMEM 1X or in specific endothelial basal medium supplemented with growth factors (EGM™-2 BulletKit™, CC-3162, Lonza, Basel, Switzerland) and the morphological differences evaluated. A comparison of endothelium formation over time under different seeding concentrations (from 1 to 10×10^6 cells/ mL) was also carried on to optimize the timing and seeding conditions. Preliminary tests have been done also by using primary HUVECs from human pooled donor (PB-CH-190-8013, PelloBiotech, Planegg, Germany) and immortalized human hepatic sinusoidal endothelial cells (IM-HHSECs, P10652-IM, Innoprot, Derio, Spain) for mimicry of the liver sinusoid. IM-HHSECs were cultured in endothelial cell medium (ECM, P60104, Innoprot), containing 1% endothelial cell growth supplement (ECGS).

5.2.4. Imaging and characterization

Labeling protocols

Compared to staining protocols presented in the previous chapters, typically used for 2D substrates, labeling of 3D models requires an optimization of the incubation times due to the presence of a thick matrix incorporating the cells. At the desired time point, the cell culture media in the multiwells containing the specimens was removed and samples were fixed by adding 1mL of 4% paraformaldehyde diluted in PBS 1X for each well and incubating for 1h at 4°C under slight agitation. Samples were washed 3 times in PBS, permeabilized with 0.1% Triton X-100 in PBS for 45 minutes at RT and washed again 3X in PBS.

Morphological labeling

Morphological staining of actin filaments and cell nuclei was performed by incubation in Phalloidin–Tetramethyl rhodamine B isothiocyanate (P1951, Sigma Aldrich) and 4',6-diamidino-2-phenylindole, dichlorhydrate (DAPI, D1306, Invitrogen™), respectively. Final dye concentrations were set at 2.5-5 µg/mL and 1-2 µg/mL for phalloidin and DAPI, respectively, with dilutions of 1/100-1/200 and 1/2500-1/5000 in PBS 1X compared to the initial stock concentrations. Dye dilution was calculated considering a volume of 300 µL per well and the amounts of the two fluorescent molecules was calculated as $V_{dye} = \frac{V_{tot}}{dilution\ factor}$. For example, considering the staining of 5 samples, thus 5 wells, the total dye volume (V_{tot}) would be of 1500 µL. Assuming a dilution factor of

200 for phalloidin and 2500 for DAPI, the final dye volumes were calculated as $V_{Phalloidin} = \frac{1500}{200} = 7.5 \mu L$ and $V_{DAPI} = \frac{1500}{2500} = 0.6 \mu L$, diluted in 1491.9 μL of PBS. Samples were incubated for 1h minimum at RT in the dark under agitation and consequently rinsed three times in PBS 1X. Scaffolds were preserved in 24 well plates in PBS 1X and sealed with Parafilm® and stored in the dark at 4°C overnight prior to imaging.

Functional labeling

Immunolabeling was performed for functional characterization of endothelium by labeling against CD31 and VE cadherin adhesion molecules in both 2D and 3D models. Selected primary and secondary antibodies are listed in **Table 5.3**.

Table 5.3. List of antibodies used for functional labeling of endothelial markers.

Staining for	Primary AB	Secondary AB
CD31/ PECAM-1	Mouse monoclonal [JC/70A] anti-CD31 (ab9498, abcam)	Goat anti-Mouse IgG1 Cross-Adsorbed Secondary Antibody, Alexa Fluor 647 (A-21240, Invitrogen™)
VE-Cadherin	Rabbit polyclonal anti-VE Cadherin (ab33168, abcam)	Donkey anti-Rabbit IgG (H+L) Highly Cross-Adsorbed Secondary Antibody, Alexa Fluor 488 (A-21206, Invitrogen™)

Testing of antibodies in 2D was performed by seeding HUVECs in 8-wells chamber slides (Nunc™ Lab-Tek™ II Chamber Slide™ System, No. 154534 and 177402). A concentration of 4×10^4 cells per well was used and cells were cultured with EGM-2 medium for a minimum of 24h. Different conditions were tested, with the specific

goal of comparing permeabilized and non-permeabilized specimens. Influence of blocking to prevent ABs cross-talk was also investigated.

For 2D ICC of cells cultured in chamber slides, cells were fixed with 4% FA for 10 minutes at RT after discarding the cell culture medium. For permeabilization, a solution of 0.1% v/v Triton X-100 in 1X PBS was used for 5 minutes at RT. For blocking, cells were incubated for 1h at RT in a solution of 1% w/v bovine serum albumin (BSA) in 1X PBS. The primary ABs were diluted in 1X PBS or in a 0.1% BSA solution for non-blocked and blocked conditions respectively and cells were incubated overnight at 4°C or 2.5 hours at RT. The dilutions used were 1/500 for both the primary antibodies. For staining with secondary ABs, cells were incubated for 1 hour at RT with Alexa Fluor 488 (staining for VE Cadherin, dilution 1/400) and Alexa Fluor 647 (staining for CD31, dilution 1/200). Each step was followed by a 3X washing with 1X PBS for a minimum of 5 minutes each. After a last washing step, the solution was discarded and the chamber removed. Cells were mounted with mounting Medium with DAPI (Aqueous, Fluoroshield, ab104139) and the glass slide covered with a #1.5 glass coverslip (Menzel-Gläser) and cured overnight at 4°C before imaging.

For 3D ICC of cultured PUDNA scaffolds, the time points were kept similar to 3D morphological labeling. After fixation with 4% FA for 1 hour at 4°C, samples were blocked by incubation in a solution of 1% w/v BSA in PBST (1X PBS additioned with 0.1% v/v Tween 20) for 1h at RT. Alternatively, a short permeabilization procedure with

0.1% v/v Triton X-100 was performed for 25 minutes at RT, followed by a blocking step by incubation for 1h at RT in a solution of 1% BSA in PBS.

Incubation with the primary ABs after dilution in PBS or in a 1% BSA in PBST solution for non-blocked and blocked scaffolds, respectively, was done overnight at 4°C. Incubation with secondary ABs diluted in PBS was carried out for 1 hour minimum at RT in the dark with the same dilutions used for 2D ICC. Eventual counterstaining with DAPI was done during or after secondary ABs. Samples were kept in PBS at 4°C in the dark until imaging.

Confocal and multiphoton imaging

Cultured scaffolds labeled as previously described were imaged using an inverted confocal microscope (LSM780, Zeiss, Oberkochen, Germany) equipped with a 10X dry objective (C-Apochromat 10x/0.45, Zeiss). A 488 nm argon laser and solid state lasers (405 and 561 nm) were used for imaging of FITC, DAPI and phalloidin-TRITC respectively. ZEN software was used for image setting and acquisition. During imaging, scaffolds were placed on a #1.5 glass coverslip covered by few drops of PBS to prevent the specimens to dry over time.

For higher resolutions and imaging depths, confocal and multiphoton (MP) imaging were done by using a TCS SP8 microscope (Leica Microsystems, Wetzlar, Germany), equipped with a 25X water immersion objective (HCX IRAPO, L25x/0.95, Leica). An excitation of 810 nm was used for MP imaging of phalloidin TRITC while

confocal imaging of DAPI, cadherin, phalloidin and CD31 were done with lasers at 405, 488, 561 and 633, respectively. LAS X software was used for image setting and acquisition. Samples were mounted on a circular plastic Petri dish and either immersed in PBS 1X or embedded in Aquasonic 100 ultrasound transmission gel (No. 01-08, Parker Laboratories, Inc., NJ, USA) to reduce light scattering. Gluing of samples was avoided to enable flipping of the specimens when needed.

The entirety of confocal and multiphoton imaging experiments was performed at the Plateforme d'imagerie photonique IMA'CRI, Centre de Recherche sur l'Inflammation, UMR 1149 Inserm, Université Paris Diderot, Paris, France.

Calculation of cell seeding density for 2D coatings

To compare the effectiveness of different cell seeding strategies and 2D coating, cell seeding densities were analyzed in Fiji ImageJ from fluorescent intensities of images acquired with the confocal LSM 780 microscope. Images of the scaffolds surface seeded with endothelial cells were considered for these calculations. Briefly, images were post-processed by creating a black and white mask of the scaffold's surface to isolate the fluorescent areas (cells) compared to the background. Calculation was performed starting from images of phalloidin staining due to higher SNR compared to DAPI images. Data were obtained with the *Analyze Particles* tool, by setting a minimum size of $400 \mu\text{m}^2$ (considering a cell diameter of $20 \mu\text{m}$, as calculated from the images themselves) to infinity to include cellular

clusters. The cellular densities were calculated as the mean gray value (MGV), corresponding to the sum of the gray values of all the pixels at the selection divided by the number of pixels.

MGV was chosen as parameter for representation of fluorescence intensity as size distribution among the samples could be considered similar. The presence of fluorescence corresponded to the cells stained, thus higher values of intensity were proportionally associated to higher dye content, thus cellular concentration, as confirmed by threshold images. Calculation of fluorescent intensities done by integrated density showed the same trend of MGV (data not shown).

Light sheet microscopy

Light sheet imaging of the full samples was performed with an Alpha³ light sheet microscope (PhaseView, Verrières-le-Buisson, France) equipped with QtSPIM software. Imaging of the scaffolds was performed in immersion in PBS 1X and both empty and endothelialized scaffolds were investigated. Images were reconstructed from raw data using Imaris. Imaging and image analysis were performed at PhaseView, Verrières-le-Buisson, France.

5.3. Results and Discussion

5.3.1. Evaluation of the cell seeding and coating methods

Comparison of seeding strategies

As explained in **Section 5.2.1**, standard gravity seeding method, commonly used for porous scaffolds, resulted to be inefficient when applied to matrices containing micropatterns due to the tendency of

the cells to precipitate and adhere to the bottom of the scaffold. We thus focused on evaluating active and mixing methods, whose main difference is the presence or absence of vacuum during the seeding, respectively. Comparison was done by analyzing the mean gray values (MGVs) of cells seeded on the surface of PUDNA scaffolds. Results of the fluorescence intensities for the active and mixing methods did not show any statistically significant difference, with both the methods giving similar results in terms of seeding densities and cellular distribution (**Figure 5.4B**). For 2D and 3D gelation post-coating strategies, the mixing method was mainly used due to the need of gently coat the microchannels during the seeding step and because of easier handling and reduced risk of contamination. For pre-coated scaffolds, since the coating was already homogeneously and selectively distributed, the active seeding was preferred to enable active pushing of the cell suspension within the channels. In this regard, further evaluation of the influence of seeding methods on endothelium formation was carried on by comparing single and double active seeding strategies.

Results showed that, despite the initial cell concentration selected, double seeding strategy, consisting in repeating the seeding step after a primary cell adhesion, led to more homogeneous distribution of cells within the microchannel, with subsequent faster formation of complete endothelium over time. Cross section images of the vascular channels showed that, at the same time point and for the same cell seeding density, double seeded scaffolds showed a fully endothelialized lumen over the length of the channel while single

seeded samples showed an incomplete endothelium. The design of a double seeding strategy allowed us not only to duplicate the nominal number of cells used for the seeding (as the seeding was repeated twice) but also to better partition them within the matrix by performing a dual step protocol. Further discussion will follow in **Section 5.3.3**.

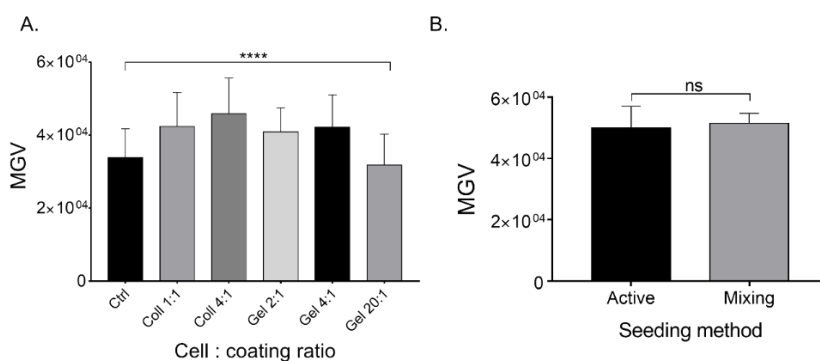


Figure 5.4. Cell seeding densities for different coatings, coating dilutions and seeding strategies. (A) Fluorescence densities for uncoated PUDNA and PUDNA coated with collagen or gelatin. Statistical analysis performed by One-way ANOVA (p value < 0.0001). Unpaired t-test between Col 4:1 and Gel 4:1 showed p -value of 0.0013 (**). (B) Fluorescence densities for scaffolds seeded by active (syringe) or mixing (vial) method. Statistical analysis performed by unpaired t-test, p -value of 0.165.

2D coatings

Preliminary trials focused on the use of either gelatin or collagen at dilutions typically used for 2D coating of culture vessels, as reported in conventional biology protocols. The diluted proteins were mixed directly with the cell suspensions at different volume ratios to find the suitable seeding parameters. Confocal images taken on the scaffolds surfaces after staining with phalloidin TRITC and DAPI were used for calculation of the MGVs.

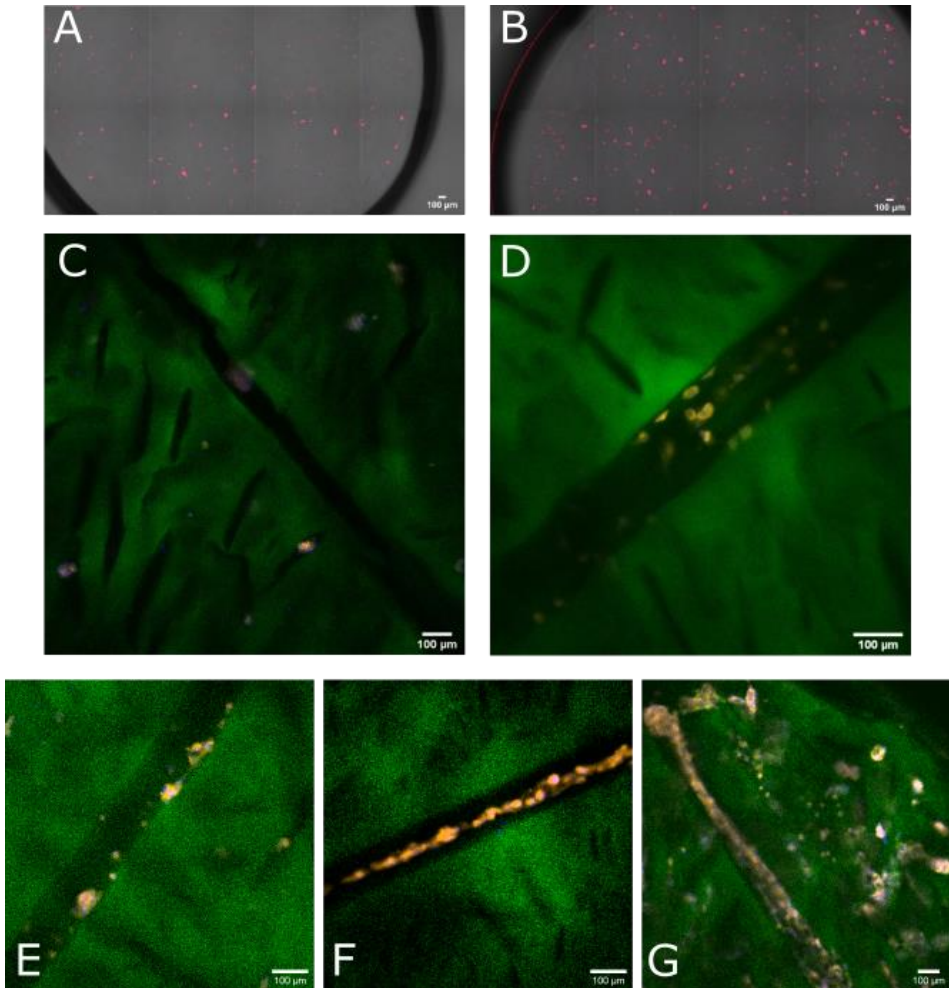


Figure 5.5. 2D Coatings and 3D neutralization post-coating. (A-B) Representative images of 2D coating evaluation by studying the cellular density (magenta) on the scaffold surface (gray) for a cellular/collagen ratio of 1:1 (A) and 4:1 (B). Collagen neutralization protocol performed by using NaOH (C) or HEPES buffer (D). Both the samples were seeded with EA.hy926, stained after 7 days from the seeding. (E-G) Evaluation of different collagen concentrations: 1 mg/mL (E), 2.5 mg/mL (F) and 5 mg/mL (G). All the samples were seeded with EA.hy926, stained after 7 days from the seeding. Staining for PUDNA (FITC, green), actin (phalloidin-TRITC, red or cyan) and nucleus (DAPI, blue). Scale bar 100 µm.

Results showed similar data for collagen and gelatin coatings, with a maximum cellular density for a cellular/protein ratio of 4:1 while higher or lower protein volumes did not improve cellular adhesion, with data comparable to the negative control (no coating of the scaffolds) (**Figure 5.4A**, **Figure 5.5.A-B**). Moreover, collagen showed statistically significant higher cellular densities compared to gelatin at the same protein concentration. On the other side, pre-coating of scaffolds with the proteins prior to seeding and without freeze-drying did not lead to significant results and no cells were found in the scaffolds during imaging. Overall, however, cells were mainly found on the surface of the matrices, often forming clusters within the pores, despite the use of mixing seeding, while microchannels resulted to be almost empty, indicating the unsuccessful inner coating, with subsequent lack of cell adhesion. These results demonstrated that coatings with protein concentrations typical of 2D biology were not sufficient to ensure spread cellular morphology nor homogeneous coating of micropatterned biomaterials. Furthermore, although direct mixing of the proteins with the cell suspension resulted to be the most effective method, ratios need to be carefully investigated, making the reproducibility and scale up of the seeding protocols a laborious and time-consuming operation.

Collagen neutralization strategies

Based on preliminary results obtained from 2D coating of PUDNA scaffolds, we selected collagen due to a higher versatility compared to gelatin and the possibility of forming a gel at higher concentrations by neutralization. The hypothesis behind this study was to use neutralized collagen in its liquid form (just after neutralization and before the gelation step) to incorporate cells and coat the inner PUDNA microchannels. After gelation, the collagen would convey the cellular adhesion to the channel walls, acting both as coating protein and physical supporting template. Two different protocols were tested for neutralizing the acidic collagen solution and obtaining a gel that could be more effectively used for coating of the matrices compared to gelatin and collagen at lower dilutions. The protocols consisted in using either NaOH-based or HEPES-based buffers to neutralize high concentration collagen type I from rat tail. The gelation was evaluated firstly by considering the physical aspect of the gels and testing their pH, to ensure effective neutralization and a pH in the range of physiological values, so as to be cytocompatible. In fact, microenvironmental pH has been demonstrated to have a fundamental role in cell metabolism, proliferation and migration [441]. Changes in the pH of the extracellular environment, as addition or depletion of salts or peroxides, induce a variation of the intracellular pH, with subsequent modification and eventual dysfunction of cellular activities [441,442]. Interestingly, variation of intracellular pH has been shown to be one of the mechanisms responsible for cellular adhesion and growth on certain substrates, as

fibronectin [443]. The effective neutralization was evaluated as well by directly mixing of collagen with the cell suspension and observation of the cell adhesion and proliferation within the channels. Preliminary results from confocal imaging showed that neutralization by NaOH by following the manufacturer's guidelines was ineffective to endothelialize the channels, with absence of cells in the patterns and sedimentation of rounded cells and aggregation within the pores. Neutralized collagen by HEPES favored instead good adhesion and spreading of cells in the microchannels after 7 days of culturing, for a collagen gel concentration of 0.3 mg/mL (**Figure 5.5C-D**). These data led us to further investigate HEPES-based neutralization and to test different gel concentrations, up to 10 mg/mL. Interestingly, high concentrations (> 2.5 mg/mL) led to formation of collagenic cords in the PUDNA channels with cells elongated and distributed over them, thus creating a matrix in a matrix, that could be an interesting solution for other applications, as for coaxial TE approaches (**Figure 5.5E-G**). However, due to the high concentration and the tendency of collagen to form hierarchical helical fibers, the use of these gels did not lead to a coating of the channels inner wall, nor it promoted cellular adhesion. Particular interest was placed in medium collagen dilutions of 0.5 and 1 mg/mL. Physical evaluations demonstrated the possibility of modulating the texture of the gels from very soft to hard, depending on the volume of neutralizing buffer added, while maintaining a physiological pH range. Despite the promising results obtained from the use of medium collagen concentrations, the post-coating

neutralization strategies often led to uneven collagen distribution within the channels, hampering uniform cell colonization. Furthermore, since the coating was performed on freeze-dried porous scaffolds, selective collagen distribution could not be obtained, with protein coating the pores of the matrix as well (**Figure 5.6A**). Therefore, pre-coating of non-porous PUDNA hydrogels prior to freeze-drying was chosen as optimal approach.

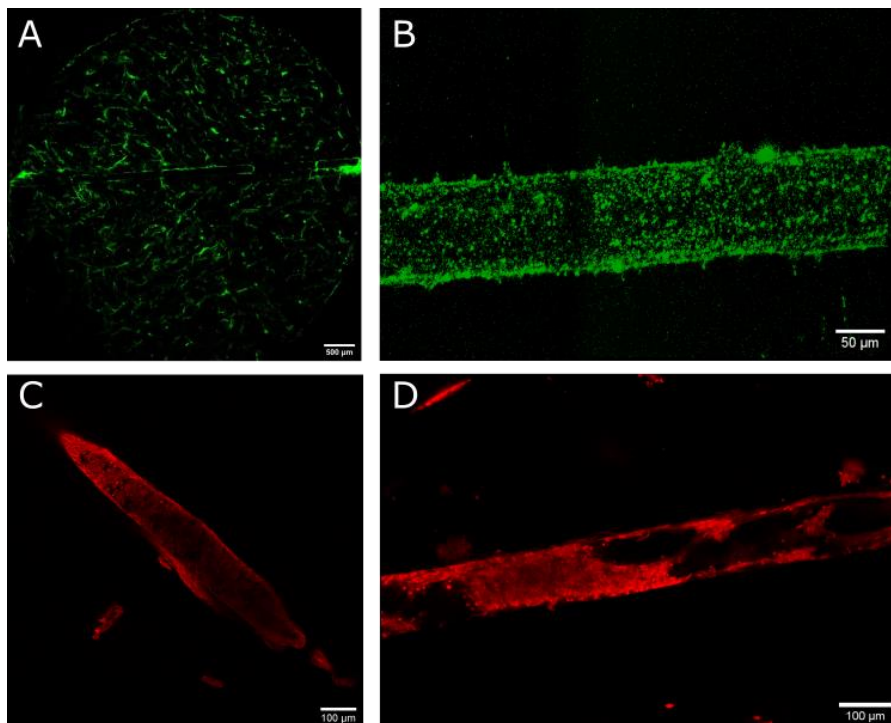


Figure 5.6. Comparison of 3D collagen coating strategies by multiphoton and SHG microscopy. SHG images of collagen (green) deposited within the PUDNA matrix by post-coating (**A**) and pre-coating (**B**, 3D projection of the microchannel) strategies. Collagen was 1 mg/mL for both the conditions. (**C**) HUVECs seeded on post-coated PUDNA scaffolds (central area of the channel). Cells adhered in a non-homogeneous pattern, depending on where the collagen was distributed. (**D**) HUVECs seeded on pre-coated PUDNA scaffolds (central area of the channel, staining for actin, red). Although the seeding concentration was

not optimized yet, cells were homogeneously distributed along the channel length and adhering to the walls. Scale bar 500 μm (A), 100 μm (C-D) and 50 μm (B).

Pre-coating strategy

Pre-coating with collagen from bovine corium of PUDNA hydrogels was performed by deposition and neutralization prior to freeze-drying. Images obtained by SHG analysis revealed the selective presence of the protein within the microchannels, uniformly distributed over the entire length while the rest of the scaffold was characterized by the absence of collagen (**Figure 5.6B**). Although collagen did not assemble into a fibrillar form, its presence was sufficient to ensure proper cell adhesion and endothelium formation, as will be discussed later in this chapter. Detailed description of the results is given in **Section 4.3.1**.

5.3.2. Evaluation of different cell culture conditions

Hybrid somatic vs vascular endothelial cell models

In parallel to coating optimization strategies, studies were carried out to evaluate the formation of endothelium by means of different endothelial cell lines of human origin. Initial experiments were performed by using somatic cells from hybrid tissue presenting endothelial morphology, called EA.hy926 cells. EA.hy926 cells have been often used in vascular TE to model endothelium [444–446]. They show the advantage that can be cultured in DMEM, thus they do not require the use of specific and expensive cell culture medium. However, works reporting the use of this cell line normally evaluated endothelium formation on 2D substrates, as electrospun biomaterials, rather than the formation of an ultimate tubular structure. Our results

using EA.hy926 eventually showed good adhesion and spread morphology in presence of proper uniform coating but the formation of homogeneous tubular endothelium resulted challenging, probably due to the non-vascular origin of this cell line. Also, the morphology after spreading resulted to be less elongated compared to other endothelial cell lines we tested, a result coherent with the literature findings [445]. An interesting paper published by INSERM in 2014 also reported how the application of shear stress did not induce cytoskeleton remodeling in EA.hy926, as it normally happens in vascular ECs, due to ineffective activation and low number of specific integrins that regulate the cellular response to the flow [447]. Furthermore, EA.hy926 have been shown to have less adhesive properties to typical ECM-like proteins, as fibronectin, collagen and gelatin, compared to HUVECs as well as reduced migration in response to VEGF gradients [448]. In view of further project development and integration of mechanical cues, as shear stress, these findings are particularly useful for our research and, together with the results we obtained, helped us in the optimal selection of ECs models. In further experiments, we thus chose a human endothelial cell line from umbilical vein/vascular endothelium, HUVECs. HUVECs either primary, commercial or isolated, or immortalized as cell lines are the most common cells used for modeling vascular and organ-specific endothelium in TE [449,450]. Extensive research has been conducted on this cell source, that has been widely adopted for forming the endothelial lining in prevascularization approaches and pathophysiology modeling [451].

Here, we used a commercial immortalized HUV-EC-C cell line and the capability of distributing, elongating and self-organizing into vascular channels was compared to that of EA.hy926. Under the same coating and seeding protocols, results showed better adhesion to the channel walls compared to hybrid ECs and organization into a monolayer, with typical polygonal and long morphology and oval nuclei (**Figure 5.7A-B**).

Difficulty of using specific immortalized human hepatic sinusoidal endothelial cells

Further experiments were performed with a commercial immortalized HHSEC cell line, with the final goal of adopting an endothelial model as close as possible to the liver sinusoid. This option was also chosen to overcome the limited availability of donors for isolation of primary cells, a long and laborious operation, and to use a model with less inter-batch variability, as for established cell lines. Culturing *in vitro* required specific products as well as need for an overnight coating of the vessels with fibronectin during the expansion to prevent a modification of the phenotype (**Figure 5.7C**). Cells resulted to be extremely delicate and favorable to contaminations and the lack of literature on their culturing and use hampered an easy adoption of this EC model. Scaffolds seeded with these cells showed their adhesion within the microchannels but we have not been able to further design the experiments with IM-HHSECs due to difficult maintenance in 2D and handling in 3D (**Figure 5.7D**).

Influence of growth factors on endothelium formation

As introduced above, cell culture medium formulations are designed depending on the cell type and source. Basal media formulations, as DMEM, are commonly additioned with antibiotics and antimycotics to prevent cell contamination, and eventually with serum. Serum, normally of bovine origin – fetal bovine serum (FBS), contains biomolecules, such as hormones, ECM components, lipids and growth factors, that promote cell metabolism and proliferation. Despite a widespread use in cellular biology, its role in the past two decades has been often debated because of ethical and scientific concerns and serum-free approaches are nowadays largely promoted [452]. For culturing of both EA.hy926 and HUVECs, we initially used DMEM added with FBS. However, specific media solutions have been formulated for targeting endothelial cells growth and proliferation and culturing of HUVECs has been performed with specific EGMTM-2 cell medium in a second phase of the project. Compared to basal medium, endothelial growth medium is supplemented, other than with FBS, with different growth factors that have been shown to have a fundamental role in the angiogenetic process, as VEGF, hFGF and hEGF, responsible for migration, proliferation and endothelial cells organization, respectively [453,454]. When comparing the use of EGMTM-2 to DMEM in the endothelium formation at fixed cellular concentrations, time-points and cell source, the differences were evident. Confocal images after 7 and 14 days of PUDNA scaffolds cultured in DMEM showed cells suspended in the microchannels forming clusters, and eventually

floating (**Figure 5.7E**). In other samples, HUVECs cultured in DMEM resulted to be compacted within the channel, eventually clogging it and with no organization resembling the endothelium. When cultured in specific EGMTM-2, organized endothelium could form within few days, depending on the cell concentration, and cells kept their adhesion to the channel walls and continued to proliferate up to 14 days *in vitro* (**Figure 5.7F**).

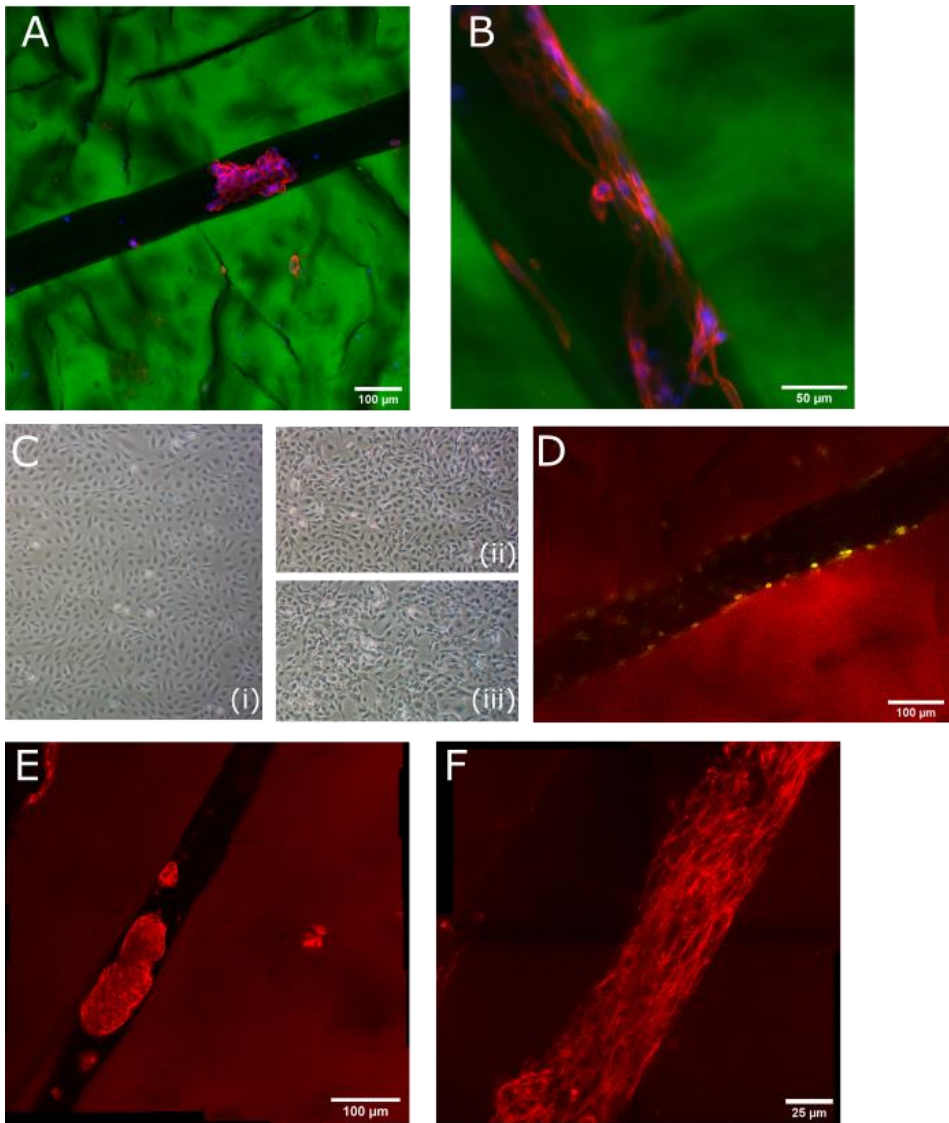


Figure 5.7. Comparison of cell culture conditions. (A) EA.hy926 and (B) HUVECs, both cultured in DMEM and seeded in FITC-PUDNA (green) post-coated with 1 mg/mL of collagen after 14 and 7 days, respectively. Staining for actin (red) and DAPI (blue). (C) Different culturing conditions for IM-HHSECs in 2D culture vessels: (i) Specific endothelial growth medium ECM on fibronectin-coated flasks (50 $\mu\text{g}/\text{mL}$); (ii) specific ECM medium in non-coated flasks and (iii) DMEM in non-coated flasks. (D) Attempts of IM-HHSECs seeding in PUDNA scaffolds, day 2. (E-F) Comparison of cell culture medium formulations

for HUVECs seeded with a cellular density of 5×10^6 cells/mL and imaged at day 7 (actin filaments in red): (E) DMEM and (F) EGMTM-2 (MIP). (D-F) Staining for actin (phalloidin-TRITC, red). The FITC-labeled PUDNA matrix was also visible in the red channel. Imaging systems: (A-B): confocal Zeiss LSM780, (C) optical microscope, (D-F) MPM Leica SP8. Scale bar 100 μ m (A, D-E), 50 μ m (B) and 25 μ m (F).

5.3.3. Formation of endothelium by optimized protocol

The definition of optimal coating protocol by pre-seeding method led to uniform and selective collagenic coating of the microchannels within the PUDNA matrices, as demonstrated by SHG data. The use of a more powerful confocal microscope, Leica SP8, with 25X immersion objective, also allowed us to fabricate thick scaffolds with standard silicon spacers (see Chapter 4, **Section 4.2.2**) without hampering the imaging of the scaffold inner features. The pre-coated thick scaffolds were used to seed HUVECs by active seeding method. The endothelial cells were cultured in EGMTM-2 complete growth medium to benefit from the presence of proangiogenic growth factors, as previously discussed.

Influence of cellular concentration on timing of endothelium formation

Different HUVECs concentrations were tested to evaluate the influence of cell seeding density on the timing of endothelium formation. Cell suspensions with concentrations of 1×10^6 /mL, 2.5×10^6 /mL and 5×10^6 /mL were seeded. Considering an absorption capacity of 100 μ L for the PUDNA scaffolds with nominal diameter of 5 mm and nominal thickness of 0.7 mm, the estimation of cells absorbed by the scaffold per seeding was of 1×10^5 , 2.5×10^5 and 5×10^5 cells for each cell density tested. The samples were stained

with phalloidin-TRITC and DAPI for actin filaments and nuclei visualization, respectively. Results showed that formation of complete endothelium, as observable from the cross-section images of the endothelial tubes, occurred in one week for double seeding of 1×10^6 cells/mL while only 4 days were necessary for complete assembly by using a concentration of 2.5×10^6 /mL. Timing of endothelium assembly was similar to previously reported data [329,455,456]. Moreover, an increase of the cell density during seeding led to faster assembly of organized endothelium in presence of growth factors. However, the seeding concentration needs to be tailored on the final application of the scaffold. For instance, biomaterials are nowadays often used as templates for the growth of tissue from stem cells, commonly arranged in the form of organoids. After seeded within the scaffolds, the stem cells need to undergo differentiation to develop a specific phenotype, with protocols lasting days to weeks [423]. When designing a complex platform including different cell types and a vascular network, the vascularization protocols should thus take into account the timing for the formation and assembly of the other cells, normally mimicking the parenchyma. In the case illustrated above, formation of endothelium within few days might be counterproductive, if stem cells are still in a differentiation stage. Vascularization should thus be initiated after parenchyma tissue formation or in parallel but with an assembly timing similar to that of the parenchyma.

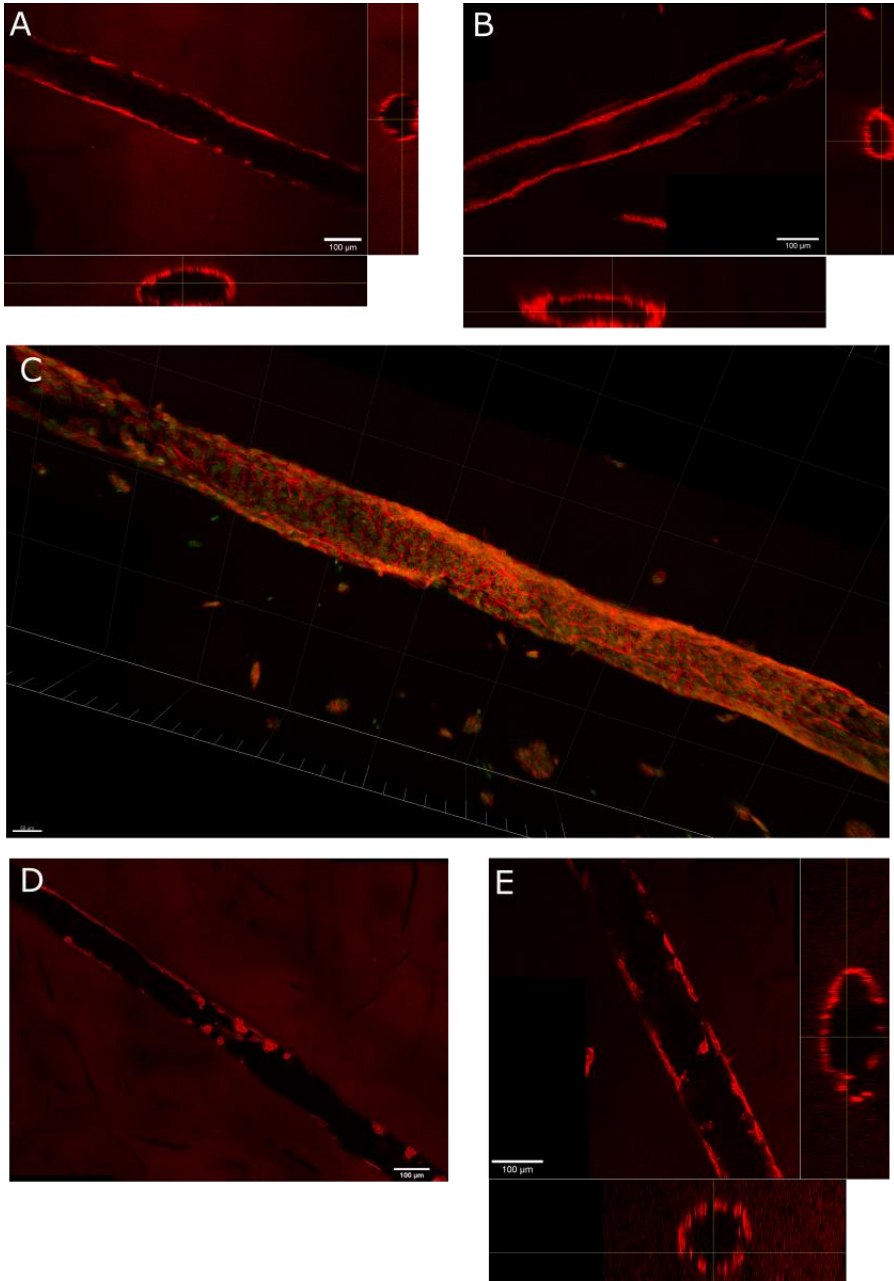


Figure 5.8. Comparison of HUVEC cells concentrations on endothelium formation by multiphoton microscopy. (A) 1×10^6 cells/mL, double seeding, day 7. (B) 2.5×10^6 cells/mL, double seeding, day 4 (orthogonal views) and (C) Endothelium reconstruction in

IMARIS (nuclei, stained with DAPI, are visible in green). (D) 1×10^6 cells/mL, single seeding, day 7 and (E) 1×10^6 cells/mL, single seeding, day 11. Staining for actin (phalloidin-TRITC, red). Scale bar 100 μm (A-B, D-E), 50 μm (C).

Nevertheless, co-culture of stem cells and ECs prior to differentiation has shown to hamper the organoids assembly due to the presence of vascular growth factors in the media and of EC signals [457]. In fact, our results demonstrated that higher cellular concentrations of 5×10^6 cells/mL after 2 weeks from the seeding presented a multilayered cellular distribution, with HUVECs starting proliferating within the lumen and eventually clogging it. This behavior would happen also at lower densities and longer times in absence of external cues. Formation and maintenance of endothelium function and morphology in long term experiments (> 2 weeks) should indeed consider the integration of other cues, as co-culture with other cell types or channels perfusion [456,458,459].

As partially discussed in **Section 5.3.1**, we also compared the influence of the seeding strategy on the timing of endothelium assembly. Our results showed that double seeding enabled faster endothelium formation with better cellular distribution. By adopting a single seeding method, the times were doubled, with complete assembly occurring after 2 weeks and 1 week for cellular concentrations of 1×10^6 /mL and 2.5×10^6 /mL, respectively. The culturing strategy also resulted to be effective, with no loss of morphology and organization over time (**Figure 5.8**). Although we considered the single seeding strategy less effective for our objective, consisting in engineering and imaging vascularized PUDNA

scaffolds, these findings should be taken into account when designing complex TE models, with the need to match the vascularization process with the tissue formation. The single seeding strategy resulted to be a valuable method for endothelialization of PUDNA scaffolds over longer times compared to double seeding.

Preliminary functional studies

In addition to morphological studies on endothelium assembly by staining with actin filaments and nucleus dyes, functional studies of endothelial cells were conducted by performing immunocytochemistry labeling of specific endothelial markers. Among the many endothelial markers, we chose two EC adhesion markers against the transmembrane protein CD31, also called platelet/endothelial cell adhesion molecule-1 (PECAM-1) and the surface molecule VE-Cadherin [460,461]. The ICC procedures were performed by indirect labeling, meaning two different antibodies were used to target the antigen. The first antibody, called primary AB, was an unconjugated antibody used to bind the cellular antigen while the secondary AB, conjugated to a fluorophore for fluorescence detection, was used against the primary AB [462]. As ABs are commonly produced in animals, ABs for different targets but from the same species might cross-react, thus causing a non-specific binding. To block non-specific binding and reduce the background, ICC protocols often provide for a blocking step, eventually repeated several times. The blocking is done by incubation of the sample with specific reagents that bind to the antigen, thus blocking the AB access. Common blocking reagents are

animal sera, as normal goat serum, and proteins, as bovine serum albumin (BSA), or commercial buffers. To prevent cross-reaction, we performed blocking by BSA incubation and we selected both the primary and secondary ABs for CD31 and VE-Cadherin from different animal species. Mouse and rabbit anti-human (as we worked with human cells) were chosen as primary ABs for CD31 and VE-Cadherin, respectively, while ABs from goat and donkey against mouse and rabbit, respectively, were chosen as conjugated secondary. Initially, the labeling was performed directly on PUDNA scaffolds by following standard ICC procedures, with a revisited timing for 3D thick samples. Samples were observed with the confocal Leica SP8 microscope.

Results for both CD31 and VE-Cadherin showed that, though cells expressed the molecules of interest, the dyes were located in the cytoplasmic region of the cells while they are normally expressed as surface proteins and appear as marked lines at the edges of the cell, corresponding to the cellular membrane region, when stained in 2D (**Figure 5.9.A-B**). The result could be attributed to the overnight incubation with the primary AB in a solution containing Tween 20. Tween 20 is in fact a non-ionic detergent commonly used for dilution of the blocking agent as well as for the antibodies to further impede non-specific interactions. However, due to the lengthy incubation steps, the use of this detergent is responsible for excessive permeabilization and membrane antigens disruption [463]. To further evaluate these findings, we thus decided to test alternative ICC protocols on HUVECs cultured on 2D flat supports and, specifically,

to investigate the function of permeabilization agents. After fixation, cells were either treated with Triton X-100 as permeabilizing agent or non-permeabilized and then incubated in a PBS solution containing 1% BSA for blocking. The addition of Tween 20 for diluting blocking agents and antibodies was avoided. Confocal images revealed that a short permeabilization step with Triton for 5 minutes did not hamper the expression of the membrane antigens (**Figure 5.9.C-D**, white arrows), however it could be already noted a more diffused presence of fluorescence in the intracellular region, compared to non-permeabilized samples, for both the ABs tested. Control samples were also prepared and imaging artifacts as autofluorescence and cross-reactivity were also evaluated (data not shown) [464]. Of note, the strong nuclei fluorescence was attributed to the strength of the DAPI-containing mounting medium, that caused a fluorescence crosstalk (also known as spectral bleedthrough) between the channels. This was confirmed by some cells that detached during the staining (**Figure 5.9D**, right, white circle), as there the nucleus was absent and the DAPI bleedthrough in the 488 nm channel as well. Images were eventually post-processed in Fiji ImageJ by using the Spectral Unmixing plugin for the artifact correction (**Figure 5.9E**).

Another drawback in confocal imaging of 3D samples was that the images of the channels, taken in the depth of the scaffolds, resulted to be relatively blurred, making it particularly difficult to localize the ABs. This issue will be further addressed in the next section.

Overall, our results showed the need to accurately design ICC protocols based on the specific target antigen (cellular location, function, ...) and for a 3D system (optimization of steps and timing). For our antigens of interest, we thus excluded the use of Tween 20 for long incubation steps while short permeabilization did not bring any specific advantage. Nevertheless, optimization steps performed in 2D should then be revised carefully for 3D PUDNA scaffolds. Besides the functional evaluation of ECs and the optimization of antibody staining protocols for 3D matrices, ICC is fundamental for distinguishing different cell types in co-cultured models. Thus, our goal of targeting specific EC markers was achieved and we will use these findings in further studies for characterization of more complex models composed of different cell sources.

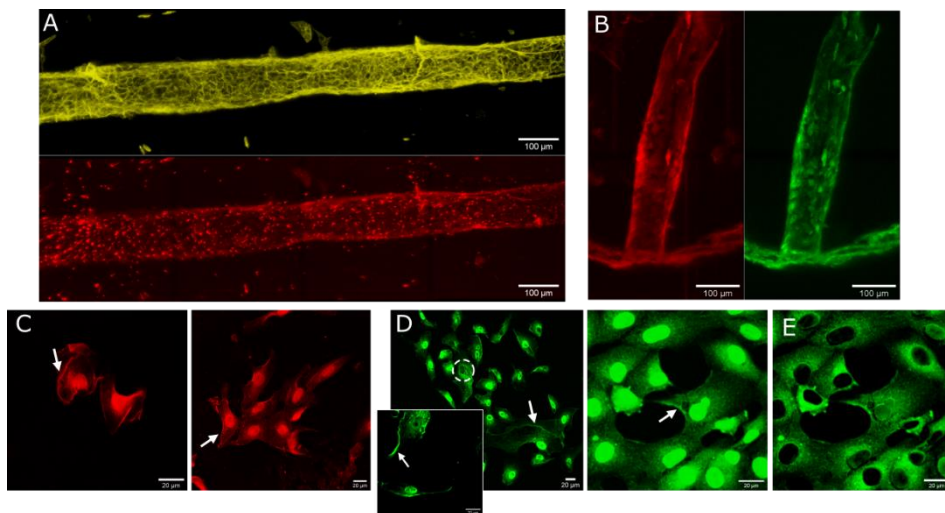


Figure 5.9. 2D and 3D functional labeling of HUVECs. (A) Complete endothelium (MIP) obtained from a double seeding with concentration of 2.5×10^6 cells/mL, day 7. Top: staining for phalloidin-TRITC, Bottom: staining for CD31. (B) Double staining of the channel entrance (MIP) for CD31 (left, red) and VE-Cadherin (right, green). (C-D) 2D immunolabeling of CD31 (C) and VE-Cadherin (D) in HUVECs without or with

permeabilization by Triton X-100 (left and right, respectively). White arrows indicate the localization at the plasma membrane. (E) Figure D (right) after unmixing for correction of DAPI bleedthrough. Scale bar 100 μm (A-B), 20 μm (C-E).

Considerations about the imaging systems

As a matter of fact, imaging is fundamental for evaluating *in vitro* biological models and good imaging is a prerequisite to obtain valuable information and take the research further. Nowadays, TE constructs are engineered with increasingly complex architectures and with a wide range of biomaterials, tailored on their final application. In this field, models are commonly three-dimensional and many efforts are now conducted to generate large constructs, more physiologically relevant [465]. Fluorescence imaging often relies on the use of confocal microscopy, which is however limited when it comes to study thick samples because of limited penetration depth, photobleaching and scattering. Though traditional histological methods, as sectioning, can be applied as well for the study of cellularized biomaterials, the investigation of intact 3D constructs would offer several advantages, notably the possibility of imaging living cells and the preservation of the original scaffold architecture [466]. Alternative imaging techniques should thus be more largely adopted for evaluating 3D models. In this context, nonlinear imaging techniques, as two-photon excited fluorescence (TPEF), are considered of great interest for imaging of biomaterials as they allow for deep imaging and reduced photodamage [467–469]. Used to characterize the biomaterials features because non-invasive, the application of TPEF has been demonstrated as well on cells and thick

tissue sections, and even on living whole organisms [470–472]. Particularly, the main difference of TPEF, that is a laser point scanning technique, compared to standard confocal microscopy relies on the restriction of the spatial localization of the fluorophore. In confocal microscopy, a single photon causes the excitation of a fluorophore molecule above and below the focal plane, thus producing an out-of-focus background fluorescent signal. The use of a pinhole allows for reduction of this signal, thus collecting information on a single focal plane and increasing the spatial resolution. However, since the excitation is generated within the whole specimen, the light absorption is responsible for photodamage and bleaching of all its sections.

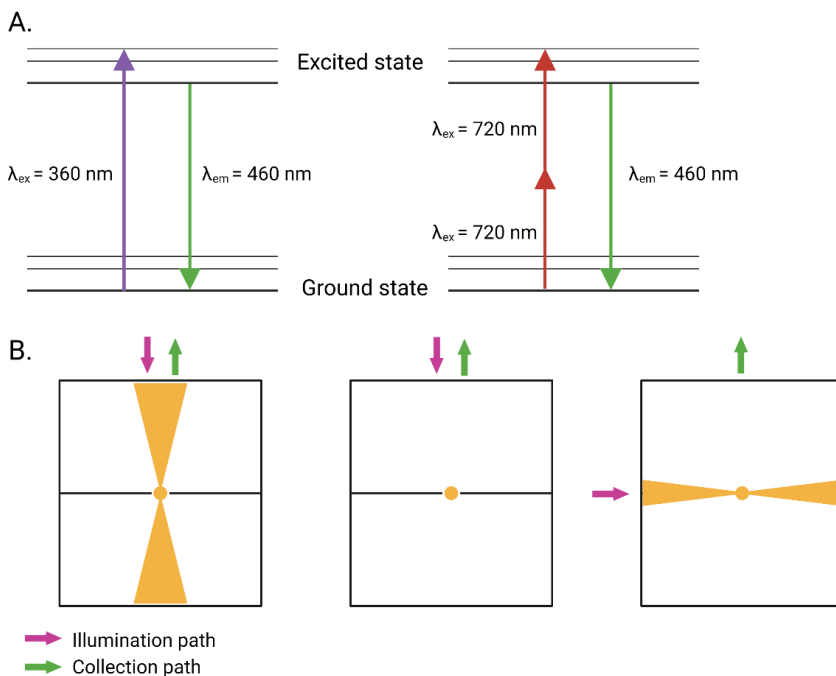


Figure 5.10. Schematic of working principle of TPEF and LSM. (A) Energy-level (Jablonski) diagram of one-photon (left) and two-photon (right) excitation. (B) Signal generation within the focal plane (black line) for confocal microscopy (left), TPEF (middle) and LSM (right). The direction of illumination and collection paths are indicated as well. Created with Biorender.com.

On the other side, TPEF relies on the excitation of a fluorophore caused by simultaneous absorption of two infrared photons, preventing the generation of signal outside the focal plane (**Figure 5.10A**). This phenomenon thus prevents the formation of out-of-focus signal, with subcellular spatial resolution. As a small volume of the sample around the focal point is excited, bleaching and toxicity are also drastically reduced, an important requisite for live and long-term imaging studies (**Figure 5.10B**). The reader is referred to [470,471] for an extensive description of TPEF principles in biology.

For endothelium imaging, we used two different confocal systems with increasing objective magnification as well as TPEF microscopy. As described in Chapter 4, since cells in the PUDNA scaffolds are located in the deep region, where the microchannels are patterned, we firstly worked on adapting the scaffolds to the imaging system, a confocal microscope from Zeiss, equipped with a 10X dry objective, thus reducing the biomaterial thickness. This way, we were able to more easily locate the channel: for instance, **Figure 5.5E-G** shows confocal images of the channels from thick PUDNA scaffolds while images in **Figure 5.7A-B** were taken on thin samples, with the same imaging system (LSM780, Zeiss). 3D images of the whole channel, however, often resulted blurred, with difficulties in resolving the

single cell morphology, resulting in a poor quality of the data and difficulty in proceeding with further experimental design. Moreover, use a FITC-functionalized PUDNA matrix was often necessary for channel localization and endothelium imaging, thus reducing the number of fluorescent dyes that could be used for cellular labeling. Blurring is a drawback we also encountered when using the Leica SP8 confocal during functional studies (**Figure 5.9B**). Though, as described above, unspecific localization of endothelium markers could be linked to suboptimal ICC protocols, the cellular and subcellular resolution was difficult to achieve with conventional confocal microscopy within thick PUDNA scaffolds. While the channel localization resulted to be easier by using the Leica system, and this allowed us to culture non-functionalized PUDNA matrices (green channel was instead used for VE-cadherin staining), imaging of ECs morphology was extremely problematic, thus hindering a further use of confocal microscopy for endothelium markers detection. On the other side, resolved images of endothelium were acquired by MPM (examples **Figure 5.7F** and **Figure 5.8**). The use of TPEF allowed in fact for imaging of wide areas of the sample for the full channel thickness with no loss of resolution nor samples photobleaching. Nevertheless, it should be noted that, since the excitation principles of TPEF are different compared to those of confocal imaging, the choice of fluorescent proteins should be done carefully. In fact, the two-photon absorption spectra differ from the one-photon absorption spectra, not always in a way that can be predicted theoretically. Therefore, many recent studies have focused

on empirical determination of absorption spectra of standard and new fluorophores [473]. For instance, the fluorescent molecule tetramethyl rhodamine isothiocyanate (TRITC), that we used here to stain actin filaments, has been previously used for MPM imaging, with an excitation spectrum of 700-1300 nm [474]. In our acquisition setup we used a wavelength of 810 nm for the phalloidin-TRITC excitation, as for simultaneous imaging of actin and collagen. However, imaging of ECs stained with both DAPI and TRITC resulted in signal in the green channel from the cellular nuclei, rather than from the SHG of collagenic components (**Figure 5.8C**), though the TPEF DAPI absorption maximum wavelength has been reported to be below 700 nm [475]. These findings suggest a great versatility of use of the TPEF imaging system and the possibility of simultaneous detection of different fluorescent molecules by using the same excitation wavelength for specific proteins. Many common proteins have been now characterized for their application in TPEF, included DAPI, FITC and many Alexa Fluor trackers, nevertheless the choice of the dye to be compatible with the MPM setup requires careful literature studies or preliminary investigation for their characterization.

As alternative to multiphoton microscopy, we also investigated the use of light sheet fluorescence microscopy (LSFM) of thick PUDNA samples in preliminary studies. While TPEF relies on precise scanning of one point at a time, thus eliminating the out-of-focus excitation compared to confocal imaging, this limits its speed for collection of large volumetric regions. As suggested by its name,

LSFM microscopy relies on the generation of sheets of light that illuminate the full focal plane simultaneously while the detection is done by placing a camera on the plane (**Figure 5.10B**). This way, the fast acquisition of large volumetric areas is done by moving in the space the excitation and detection components, determining a multispot scanning modality [476]. Compared to standard confocal approach, LSFM allows for reduced photodamage due to selective illumination of a single plane while it offers higher scanning speeds and simplicity compared to TPEF. In fact, as it relies on one-photon excitation, fluorescent dyes show the same absorption spectra of confocal microscopy, with no need for preliminary research and adaptation to TPEF principles. Because of its features, LSFM is particularly useful for imaging of thick and living samples and finds its main application in neuroscience and development biology, as well as for imaging at the subcellular level [477–479]. In the field of TE, LSFM holds great potential for imaging of 3D tissue models, as organoids and spheroids, and for imaging of thick cellularized bioconstructs[480]. Nevertheless, some differences compared to confocal and TPEF microscopy should be taken into account: primarily, as the sample is imaged in 3D, preparation and mounting is done not by using coverslips but by embedding or clipping the sample within specific chambers. Moreover, as tissues often contain molecules with high refractive index, they often need to be cleared with specific protocols to reduce scattering, opaqueness and overall imaging artifacts [481,482]. Then, acquisition with LSFM systems produces heavy raw data, normally of the order of terabytes, that

cannot be condensed in standard image formats, commonly adopted for other imaging techniques. This feature poses a challenge for both the storage and the processing, that should be done with dedicated hardwares and softwares.

We performed preliminary evaluation of LSFM on our samples, by imaging both empty and cellularized FITC-labeled PUDNA matrices. Results showed the possibility of imaging the whole samples in their full thickness in reduced times compared to other imaging techniques and with no need for clearing nor for specific and laborious sample preparation or embedding (**Figure 5.11**).

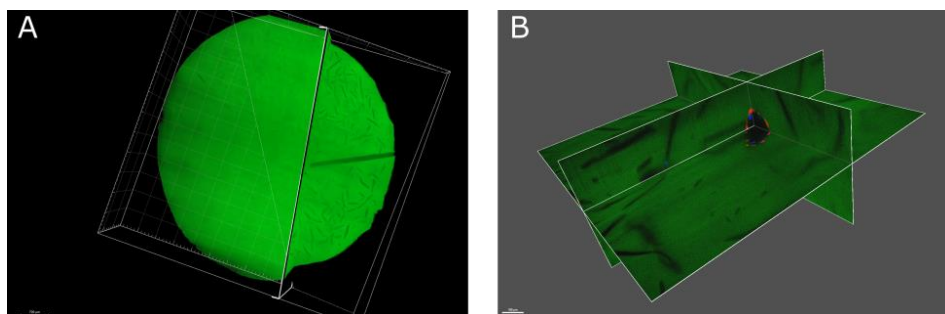


Figure 5.11. LSFM of PUDNA scaffolds before and after cellularization. (A) Frame of a video showing a FITC-labeled PUDNA scaffold (non seeded). It is possible to see both the external surface and a cross-section of the biomaterial, containing the microchannel. Scale bar 700 μm . (B) Orthogonal view of a FITC-labeled PUDNA scaffold with complete endothelium. Scale bar 100 μm .

The adoption of LSFM would thus allow us for more freedom in the biomaterials design, as physical properties as the thickness or density would not pose a constrain for the imaging. Moreover, it would enable fast scanning of the whole matrices, giving a complete overview of the experimental setup, a feature particularly interesting when building complex multi-cellular models and to study

phenomena, such as cellular-matrix interaction and matrix remodeling over time.

In conclusion, this paragraph depicts the different imaging techniques used for imaging and characterization of a vascularized biomaterial. Conventional confocal microscopy gives a deeper insight about endothelium formation compared to what can be seen during the culture steps with optical microscopes. It is however limited when cells locate and arrange within the scaffold, and the only possibility to resolve them is to adapt the matrix to the imaging system. Alternatively, laser point scanning techniques, as TPEF, and light sheet microscopy, can be used for better resolution, higher imaging depths and investigation of 3D volumes. Each technique has specific drawbacks, as careful choice of the fluorophores for TPEF and big data analysis for LSFM, but these microscopy techniques hold great promise for faster and better characterization of biomaterials and tissue engineered models and more efforts should be made for their wider application in the field of TE.

5.4. Conclusions and future perspectives

In this chapter, the engineering of endothelium within a 3D biopolymeric microchanneled template was presented. We have firstly introduced the importance of including a vascular network in tissue engineered models to enable easier, better and faster tissue regeneration. Different vascularization approaches have been discussed, with a focus on prevascularization techniques. A brief introduction to the anatomical and physiological properties of the

vasculature has been given to illustrate the fundamental parameters that should be considered when designing an artificial vascularized construct. Current limitations and drawbacks have also been addressed. To vascularize prepatterned pullulan-based (PUDNA) scaffolds, our research was developed in various and parallel directions. Different cell culture methods, cell sources, coating strategies and imaging techniques have been analyzed and compared until identifying the optimal experimental setup to build the endothelial model. Then, the formation of complete and functional endothelium over time was assessed by setting up different seeding conditions. Functional studies were also performed, along with morphological analyses. Results showed the possibility to build a 3D functional model, expressing typical endothelial markers, and, more importantly, the capability of tuning its assembly over time by modifying the seeding conditions. This feature is of particular interest because it enables to tailor the formation of vasculature based on the properties and final application of the engineered model of interest. Nevertheless, further investigation should be conducted to optimize the existing model and increase its complexity. Important aspects, as integration of other cell types via co-culturing strategies, application of external stimuli, as perfusion of the microchannels, long-term maintenance and development of the network would add more value to the current model and would increase its applicability as tissue-specific vascularized TE platform.

6. General conclusion and future outlook

In this dissertation, different project lines have been presented, with the aim of overcoming some of the main limitations of microfluidics, tissue engineering and microscopy technologies. In the context of microfluidic, the study of an alternative material to conventional polydimethylsiloxane has been proposed. An innovative soft thermoplastic elastomer, Flexdym™ was chosen for high-throughput fabrication of membrane-based devices for OOaC applications. By using a hot embossing process and self-sealing, platforms composed of Flexdym™ and a commercially available polycarbonate membrane could be produced in less than 2.5 hours. The devices could withstand pressures over 500 mbar with no delamination occurring, as tested by an automated bonding strength system. Preliminary cell culture studies demonstrated cellular adhesion, proliferation and high viability for 7 days, confirming the suitability of Flexdym™ - based platforms for OOaC applications.

In line with the key objectives of DeLIVER Consortium microfluidics has also been used as a tool for super-resolution imaging studies of cells in a dynamic environment. To do so, a part of the project was focused on the design and adaptation of microfluidic devices to standard SR-SIM platforms, with the introduction of the microfluidic chip in a dish, produced in PDMS and glass. Optimization of the design and fabrication parameters has been carried out to obtain stable and easily manageable devices. Results from *in vitro* studies showed the possibility of culturing cell lines under passive flow in long term experiments while primary LSECs preserved a healthy phenotype short-term. SR-SIM imaging

was performed to analyze the real-time cellular response to flow of molecules on-chip, confirming the compatibility and the feasible combination of microfluidics and SR microscopy.

However, little versatility is given by SRM techniques, as samples are generally imaged on coverslips, thus limiting the design of more complex physiological models. We thus decided to adopt TE approaches for the development of a 3D vascularized construct, that could be eventually applied for TE liver applications. The worked focused on the development and optimization of pullulan-based biopolymeric scaffolds. To allow for endothelium formation via pre-vascularization strategies, the scaffolds were prepatterned for formation of microchannels. The templating strategy, study of the process parameters and selective coating strategies were discussed and the constructs fully characterized. *In vitro* studies for formation of functional and complete endothelium focused on the parallel optimization of coating, seeding and culturing parameters. Our endothelium model expressed typical endothelial markers, as confirmed by functional imaging studies and its formation could be tuned over time by tuning the culture parameters. Moreover, the study of these constructs was conducted by evaluating alternative imaging techniques to standard confocal microscopy, that are specific for thick 3D matrices. Particularly, multiphoton and light sheet imaging were tested, confirming the possibility to image deeper in the scaffolds, with augmented resolution and reduced photobleaching and damage.

This research project has demonstrated some interesting results, notably the feasible application of soft thermoplastic elastomers for OOaCs, the combination of microfluidics and SR-SIM with real-time imaging of dynamic events, and the tunable vascularization of bioengineered polymers. Nevertheless, these studies suffer from some limitations, that would need further investigation to build a complete overview of these topics. Here, we suggest possible research lines for future perspectives.

The FlexdymTM – based platform could be used to build more complex OOaC models, with presence of constant flow and eventual study of response to drugs or molecules of interest. Testing of alternative materials to the commercial polycarbonate membrane we adopted here would also be interesting. As FlexdymTM shows elastic properties, missing to the polycarbonate, production of FlexdymTM porous membranes would also be of scientific relevance. This would surely increase the production timing, so it was beyond our purposes of designing a fast and scalable process, but could lead to the design of an entirely FlexdymTM - based microfluidic platform as alternative to PDMS.

Combination of microfluidics and SR-SIM could be further implemented to create a standardized setup for dynamic acquisitions. From the preliminary data presented in this thesis, sustained culture of human LSECs could be established on-chip for the study of fenestrations dynamics under flow. Nevertheless, this project remains ambitious as it depends on the availability of donor tissues for cells isolation and, mainly, it requires the colocalization of biology

laboratories and microscopy facilities to run living cell experiments. SR-SIM microscopes, however, are not available in any imaging facility as they do not represent standard optical equipments but with different models now available on the market and the continuous research improvements, we believe they will become more largely diffused and available. Combination of microfluidics with other SR imaging techniques would also be of interest in the scientific community. An increased complexity of the microfluidic device in a dish could also be envisioned, by inclusion of hydrogels and other cell types while preserving the compatibility with the imaging system. This would allow researchers to overcome traditional horizontal OOaC designs and combine biomaterials and microfluidics in a more biomimetic environment.

Biopolymeric materials designed for prevascularization can also be further implemented. As we have shown expression of functional markers, the integration of other cell types would thus represent a precondition to investigate the cell-cell interactions by functional studies and to build more relevant models. Also, perfusion of the channels would provide important external stimuli, well known for influencing cellular behavior and endothelium assembly. The development of a complex network with branched and interconnecting channels would also increase the applicability of the model and spontaneous angiogenesis should be considered for its formation from the main channel.

Further development of these research lines would have important implications in the domains of microfluidics, super-resolution

microscopy and vascularized tissue engineered models. The results presented here thus lay the foundations for the development of innovative tools and for the expansion of bioengineering technologies towards domains still scarcely investigated.

References

- [1] M. Kutz, *Biomedical Engineering Fundamentals*, Third Edition, (2021) 736.
<https://www.accessengineeringlibrary.com/content/book/9781260136265>.
- [2] D. Huh, G.A. Hamilton, D.E. Ingber, From 3D cell culture to organs-on-chips, *Trends Cell Biol.* 21 (2011) 745–754.
<https://doi.org/10.1016/j.tcb.2011.09.005>.
- [3] C. Jensen, Y. Teng, Is it time to start transitioning from 2D to 3D cell culture?, *Front. Mol. Biosci.* 7 (2020) 33.
<https://doi.org/10.3389/fmolb.2020.00033>.
- [4] W.B. Amos, J.G. White, M. Fordham, Use of confocal imaging in the study of biological structures, *Appl. Opt.* 26 (1987) 3239–3243.
- [5] L. Schermelleh, R. Heintzmann, H. Leonhardt, A guide to super-resolution fluorescence microscopy, *J. Cell Biol.* 190 (2010) 165–175.
<https://doi.org/10.1083/jcb.201002018>.
- [6] K. Duval, H. Grover, L.-H. Han, Y. Mou, A.F. Pegoraro, J. Fredberg, Z. Chen, Modeling physiological events in 2D vs. 3D cell culture, *Physiology.* 32 (2017) 266–277.
<https://doi.org/10.1152/physiol.00036.2016>.
- [7] Y. Wu, H. Shroff, Faster, sharper, and deeper: structured illumination microscopy for biological imaging, *Nat. Methods.* 15 (2018) 1011–1019.
<https://doi.org/10.1038/s41592-018-0211-z>.
- [8] R.M. Power, J. Huisken, A guide to light-sheet fluorescence microscopy for multiscale imaging, *Nat. Methods.* 14 (2017) 360–373.
<https://doi.org/10.1038/nmeth.4224>.
- [9] J.C. McDonald, G.M. Whitesides, Poly(dimethylsiloxane) as a material for fabricating microfluidic devices, *Acc. Chem. Res.* 35 (2002) 491–499.
<https://doi.org/10.1021/ar010110q>.
- [10] B. Sebastian, P.S. Dittich, Microfluidics to Mimic Blood Flow in Health and Disease, *Annu. Rev. Fluid Mech.* 50 (2018) 483–504.
<https://doi.org/10.1146/annurev-fluid-010816-060246>.
- [11] S. Chung, R. Sudo, V. Vickerman, I.K. Zervantonakis, R.D. Kamm, Microfluidic platforms for studies of angiogenesis, cell migration, and cell-cell interactions: Sixth international bio-fluid mechanics symposium and workshop March 28-30, 2008 Pasadena, California, in: *Ann. Biomed. Eng.*, Springer, 2010: pp. 1164–1177. <https://doi.org/10.1007/s10439-010-9899-3>.
- [12] D. Huh, B.D. Matthews, A. Mammoto, M. Montoya-Zavala, H.Y. Hsin, D.E. Ingber, Reconstituting organ-level lung functions on a chip, *Science*

- (80-.). 328 (2010) 1662–1668. <https://doi.org/10.1126/science.1188302>.
- [13] A. Dellaquila, E.K. Thomée, A.H. McMillan, S.C. Leshner-Pérez, Lung-on-a-chip platforms for modeling disease pathogenesis, in: *Organ-on-a-Chip Eng. Microenviron. Saf. Effic. Test.*, Elsevier, 2019: pp. 133–180. <https://doi.org/10.1016/B978-0-12-817202-5.00004-8>.
- [14] A. Williamson, S. Singh, U. Fernekorn, A. Schober, The future of the patient-specific Body-on-a-chip, *Lab Chip*. 13 (2013) 3471–3480. <https://doi.org/10.1039/c3lc50237f>.
- [15] B. Zhang, M. Radisic, Organ-on-A-chip devices advance to market, *Lab Chip*. 17 (2017) 2395–2420. <https://doi.org/10.1039/c6lc01554a>.
- [16] J.P. Vacanti, C.A. Vacanti, The History and Scope of Tissue Engineering, in: *Princ. Tissue Eng. Fourth Ed.*, Elsevier Inc., 2013: pp. 3–8. <https://doi.org/10.1016/B978-0-12-398358-9.00001-X>.
- [17] R. Lanza, R. Langer, J.P. Vacanti, *Principles of Tissue Engineering: Fourth Edition*, Elsevier Inc., 2013. <https://doi.org/10.1016/C2011-0-07193-4>.
- [18] R.S. Ambekar, B. Kandasubramanian, Progress in the Advancement of Porous Biopolymer Scaffold: Tissue Engineering Application, *Ind. Eng. Chem. Res.* 58 (2019) 6163–6194. <https://doi.org/10.1021/acs.iecr.8b05334>.
- [19] R. Ravichandran, S. Sundarajan, J.R. Venugopal, S. Mukherjee, S. Ramakrishna, *Advances in Polymeric Systems for Tissue Engineering and Biomedical Applications*, *Macromol. Biosci.* 12 (2012) 286–311. <https://doi.org/10.1002/mabi.201100325>.
- [20] D.C. Duffy, J.C. McDonald, O.J.A. Schueller, G.M. Whitesides, Rapid prototyping of microfluidic systems in poly(dimethylsiloxane), *Anal. Chem.* 70 (1998) 4974–4984. <https://doi.org/10.1021/ac980656z>.
- [21] S.B. Campbell, Q. Wu, J. Yazbeck, C. Liu, S. Okhovatian, M. Radisic, Beyond Polydimethylsiloxane: Alternative Materials for Fabrication of Organ-on-a-Chip Devices and Microphysiological Systems, *ACS Biomater. Sci. Eng.* (2020). <https://doi.org/10.1021/acsbiomaterials.0c00640>.
- [22] S. Jalili-Firoozinezhad, F.S. Gazzaniga, E.L. Calamari, D.M. Camacho, C.W. Fadel, A. Bein, B. Swenor, B. Nestor, M.J. Crouce, A. Tovaglieri, O. Levy, K.E. Gregory, D.T. Breault, J.M.S. Cabral, D.L. Kasper, R. Novak, D.E. Ingber, A complex human gut microbiome cultured in an anaerobic intestine-on-a-chip, *Nat. Biomed. Eng.* 3 (2019) 520–531. <https://doi.org/10.1038/s41551-019-0397-0>.
- [23] V. Mönkemöller, M. Schüttpelz, P. McCourt, K. Sørensen, B. Smedsrød, T. Huser, Imaging fenestrations in liver sinusoidal endothelial cells by optical localization microscopy, *Phys. Chem. Chem. Phys.* 16 (2014) 12576–12581. <https://doi.org/10.1039/c4cp01574f>.

References

- [24] V.C. Cogger, N.J. Hunt, D.G. Le Couteur, Fenestrations in the Liver Sinusoidal Endothelial Cell, in: *Liver*, Wiley, 2020: pp. 435–443. <https://doi.org/10.1002/9781119436812.ch35>.
- [25] E.C. Novosel, C. Kleinhaus, P.J. Kluger, Vascularization is the key challenge in tissue engineering, *Adv. Drug Deliv. Rev.* 63 (2011) 300–311. <https://doi.org/10.1016/j.addr.2011.03.004>.
- [26] J. Rouwkema, A. Khademhosseini, Vascularization and Angiogenesis in Tissue Engineering: Beyond Creating Static Networks, *Trends Biotechnol.* 34 (2016) 733–745. <https://doi.org/10.1016/j.tibtech.2016.03.002>.
- [27] J. Lachaux, C. Alcaine, B. Gómez-Escoda, C.M. Perrault, D.O. Duplan, P.Y.J. Wu, I. Ochoa, L. Fernandez, O. Mercier, D. Coudreuse, E. Roy, Thermoplastic elastomer with advanced hydrophilization and bonding performances for rapid (30 s) and easy molding of microfluidic devices, *Lab Chip.* 17 (2017) 2581–2594. <https://doi.org/10.1039/c7lc00488e>.
- [28] A.H. McMillan, E.K. Thomée, A. Dellaquila, H. Nassman, T. Segura, S.C. Leshner-Pérez, Rapid fabrication of membrane-integrated thermoplastic elastomer microfluidic devices, *Micromachines.* 11 (2020) 731. <https://doi.org/10.3390/M11080731>.
- [29] A. Autissier, C. Le Visage, C. Pouzet, F. Chaubet, D. Letourneur, Fabrication of porous polysaccharide-based scaffolds using a combined freeze-drying/cross-linking process, *Acta Biomater.* 6 (2010) 3640–3648. <https://doi.org/10.1016/j.actbio.2010.03.004>.
- [30] G.M. Whitesides, The origins and the future of microfluidics, *Nature.* 442 (2006) 368. <https://doi.org/10.1038/nature05058>.
- [31] K. Ohno, K. Tachikawa, A. Manz, Microfluidics: Applications for analytical purposes in chemistry and biochemistry, *Electrophoresis.* 29 (2008) 4443–4453. <https://doi.org/10.1002/elps.200800121>.
- [32] B. Xiong, K. Ren, Y. Shu, Y. Chen, B. Shen, H. Wu, Recent Developments in Microfluidics for Cell Studies, *Adv. Mater.* 26 (2014) 5525–5532. <https://doi.org/10.1002/adma.201305348>.
- [33] L. Shang, Y. Cheng, Y. Zhao, Emerging Droplet Microfluidics, *Chem. Rev.* 117 (2017) 7964–8040. <https://doi.org/10.1021/acs.chemrev.6b00848>.
- [34] G. Whitesides, Microfluidics in Late Adolescence, *ArXiv Prepr. ArXiv1802.05595.* (2018).
- [35] G.M. Whitesides, E. Ostuni, S. Takayama, X. Jiang, D.E. Ingber, Soft lithography in biology and biochemistry, *Annu. Rev. Biomed. Eng.* 3 (2001) 335–373. <https://doi.org/10.1146/annurev.bioeng.3.1.335>.
- [36] A. Bohr, S. Colombo, H. Jensen, Future of microfluidics in research and in the market, in: *Microfluid. Pharm. Appl. From Nano/Micro Syst. Fabr. to Control. Drug Deliv.*, Elsevier, 2018: pp. 425–465. <https://doi.org/10.1016/B978-0-12-812659-2.00016-8>.

- [37] C. Webb, N. Forbes, C.B. Roces, G. Anderluzzi, G. Lou, S. Abraham, L. Ingalls, K. Marshall, T.J. Leaver, J.A. Watts, J.W. Aylott, Y. Perrie, Using microfluidics for scalable manufacturing of nanomedicines from bench to GMP: A case study using protein-loaded liposomes, *Int. J. Pharm.* 582 (2020) 119266. <https://doi.org/10.1016/j.ijpharm.2020.119266>.
- [38] M.T. Guo, A. Rotem, J.A. Heyman, D.A. Weitz, Droplet microfluidics for high-throughput biological assays, *Lab Chip*. 12 (2012) 2146–2155. <https://doi.org/10.1039/c2lc21147e>.
- [39] O. Scheler, W. Postek, P. Garstecki, Recent developments of microfluidics as a tool for biotechnology and microbiology, *Curr. Opin. Biotechnol.* 55 (2019) 60–67. <https://doi.org/10.1016/j.copbio.2018.08.004>.
- [40] S. Vyawahare, A.D. Griffiths, C.A. Merten, Miniaturization and parallelization of biological and chemical assays in microfluidic devices, *Chem. Biol.* 17 (2010) 1052–1065. <https://doi.org/10.1016/j.chembiol.2010.09.007>.
- [41] J.R. Mejía-Salazar, K. Rodrigues Cruz, E.M. Materón Vásques, O. Novais de Oliveira Jr., Microfluidic Point-of-Care Devices: New Trends and Future Prospects for eHealth Diagnostics, *Sensors*. 20 (2020) 1951. <https://doi.org/10.3390/s20071951>.
- [42] P.S. Dittrich, A. Manz, Lab-on-a-chip: Microfluidics in drug discovery, *Nat. Rev. Drug Discov.* 5 (2006) 210–218. <https://doi.org/10.1038/nrd1985>.
- [43] C. Haber, Microfluidics in commercial applications; an industry perspective, *Lab Chip*. 6 (2006) 1118–1121. <https://doi.org/10.1039/b610250f>.
- [44] A.C. Fernandes, K. V. Gernaey, U. Krühne, “Connecting worlds – a view on microfluidics for a wider application,” *Biotechnol. Adv.* 36 (2018) 1341–1366. <https://doi.org/10.1016/j.biotechadv.2018.05.001>.
- [45] J. You, K. Kang, T. Tran, H. Park, W.R. Hwang, J. Kim, S. Im, PDMS-based turbulent microfluidic mixer, *Lab Chip*. 15 (2015). <https://doi.org/10.1039/c5lc00070j>.
- [46] G. Whitesides, A.D. Stroock, Flexible methods for microfluidics, *Phys. Today*. (2001) 42–48. <https://datascience.iq.harvard.edu/files/gmwgroup/files/764.pdf> (accessed May 3, 2021).
- [47] R.M. Nerem, R.W. Alexander, D.C. Chappell, R.M. Medford, S.E. Varner, W. Robert Taylor, The Study of the Influence of Flow on Vascular Endothelial Biology, *Am. J. Med. Sci.* 316 (1998) 169–175. [https://doi.org/10.1016/s0002-9629\(15\)40397-0](https://doi.org/10.1016/s0002-9629(15)40397-0).
- [48] D. Irimia, D.A. Geba, M. Toner, Universal microfluidic gradient generator, *Anal. Chem.* 78 (2006) 3472–3477. <https://doi.org/10.1021/ac0518710>.

References

- [49] S. Lee, J. Ko, D. Park, S.R. Lee, M. Chung, Y. Lee, N.L. Jeon, Microfluidic-based vascularized microphysiological systems, *Lab Chip*. 18 (2018) 2686–2709. <https://doi.org/10.1039/c8lc00285a>.
- [50] Q. Smith, S. Gerecht, Going with the flow: Microfluidic platforms in vascular tissue engineering, *Curr. Opin. Chem. Eng.* 3 (2014) 42–50. <https://doi.org/10.1016/j.coche.2013.11.001>.
- [51] H.E. Abaci, R. Devendra, R. Soman, G. Drazer, S. Gerecht, Microbioreactors to manipulate oxygen tension and shear stress in the microenvironment of vascular stem and progenitor cells, *Biotechnol. Appl. Biochem.* 59 (2012) 97–105. <https://doi.org/10.1002/bab.1010>.
- [52] L. Yi, J.M. Lin, Development and Applications of Microfluidic Devices for Cell Culture in Cell Biology, *Mol. Biol.* s1 (2016). <https://doi.org/10.4172/2168-9547.1000182>.
- [53] H. Chen, Z. Yu, S. Bai, H. Lu, D. Xu, C. Chen, D. Liu, Y. Zhu, Microfluidic models of physiological or pathological flow shear stress for cell biology, disease modeling and drug development, *TrAC - Trends Anal. Chem.* 117 (2019) 186–199. <https://doi.org/10.1016/j.trac.2019.06.023>.
- [54] M.M. Islam, S. Beverung, R. Steward Jr., Bio-Inspired Microdevices that Mimic the Human Vasculature, *Micromachines*. 8 (2017) 299. <https://doi.org/10.3390/mi8100299>.
- [55] D. Gao, H. Liu, Y. Jiang, J.M. Lin, D. Gao, H. Liu, Y. Jiang, Recent developments in microfluidic devices for in vitro cell culture for cell-biology research, *TrAC - Trends Anal. Chem.* 35 (2012) 150–164. <https://doi.org/10.1016/j.trac.2012.02.008>.
- [56] K. Ronaldson-Bouchard, G. Vunjak-Novakovic, Organs-on-a-Chip: A Fast Track for Engineered Human Tissues in Drug Development, *Cell Stem Cell*. 22 (2018) 310–324. <https://doi.org/10.1016/j.stem.2018.02.011>.
- [57] A.K.H. Achyuta, A.J. Conway, R.B. Crouse, E.C. Bannister, R.N. Lee, C.P. Katnik, A.A. Behensky, J. Cuevas, S.S. Sundaram, A modular approach to create a neurovascular unit-on-a-chip, *Lab Chip*. 13 (2013) 542–553. <https://doi.org/10.1039/c2lc41033h>.
- [58] K. Rennert, S. Steinborn, M. Gröger, B. Ungerböck, A.M. Jank, J. Ehgartner, S. Nietzsche, J. Dinger, M. Kiehntopf, H. Funke, F.T. Peters, A. Lupp, C. Gärtner, T. Mayr, M. Bauer, O. Huber, A.S. Mosig, A microfluidically perfused three dimensional human liver model, *Biomaterials*. 71 (2015) 119–131. <https://doi.org/10.1016/j.biomaterials.2015.08.043>.
- [59] K.-J. Jang, A.P. Mehr, G.A. Hamilton, L.A. McPartlin, S. Chung, K.-Y. Suh, D.E. Ingber, Human kidney proximal tubule-on-a-chip for drug transport and nephrotoxicity assessment, *Integr. Biol.* 5 (2013) 1119–1129. <https://doi.org/10.1039/c3ib40049b>.

- [60] H.J. Kim, D.E. Ingber, Gut-on-a-Chip microenvironment induces human intestinal cells to undergo villus differentiation, *Integr. Biol.* 5 (2013) 1130. <https://doi.org/10.1039/c3ib40126j>.
- [61] S.N. Bhatia, D.E. Ingber, Microfluidic organs-on-chips, *Nat. Biotechnol.* 32 (2014) 760–772. <https://doi.org/10.1038/nbt.2989>.
- [62] E.W. Esch, A. Bahinski, D. Huh, Organs-on-chips at the frontiers of drug discovery, *Nat. Rev. Drug Discov.* 14 (2015) 248. <https://doi.org/doi.org/10.1038/nrd4539>.
- [63] C. Moraes, J.M. Labuz, B.M. Leung, M. Inoue, T.-H. Chun, S. Takayama, On being the right size: scaling effects in designing a human-on-a-chip, *Integr. Biol.* 5 (2013) 1149–1161. <https://doi.org/10.1039/c3ib40040a>.
- [64] J.M. Wilkinson, Need for alternative testing methods and opportunities for organ-on-a-chip systems, in: *Organ-on-a-Chip*, Elsevier, 2020: pp. 1–11. <https://doi.org/10.1016/b978-0-12-817202-5.00001-2>.
- [65] J. Castillo-León, Microfluidics and lab-on-a-chip devices: history and challenges, in: *Lab-on-a-Chip Devices Micro-Total Anal. Syst.*, Springer, 2015: pp. 1–15.
- [66] J.M. Heather, B. Chain, The sequence of sequencers: the history of sequencing DNA, *Genomics.* 107 (2016) 1–8. <https://doi.org/10.1016/j.ygeno.2015.11.003>.
- [67] P. Camilleri, *Capillary electrophoresis: theory and practice*, CRC press, 1997.
- [68] H. Choi, C.C.M. Mody, The long history of molecular electronics: Microelectronics origins of nanotechnology, *Soc. Stud. Sci.* 39 (2009) 11–50. <https://doi.org/doi.org/10.1177/0306312708097288>.
- [69] Y. Xia, G.M. Whitesides, Soft lithography, *Angew Chemie Int. Ed.* 37 (1998) 550–575. [https://doi.org/10.1002/\(SICI\)1521-3773\(19980316\)37:5<550::AID-ANIE550>3.0.CO;2-G](https://doi.org/10.1002/(SICI)1521-3773(19980316)37:5<550::AID-ANIE550>3.0.CO;2-G).
- [70] S. C. Terry, H. Jerman, J. B. Angell, A Gas Chromatograph Air Analyzer Fabricated on a Silicon Wafer, *Electron Devices*, *IEEE Trans.* 26 (1980) 1880–1886. <https://doi.org/10.1109/T-ED.1979.19791>.
- [71] A. Manz, N. Graber, H. Widmer, Miniaturized total chemical analysis systems: a novel concept for chemical sensing, *Sensors Actuators B Chem.* 1 (1990) 244–248. [https://doi.org/10.1016/0925-4005\(90\)80209-I](https://doi.org/10.1016/0925-4005(90)80209-I).
- [72] D.J. Harrison, K. Fluri, K. Seiler, Z. Fan, C.S. Effenhauser, A. Manz, Micromachining a miniaturized capillary electrophoresis-based chemical analysis system on a chip, *Science* (80-.). 261 (1993) 895–897. <https://doi.org/10.1126/science.261.5123.895>.
- [73] S.C. Terry, J.H. Jerman, J.B. Angell, A gas chromatographic air analyzer fabricated on a silicon wafer, *IEEE Trans. Electron Devices.* 26 (1979)

References

- 1880–1886. <https://doi.org/10.1109/T-ED.1979.19791>.
- [74] K. Ronaldson-Bouchard, G. Vunjak-Novakovic, Organs-on-a-Chip: A Fast Track for Engineered Human Tissues in Drug Development, *Cell Stem Cell*. 22 (2018) 310–324. <https://doi.org/10.1016/j.stem.2018.02.011>.
- [75] A. Mata, A.J. Fleischman, S. Roy, Characterization of Polydimethylsiloxane (PDMS) Properties for Biomedical Micro/Nanosystems, *Biomed. Microdevices*. 7 (2005) 281–293. <https://doi.org/10.1007/s10544-005-6070-2>.
- [76] S. Deguchi, J. Hotta, S. Yokoyama, T.S. Matsui, Viscoelastic and optical properties of four different PDMS polymers, *J. Micromechanics Microengineering*. 25 (2015) 097002. <https://doi.org/10.1088/0960-1317/25/9/097002>.
- [77] I.D. Johnston, D.K. McCluskey, C.K.L. Tan, M.C. Tracey, Mechanical characterization of bulk Sylgard 184 for microfluidics and microengineering, *J. Micromechanics Microengineering*. 24 (2014) 035017. <https://doi.org/10.1088/0960-1317/24/3/035017>.
- [78] M.W. Toepke, D.J. Beebe, PDMS absorption of small molecules and consequences in microfluidic applications, *Lab Chip*. 6 (2006) 1484–1486. <https://doi.org/10.1039/b612140c>.
- [79] X. Su, E.W.K. Young, H.A.S. Underkofler, T.J. Kamp, C.T. January, D.J. Beebe, Microfluidic cell culture and its application in high-throughput drug screening: Cardiotoxicity assay for hERG channels, *J. Biomol. Screen*. 16 (2011) 101–111. <https://doi.org/10.1177/1087057110386218>.
- [80] K.J. Regehr, M. Domenech, J.T. Koepsel, K.C. Carver, S.J. Ellison-Zelski, W.L. Murphy, L.A. Schuler, E.T. Alarid, D.J. Beebe, Biological implications of polydimethylsiloxane-based microfluidic cell culture, *Lab Chip*. 9 (2009) 2132–2139. <https://doi.org/10.1039/b903043c>.
- [81] D.T. Eddington, J.P. Puccinelli, D.J. Beebe, Thermal aging and reduced hydrophobic recovery of polydimethylsiloxane, *Sensors Actuators B*. 114 (2006) 170–172. <https://doi.org/10.1016/j.snb.2005.04.037>.
- [82] R. Mukhopadhyay, When PDMS isn't the best, *Anal. Chem.* (2007) 3248–3253. <https://doi.org/10.1021/ac071903e>.
- [83] A.K. Capulli, K. Tian, N. Mehandru, A. Bukhta, S.F. Choudhury, M. Suchyta, K.K. Parker, Approaching the in vitro clinical trial: Engineering organs on chips, *Lab Chip*. 14 (2014) 3181–3186. <https://doi.org/10.1039/c4lc00276h>.
- [84] C. Ding, X. Chen, Q. Kang, X. Yan, Biomedical Application of Functional Materials in Organ-on-a-Chip, *Front. Bioeng. Biotechnol.* 8 (2020) 823. <https://doi.org/10.3389/fbioe.2020.00823>.
- [85] G. Sriram, M. Alberti, Y. Dancik, B. Wu, R. Wu, Z. Feng, S. Ramasamy, P.L. Bigliardi, M. Bigliardi-Qi, Z. Wang, Full-thickness human skin-on-

- chip with enhanced epidermal morphogenesis and barrier function, *Mater. Today*. 21 (2018) 326–340. <https://doi.org/10.1016/j.mattod.2017.11.002>.
- [86] M. Humayun, C.W. Chow, E.W.K. Young, Microfluidic lung airway-on-a-chip with arrayable suspended gels for studying epithelial and smooth muscle cell interactions, *Lab Chip*. 18 (2018) 1298–1309. <https://doi.org/10.1039/c7lc01357d>.
- [87] P. Shah, J. V. Fritz, E. Glaab, M.S. Desai, K. Greenhalgh, A. Frchet, M. Niegowska, M. Estes, C. Jäger, C. Seguin-Devaux, F. Zenhausem, P. Wilmes, A microfluidics-based in vitro model of the gastrointestinal human-microbe interface, *Nat. Commun.* 7 (2016) 1–15. <https://doi.org/10.1038/ncomms11535>.
- [88] P.M. Van Midwoud, A. Janse, M.T. Merema, G.M.M. Groothuis, E. Verpoorte, Comparison of biocompatibility and adsorption properties of different plastics for advanced microfluidic cell and tissue culture models, *Anal. Chem.* 84 (2012) 3938–3944. <https://doi.org/10.1021/ac300771z>.
- [89] B. Zhang, B. Fook, L. Lai, R. Xie, L. Davenport Huyer, M. Montgomery, M. Radisic, Microfabrication of AngioChip, a biodegradable polymer scaffold with microfluidic vasculature Microengineered biomimetic systems for organ-on-a, *Nat. Pr.* 13 (2018) 1793–1813. <https://doi.org/10.1038/s41596-018-0015-8>.
- [90] B. Zhang, M. Montgomery, M.D. Chamberlain, S. Ogawa, A. Korolj, A. Pahnke, L.A. Wells, S. Masse, J. Kim, L. Reis, A. Momen, S.S. Nunes, A.R. Wheeler, K. Nanthakumar, G. Keller, M. V. Sefton, M. Radisic, Biodegradable scaffold with built-in vasculature for organ-on-a-chip engineering and direct surgical anastomosis, *Nat. Mater.* 15 (2016) 669–678. <https://doi.org/10.1038/nmat4570>.
- [91] S. Massa, M.A. Sakr, J. Seo, P. Bandaru, A. Arneri, S. Bersini, E. Zare-Eelanjegh, E. Jalilian, B.H. Cha, S. Antona, A. Enrico, Y. Gao, S. Hassan, J.P. Acevedo, M.R. Dokmeci, Y.S. Zhang, A. Khademhosseini, S.R. Shin, Bioprinted 3D vascularized tissue model for drug toxicity analysis, *Biomicrofluidics*. 11 (2017) 044109. <https://doi.org/10.1063/1.4994708>.
- [92] Y.S. Zhang, A. Arneri, S. Bersini, S.R. Shin, K. Zhu, Z. Goli-Malekabadi, J. Aleman, C. Colosi, F. Busignani, V. Dell’Erba, C. Bishop, T. Shupe, D. Demarchi, M. Moretti, M. Rasponi, M.R. Dokmeci, A. Atala, A. Khademhosseini, Bioprinting 3D microfibrinous scaffolds for engineering endothelialized myocardium and heart-on-a-chip, *Biomaterials*. 110 (2016) 45–59. <https://doi.org/10.1016/j.biomaterials.2016.09.003>.
- [93] M.P. Cuchiara, A.C.B. Allen, T.M. Chen, J.S. Miller, J.L. West, Multilayer microfluidic PEGDA hydrogels, *Biomaterials*. 31 (2010) 5491–5497. <https://doi.org/10.1016/j.biomaterials.2010.03.031>.
- [94] K.A. Homan, D.B. Kolesky, M.A. Skylar-Scott, J. Herrmann, H. Obuobi, A. Moisan, J.A. Lewis, Bioprinting of 3D Convulated Renal Proximal

References

- Tubules on Perfusable Chips, *Sci. Rep.* 6 (2016) 1–13. <https://doi.org/10.1038/srep34845>.
- [95] N. Jusoh, S. Oh, S. Kim, J. Kim, N.L. Jeon, Microfluidic vascularized bone tissue model with hydroxyapatite-incorporated extracellular matrix, *Lab Chip.* 15 (2015) 3984–3988. <https://doi.org/10.1039/c5lc00698h>.
- [96] H.E. Abaci, Z. Guo, A. Coffman, B. Gillette, W.H. Lee, S.K. Sia, A.M. Christiano, Human Skin Constructs with Spatially Controlled Vasculature Using Primary and iPSC-Derived Endothelial Cells, *Adv. Healthc. Mater.* 5 (2016) 1800–1807. <https://doi.org/10.1002/adhm.201500936>.
- [97] N. Mori, Y. Akagi, Y. Imai, Y. Takayama, Y.S. Kida, Fabrication of Perfusable Vascular Channels and Capillaries in 3D Liver-like Tissue, *Sci. Rep.* 10 (2020) 5646. <https://doi.org/10.1038/s41598-020-62286-3>.
- [98] J.Y. Park, H. Ryu, B. Lee, D.H. Ha, M. Ahn, S. Kim, J.Y. Kim, N.L. Jeon, D.W. Cho, Development of a functional airway-on-a-chip by 3D cell printing, *Biofabrication.* 11 (2019) 015002. <https://doi.org/10.1088/1758-5090/aae545>.
- [99] G.Y. Huang, L.H. Zhou, Q.C. Zhang, Y.M. Chen, W. Sun, F. Xu, T.J. Lu, Microfluidic hydrogels for tissue engineering, *Biofabrication.* 3 (2011). <https://doi.org/10.1088/1758-5082/3/1/012001>.
- [100] A.P. Sudarsan, J. Wang, V.M. Ugaz, Thermoplastic elastomer gels: An advanced substrate for microfluidic chemical analysis systems, *Anal. Chem.* 77 (2005) 5167–5173. <https://doi.org/10.1021/ac050448o>.
- [101] E. Roy, M. Geissler, J.-C. Galas, T. Veres, Prototyping of microfluidic systems using a commercial thermoplastic elastomer, (n.d.). <https://doi.org/10.1007/s10404-011-0789-2>.
- [102] M.D. Guillemette, E. Roy, F.A. Auger, T. Veres, Rapid isothermal substrate microfabrication of a biocompatible thermoplastic elastomer for cellular contact guidance, *Acta Biomater.* 7 (2011) 2492–2498. <https://doi.org/10.1016/j.actbio.2011.02.019>.
- [103] E. Roy, G. Stewart, M. Mounier, L. Malic, R. Peytavi, L. Clime, M. Madou, M. Bossinot, M.G. Bergeron, T. Veres, From cellular lysis to microarray detection, an integrated thermoplastic elastomer (TPE) point of care Lab on a Disc, *Lab Chip.* 15 (2015) 406–416. <https://doi.org/10.1039/c4lc00947a>.
- [104] K. Domansky, J.D. Sliz, N. Wen, C. Hinojosa, G. Thompson, J.P. Fraser, T. Hamkins-Indik, G.A. Hamilton, D. Levner, D.E. Ingber, SEBS elastomers for fabrication of microfluidic devices with reduced drug absorption by injection molding and extrusion, *Microfluid. Nanofluidics.* 21 (2017) 1–12. <https://doi.org/10.1007/s10404-017-1941-4>.
- [105] M.D. Borysiak, K.S. Bielawski, N.J. Sniadecki, C.F. Jenkel, B.D. Vogt, J.D. Posner, Simple replica micromolding of biocompatible styrenic

- elastomers, *Lab Chip*. 13 (2013) 2773–2784.
<https://doi.org/10.1039/c3lc50426c>.
- [106] S. Boyden, The chemotactic effect of mixtures of antibody and antigen on polymorphonuclear leucocytes., *J. Exp. Med.* 115 (1962) 453–466.
<https://doi.org/10.1084/jem.115.3.453>.
- [107] H. Lin, H. Li, H.J. Cho, S. Bian, H.J. Roh, M.K. Lee, S.K. Jung, S.J. Chung, C.K. Shim, D.D. Kim, Air-Liquid Interface (ALI) culture of human bronchial epithelial cell monolayers as an in vitro model for airway drug transport studies, *J. Pharm. Sci.* 96 (2007) 341–350.
<https://doi.org/10.1002/jps.20803>.
- [108] S.D. Sheridan, S. Gil, M. Wilgo, A. Pitt, Microporous Membrane Growth Substrates for Embryonic Stem Cell Culture and Differentiation, *Methods Cell Biol.* 86 (2008) 29–57. [https://doi.org/10.1016/S0091-679X\(08\)00003-4](https://doi.org/10.1016/S0091-679X(08)00003-4).
- [109] L.J. Chen, S. Ito, H. Kai, K. Nagamine, N. Nagai, M. Nishizawa, T. Abe, H. Kaji, Microfluidic co-cultures of retinal pigment epithelial cells and vascular endothelial cells to investigate choroidal angiogenesis, *Sci. Rep.* 7 (2017) 1–9. <https://doi.org/10.1038/s41598-017-03788-5>.
- [110] O.Y.F. Henry, R. Villenave, M.J. Crounce, W.D. Leineweber, M.A. Benz, D.E. Ingber, Organs-on-chips with integrated electrodes for trans-epithelial electrical resistance (TEER) measurements of human epithelial barrier function, *Lab Chip*. 17 (2017) 2264–2271.
<https://doi.org/10.1039/c7lc00155j>.
- [111] J.W. Song, S.P. Cavnar, A.C. Walker, K.E. Luker, M. Gupta, Y.-C. Tung, G.D. Luker, S. Takayama, Microfluidic Endothelium for Studying the Intravascular Adhesion of Metastatic Breast Cancer Cells, *PLoS One*. 4 (2009) e5756. <https://doi.org/10.1371/journal.pone.0005756>.
- [112] H. Le-The, M. Tibbe, J. Loessberg-Zahl, M. Palma Do Carmo, M. Van Der Helm, J. Bomer, A. Van Den Berg, A. Leferink, L. Segerink, J. Eijkkel, Large-scale fabrication of free-standing and sub- μm PDMS through-hole membranes, *Nanoscale*. 10 (2018) 7711–7718.
<https://doi.org/10.1039/c7nr09658e>.
- [113] W.F. Quirós-Solano, N. Gaio, O.M.J.A. Stassen, Y.B. Arik, C. Silvestri, N.C.A. Van Engeland, A. Van der Meer, R. Passier, C.M. Sahlgren, C.V.C. Bouten, A. van den Berg, R. Dekker, P.M. Sarro, Microfabricated tuneable and transferable porous PDMS membranes for Organs-on-Chips, *Sci. Rep.* 8 (2018) 1–11. <https://doi.org/10.1038/s41598-018-31912-6>.
- [114] D. Huh, H.J. Kim, J.P. Fraser, D.E. Shea, M. Khan, A. Bahinski, G.A. Hamilton, D.E. Ingber, Microfabrication of human organs-on-chips, *Nat. Protoc.* 8 (2013) 2135–2157. <https://doi.org/10.1038/nprot.2013.137>.
- [115] X. Fan, C. Jia, J. Yang, G. Li, H. Mao, Q. Jin, J. Zhao, A microfluidic chip integrated with a high-density PDMS-based microfiltration membrane for

References

- rapid isolation and detection of circulating tumor cells, *Biosens. Bioelectron.* 71 (2015) 380–386.
<https://doi.org/10.1016/j.bios.2015.04.080>.
- [116] H.H. Chung, M. Mireles, B.J. Kwarta, T.R. Gaborski, Use of porous membranes in tissue barrier and co-culture models, *Lab Chip.* 18 (2018) 1671–1689. <https://doi.org/10.1039/c7lc01248a>.
- [117] P. Apel, Track etching technique in membrane technology, in: *Radiat. Meas.*, Pergamon, 2001: pp. 559–566. [https://doi.org/10.1016/S1350-4487\(01\)00228-1](https://doi.org/10.1016/S1350-4487(01)00228-1).
- [118] Y.I. Wang, H.E. Abaci, M.L. Shuler, Microfluidic blood–brain barrier model provides in vivo-like barrier properties for drug permeability screening, *Biotechnol. Bioeng.* 114 (2017) 184–194.
<https://doi.org/10.1002/bit.26045>.
- [119] H. Becker, C. Gärtner, Polymer microfabrication technologies for microfluidic systems, *Anal. Bioanal. Chem.* 390 (2008) 89–111.
<https://doi.org/10.1007/s00216-007-1692-2>.
- [120] E. Roy, A. Pallandre, B. Zribi, M.-C. Horny, F.D. Delapierre, A. Cattoni, J. Gamby, A.-M. Haghiri-Gosnet, Overview of Materials for Microfluidic Applications, in: X.-Y. Yu (Ed.), *Adv. Microfluid. New Appl. Biology, Energy Mater. Sci.*, IntechOpen, 2016: pp. 335–356.
- [121] R. Booth, H. Kim, Characterization of a microfluidic in vitro model of the blood-brain barrier (μ BBB), *Lab Chip.* 12 (2012) 1784–1792.
<https://doi.org/10.1039/C2LC40094D>.
- [122] D. Gao, H. Liu, J.M. Lin, Y. Wang, Y. Jiang, Characterization of drug permeability in Caco-2 monolayers by mass spectrometry on a membrane-based microfluidic device, *Lab Chip.* 13 (2013) 978–985.
<https://doi.org/10.1039/c2lc41215b>.
- [123] A.O. Stucki, J.D. Stucki, S.R.R. Hall, M. Felder, Y. Mermoud, R.A. Schmid, T. Geiser, O.T. Guenat, A lung-on-a-chip array with an integrated bio-inspired respiration mechanism, *Lab Chip.* 15 (2015) 1302–1310.
<https://doi.org/10.1039/c4lc01252f>.
- [124] H.J. Kim, D. Huh, G. Hamilton, D.E. Ingber, Human gut-on-a-chip inhabited by microbial flora that experiences intestinal peristalsis-like motions and flow, *Lab Chip.* 12 (2012) 2165–2174.
<https://doi.org/10.1039/c2lc40074j>.
- [125] M.Y. Kim, D.J. Li, L.K. Pham, B.G. Wong, E.E. Hui, Microfabrication of high-resolution porous membranes for cell culture, *J. Memb. Sci.* 452 (2014) 460–469. <https://doi.org/10.1016/j.memsci.2013.11.034>.
- [126] S.H. Ma, L.A. Lepak, R.J. Hussain, W. Shain, M.L. Shuler, An endothelial and astrocyte co-culture model of the blood-brain barrier utilizing an ultra-thin, nanofabricated silicon nitride membrane, *Lab Chip.* 5 (2005) 74–85.

<https://doi.org/10.1039/b405713a>.

- [127] M. Mireles, T.R. Gaborski, Fabrication techniques enabling ultrathin nanostructured membranes for separations, *Electrophoresis*. 38 (2017) 2374–2388. <https://doi.org/10.1002/elps.201700114>.
- [128] Y. Temiz, R.D. Lovchik, G. V. Kaigala, E. Delamarche, Lab-on-a-chip devices: How to close and plug the lab?, *Microelectron. Eng.* 132 (2015) 156–175. <https://doi.org/10.1016/j.mee.2014.10.013>.
- [129] B.H. Chueh, D. Huh, C.R. Kyrtos, T. Houssin, N. Futai, S. Takayama, Leakage-free bonding of porous membranes into layered microfluidic array systems, *Anal. Chem.* 79 (2007) 3504–3508. <https://doi.org/10.1021/ac062118p>.
- [130] L.S. Shiroma, M.H.O. Piazzetta, G.F. Duarte-Junior, W.K.T. Coltro, E. Carrilho, A.L. Gobbi, R.S. Lima, Self-regenerating and hybrid irreversible/reversible PDMS microfluidic devices, *Sci. Rep.* 6 (2016) 1–12. <https://doi.org/10.1038/srep26032>.
- [131] M. Serra, I. Pereiro, A. Yamada, J.L. Viovy, S. Descroix, D. Ferraro, A simple and low-cost chip bonding solution for high pressure, high temperature and biological applications, *Lab Chip*. 17 (2017) 629–634. <https://doi.org/10.1039/c6lc01319h>.
- [132] U. Abidin, N.A.S.M. Daud, V. Le Brun, Replication and leakage test of polydimethylsiloxane (PDMS) microfluidics channel, in: *AIP Conf. Proc.*, American Institute of Physics Inc., 2019: p. 020064. <https://doi.org/10.1063/1.5086611>.
- [133] S. Bhattacharya, A. Datta, J.M. Berg, S. Gangopadhyay, Studies on surface wettability of poly(dimethyl) siloxane (PDMS) and glass under oxygen-plasma treatment and correlation with bond strength, *J. Microelectromechanical Syst.* 14 (2005) 590–597. <https://doi.org/10.1109/JMEMS.2005.844746>.
- [134] M.A. Eddings, M.A. Johnson, B.K. Gale, Determining the optimal PDMS-PDMS bonding technique for microfluidic devices, *J. Micromechanics Microengineering*. 18 (2008) 067001. <https://doi.org/10.1088/0960-1317/18/6/067001>.
- [135] J.C. McDonald, D.C. Duffy, J.R. Anderson, D.T. Chiu, H. Wu, O.J.A. Schueller, G.M. Whitesides, Fabrication of microfluidic systems in poly (dimethylsiloxane), *Electrophor. An Int. J.* 21 (2000) 27–40. [https://doi.org/10.1002/\(SICI\)1522-2683\(20000101\)21:1<27::AID-ELPS27>3.0.CO;2-C](https://doi.org/10.1002/(SICI)1522-2683(20000101)21:1<27::AID-ELPS27>3.0.CO;2-C).
- [136] K. Aran, L.A. Sasso, N. Kamdar, J.D. Zahn, Irreversible, direct bonding of nanoporous polymer membranes to PDMS or glass microdevices, *Lab Chip*. 10 (2010) 548–552. <https://doi.org/10.1039/b924816a>.
- [137] J. El-Ali, P.K. Sorger, K.F. Jensen, Cells on chips, *Nature*. 442 (2006)

References

- 403–411. <https://doi.org/10.1038/nature05063>.
- [138] H. Rashidi, S. Alhaque, D. Szkolnicka, O. Flint, D.C. Hay, Fluid shear stress modulation of hepatocyte-like cell function, *Arch. Toxicol.* 90 (2016) 1757–1761. <https://doi.org/10.1007/s00204-016-1689-8>.
- [139] R.S. Reneman, T. Arts, A.P.G. Hoeks, Wall Shear Stress – an Important Determinant of Endothelial Cell Function and Structure – in the Arterial System in vivo, *J. Vasc. Res.* 43 (2006) 251–269. <https://doi.org/10.1159/000091648>.
- [140] D. Huh, H. Fujioka, Y.C. Tung, N. Futai, R. Paine, J.B. Grotberg, S. Takayama, Acoustically detectable cellular-level lung injury induced by fluid mechanical stresses in microfluidic airway systems, *Proc. Natl. Acad. Sci. U. S. A.* 104 (2007) 18886–18891. <https://doi.org/10.1073/pnas.0610868104>.
- [141] L. Kim, M.D. Vahey, H.Y. Lee, J. Voldman, Microfluidic arrays for logarithmically perfused embryonic stem cell culture, *Lab Chip.* 6 (2006) 394–406. <https://doi.org/10.1039/b511718f>.
- [142] L. Kim, Y.C. Toh, J. Voldman, H. Yu, A practical guide to microfluidic perfusion culture of adherent mammalian cells, *Lab Chip.* 7 (2007) 681–694. <https://doi.org/10.1039/b704602b>.
- [143] J. Lachaux, H. Salmon, F. Loisel, N. Arouche, I. Ochoa, L.L. Fernandez, G. Uzan, O. Mercier, T. Veres, E. Roy, Soft Thermoplastic Elastomer for Easy and Rapid Spin-Coating Fabrication of Microfluidic Devices with High Hydrophilization and Bonding Performances, *Adv. Mater. Technol.* 4 (2019) 1800308. <https://doi.org/10.1002/admt.201800308>.
- [144] H. Odani, K. Taira, N. Nemoto, M. Kurata, Diffusion and solution of gases and vapors in styrene-butadiene block copolymers, *Polym. Eng. Sci.* 17 (1977) 527–534. <https://doi.org/10.1002/pen.760170808>.
- [145] A. Senuma, Gas permeability coefficients of ethylene-vinyl acetate copolymer-modified poly(dimethylsiloxane) membranes. Double-column approach for two-phase materials, *Macromol. Chem. Phys.* 201 (2000) 568–576. [https://doi.org/10.1002/\(SICI\)1521-3935\(20000301\)201:5<568::AID-MACP568>3.0.CO;2-J](https://doi.org/10.1002/(SICI)1521-3935(20000301)201:5<568::AID-MACP568>3.0.CO;2-J).
- [146] A. Cochrane, H.J. Albers, R. Passier, C.L. Mummery, A. van den Berg, V. V. Orlova, A.D. van der Meer, Advanced in vitro models of vascular biology: Human induced pluripotent stem cells and organ-on-chip technology, *Adv. Drug Deliv. Rev.* 140 (2019) 68–77. <https://doi.org/10.1016/j.addr.2018.06.007>.
- [147] S.J. Sahl, S.W. Hell, S. Jakobs, Fluorescence nanoscopy in cell biology, *Nat. Rev. Mol. Cell Biol.* 18 (2017) 685. <https://doi.org/10.1038/nrm.2017.71>.
- [148] S. Cox, Super-resolution imaging in live cells, *Dev. Biol.* 401 (2015) 175–

181. <https://doi.org/10.1016/j.ydbio.2014.11.025>.
- [149] S.W. Hell, S.J. Sahl, M. Bates, X. Zhuang, R. Heintzmann, M.J. Booth, J. Bewersdorf, G. Shtengel, H. Hess, P. Tinnefeld, A. Honigmann, S. Jakobs, I. Testa, L. Cognet, B. Lounis, H. Ewers, S.J. Davis, C. Eggeling, D. Klenerman, K.I. Willig, G. Vicidomini, M. Castello, A. Diaspro, T. Cordes, The 2015 super-resolution microscopy roadmap, *J. Phys. D. Appl. Phys.* 48 (2015) 443001. <https://doi.org/10.1088/0022-3727/48/44/443001>.
- [150] A.J. Koster, J. Klumperman, Electron microscopy in cell biology: integrating structure and function, *Nat. Rev. Mol. Cell Biol.* 4 (2003) SS6–SS9.
- [151] P.C. Montgomery, A. Leong-Hoi, Emerging optical nanoscopy techniques, *Nanotechnol. Sci. Appl.* 8 (2015) 31–44. <https://doi.org/10.2147/NSA.S50042>.
- [152] L. Schermelleh, A. Ferrand, T. Huser, C. Eggeling, M. Sauer, O. Biehlmaier, G.P.C. Drummen, Super-resolution microscopy demystified, *Nat. Cell Biol.* 21 (2019) 72–84. <https://doi.org/10.1038/s41556-018-0251-8>.
- [153] S.W. Hell, Toward fluorescence nanoscopy, *Nat. Biotechnol.* 21 (2003) 1347–1355. <https://doi.org/10.1038/nbt895>.
- [154] A.M. Sydor, K.J. Czymmek, E.M. Puchner, V. Mennella, Super-Resolution Microscopy: From Single Molecules to Supramolecular Assemblies, *Trends Cell Biol.* 25 (2015) 730–748. <https://doi.org/10.1016/j.tcb.2015.10.004>.
- [155] D. Maschi, V.A. Klyachko, A nanoscale resolution view on synaptic vesicle dynamics, *Synapse.* 69 (2015) 256–267. <https://doi.org/10.1002/syn.21795>.
- [156] S. Jakobs, T. Stephan, P. Ilgen, C. Brüser, Light Microscopy of Mitochondria at the Nanoscale, *Annu. Rev. Biophys.* 49 (2020) 289–308. <https://doi.org/10.1146/annurev-biophys-121219-081550>.
- [157] S.H. Shim, C. Xia, G. Zhong, H.P. Babcock, J.C. Vaughan, B. Huang, X. Wang, C. Xu, G.Q. Bi, X. Zhuang, Super-resolution fluorescence imaging of organelles in live cells with photoswitchable membrane probes, *Proc. Natl. Acad. Sci. U. S. A.* 109 (2012) 13978–13983. <https://doi.org/10.1073/pnas.1201882109>.
- [158] B. Huang, H. Babcock, X. Zhuang, Breaking the diffraction barrier: Super-resolution imaging of cells, *Cell.* 143 (2010) 1047–1058. <https://doi.org/10.1016/j.cell.2010.12.002>.
- [159] C. Li, C. Kuang, X. Liu, Prospects for Fluorescence Nanoscopy, *ACS Nano.* 12 (2018) 4081–4085. <https://doi.org/10.1021/acsnano.8b02142>.
- [160] B.C. Chen, W.R. Legant, K. Wang, L. Shao, D.E. Milkie, M.W. Davidson, C. Janetopoulos, X.S. Wu, J.A. Hammer, Z. Liu, B.P. English, Y. Mimori-

References

- Kiyosue, D.P. Romero, A.T. Ritter, J. Lippincott-Schwartz, L. Fritz-Laylin, R.D. Mullins, D.M. Mitchell, J.N. Bembenek, A.C. Reymann, R. Böhme, S.W. Grill, J.T. Wang, G. Seydoux, U.S. Tulu, D.P. Kiehart, E. Betzig, Lattice light-sheet microscopy: Imaging molecules to embryos at high spatiotemporal resolution, *Science* (80-.). 346 (2014) 1257998. <https://doi.org/10.1126/science.1257998>.
- [161] F. Aguet, S. Upadhyayula, R. Gaudin, Y.Y. Chou, E. Cocucci, K. He, B.C. Chen, K. Mosaliganti, M. Pasham, W. Skillern, W.R. Legant, T.L. Liu, G. Findlay, E. Marino, G. Danuser, S. Megason, E. Betzig, T. Kirchhausen, Membrane dynamics of dividing cells imaged by lattice light-sheet microscopy, *Mol. Biol. Cell.* 27 (2016) 3418–3435. <https://doi.org/10.1091/mbc.E16-03-0164>.
- [162] S. So, M. Kim, D. Lee, D.M. Nguyen, J. Rho, Overcoming diffraction limit: From microscopy to nanoscopy, *Appl. Spectrosc. Rev.* 53 (2018) 290–312. <https://doi.org/10.1080/05704928.2017.1323309>.
- [163] K. Prakash, R. Heintzmann, L. Schermelleh, B. Diederich, S. Reichelt, Super-resolution structured illumination microscopy: past, present and future, (n.d.). <https://doi.org/10.1098/rsta.2020.0143>.
- [164] M. Saxena, G. Eluru, S.S. Gorthi, Structured illumination microscopy, *Adv. Opt. Photonics.* 7 (2015) 241. <https://doi.org/10.1364/AOP.7.000241>.
- [165] R. Heintzmann, T. Huser, Super-resolution structured illumination microscopy, *Chem. Rev.* 117 (2017) 13890–13908. <https://doi.org/10.1021/acs.chemrev.7b00218>.
- [166] M.G.L. Gustafsson, L. Shao, P.M. Carlton, C.J.R. Wang, I.N. Golubovskaya, W.Z. Cande, D.A. Agard, J.W. Sedat, Three-dimensional resolution doubling in wide-field fluorescence microscopy by structured illumination, *Biophys. J.* 94 (2008) 4957–4970. <https://doi.org/10.1529/biophysj.107.120345>.
- [167] L. Shao, P. Kner, E.H. Rego, M.G.L. Gustafsson, Super-resolution 3D microscopy of live whole cells using structured illumination, *Nat. Methods.* 8 (2011) 1044–1048. <https://doi.org/10.1038/nmeth.1734>.
- [168] F.M. Jradi, L.D. Lavis, Chemistry of Photosensitive Fluorophores for Single-Molecule Localization Microscopy, *ACS Chem. Biol.* 14 (2019) 1077–1090. <https://doi.org/10.1021/acscchembio.9b00197>.
- [169] J.R. Allen, S.T. Ross, M.W. Davidson, Structured illumination microscopy for superresolution, *ChemPhysChem.* 15 (2014) 566–576. <https://doi.org/10.1002/cphc.201301086>.
- [170] E.H. Rego, L. Shao, J.J. Macklin, L. Winoto, G.A. Johansson, N. Kamps-Hughes, M.W. Davidson, M.G.L. Gustafsson, Nonlinear structured-illumination microscopy with a photoswitchable protein reveals cellular structures at 50-nm resolution, *Proc. Natl. Acad. Sci. U. S. A.* 109 (2012) E135–E143. <https://doi.org/10.1073/pnas.1107547108>.

- [171] M.G.L. Gustafsson, Nonlinear structured-illumination microscopy: Wide-field fluorescence imaging with theoretically unlimited resolution, *Proc. Natl. Acad. Sci. U. S. A.* 102 (2005) 13081–13086. <https://doi.org/10.1073/pnas.0406877102>.
- [172] A.G. York, S.H. Parekh, D.D. Nogare, R.S. Fischer, K. Temprine, M. Mione, A.B. Chitnis, C.A. Combs, H. Shroff, Resolution doubling in live, multicellular organisms via multifocal structured illumination microscopy, *Nat. Methods.* 9 (2012) 749–754. <https://doi.org/10.1038/nmeth.2025>.
- [173] M. Ingaramo, A.G. York, P. Wawrzusin, O. Milberg, A. Hong, R. Weigert, H. Shroff, G.H. Patterson, Two-photon excitation improves multifocal structured illumination microscopy in thick scattering tissue, *Proc. Natl. Acad. Sci. U. S. A.* 111 (2014) 5254–5259. <https://doi.org/10.1073/pnas.1314447111>.
- [174] V. Mönkemöller, C. Øie, W. Hübner, T. Huser, P. McCourt, Multimodal super-resolution optical microscopy visualizes the close connection between membrane and the cytoskeleton in liver sinusoidal endothelial cell fenestrations, *Sci. Rep.* 5 (2015) 16279. <https://doi.org/10.1038/srep16279>.
- [175] L. Gao, L. Shao, C.D. Higgins, J.S. Poulton, M. Peifer, M.W. Davidson, X. Wu, B. Goldstein, E. Betzig, Noninvasive imaging beyond the diffraction limit of 3D dynamics in thickly fluorescent specimens, *Cell.* 151 (2012) 1370–1385. <https://doi.org/10.1016/j.cell.2012.10.008>.
- [176] Y. Hirano, A. Matsuda, Y. Hiraoka, Recent advancements in structured-illumination microscopy toward live-cell imaging, *Microscopy.* 64 (2015) 237–249. <https://doi.org/10.1093/jmicro/dfv034>.
- [177] M.F. Langhorst, J. Schaffer, B. Goetze, Structure brings clarity: Structured illumination microscopy in cell biology, *Biotechnol. J.* 4 (2009) 858–865. <https://doi.org/10.1002/biot.200900025>.
- [178] R. Fiolka, L. Shao, E. Hesper Rego, M.W. Davidson, M.G.L. Gustafsson, Time-lapse two-color 3D imaging of live cells with doubled resolution using structured illumination, *Proc. Natl. Acad. Sci. U. S. A.* 109 (2012) 5311–5315. <https://doi.org/10.1073/pnas.1119262109>.
- [179] D.T. Burnette, L. Shao, C. Ott, A.M. Pasapera, R.S. Fischer, M.A. Baird, C. Der Loughian, H. Delanoe-Ayari, M.J. Paszek, M.W. Davidson, E. Betzig, J. Lippincott-Schwartz, A contractile and counterbalancing adhesion system controls the 3D shape of crawling cells, *J. Cell Biol.* 205 (2014) 83–96. <https://doi.org/10.1083/jcb.201311104>.
- [180] J. Poisson, S. Lemoine, C. Boulanger, F. Durand, R. Moreau, D. Valla, P.-E. Rautou, Liver sinusoidal endothelial cells: physiology and role in liver diseases, *J. Hepatol.* 66 (2017) 212–227. <https://doi.org/10.1016/j.jhep.2016.07.009>.
- [181] J. Gracia-Sancho, E. Caparrós, A. Fernández-Iglesias, R. Francés, Role of liver sinusoidal endothelial cells in liver diseases, *Nat. Rev. Gastroenterol.*

References

- Hepatol. (2021) 1–21. <https://doi.org/10.1038/s41575-020-00411-3>.
- [182] S. Shetty, P.F. Lalor, D.H. Adams, Liver sinusoidal endothelial cells — gatekeepers of hepatic immunity, *Nat. Rev. Gastroenterol. Hepatol.* 15 (2018) 555–567. <https://doi.org/10.1038/s41575-018-0020-y>.
- [183] W.C. Aird, Phenotypic heterogeneity of the endothelium: I. Structure, function, and mechanisms, *Circ. Res.* 100 (2007) 158–173. <https://doi.org/10.1161/01.RES.0000255691.76142.4a>.
- [184] W.C. Aird, Phenotypic heterogeneity of the endothelium: II. Representative vascular beds, *Circ. Res.* 100 (2007) 174–190. <https://doi.org/10.1161/01.RES.0000255690.03436.ae>.
- [185] F. Braet, E. Wisse, Structural and functional aspects of liver sinusoidal endothelial cell fenestrae: a review, *Comp. Hepatol.* 1 (2002) 1. <https://doi.org/10.1186/1476-5926-1-1>.
- [186] S. March, E.E. Hui, G.H. Underhill, S. Khetani, S.N. Bhatia, Microenvironmental regulation of the sinusoidal endothelial cell phenotype in vitro, *Hepatology.* 50 (2009) 920–928. <https://doi.org/10.1002/hep.23085>.
- [187] D. Svistounov, A. Warren, G.P. Mc Nerney, D.M. Owen, D. Zencak, S.N. Zykova, H. Crane, T. Huser, R.J. Quinn, B. Smedsrød, The relationship between fenestrations, sieve plates and rafts in liver sinusoidal endothelial cells, *PLoS One.* 7 (2012) e46134. <https://doi.org/10.1371/journal.pone.0046134>.
- [188] C.I. Øie, V. Mönkemöller, W. Hübner, M. Schüttpelz, H. Mao, B.S. Ahluwalia, T.R. Huser, P. McCourt, New ways of looking at very small holes—using optical nanoscopy to visualize liver sinusoidal endothelial cell fenestrations, *Nanophotonics.* 7 (2018) 575–596. <https://doi.org/10.1515/nanoph-2017-0055>.
- [189] R. Fraser, V.C. Cogger, B. Dobbs, H. Jamieson, A. Warren, S.N. Hilmer, D.G. Le Couteur, The liver sieve and atherosclerosis, *Pathology.* 44 (2012) 181–186. <https://doi.org/10.1097/PAT.0b013e328351bcc8>.
- [190] B. Vollmar, M.D. Menger, The hepatic microcirculation: Mechanistic contributions and therapeutic targets in liver injury and repair, *Physiol. Rev.* 89 (2009) 1269–1339. <https://doi.org/10.1152/physrev.00027.2008>.
- [191] V.C. Cogger, G.P. Mc Nerney, T. Nyunt, L.D. DeLeve, P. McCourt, B. Smedsrød, D.G. Le Couteur, T.R. Huser, Three-dimensional structured illumination microscopy of liver sinusoidal endothelial cell fenestrations, *J. Struct. Biol.* 171 (2010) 382–388. <https://doi.org/10.1016/J.JSB.2010.06.001>.
- [192] V. Natarajan, E.N. Harris, S. Kidambi, SECs (Sinusoidal Endothelial Cells), Liver Microenvironment, and Fibrosis, *Biomed Res. Int.* 2017 (2017). <https://doi.org/10.1155/2017/4097205>.

- [193] E. Wisse, An electron microscopic study of the fenestrated endothelial lining of rat liver sinusoids, *J. Ultrastructure Res.* 31 (1970) 125–150. [https://doi.org/10.1016/S0022-5320\(70\)90150-4](https://doi.org/10.1016/S0022-5320(70)90150-4).
- [194] E. Wisse, R.B. de Zanger, K. Charels, P. van der Smissen, R.S. McCuskey, The liver sieve: Considerations concerning the structure and function of endothelial fenestrae, the sinusoidal wall and the space of disse, *Hepatology.* 5 (1985) 683–692. <https://doi.org/10.1002/hep.1840050427>.
- [195] N.J. Hunt, G.P. Lockwood, A. Warren, H. Mao, P.A.G. McCourt, D.G. Le Couteur, V.C. Cogger, Manipulating fenestrations in young and old liver sinusoidal endothelial cells, *Am. J. Physiol. - Gastrointest. Liver Physiol.* 316 (2019) G144–G154. <https://doi.org/10.1152/ajpgi.00179.2018>.
- [196] V.C. Cogger, U. Roessner, A. Warren, R. Fraser, D.G. Le Couteur, A sieve-raft hypothesis for the regulation of endothelial fenestrations, *Comput. Struct. Biotechnol. J.* 8 (2013) e201308003. <https://doi.org/10.5936/csbj.201308003>.
- [197] J. Di Martino, P. Mascalchi, P. Legros, S. Lacomme, E. Gontier, P. Bioulac-Sage, C. Balabaud, V. Moreau, F. Saltel, Actin Depolymerization in Dedifferentiated Liver Sinusoidal Endothelial Cells Promotes Fenestrae Re-Formation, *Hepatol. Commun.* 3 (2019) 213–219. <https://doi.org/10.1002/hep4.1301>.
- [198] B. Zapotoczny, K. Szafranska, K. Owczarczyk, E. Kus, S. Chlopicki, & M. Szymonski, Atomic Force Microscopy Reveals the Dynamic Morphology of Fenestrations in Live Liver Sinusoidal Endothelial Cells OPEN, *Sci. Rep.* 7 (2017) 7994. <https://doi.org/10.1038/s41598-017-08555-0>.
- [199] F. Braet, E. Wisse, AFM imaging of fenestrated liver sinusoidal endothelial cells, *Micron.* 43 (2012) 1252–1258. <https://doi.org/10.1016/j.micron.2012.02.010>.
- [200] I. Martinez, G.I. Nedredal, C.I. Øie, A. Warren, O. Johansen, D.G. Le Couteur, B. Smedsrød, The influence of oxygen tension on the structure and function of isolated liver sinusoidal endothelial cells, *Comp. Hepatol.* 7 (2008) 1–11. <https://doi.org/10.1186/1476-5926-7-4>.
- [201] A. Haque, P. Gheibi, Y. Gao, E. Foster, K.J. Son, J. You, G. Stybayeva, D. Patel, A. Revzin, Cell biology is different in small volumes: endogenous signals shape phenotype of primary hepatocytes cultured in microfluidic channels OPEN, (2016). <https://doi.org/10.1038/srep33980>.
- [202] L. Prodanov, R. Jindal, S.S. Bale, M. Hegde, W.J. Mccarty, I. Golberg, A. Bhushan, M.L. Yarmush, O.B. Usta, Long-term maintenance of a microfluidic 3D human liver sinusoid, *Biotechnol. Bioeng.* 113 (2016) 241–246. <https://doi.org/10.1002/bit.25700>.
- [203] Y. Zhou, S. Basu, K.J. Wohlfahrt, S.F. Lee, D. Klenerman, E.D. Laue, A.A. Seshia, A microfluidic platform for trapping, releasing and super-resolution imaging of single cells, *Sensors Actuators B Chem.* 232 (2016)

References

- 680–691. <https://doi.org/10.1016/j.snb.2016.03.131>.
- [204] D.I. Cattoni, J.B. Fiche, A. Valeri, T. Mignot, M. Nöllmann, Super-Resolution Imaging of Bacteria in a Microfluidics Device, *PLoS One*. 8 (2013) 76268. <https://doi.org/10.1371/journal.pone.0076268>.
- [205] J. Tam, G.A. Cordier, S. Bálint, A.A. Sandoval, J.S. Borbely, M. Lakadamyali, A Microfluidic Platform for Correlative Live-Cell and Super-Resolution Microscopy, (2014). <https://doi.org/10.1371/journal.pone.0115512>.
- [206] S.H. Chu, L.L. Lo, R.L. Lai, T. Tony Yang, R.R. Weng, J.C. Liao, N.T. Huang, A microfluidic device for in situ fixation and super-resolved mechanosensation studies of primary cilia, *Biomicrofluidics*. 13 (2019) 014105. <https://doi.org/10.1063/1.5081756>.
- [207] K. Mogi, Y. Sugii, Visualization of near surface flow of endothelial cells based on confocal micro-PIV and super-resolution microscopy, in: 10th Pacific Symp. Flow Vis. Image Process., 2016.
- [208] B. Zhang, A. Korolj, B.F.L. Lai, M. Radisic, Advances in organ-on-a-chip engineering, *Nat. Rev. Mater.* 3 (2018) 257–278. <https://doi.org/10.1038/s41578-018-0034-7>.
- [209] N.Y.C. Lin, K.A. Homan, S.S. Robinson, D.B. Kolesky, N. Duarte, A. Moisan, J.A. Lewis, Renal reabsorption in 3D vascularized proximal tubule models, *Proc. Natl. Acad. Sci. U. S. A.* 116 (2019) 5399–5404. <https://doi.org/10.1073/pnas.1815208116>.
- [210] W. Jia, P.S. Gungor-Ozkerim, Y.S. Zhang, K. Yue, K. Zhu, W. Liu, Q. Pi, B. Byambaa, M.R. Dokmeci, S.R. Shin, A. Khademhosseini, Direct 3D bioprinting of perfusable vascular constructs using a blend bioink, *Biomaterials*. 106 (2016) 58–68. <https://doi.org/10.1016/j.biomaterials.2016.07.038>.
- [211] C. Ding, X. Chen, Q. Kang, X. Yan, Biomedical Application of Functional Materials in Organ-on-a-Chip, *Front. Bioeng. Biotechnol.* 8 (2020) 823. <https://doi.org/10.3389/fbioe.2020.00823>.
- [212] S. Ahadian, R. Civitarese, D. Bannerman, M.H. Mohammadi, R. Lu, E. Wang, L. Davenport-Huyer, B. Lai, B. Zhang, Y. Zhao, S. Mandla, A. Korolj, M. Radisic, Organ-On-A-Chip Platforms: A Convergence of Advanced Materials, Cells, and Microscale Technologies, *Adv. Healthc. Mater.* 7 (2018) 1700506. <https://doi.org/10.1002/adhm.201700506>.
- [213] P.F. Lalor, S. Edwards, G. McNab, M. Salmi, S. Jalkanen, D.H. Adams, Vascular Adhesion Protein-1 Mediates Adhesion and Transmigration of Lymphocytes on Human Hepatic Endothelial Cells, *J. Immunol.* 169 (2002) 983–992. <https://doi.org/10.4049/jimmunol.169.2.983>.
- [214] P.L. Shields, C.M. Morland, M. Salmon, S. Qin, S.G. Hubscher, D.H. Adams, Chemokine and Chemokine Receptor Interactions Provide a

- Mechanism for Selective T Cell Recruitment to Specific Liver Compartments Within Hepatitis C-Infected Liver, *J. Immunol.* 163 (1999) 6236 LP – 6243. <http://www.jimmunol.org/content/163/11/6236.abstract>.
- [215] K.F. Yoong, G. McNab, S.G. Hübscher, D.H. Adams, Vascular Adhesion Protein-1 and ICAM-1 Support the Adhesion of Tumor-Infiltrating Lymphocytes to Tumor Endothelium in Human Hepatocellular Carcinoma, *J. Immunol.* 160 (1998) 3978 LP – 3988. <http://www.jimmunol.org/content/160/8/3978.abstract>.
- [216] J. Schindelin, I. Arganda-Carreras, E. Frise, V. Kaynig, M. Longair, T. Pietzsch, S. Preibisch, C. Rueden, S. Saalfeld, B. Schmid, J.Y. Tinevez, D.J. White, V. Hartenstein, K. Eliceiri, P. Tomancak, A. Cardona, Fiji: An open-source platform for biological-image analysis, *Nat. Methods.* 9 (2012) 676–682. <https://doi.org/10.1038/nmeth.2019>.
- [217] S.M. Ali Haghpars, T. Kihara, J. Miyake, Distinct mechanical behavior of HEK293 cells in adherent and suspended states, *PeerJ.* 2015 (2015) e1131. <https://doi.org/10.7717/peerj.1131>.
- [218] M. Malm, R. Saghaleyni, M. Lundqvist, M. Giudici, V. Chotteau, R. Field, P.G. Varley, D. Hatton, L. Grassi, T. Svensson, J. Nielsen, J. Rockberg, Evolution from adherent to suspension: systems biology of HEK293 cell line development, *Sci. Reports* |. 10 (123AD) 18996. <https://doi.org/10.1038/s41598-020-76137-8>.
- [219] E. Petiot, D. Jacob, S. Lanthier, V. Lohr, S. Ansoorge, A.A. Kamen, Metabolic and Kinetic analyses of influenza production in perfusion HEK293 cell culture, *BMC Biotechnol.* 11 (2011) 1–12. <https://doi.org/10.1186/1472-6750-11-84>.
- [220] T.T.G. Nieskens, M.J. Wilmer, Kidney-on-a-chip technology for renal proximal tubule tissue reconstruction, *Eur. J. Pharmacol.* 790 (2016) 46–56. <https://doi.org/10.1016/j.ejphar.2016.07.018>.
- [221] H. Kaji, T. Yokoi, T. Kawashima, M. Nishizawa, Directing the flow of medium in controlled cocultures of HeLa cells and human umbilical vein endothelial cells with a microfluidic device, *Lab Chip.* 10 (2010) 2374–2379. <https://doi.org/10.1039/c004583g>.
- [222] R. Huang, W. Zheng, W. Liu, W. Zhang, Y. Long, X. Jiang, Investigation of Tumor Cell Behaviors on a Vascular Microenvironment-Mimicking Microfluidic Chip, *Sci. Rep.* 5 (2015) 17768. <https://doi.org/10.1038/srep17768>.
- [223] C. Zheng, L. Zhao, G. Chen, Y. Zhou, Y. Pang, Y. Huang, Quantitative study of the dynamic tumor-endothelial cell interactions through an integrated microfluidic coculture system, *Anal. Chem.* 84 (2012) 2088–2093. <https://doi.org/10.1021/ac2032029>.
- [224] J. Chen, J. Li bc, Y. Sun, Microfluidic approaches for cancer cell detection, characterization, and separation, *Lab Chip.* 12 (2012) 1753–1767.

References

- <https://doi.org/10.1039/c2lc21273k>.
- [225] K.H. Benam, R. Villenave, C. Lucchesi, A. Varone, C. Hubeau, H.H. Lee, S.E. Alves, M. Salmon, T.C. Ferrante, J.C. Weaver, A. Bahinski, G.A. Hamilton, D.E. Ingber, Small airway-on-a-chip enables analysis of human lung inflammation and drug responses in vitro, *Nat. Methods*. 13 (2016) 151–157. <https://doi.org/10.1038/nmeth.3697>.
- [226] N. Mori, Y. Morimoto, S. Takeuchi, Skin integrated with perfusable vascular channels on a chip, *Biomaterials*. 116 (2017) 48–56. <https://doi.org/10.1016/j.biomaterials.2016.11.031>.
- [227] V. Mönkemöller, C. Øie, W. Hübner, T. Huser, P. Mccourt, Multimodal super-resolution optical microscopy visualizes the close connection between membrane and the cytoskeleton in liver sinusoidal endothelial cell fenestrations OPEN, (2015). <https://doi.org/10.1038/srep16279>.
- [228] P.J. Lee, P.J. Hung, L.P. Lee, An artificial liver sinusoid with a microfluidic endothelial-like barrier for primary hepatocyte culture, *Biotechnol. Bioeng.* 97 (2007) 1340–1346. <https://doi.org/10.1002/bit.21360>.
- [229] A. Carraro, W.M. Hsu, K.M. Kulig, W.S. Cheung, M.L. Miller, E.J. Weinberg, E.F. Swart, M. Kaazempur-Mofrad, J.T. Borenstein, J.P. Vacanti, C. Neville, In vitro analysis of a hepatic device with intrinsic microvascular-based channels, *Biomed. Microdevices*. 10 (2008) 795–805. <https://doi.org/10.1007/s10544-008-9194-3>.
- [230] Y.S. Weng, S.F. Chang, M.C. Shih, S.H. Tseng, C.H. Lai, Scaffold-Free Liver-On-A-Chip with Multiscale Organotypic Cultures, *Adv. Mater.* 29 (2017) 1701545. <https://doi.org/10.1002/adma.201701545>.
- [231] Y. Du, N. Li, H. Yang, C. Luo, Y. Gong, C. Tong, Y. Gao, S. Lü, M. Long, Mimicking liver sinusoidal structures and functions using a 3D-configured microfluidic chip, *Lab Chip*. 17 (2017) 782–794. <https://doi.org/10.1039/c6lc01374k>.
- [232] H. Lee, S. Chae, J.Y. Kim, W. Han, J. Kim, Y. Choi, D.W. Cho, Cell-printed 3D liver-on-a-chip possessing a liver microenvironment and biliary system, *Biofabrication*. 11 (2019) 025001. <https://doi.org/10.1088/1758-5090/aaf9fa>.
- [233] A. Wnorowski, H. Yang, J.C. Wu, Progress, obstacles, and limitations in the use of stem cells in organ-on-a-chip models, *Adv. Drug Deliv. Rev.* 140 (2019) 3–11. <https://doi.org/10.1016/j.addr.2018.06.001>.
- [234] H.M.M. Ahmed, S. Salerno, S. Morelli, L. Giorno, L. De Bartolo, 3D liver membrane system by co-culturing human hepatocytes, sinusoidal endothelial and stellate cells, *Biofabrication*. 9 (2017) 025022. <https://doi.org/10.1088/1758-5090/aa70c7>.
- [235] V. Mönkemöller, H. Mao, W. Hübner, G. Dumitriu, P. Heimann, G. Levy,

- T. Huser, B. Kaltschmidt, C. Kaltschmidt, C.I. Øie, Primary rat LSECs preserve their characteristic phenotype after cryopreservation, *Sci. Rep.* 8 (2018) 1–10. <https://doi.org/10.1038/s41598-018-32103-z>.
- [236] A.C. Taylor, Responses of cells to pH changes in the medium., *J. Cell Biol.* 15 (1962) 201–209. <https://doi.org/10.1083/jcb.15.2.201>.
- [237] Y. Han, M. Li, F. Qiu, M. Zhang, Y.H. Zhang, Cell-permeable organic fluorescent probes for live-cell long-term super-resolution imaging reveal lysosome-mitochondrion interactions, *Nat. Commun.* 8 (2017) 1–9. <https://doi.org/10.1038/s41467-017-01503-6>.
- [238] I. Rasnik, S.A. McKinney, T. Ha, Nonblinking and long-lasting single-molecule fluorescence imaging, (2006). <https://doi.org/10.1038/NMETH934>.
- [239] K. Pinkwart, F. Schneider, M. Lukoseviciute, T. Sauka-Spengler, E. Lyman, C. Eggeling, E. Sezgin, Nanoscale dynamics of cholesterol in the cell membrane, *J. Biol. Chem.* 294 (2019) 12599–12609. <https://doi.org/10.1074/jbc.RA119.009683>.
- [240] A.F. Carisey, E.M. Mace, M.B. Saeed, D.M. Davis, J.S. Orange, Nanoscale Dynamism of Actin Enables Secretory Function in Cytolytic Cells, *Curr. Biol.* 28 (2018) 489–502.e9. <https://doi.org/10.1016/j.cub.2017.12.044>.
- [241] C. Yeung-Wah Lo, S. Chen, S. Jayne Creed, M. Kang, N. Zhao, B. Zhong Tang, K. Diana Elgass, Novel super-resolution capable mitochondrial probe, MitoRed AIE, enables assessment of real-time molecular mitochondrial dynamics, *Sci. Rep.* 6 (2016) 30855. <https://doi.org/10.1038/srep30855>.
- [242] H. Mazloom-Farsibaf, F. Farzam, M. Fazel, M.J. Westerid, M.B.M. Meddens, K.A. Lidkeid, Comparing lifeact and phalloidin for super-resolution imaging of actin in fixed cells, *PLoS One.* 16 (2021) e0246138. <https://doi.org/10.1371/journal.pone.0246138>.
- [243] M. Klevanski, F. Herrmannsdoerfer, S. Sass, V. Venkataramani, M. Heilemann, T. Kuner, Automated highly multiplexed super-resolution imaging of protein nano-architecture in cells and tissues, *Nat. Commun.* 11 (2020) 1–11. <https://doi.org/10.1038/s41467-020-15362-1>.
- [244] K.J. Amann, T.D. Pollard, Direct real-time observation of actin filament branching mediated by Arp2/3 complex using total internal reflection fluorescence microscopy, *Proc. Natl. Acad. Sci. U. S. A.* 98 (2001) 15009–15013. <https://doi.org/10.1073/pnas.211556398>.
- [245] D.F. Cedillo-Alcantar, Y.D. Han, J. Choi, J.L. Garcia-Cordero, A. Revzin, Automated Droplet-Based Microfluidic Platform for Multiplexed Analysis of Biochemical Markers in Small Volumes, *Anal. Chem.* 91 (2019) 5133–5141. <https://doi.org/10.1021/acs.analchem.8b05689>.
- [246] J.F. Casella, M.D. Flanagan, S. Lin, Cytochalasin D inhibits actin

References

- polymerization and induces depolymerization of actin filaments formed during platelet shape change, *Nature*. 293 (1981) 302–305.
<https://doi.org/10.1038/293302a0>.
- [247] R. Kretz, L. Wendt, S. Wongkanoun, J.J. Luangsa-Ard, F. Surup, S.E. Helaly, S.R. Noumeur, M. Stadler, T.E.B. Stradal, The effect of cytochalasins on the actin cytoskeleton of eukaryotic cells and preliminary structure–activity relationships, *Biomolecules*. 9 (2019) 73.
<https://doi.org/10.3390/biom9020073>.
- [248] S.G. Axline, E.P. Reaven, Inhibition of phagocytosis and plasma membrane mobility of the cultivated macrophage by cytochalasin B: Role of subplasmalemmal microfilaments, *J. Cell Biol.* 62 (1974) 647–659.
<https://doi.org/10.1083/jcb.62.3.647>.
- [249] S. Waldchen, J. Lehmann, T. Klein, S. Van De Linde, M. Sauer, Light-induced cell damage in live-cell super-resolution microscopy, *Sci. Rep.* 5 (2015) 1–12. <https://doi.org/10.1038/srep15348>.
- [250] R. Langer, J.P. Vacanti, Tissue engineering, *Science* (80-.). 260 (1993) 920–926. <https://doi.org/10.1126/science.8493529>.
- [251] Y. Ikada, Challenges in tissue engineering, *J. R. Soc. Interface*. 3 (2006) 589–601. <https://doi.org/10.1098/rsif.2006.0124>.
- [252] L.J. Bonassar, C.A. Vacanti, Tissue Engineering: The First Decade and Beyond, 1998. [https://doi.org/10.1002/\(SICI\)1097-4644\(1998\)72:30/31](https://doi.org/10.1002/(SICI)1097-4644(1998)72:30/31).
- [253] G.M. Abouna, Organ Shortage Crisis: Problems and Possible Solutions, *Transplant. Proc.* 40 (2008) 34–38.
<https://doi.org/10.1016/j.transproceed.2007.11.067>.
- [254] S. Petit-Zeman, Regenerative medicine: The regeneration of tissues and organs offers a radical new approach to the treatment of injury and disease. It's a new medicine for a new millennium, but does the reality match the hype?, *Nat. Biotechnol.* 19 (2001) 201–206. <https://doi.org/10.1038/85619>.
- [255] C. Mason, P. Dunnill, A brief definition of regenerative medicine, *Regen. Med.* 3 (2008) 1–5. <https://doi.org/10.2217/17460751.3.1.1>.
- [256] R.M. Nerem, S.C. Schutte, The Challenge of Imitating Nature, in: *Princ. Tissue Eng.* Fourth Ed., Elsevier Inc., 2013: pp. 9–24.
<https://doi.org/10.1016/B978-0-12-398358-9.00002-1>.
- [257] P. Bianco, P.G. Robey, Stem cells in tissue engineering, *Nature*. 414 (2001) 118–121. <https://doi.org/10.1038/35102181>.
- [258] R.E.B. Fitzsimmons, M.S. Mazurek, A. Soos, C.A. Simmons, Mesenchymal stromal/stem cells in regenerative medicine and tissue engineering, *Stem Cells Int.* 2018 (2018).
<https://doi.org/10.1155/2018/8031718>.
- [259] J.A. Hubbell, Biomaterials in tissue engineering, *Nat. Biotechnol.* 13

(1995) 565.

- [260] S.J. Lee, J.J. Yoo, A. Atala, Biomaterials and tissue engineering, in: Clin. Regen. Med. Urol., Springer Singapore, 2017: pp. 17–51. https://doi.org/10.1007/978-981-10-2723-9_2.
- [261] E.S. Place, N.D. Evans, M.M. Stevens, Complexity in biomaterials for tissue engineering, Nat. Mater. 8 (2009) 457–470. <https://doi.org/10.1038/nmat2441>.
- [262] F. Khan, M. Tanaka, Designing smart biomaterials for tissue engineering, Int. J. Mol. Sci. 19 (2018) 17. <https://doi.org/10.3390/ijms19010017>.
- [263] T.J. Keane, S.F. Badylak, Biomaterials for tissue engineering applications, Semin. Pediatr. Surg. 23 (2014) 112–118. <https://doi.org/10.1053/j.sempedsurg.2014.06.010>.
- [264] M.S.B. Reddy, D. Ponnamma, R. Choudhary, K.K. Sadasivuni, A comparative review of natural and synthetic biopolymer composite scaffolds, Polymers (Basel). 13 (2021) 1105. <https://doi.org/10.3390/polym13071105>.
- [265] K. Joyce, G.T. Fabra, Y. Bozkurt, A. Pandit, Bioactive potential of natural biomaterials: identification, retention and assessment of biological properties, Signal Transduct. Target. Ther. 6 (2021) 1–28. <https://doi.org/10.1038/s41392-021-00512-8>.
- [266] A. Vishwakarma, N.S. Bhise, M.B. Evangelista, J. Rouwkema, M.R. Dokmeci, A.M. Ghaemmaghami, N.E. Vrana, A. Khademhosseini, Engineering Immunomodulatory Biomaterials To Tune the Inflammatory Response, Trends Biotechnol. 34 (2016) 470–482. <https://doi.org/10.1016/j.tibtech.2016.03.009>.
- [267] J.A. Hubbell, Bioactive biomaterials, Curr. Opin. Biotechnol. 10 (1999) 123–129. [https://doi.org/10.1016/S0958-1669\(99\)80021-4](https://doi.org/10.1016/S0958-1669(99)80021-4).
- [268] Y. Luo, G. Engelmayr, D.T. Auguste, L. da Silva Ferreira, J.M. Karp, R. Saigal, R. Langer, 3D Scaffolds, in: Princ. Tissue Eng. Fourth Ed., Elsevier Inc., 2013: pp. 475–494. <https://doi.org/10.1016/B978-0-12-398358-9.00024-0>.
- [269] H. Lv, L. Li, M. Sun, Y. Zhang, L. Chen, Y. Rong, Y. Li, Mechanism of regulation of stem cell differentiation by matrix stiffness, Stem Cell Res. Ther. 6 (2015) 1–11. <https://doi.org/10.1186/s13287-015-0083-4>.
- [270] J. Nam, J. Johnson, J.J. Lannutti, S. Agarwal, Modulation of embryonic mesenchymal progenitor cell differentiation via control over pure mechanical modulus in electrospun nanofibers, Acta Biomater. 7 (2011) 1516–1524. <https://doi.org/10.1016/j.actbio.2010.11.022>.
- [271] U. Jammalamadaka, K. Tappa, Recent advances in biomaterials for 3D printing and tissue engineering, J. Funct. Biomater. 9 (2018) 22. <https://doi.org/10.3390/jfb9010022>.

References

- [272] B. Dhandayuthapani, Y. Yoshida, T. Maekawa, D.S. Kumar, Polymeric scaffolds in tissue engineering application: a review, *Int. J. Polym. Sci.* 2011 (2011). <https://doi.org/10.1155/2011/290602>.
- [273] C.J. Bettinger, J.T. Borenstein, R. Langer, Micro-and nanofabricated scaffolds, in: *Princ. Tissue Eng.*, Elsevier, 2007: pp. 341–358.
- [274] M.B. Murphy, A.G. Mikos, Polymer scaffold fabrication, in: *Princ. Tissue Eng.*, Elsevier, 2007: pp. 309–321.
- [275] F. Khan, M. Tanaka, S.R. Ahmad, Fabrication of polymeric biomaterials: a strategy for tissue engineering and medical devices, *J. Mater. Chem. B.* 3 (2015) 8224–8249. <https://doi.org/10.1039/c5tb01370d>.
- [276] A. Eltom, G. Zhong, A. Muhammad, Scaffold Techniques and Designs in Tissue Engineering Functions and Purposes: A Review, *Adv. Mater. Sci. Eng.* 2019 (2019). <https://doi.org/10.1155/2019/3429527>.
- [277] V. Raeisdasteh Hokmabad, S. Davaran, A. Ramazani, R. Salehi, Design and fabrication of porous biodegradable scaffolds: a strategy for tissue engineering, *J. Biomater. Sci. Polym. Ed.* 28 (2017) 1797–1825. <https://doi.org/10.1080/09205063.2017.1354674>.
- [278] R.D. Pedde, B. Mirani, A. Navaei, T. Styan, S. Wong, M. Mehrali, A. Thakur, N.K. Mohtaram, A. Bayati, A. Dolatshahi-Pirouz, M. Nikkhah, S.M. Willerth, M. Akbari, Emerging Biofabrication Strategies for Engineering Complex Tissue Constructs, *Adv. Mater.* 29 (2017). <https://doi.org/10.1002/adma.201606061>.
- [279] Y.S. Zhang, A. Khademhosseini, *Advances in engineering hydrogels, Science (80-)*. 356 (2017). <https://doi.org/10.1126/science.aaf3627>.
- [280] X. Guan, M. Avci-Adali, E. Alarçin, H. Cheng, S.S. Kashaf, Y. Li, A. Chawla, H.L. Jang, A. Khademhosseini, Development of hydrogels for regenerative engineering, *Biotechnol. J.* 12 (2017). <https://doi.org/10.1002/biot.201600394>.
- [281] W. Hu, Z. Wang, Y. Xiao, S. Zhang, J. Wang, Advances in crosslinking strategies of biomedical hydrogels, *Biomater. Sci.* 7 (2019) 843–855. <https://doi.org/10.1039/c8bm01246f>.
- [282] J.G. Nemen-Guanzon, S. Lee, J.R. Berg, Y.H. Jo, J.E. Yeo, B.M. Nam, Y.-G. Koh, J.I. Lee, Trends in tissue engineering for blood vessels., *J. Biomed. Biotechnol.* 2012 (2012) 956345. <https://doi.org/10.1155/2012/956345>.
- [283] P. Bajaj, R.M. Schweller, A. Khademhosseini, J.L. West, R. Bashir, 3D Biofabrication Strategies for Tissue Engineering and Regenerative Medicine, *Annu. Rev. Biomed. Eng.* 16 (2014) 247–276. <https://doi.org/10.1146/annurev-bioeng-071813-105155>.
- [284] J.W. Nichol, A. Khademhosseini, Modular tissue engineering: Engineering biological tissues from the bottom up, *Soft Matter.* 5 (2009) 1312–1319.

<https://doi.org/10.1039/b814285h>.

- [285] A. Prasad, M.R. Sankar, V. Katiyar, State of Art on Solvent Casting Particulate Leaching Method for Orthopedic Scaffolds Fabrication, in: *Mater. Today Proc.*, Elsevier Ltd, 2017: pp. 898–907.
<https://doi.org/10.1016/j.matpr.2017.01.101>.
- [286] R. V. Badhe, D. Bijukumar, D.R. Chejara, M. Mabrouk, Y.E. Choonara, P. Kumar, L.C. du Toit, P.P.D. Kondiah, V. Pillay, A composite chitosan-gelatin bi-layered, biomimetic macroporous scaffold for blood vessel tissue engineering, *Carbohydr. Polym.* 157 (2017) 1215–1225.
<https://doi.org/10.1016/j.carbpol.2016.09.095>.
- [287] T. Garg, O. Singh, S. Arora, R.S.R. Murthy, Scaffold: a novel carrier for cell and drug delivery, *Crit. Rev. Ther. Drug Carr. Syst.* 29 (2012).
<https://doi.org/10.1615/critrevtherdrugcarriersyst.v29.i1.10>.
- [288] Z. Fereshteh, Freeze-drying technologies for 3D scaffold engineering, in: *Funct. 3D Tissue Eng. Scaffolds Mater. Technol. Appl.*, Elsevier, 2018: pp. 151–174. <https://doi.org/10.1016/B978-0-08-100979-6.00007-0>.
- [289] W. Lin, W. Lan, Y. Wu, D. Zhao, Y. Wang, X. He, J. Li, Z. Li, F. Luo, H. Tan, Q. Fu, Aligned 3D porous polyurethane scaffolds for biological anisotropic tissue regeneration, *Regen. Biomater.* 7 (2020) 19–27.
<https://doi.org/10.1093/rb/rbz031>.
- [290] R. Ghafari, M. Jonoobi, L.M. Amirabad, K. Oksman, A.R. Taheri, Fabrication and characterization of novel bilayer scaffold from nanocellulose based aerogel for skin tissue engineering applications, *Int. J. Biol. Macromol.* 136 (2019) 796–803.
<https://doi.org/10.1016/j.ijbiomac.2019.06.104>.
- [291] A. Tampieri, M. Sandri, E. Landi, D. Pressato, S. Francioli, R. Quarto, I. Martin, Design of graded biomimetic osteochondral composite scaffolds, *Biomaterials.* 29 (2008) 3539–3546.
<https://doi.org/10.1016/j.biomaterials.2008.05.008>.
- [292] S. Minardi, B. Corradetti, F. Taraballi, M. Sandri, J. Van Eps, F.J. Cabrera, B.K. Weiner, A. Tampieri, E. Tasciotti, Evaluation of the osteoinductive potential of a bio-inspired scaffold mimicking the osteogenic niche for bone augmentation, *Biomaterials.* 62 (2015) 128–137.
- [293] J.C. Fricain, S. Schlaubitz, C. Le Visage, I. Arnault, S.M. Derkaoui, R. Siadous, S. Catros, C. Lalande, R. Bareille, M. Renard, T. Fabre, S. Cornet, M. Durand, A. Léonard, N. Sahaoui, D. Letourneur, J. Amédée, A nano-hydroxyapatite - Pullulan/dextran polysaccharide composite macroporous material for bone tissue engineering, *Biomaterials.* 34 (2013) 2947–2959.
<https://doi.org/10.1016/j.biomaterials.2013.01.049>.
- [294] A. Rahmani Del Bakhshayesh, E. Mostafavi, E. Alizadeh, N. Asadi, A. Akbarzadeh, S. Davaran, Fabrication of Three-Dimensional Scaffolds Based on Nano-biomimetic Collagen Hybrid Constructs for Skin Tissue

References

- Engineering, ACS Omega. 3 (2018) 8605–8611.
<https://doi.org/10.1021/acsomega.8b01219>.
- [295] R.F. Canadas, T. Ren, A. Tocchio, A.P. Marques, J.M. Oliveira, R.L. Reis, U. Demirci, Tunable anisotropic networks for 3-D oriented neural tissue models, *Biomaterials*. 181 (2018) 402–414.
<https://doi.org/10.1016/j.biomaterials.2018.07.055>.
- [296] S.K. Norouzi, A. Shamloo, Bilayered heparinized vascular graft fabricated by combining electrospinning and freeze drying methods, *Mater. Sci. Eng. C*. 94 (2019) 1067–1076. <https://doi.org/10.1016/j.msec.2018.10.016>.
- [297] T. Simon-Yarza, M.N. Labour, R. Aid, D. Letourneur, Channeled polysaccharide-based hydrogel reveals influence of curvature to guide endothelial cell arrangement in vessel-like structures, *Mater. Sci. Eng. C*. 118 (2021) 111369. <https://doi.org/10.1016/j.msec.2020.111369>.
- [298] E. Dattola, E.I. Parrotta, S. Scalise, G. Perozziello, T. Limongi, P. Candeloro, M.L. Coluccio, C. Maletta, L. Bruno, M.T. De Angelis, G. Santamaria, V. Mollace, E. Lamanna, E. Di Fabrizio, G. Cuda, Development of 3D PVA scaffolds for cardiac tissue engineering and cell screening applications, *RSC Adv*. 9 (2019) 4246–4257.
<https://doi.org/10.1039/C8RA08187E>.
- [299] E. Marsich, F. Bellomo, G. Turco, A. Travan, I. Donati, S. Paoletti, Nano-composite scaffolds for bone tissue engineering containing silver nanoparticles: preparation, characterization and biological properties, *J. Mater. Sci. Mater. Med*. 24 (2013) 1799–1807.
<https://doi.org/10.1007/s10856-013-4923-4>.
- [300] A.C. Akman, R.S. Tigli, M. Gumusderelioglu, R.M. Nohutcu, bFGF-loaded HA-chitosan: A promising scaffold for periodontal tissue engineering, *J. Biomed. Mater. Res. - Part A*. 92 (2010) 953–962.
<https://doi.org/10.1002/jbm.a.32428>.
- [301] V. Mironov, V. Kasyanov, R.R. Markwald, Nanotechnology in vascular tissue engineering: from nanoscaffolding towards rapid vessel biofabrication, *Trends Biotechnol*. 26 (2008) 338–344.
<https://doi.org/10.1016/j.tibtech.2008.03.001>.
- [302] A. Hasan, A. Memic, N. Annabi, M. Hossain, A. Paul, M.R. Dokmeci, F. Dehghani, A. Khademhosseini, Electrospun scaffolds for tissue engineering of vascular grafts, *Acta Biomater*. 10 (2014) 11–25.
<https://doi.org/10.1016/j.actbio.2013.08.022>.
- [303] L.A. Smith, P.X. Ma, Nano-fibrous scaffolds for tissue engineering, *Colloids Surfaces B Biointerfaces*. 39 (2004) 125–131.
<https://doi.org/10.1016/j.colsurfb.2003.12.004>.
- [304] V. Mironov, T. Trusk, V. Kasyanov, S. Little, R. Swaja, R. Markwald, Biofabrication: a 21st century manufacturing paradigm, *Biofabrication*. 1 (2009) 022001. <https://doi.org/10.1088/1758-5082/1/2/022001>.

- [305] N. Goonoo, Vascularization and angiogenesis in electrospun tissue engineered constructs: towards the creation of long-term functional networks, *Biomed. Phys. Eng. Express.* 4 (2018) 32001. <https://doi.org/10.1088/2057-1976/aaab03>.
- [306] E.D. Boland, J.A. Matthews, K.J. Pawlowski, D.G. Simpson, G.E. Wnek, G.L. Bowlin, Electrospinning collagen and elastin: preliminary vascular tissue engineering, *Front Biosci.* 9 (2004) e32. <https://doi.org/10.2741/1313>.
- [307] M. Liu, X.P. Duan, Y.M. Li, D.P. Yang, Y.Z. Long, Electrospun nanofibers for wound healing, *Mater. Sci. Eng. C.* 76 (2017) 1413–1423. <https://doi.org/10.1016/j.msec.2017.03.034>.
- [308] A. De Mori, M.P. Fernández, G. Blunn, G. Tozzi, M. Roldo, 3D printing and electrospinning of composite hydrogels for cartilage and bone tissue engineering, *Polymers (Basel).* 10 (2018) 285. <https://doi.org/10.3390/polym10030285>.
- [309] A. Martins, J. V. Araújo, R.L. Reis, N.M. Neves, Electrospun nanostructured scaffolds for tissue engineering applications, *Nanomedicine.* 2 (2007) 929–942. <https://doi.org/10.2217/17435889.2.6.929>.
- [310] V.S. Joshi, N.Y. Lei, C.M. Walthers, B. Wu, J.C.Y. Dunn, Macroporosity enhances vascularization of electrospun scaffolds, *J. Surg. Res.* 183 (2013) 18–26. <https://doi.org/10.1016/j.jss.2013.01.005>.
- [311] S.B. Orr, A. Chainani, K.J. Hippensteel, A. Kishan, C. Gilchrist, N.W. Garrigues, D.S. Ruch, F. Guilak, D. Little, Aligned multilayered electrospun scaffolds for rotator cuff tendon tissue engineering, *Acta Biomater.* 24 (2015) 117–126. <https://doi.org/10.1016/j.actbio.2015.06.010>.
- [312] G. Gao, X. Cui, Three-dimensional bioprinting in tissue engineering and regenerative medicine, *Biotechnol. Lett.* 38 (2016) 203–211. <https://doi.org/10.1007/s10529-015-1975-1>.
- [313] T. Woodfield, K. Lim, P. Morouço, R. Levato, J. Malda, F. Melchels, 5.14 biofabrication in tissue engineering, *Compr. Biomater. II.* 5 (2017) 236–266.
- [314] X. Zhang, Y. Zhang, Tissue Engineering Applications of Three-Dimensional Bioprinting, *Cell Biochem. Biophys.* 72 (2015) 777–782. <https://doi.org/10.1007/s12013-015-0531-x>.
- [315] S. Derakhshanfar, R. Mbeleck, K. Xu, X. Zhang, W. Zhong, M. Xing, 3D bioprinting for biomedical devices and tissue engineering: A review of recent trends and advances, *Bioact. Mater.* 3 (2018) 144–156. <https://doi.org/10.1016/j.bioactmat.2017.11.008>.
- [316] N.A. Sears, D.R. Seshadri, P.S. Dhavalikar, E. Cosgriff-Hernandez, A

References

- review of three-dimensional printing in tissue engineering, *Tissue Eng. Part B Rev.* 22 (2016) 298–310. <https://doi.org/10.1089/ten.teb.2015.0464>
View article.
- [317] A.A. Zadpoor, Bone tissue regeneration: The role of scaffold geometry, *Biomater. Sci.* 3 (2015) 231–245. <https://doi.org/10.1039/c4bm00291a>.
- [318] L. Zhu, D. Luo, Y. Liu, Effect of the nano/microscale structure of biomaterial scaffolds on bone regeneration, *Int. J. Oral Sci.* 12 (2020) 1–15. <https://doi.org/10.1038/s41368-020-0073-y>.
- [319] A. Hasan, A. Paul, A. Memic, A. Khademhosseini, A multilayered microfluidic blood vessel-like structure, *Biomed. Microdevices.* 17 (2015) 88. <https://doi.org/10.1007/s10544-015-9993-2>.
- [320] A. Hasan, A. Paul, N.E. Vrana, X. Zhao, A. Memic, Y.S. Hwang, M.R. Dokmeci, A. Khademhosseini, Microfluidic techniques for development of 3D vascularized tissue, *Biomaterials.* 35 (2014) 7308–7325. <https://doi.org/10.1016/j.biomaterials.2014.04.091>.
- [321] J. Tien, Microfluidic approaches for engineering vasculature, *Curr. Opin. Chem. Eng.* 3 (2014) 36–41. <https://doi.org/10.1016/j.coche.2013.10.006>.
- [322] A.K. Miri, A. Khalilpour, B. Cecen, S. Maharjan, S.R. Shin, A. Khademhosseini, Multiscale bioprinting of vascularized models, *Biomaterials.* 198 (2019) 204–216. <https://doi.org/10.1016/j.biomaterials.2018.08.006>.
- [323] Y. Du, M. Ghodousi, H. Qi, N. Haas, W. Xiao, A. Khademhosseini, Sequential assembly of cell-laden hydrogel constructs to engineer vascular-like microchannels, *Biotechnol. Bioeng.* 108 (2011) 1693–1703. <https://doi.org/10.1002/bit.23102>.
- [324] J.J. Stankus, L. Soletti, K. Fujimoto, Y. Hong, D.A. Vorp, W.R. Wagner, Fabrication of cell microintegrated blood vessel constructs through electrohydrodynamic atomization, *Biomaterials.* 28 (2007) 2738–2746. <https://doi.org/10.1016/j.biomaterials.2007.02.012>.
- [325] P. Coimbra, P. Santos, P. Alves, S.P. Miguel, M.P. Carvalho, K.D. de Sá, I.J. Correia, P. Ferreira, Coaxial electrospun PCL/Gelatin-MA fibers as scaffolds for vascular tissue engineering, *Colloids Surfaces B Biointerfaces.* 159 (2017) 7–15. <https://doi.org/10.1016/j.colsurfb.2017.07.065>.
- [326] L. Ye, J. Cao, L. Chen, X. Geng, A.-Y. Zhang, L.-R. Guo, Y.-Q. Gu, Z.-G. Feng, The fabrication of double layer tubular vascular tissue engineering scaffold *via* coaxial electrospinning and its 3D cell coculture, *J. Biomed. Mater. Res. Part A.* 103 (2015) 3863–3871. <https://doi.org/10.1002/jbm.a.35531>.
- [327] N. Duan, X. Geng, L. Ye, A. Zhang, Z. Feng, L. Guo, Y. Gu, A vascular tissue engineering scaffold with core–shell structured nano-fibers formed

- by coaxial electrospinning and its biocompatibility evaluation, *Biomed. Mater.* 11 (2016) 035007. <https://doi.org/10.1088/1748-6041/11/3/035007>.
- [328] Y.M. Ju, J.S. Choi, A. Atala, J.J. Yoo, S.J. Lee, Bilayered scaffold for engineering cellularized blood vessels, *Biomaterials.* 31 (2010) 4313–4321. <https://doi.org/10.1016/j.biomaterials.2010.02.002>.
- [329] W. Jia, P.S. Gungor-Ozkerim, Y.S. Zhang, K. Yue, K. Zhu, W. Liu, Q. Pi, B. Byambaa, M.R. Dokmeci, S.R. Shin, A. Khademhosseini, Direct 3D bioprinting of perfusable vascular constructs using a blend bioink, *Biomaterials.* 106 (2016) 58–68. <https://doi.org/10.1016/j.biomaterials.2016.07.038>.
- [330] Q. Pi, S. Maharjan, X. Yan, X. Liu, B. Singh, A.M. van Genderen, F. Robledo-Padilla, R. Parra-Saldivar, N. Hu, W. Jia, C. Xu, J. Kang, S. Hassan, H. Cheng, X. Hou, A. Khademhosseini, Y.S. Zhang, Digitally Tunable Microfluidic Bioprinting of Multilayered Cannular Tissues, *Adv. Mater.* 30 (2018) 1706913. <https://doi.org/10.1002/adma.201706913>.
- [331] O. Kérourédan, D. Hakobyan, M. Rémy, S. Ziane, N. Dusserre, J.-C. Fricain, S. Delmond, N.B. Thébaud, R. Devillard, In situ prevascularization designed by laser-assisted bioprinting: effect on bone regeneration, *Biofabrication.* 11 (2019) 045002. <https://doi.org/10.1088/1758-5090/ab2620>.
- [332] D. Shahriari, G. Loke, I. Tafel, S. Park, P.H. Chiang, Y. Fink, P. Anikeeva, Scalable Fabrication of Porous Microchannel Nerve Guidance Scaffolds with Complex Geometries, *Adv. Mater.* 31 (2019) 1902021. <https://doi.org/10.1002/adma.201902021>.
- [333] I. Stankovic, Pullulan Chemical and Technical Assessment, *Clin. Tech. Assess.* 65th JECFA. (2002) 1–8.
- [334] K.C. Cheng, A. Demirci, J.M. Catchmark, Pullulan: Biosynthesis, production, and applications, *Appl. Microbiol. Biotechnol.* 92 (2011) 29–44. <https://doi.org/10.1007/s00253-011-3477-y>.
- [335] R.S. Singh, N. Kaur, V. Rana, J.F. Kennedy, Recent insights on applications of pullulan in tissue engineering, *Carbohydr. Polym.* 153 (2016) 455–462. <https://doi.org/10.1016/j.carbpol.2016.07.118>.
- [336] M.R. Rekha, C.P. Sharma, Pullulan as a promising biomaterial for biomedical applications: a perspective, *Trends Biomater Artif Organs.* 20 (2007) 116–121.
- [337] A. Autissier, D. Letourneur, C. Le Visage, Pullulan-based hydrogel for smooth muscle cell culture, *J. Biomed. Mater. Res. - Part A.* 82 (2007) 336–342. <https://doi.org/10.1002/jbm.a.30998>.
- [338] C. Le Visage, D. Letourneur, US9522218B2 - Method for preparing porous scaffold for tissue engineering, cell culture and cell delivery - Google Patents, WO2009/047346, n.d.

References

- <https://patents.google.com/patent/US9522218B2/en> (accessed May 31, 2021).
- [339] M. Naessens, A. Cerdobbel, W. Soetaert, E.J. Vandamme, Leuconostoc dextranucrase and dextran: Production, properties and applications, *J. Chem. Technol. Biotechnol.* 80 (2005) 845–860. <https://doi.org/10.1002/jctb.1322>.
- [340] G. Sun, J.J. Mao, Engineering dextran-based scaffolds for drug delivery and tissue repair, *Nanomedicine.* 7 (2012) 1771–1784. <https://doi.org/10.2217/nnm.12.149>.
- [341] B. Trappmann, B.M. Baker, W.J. Polacheck, C.K. Choi, J.A. Burdick, C.S. Chen, Matrix degradability controls multicellularity of 3D cell migration, *Nat. Commun.* 8 (2017) 1–8. <https://doi.org/10.1038/s41467-017-00418-6>.
- [342] K. Lin, D. Zhang, M.H. Macedo, W. Cui, B. Sarmiento, G. Shen, Advanced Collagen-Based Biomaterials for Regenerative Biomedicine, *Adv. Funct. Mater.* 29 (2019) 1804943. <https://doi.org/10.1002/adfm.201804943>.
- [343] N. Gostynska, G.S. Krishnakumar, E. Campodoni, S. Panseri, M. Montesi, S. Sprio, E. Kon, M. Marcacci, A. Tampieri, M. Sandri, 3D porous collagen scaffolds reinforced by glycation with ribose for tissue engineering application, *Biomed. Mater.* 12 (2017) 055002. <https://doi.org/10.1088/1748-605X/AA7694>.
- [344] E. Breel, Characterizing the micro-mechanical properties of immersed hydrogels by nanoindentation., *Tech. Rep.* (2015). <https://doi.org/10.13140/2.1.3580.9606>.
- [345] A.R. do Vale Morais, É. do Nascimento Alencar, F.H.X. Júnior, C.M. De Oliveira, H.R. Marcelino, G. Barratt, H. Fessi, E.S.T. Do Egito, A. Elaissari, Freeze-drying of emulsified systems: A review, *Int. J. Pharm.* 503 (2016) 102–114. <https://doi.org/10.1016/j.ijpharm.2016.02.047>.
- [346] L. Rittié, Method for picosirius red-polarization detection of collagen fibers in tissue sections, in: *Methods Mol. Biol.*, Humana Press Inc., 2017: pp. 395–407. https://doi.org/10.1007/978-1-4939-7113-8_26.
- [347] C.G. Fuentes-Corona, J. Licea-Rodriguez, R. Younger, R. Rangel-Rojo, E.O. Potma, I. Rocha-Mendoza, Second harmonic generation signal from type I collagen fibers grown in vitro, *Biomed. Opt. Express.* 10 (2019) 6449. <https://doi.org/10.1364/boe.10.006449>.
- [348] X. Chen, O. Nadiarynkh, S. Plotnikov, P.J. Campagnola, Second harmonic generation microscopy for quantitative analysis of collagen fibrillar structure, *Nat. Protoc.* 7 (2012) 654–669. <https://doi.org/10.1038/nprot.2012.009>.
- [349] R.M. Williams, W.R. Zipfel, W.W. Webb, Interpreting second-harmonic generation images of collagen I fibrils, *Biophys. J.* 88 (2005) 1377–1386. <https://doi.org/10.1529/biophysj.104.047308>.

- [350] P.J. Campagnola, A.C. Millard, M. Terasaki, P.E. Hoppe, C.J. Malone, W.A. Mohler, Three-dimensional high-resolution second-harmonic generation imaging of endogenous structural proteins in biological tissues, *Biophys. J.* 82 (2002) 493–508. [https://doi.org/10.1016/S0006-3495\(02\)75414-3](https://doi.org/10.1016/S0006-3495(02)75414-3).
- [351] E.G. Pendleton, K.F. Tehrani, R.P. Barrow, L.J. Mortensen, Second harmonic generation characterization of collagen in whole bone, *Biomed. Opt. Express.* 11 (2020) 4379–4396. <https://doi.org/10.1364/BOE.391866>.
- [352] Q.L. Loh, C. Choong, Three-dimensional scaffolds for tissue engineering applications: Role of porosity and pore size, *Tissue Eng. - Part B Rev.* 19 (2013) 485–502. <https://doi.org/10.1089/ten.teb.2012.0437>.
- [353] J. Grenier, H. Duval, F. Barou, P. Lv, B. David, D. Letourneur, Mechanisms of pore formation in hydrogel scaffolds textured by freeze-drying, *Acta Biomater.* 94 (2019) 195–203. <https://doi.org/10.1016/j.actbio.2019.05.070>.
- [354] S. Lack, V. Dulong, D. Le Cerf, L. Picton, J.F. Argillier, G. Muller, Hydrogels based on pullulan crosslinked with sodium trimetaphosphate (STMP): Rheological study, *Polym. Bull.* 52 (2004) 429–436. <https://doi.org/10.1007/s00289-004-0299-4>.
- [355] J. Varani, S.E.G. Fligiel, D.R. Inman, T.F. Beals, W.J. Hillegas, Modulation of adhesive properties of DEAE-dextran with laminin, *J. Biomed. Mater. Res.* 29 (1995) 993–997. <https://doi.org/10.1002/jbm.820290811>.
- [356] M.-N. Labour, C. Le Guilcher, R. Aid-Launais, N. El Samad, S. Lanouar, T. Simon-Yarza, D. Letourneur, Development of 3D Hepatic Constructs Within Polysaccharide-Based Scaffolds with Tunable Properties, *Int. J. Mol. Sci.* 21 (2020) 3644. <https://doi.org/10.3390/ijms21103644>.
- [357] T. Riaz, R. Zeeshan, F. Zarif, K. Ilyas, N. Muhammad, S.Z. Safi, A. Rahim, S.A.A. Rizvi, I.U. Rehman, FTIR analysis of natural and synthetic collagen, *Appl. Spectrosc. Rev.* 53 (2018) 703–746. <https://doi.org/10.1080/05704928.2018.1426595>.
- [358] G.S. Krishnakumar, N. Gostynska, E. Campodoni, M. Dapporto, M. Montesi, S. Panseri, A. Tampieri, E. Kon, M. Marcacci, S. Sprio, Ribose mediated crosslinking of collagen-hydroxyapatite hybrid scaffolds for bone tissue regeneration using biomimetic strategies, *Mater. Sci. Eng. C.* 77 (2017) 594–605. <https://doi.org/10.1016/j.msec.2017.03.255>.
- [359] J. Kong, S. Yu, Fourier transform infrared spectroscopic analysis of protein secondary structures, *Acta Biochim. Biophys. Sin. (Shanghai)*. 39 (2007) 549–559. <https://doi.org/10.1111/j.1745-7270.2007.00320.x>.
- [360] N.P. Camacho, P. West, P.A. Torzilli, R. Mendelsohn, FTIR microscopic imaging of collagen and proteoglycan in bovine cartilage, *Biopolym. Orig. Res. Biomol.* 62 (2001) 1–8. <https://doi.org/10.1002/1097->

References

- 0282(2001)62:1<1::AID-BIP10>3.0.CO;2-O.
- [361] Y. Maréchal, The molecular structure of liquid water delivered by absorption spectroscopy in the whole IR region completed with thermodynamics data, *J. Mol. Struct.* 1004 (2011) 146–155. <https://doi.org/10.1016/J.MOLSTRUC.2011.07.054>.
- [362] N.N. Bailore, S.K. Balladka, S.J.D.S. Doddapaneni, M.S. Mudiaryu, Fabrication of Environmentally Compatible Biopolymer Films of Pullulan/Piscine Collagen/ZnO Nanocomposite and Their Antifungal Activity, *J. Polym. Environ.* 29 (2021) 1192–1201. <https://doi.org/10.1007/s10924-020-01953-y>.
- [363] S. Iswariya, A. V. Bhanukeerthi, P. Velswamy, T.S. Uma, P.T. Perumal, Design and development of a piscine collagen blended pullulan hydrogel for skin tissue engineering, *RSC Adv.* 6 (2016) 57863–57871. <https://doi.org/10.1039/c6ra03578g>.
- [364] G.G. Giobbe, C. Crowley, C. Luni, S. Campinoti, M. Khedr, K. Kretzschmar, M.M. De Santis, E. Zambaiti, F. Michielin, L. Meran, Extracellular matrix hydrogel derived from decellularized tissues enables endodermal organoid culture, *Nat. Commun.* 10 (2019) 1–14. <https://doi.org/10.1038/s41467-019-13605-4>.
- [365] L. Qian, H. Zhao, Nanoindentation of soft biological materials, *Micromachines.* 9 (2018) 654. <https://doi.org/10.3390/mi9120654>.
- [366] T.H. Qazi, D.J. Mooney, G.N. Duda, S. Geissler, Niche-mimicking interactions in peptide-functionalized 3D hydrogels amplify mesenchymal stromal cell paracrine effects, *Biomaterials.* 230 (2020) 119639. <https://doi.org/10.1016/j.biomaterials.2019.119639>.
- [367] S. V Kontomaris, A. Malamou, Hertz model or Oliver & Pharr analysis? Tutorial regarding AFM nanoindentation experiments on biological samples, *Mater. Res. Express.* 7 (2020) 33001. <https://doi.org/10.1088/2053-1591/ab79ce>.
- [368] H. Li, J. Yang, X. Hu, J. Liang, Y. Fan, X. Zhang, Superabsorbent polysaccharide hydrogels based on pullulan derivate as antibacterial release wound dressing, *J. Biomed. Mater. Res. - Part A.* 98 A (2011) 31–39. <https://doi.org/10.1002/jbm.a.33045>.
- [369] D. Atila, D. Keskin, A. Tezcaner, Crosslinked pullulan/cellulose acetate fibrous scaffolds for bone tissue engineering, *Mater. Sci. Eng. C.* 69 (2016) 1103–1115. <https://doi.org/10.1016/j.msec.2016.08.015>.
- [370] G. Selvakumar, S. Lonchin, Fabrication and characterization of collagen-oxidized pullulan scaffold for biomedical applications, *Int. J. Biol. Macromol.* 164 (2020) 1592–1599. <https://doi.org/10.1016/j.ijbiomac.2020.07.264>.
- [371] G. Della Giustina, A. Gandin, L. Brigo, T. Panciera, S. Giullitti, P.

- Sgarbossa, D. D'Alessandro, L. Trombi, S. Danti, G. Brusatin, Polysaccharide hydrogels for multiscale 3D printing of pullulan scaffolds, *Mater. Des.* 165 (2019) 107566. <https://doi.org/10.1016/j.matdes.2018.107566>.
- [372] J.P. Gleeson, N.A. Plunkett, F.J. O'Brien, Addition of hydroxyapatite improves stiffness, interconnectivity and osteogenic potential of a highly porous collagen-based scaffold for bone tissue regeneration, *Eur. Cells Mater.* 20 (2010) 218–230. <https://doi.org/10.22203/eCM.v020a18>.
- [373] B.N. Mason, A. Starchenko, R.M. Williams, L.J. Bonassar, C.A. Reinhart-King, Tuning three-dimensional collagen matrix stiffness independently of collagen concentration modulates endothelial cell behavior, *Acta Biomater.* 9 (2013) 4635–4644. <https://doi.org/10.1016/j.actbio.2012.08.007>.
- [374] S.A. Ghodbane, M.G. Dunn, Physical and mechanical properties of cross-linked type I collagen scaffolds derived from bovine, porcine, and ovine tendons, *J. Biomed. Mater. Res. Part A.* 104 (2016) 2685–2692. <https://doi.org/10.1002/jbm.a.35813>.
- [375] C.F. Guimarães, L. Gasperini, A.P. Marques, R.L. Reis, The stiffness of living tissues and its implications for tissue engineering, *Nat. Rev. Mater.* 5 (2020) 351–370. <https://doi.org/10.1038/s41578-019-0169-1>.
- [376] W. Megone, N. Roohpour, J.E. Gautrot, Impact of surface adhesion and sample heterogeneity on the multiscale mechanical characterisation of soft biomaterials, *Sci. Rep.* 8 (2018) 6780. <https://doi.org/10.1038/s41598-018-24671-x>.
- [377] C.F. Guimarães, L. Gasperini, A.P. Marques, R.L. Reis, The stiffness of living tissues and its implications for tissue engineering, *Nat. Rev. Mater.* 5 (2020) 351–370. <https://doi.org/10.1038/s41578-019-0169-1>.
- [378] N. Fekete, A. V Béland, K. Campbell, S.L. Clark, C.A. Hoesli, Bags versus flasks: a comparison of cell culture systems for the production of dendritic cell-based immunotherapies, *Transfusion.* 58 (2018) 1800–1813. <https://doi.org/10.1111/trf.14621>.
- [379] A. Vedadghavami, F. Minooei, M.H. Mohammadi, S. Khetani, A.R. Kolahchi, S. Mashayekhan, A. Sanati-Nezhad, Manufacturing of hydrogel biomaterials with controlled mechanical properties for tissue engineering applications, *Acta Biomater.* 62 (2017) 42–63. <https://doi.org/10.1016/j.actbio.2017.07.028>.
- [380] C. Hu, Y. Chen, M.J.A. Tan, K. Ren, H. Wu, Microfluidic technologies for vasculature biomimicry, *Analyst.* 144 (2019) 4461–4471. <https://doi.org/10.1039/c9an00421a>.
- [381] K. Haase, R.D. Kamm, Advances in on-chip vascularization, *Regen. Med.* 12 (2017) 285–302. <https://doi.org/10.2217/rme-2016-0152>.
- [382] H. Jian, M. Wang, S. Wang, A. Wang, S. Bai, 3D bioprinting for cell

References

- culture and tissue fabrication, *Bio-Design Manuf.* 1 (2018) 45–61. <https://doi.org/10.1007/s42242-018-0006-1>.
- [383] M. Domenech, L. Polo-Corrales, J.E. Ramirez-Vick, D.O. Freytes, Tissue engineering strategies for myocardial regeneration: acellular versus cellular scaffolds?, *Tissue Eng. Part B Rev.* 22 (2016) 438–458. <https://doi.org/10.1089/ten.TEB.2015.0523>.
- [384] J. Gilbert-Honick, S.R. Iyer, S.M. Somers, R.M. Lovering, K. Wagner, H.-Q. Mao, W.L. Grayson, Engineering functional and histological regeneration of vascularized skeletal muscle, *Biomaterials.* 164 (2018) 70–79. <https://doi.org/10.1016/j.biomaterials.2018.02.006>.
- [385] D.S.Y. Lin, F. Guo, B. Zhang, Modeling organ-specific vasculature with organ-on-a-chip devices, *Nanotechnology.* 30 (2019) 024002. <https://doi.org/10.1088/1361-6528/AAE7DE>.
- [386] S. Kim, W. Kim, S. Lim, J.S. Jeon, Vasculature-on-a-chip for in vitro disease models, *Bioengineering.* 4 (2017). <https://doi.org/10.3390/bioengineering4010008>.
- [387] A.D. Bannerman, R.X. Ze Lu, A. Korolj, L.H. Kim, M. Radisic, The use of microfabrication technology to address the challenges of building physiologically relevant vasculature, *Curr. Opin. Biomed. Eng.* 6 (2018) 8–16. <https://doi.org/10.1016/j.cobme.2017.12.003>.
- [388] D. Antoni, H. Burckel, E. Josset, G. Noel, Three-Dimensional Cell Culture: A Breakthrough in Vivo, *Int. J. Mol. Sci.* 16 (2015) 5517–5527. <https://doi.org/10.3390/ijms16035517>.
- [389] S. Jalili-Firoozinezhad, M. Filippi, F. Mohabatpour, D. Letourneur, A. Scherberich, Chicken egg white: Hatching of a new old biomaterial, *Mater. Today.* 40 (2020) 193–214. <https://doi.org/10.1016/j.mattod.2020.05.022>.
- [390] F.A. Auger, L. Gibot, D. Lacroix, The Pivotal Role of Vascularization in Tissue Engineering, *Annu. Rev. Biomed. Eng.* 15 (2013) 177–200. <https://doi.org/10.1146/annurev-bioeng-071812-152428>.
- [391] W.D. Tucker, K. Mahajan, *Anatomy, Blood Vessels*, StatPearls Publishing, 2018. <http://www.ncbi.nlm.nih.gov/pubmed/29262226> (accessed December 17, 2020).
- [392] E. Witzleb, Functions of the Vascular System, in: *Hum. Physiol.*, Springer Berlin Heidelberg, 1989: pp. 480–542. https://doi.org/10.1007/978-3-642-73831-9_20.
- [393] E. Bianconi, A. Piovesan, F. Facchin, A. Beraudi, R. Casadei, F. Frabetti, L. Vitale, M.C. Pelleri, S. Tassani, F. Piva, S. Perez-Amodio, P. Strippoli, S. Canaider, An estimation of the number of cells in the human body, *Ann. Hum. Biol.* 40 (2013) 463–471. <https://doi.org/10.3109/03014460.2013.807878>.
- [394] A. Dellaquila, C. Le Bao, D. Letourneur, T. Simon-Yarza, *In Vitro*

- Strategies to Vascularize 3D Physiologically Relevant Models, *Adv. Sci.* (2021) 2100798. <https://doi.org/10.1002/ADVS.202100798>.
- [395] L.K. Fiddes, N. Raz, S. Srigunapalan, E. Tumarkan, C.A. Simmons, A.R. Wheeler, E. Kumacheva, A circular cross-section PDMS microfluidics system for replication of cardiovascular flow conditions, *Biomaterials*. 31 (2010) 3459–3464. <https://doi.org/10.1016/j.biomaterials.2010.01.082>.
- [396] J. He, R. Chen, Y. Lu, L. Zhan, Y. Liu, D. Li, Z. Jin, Fabrication of circular microfluidic network in enzymatically-crosslinked gelatin hydrogel, *Mater. Sci. Eng. C*. 59 (2016) 53–60. <https://doi.org/10.1016/j.msec.2015.09.104>.
- [397] T. Simon-Yarza, M.N. Labour, R. Aid, D. Letourneur, Channeled polysaccharide-based hydrogel reveals influence of curvature to guide endothelial cell arrangement in vessel-like structures, *Mater. Sci. Eng. C*. 118 (2021) 111369. <https://doi.org/10.1016/j.msec.2020.111369>.
- [398] K.K. Sørensen, P. McCourt, T. Berg, C. Crossley, D. Le Couteur, K. Wake, B. Smedsrød, The scavenger endothelial cell: a new player in homeostasis and immunity, *Am. J. Physiol. Integr. Comp. Physiol.* 303 (2012) R1217–R1230. <https://doi.org/10.1152/ajpregu.00686.2011>.
- [399] T. Tilling, D. Korte, D. Hoheisel, H.J. Galla, Basement membrane proteins influence brain capillary endothelial barrier function in vitro, *J. Neurochem.* 71 (1998) 1151–1157. <https://doi.org/10.1046/j.1471-4159.1998.71031151.x>.
- [400] Y. Kubota, H.K. Kleinman, G.R. Martin, T.J. Lawley, Role of laminin and basement membrane in the morphological differentiation of human endothelial cells into capillary-like structures., *J. Cell Biol.* 107 (1988) 1589–1598. <https://doi.org/10.1083/jcb.107.4.1589>.
- [401] D.M. Form, B.M. Pratt, J.A. Madri, Endothelial cell proliferation during angiogenesis. In vitro modulation by basement membrane components, *Lab. Investig.* 55 (1986) 521–530. <https://europepmc.org/article/med/2430138> (accessed December 18, 2020).
- [402] J.S. Lowe, P.G. Anderson, Support Cells and the Extracellular Matrix, in: *Stevens Lowes Hum. Histol.*, Elsevier, 2015: pp. 55–70. <https://doi.org/10.1016/b978-0-7234-3502-0.00004-8>.
- [403] J.H. Miner, N.M. Nguyen, Extracellular Matrix, in: *Encycl. Respir. Med. Four-Volume Set*, Elsevier Inc., 2006: pp. 157–162. <https://doi.org/10.1016/B0-12-370879-6/00143-5>.
- [404] S. Kim, H. Lee, M. Chung, N.L. Jeon, Engineering of functional, perfusable 3D microvascular networks on a chip, *Lab Chip*. 13 (2013) 1489–1500. <https://doi.org/10.1039/c3lc41320a>.
- [405] R. Pimentel C., S.K. Ko, C. Caviglia, A. Wolff, J. Emnéus, S.S. Keller, M. Dufva, Three-dimensional fabrication of thick and densely populated soft

References

- constructs with complex and actively perfused channel network, *Acta Biomater.* 65 (2018) 174–184.
<https://doi.org/10.1016/j.actbio.2017.10.047>.
- [406] M. Chaouat, C. Le Visage, W.E. Baille, B. Escoubet, F. Chaubet, M.A. Mateescu, D. Letourneur, A novel cross-linked poly(vinyl alcohol) (PVA) for vascular grafts, *Adv. Funct. Mater.* 18 (2008) 2855–2861.
<https://doi.org/10.1002/adfm.200701261>.
- [407] M. Atlan, T. Simon-Yarza, J.M. Ino, V. Hunsinger, L. Corté, P. Ou, R. Aid-Launais, M. Chaouat, D. Letourneur, Design, characterization and in vivo performance of synthetic 2 mm-diameter vessel grafts made of PVA-gelatin blends, *Sci. Rep.* 8 (2018) 7417. <https://doi.org/10.1038/s41598-018-25703-2>.
- [408] A. Ovsianikov, A. Khademhosseini, V. Mironov, The synergy of scaffold-based and scaffold-free tissue engineering strategies, *Trends Biotechnol.* 36 (2018) 348–357. <https://doi.org/10.1016/j.tibtech.2018.01.005>.
- [409] C. Norotte, F.S. Marga, L.E. Niklason, G. Forgacs, Scaffold-free vascular tissue engineering using bioprinting, *Biomaterials.* 30 (2009) 5910–5917.
<https://doi.org/10.1016/j.biomaterials.2009.06.034>.
- [410] F.C. Teixeira, S. Chaves, A.L. Torres, C.C. Barrias, S.J. Bidarra, Engineering a Vascularized 3D Hybrid System to Model Tumor-Stroma Interactions in Breast Cancer, *Front. Bioeng. Biotechnol.* 9 (2021) 166.
<https://doi.org/10.3389/fbioe.2021.647031>.
- [411] S. Chen, N. Kawazoe, G. Chen, Biomimetic Assembly of Vascular Endothelial Cells and Muscle Cells in Microgrooved Collagen Porous Scaffolds, *Tissue Eng. - Part C Methods.* 23 (2017) 367–376.
<https://doi.org/10.1089/ten.tec.2017.0088>.
- [412] E. Ercolani, C. Del Gaudio, A. Bianco, Vascular tissue engineering of small-diameter blood vessels: Reviewing the electrospinning approach, *J. Tissue Eng. Regen. Med.* 9 (2015) 861–888.
<https://doi.org/10.1002/term.1697>.
- [413] S. Salerno, F. Tasselli, E. Drioli, L. De Bartolo, Poly (ϵ -Caprolactone) Hollow Fiber Membranes for the Biofabrication of a Vascularized Human Liver Tissue, *Membranes (Basel).* 10 (2020) 112.
<https://doi.org/10.3390/membranes10060112>.
- [414] M.D. Sarker, S. Naghieh, N.K. Sharma, X. Chen, 3D biofabrication of vascular networks for tissue regeneration: A report on recent advances, *J. Pharm. Anal.* 8 (2018) 277–296.
<https://doi.org/10.1016/j.jpha.2018.08.005>.
- [415] G. Yang, B. Mahadik, J.Y. Choi, J.P. Fisher, Vascularization in tissue engineering: fundamentals and state-of-art, *Prog. Biomed. Eng.* 2 (2020) 012002. <https://doi.org/10.1088/2516-1091/ab5637>.

- [416] S. Ramesh, Y. Zhang, D.R. Cormier, I. V Rivero, O.L.A. Harrysson, P.K. Rao, A. Tamayol, Extrusion bioprinting: Recent progress, challenges, and future opportunities, *Bioprinting*. 21 (2020) e00116. <https://doi.org/10.1016/j.bprint.2020.e00116>.
- [417] A. Kjar, B. McFarland, K. Mecham, N. Harward, Y. Huang, Engineering of tissue constructs using coaxial bioprinting, *Bioact. Mater.* 6 (2021) 460–471. <https://doi.org/10.1016/j.bioactmat.2020.08.020>.
- [418] L. Shao, Q. Gao, C. Xie, J. Fu, M. Xiang, Y. He, Directly coaxial 3D bioprinting of large-scale vascularized tissue constructs, *Biofabrication*. 12 (2020). <https://doi.org/10.1088/1758-5090/ab7e76>.
- [419] P.D. Dalton, T.B.F. Woodfield, V. Mironov, J. Groll, Advances in Hybrid Fabrication toward Hierarchical Tissue Constructs, *Adv. Sci.* 7 (2020). <https://doi.org/10.1002/advs.201902953>.
- [420] S. Knowlton, B. Yenilmez, S. Tasoglu, Towards Single-Step Biofabrication of Organs on a Chip via 3D Printing, *Trends Biotechnol.* 34 (2016) 685–688. <https://doi.org/10.1016/j.tibtech.2016.06.005>.
- [421] M. Yeo, G.H. Kim, Micro/nano-hierarchical scaffold fabricated using a cell electrospinning/3D printing process for co-culturing myoblasts and HUVECs to induce myoblast alignment and differentiation, *Acta Biomater.* 107 (2020) 102–114. <https://doi.org/10.1016/j.actbio.2020.02.042>.
- [422] F. Yu, D. Choudhury, Microfluidic bioprinting for organ-on-a-chip models, *Drug Discov. Today*. 24 (2019) 1248–1257. <https://doi.org/10.1016/j.drudis.2019.03.025>.
- [423] K.A. Homan, N. Gupta, K.T. Kroll, D.B. Kolesky, M. Skylar-Scott, T. Miyoshi, D. Mau, M.T. Valerius, T. Ferrante, J. V. Bonventre, J.A. Lewis, R. Morizane, Flow-enhanced vascularization and maturation of kidney organoids in vitro, *Nat. Methods*. 16 (2019) 255–262. <https://doi.org/10.1038/s41592-019-0325-y>.
- [424] V. van Duinen, D. Zhu, C. Ramakers, A.J. van Zonneveld, P. Vulto, T. Hankemeier, Perfused 3D angiogenic sprouting in a high-throughput in vitro platform, *Angiogenesis*. 22 (2019) 157–165. <https://doi.org/10.1007/s10456-018-9647-0>.
- [425] W.Y. Wang, D. Lin, E.H. Jarman, W.J. Polacheck, B.M. Baker, Functional angiogenesis requires microenvironmental cues balancing endothelial cell migration and proliferation, *Lab Chip*. 20 (2020) 1153–1166. <https://doi.org/10.1039/c9lc01170f>.
- [426] R. Pimentel C., S.K. Ko, C. Caviglia, A. Wolff, J. Emnéus, S.S. Keller, M. Dufva, Three-dimensional fabrication of thick and densely populated soft constructs with complex and actively perfused channel network, *Acta Biomater.* 65 (2018) 174–184. <https://doi.org/10.1016/j.actbio.2017.10.047>.

References

- [427] K.A. Heintz, M.E. Bregenzer, J.L. Mantle, K.H. Lee, J.L. West, J.H. Slater, Fabrication of 3D Biomimetic Microfluidic Networks in Hydrogels, *Adv. Healthc. Mater.* 5 (2016) 2153–2160. <https://doi.org/10.1002/adhm.201600351>.
- [428] A. Geraili, P. Jafari, M.S. Hassani, B.H. Araghi, M.H. Mohammadi, A.M. Ghafari, S.H. Tamrin, H.P. Modarres, A.R. Kolahchi, S. Ahadian, A. Sanati-Nezhad, Controlling Differentiation of Stem Cells for Developing Personalized Organ-on-Chip Platforms, *Adv. Healthc. Mater.* 7 (2018) 1700426. <https://doi.org/10.1002/adhm.201700426>.
- [429] J. Drost, H. Clevers, Organoids in cancer research, *Nat. Rev. Cancer.* 18 (2018) 407–418. <https://doi.org/10.1038/s41568-018-0007-6>.
- [430] L.A. van Grunsven, 3D in vitro models of liver fibrosis, *Adv. Drug Deliv. Rev.* 121 (2017) 133–146. <https://doi.org/10.1016/j.addr.2017.07.004>.
- [431] K.H.K. Wong, J.G. Truslow, A.H. Khankhel, K.L.S. Chan, J. Tien, Artificial lymphatic drainage systems for vascularized microfluidic scaffolds, *J. Biomed. Mater. Res. Part A.* 101A (2013) 2181–2190. <https://doi.org/10.1002/jbm.a.34524>.
- [432] M. Sato, N. Sasaki, M. Ato, S. Hirakawa, K. Sato, K. Sato, Microcirculation-on-a-Chip: A Microfluidic Platform for Assaying Blood- and Lymphatic-Vessel Permeability, (2015). <https://doi.org/10.1371/journal.pone.0137301>.
- [433] I. Choi, S. Lee, Y.K. Hong, The new era of the lymphatic system: No longer secondary to the blood vascular system, *Cold Spring Harb. Perspect. Med.* 2 (2012). <https://doi.org/10.1101/cshperspect.a006445>.
- [434] A. Aspelund, M.R. Robciuc, S. Karaman, T. Makinen, K. Alitalo, Lymphatic System in Cardiovascular Medicine, *Circ. Res.* 118 (2016) 515–530. <https://doi.org/10.1161/CIRCRESAHA.115.306544>.
- [435] T.P. Padera, E.F.J. Meijer, L.L. Munn, The Lymphatic System in Disease Processes and Cancer Progression, *Annu. Rev. Biomed. Eng.* 18 (2016) 125–158. <https://doi.org/10.1146/annurev-bioeng-112315-031200>.
- [436] S. Yasotharan, S. Pinto, J.G. Sled, S.S. Bolz, A. Günther, Artery-on-a-chip platform for automated, multimodal assessment of cerebral blood vessel structure and function, *Lab Chip.* 15 (2015) 2660–2669. <https://doi.org/10.1039/c5lc00021a>.
- [437] R. Novak, M. Ingram, S. Marquez, D. Das, A. Delahanty, A. Herland, B.M. Maoz, S.S.F. Jeanty, M.R. Somayaji, M. Burt, E. Calamari, A. Chalkiadaki, A. Cho, Y. Choe, D.B. Chou, M. Cronce, S. Dauth, T. Divic, J. Fernandez-Alcon, T. Ferrante, J. Ferrier, E.A. FitzGerald, R. Fleming, S. Jalili-Firoozinezhad, T. Grevesse, J.A. Goss, T. Hamkins-Indik, O. Henry, C. Hinojosa, T. Huffstater, K.-J. Jang, V. Kujala, L. Leng, R. Mannix, Y. Milton, J. Nawroth, B.A. Nestor, C.F. Ng, B. O'Connor, T.-E. Park, H. Sanchez, J. Sliz, A. Sontheimer-Phelps, B. Swenor, G. Thompson, G.J.

- Touloumes, Z. Tranchemontagne, N. Wen, M. Yadid, A. Bahinski, G.A. Hamilton, D. Levner, O. Levy, A. Przekwas, R. Prantil-Baun, K.K. Parker, D.E. Ingber, Robotic fluidic coupling and interrogation of multiple vascularized organ chips, *Nat. Biomed. Eng.* 4 (2020) 407–420. <https://doi.org/10.1038/s41551-019-0497-x>.
- [438] J.P. Wiksw, F.E. Block, D.E. Cliffler, C.R. Goodwin, C.C. Marasco, D.A. Markov, D.L. McLean, J.A. McLean, J.R. McKenzie, R.S. Reiserer, P.C. Samson, D.K. Schaffer, K.T. Seale, S.D. Sherrod, Engineering challenges for instrumenting and controlling integrated organ-on-chip systems, *IEEE Trans. Biomed. Eng.* 60 (2013) 682–690. <https://doi.org/10.1109/TBME.2013.2244891>.
- [439] Y.S. Zhang, Q. Pi, A.M. van Genderen, Microfluidic bioprinting for engineering vascularized tissues and organoids, *J. Vis. Exp.* 2017 (2017) 1–8. <https://doi.org/10.3791/55957>.
- [440] J.F. Wong, M.D. Mohan, E.W.K. Young, C.A. Simmons, Integrated electrochemical measurement of endothelial permeability in a 3D hydrogel-based microfluidic vascular model, *Biosens. Bioelectron.* 147 (2020) 111757. <https://doi.org/10.1016/j.bios.2019.111757>.
- [441] C.G. Mackenzie, J.B. Mackenzie, P. Beck, The effect of pH on growth, protein synthesis, and lipid-rich particles of cultured mammalian cells, *J. Cell Biol.* 9 (1961) 141–156.
- [442] M. Ikebuchi, A. Kashiwagi, T. Asahina, Y. Tanaka, Y. Takagi, Y. Nishio, H. Hidaka, R. Kikkawa, Y. Shigeta, Effect of medium pH on glutathione redox cycle in cultured human umbilical vein endothelial cells, *Metabolism.* 42 (1993) 1121–1126. [https://doi.org/10.1016/0026-0495\(93\)90269-T](https://doi.org/10.1016/0026-0495(93)90269-T).
- [443] D.E. Ingber, D. Prusty, J. V Frangioni, E.J. Cragoe Jr, C. Lechene, M.A. Schwartz, Control of intracellular pH and growth by fibronectin in capillary endothelial cells., *J. Cell Biol.* 110 (1990) 1803–1811. <https://doi.org/10.1083/jcb.110.5.1803>.
- [444] A. Abdal-Hay, A. Memic, K.H. Hussein, Y.S. Oh, M. Fouad, F.F. Al-Jassir, H.-M. Woo, Y. Morsi, X. Mo, S. Ivanovski, Rapid fabrication of highly porous and biocompatible composite textile tubular scaffold for vascular tissue engineering, *Eur. Polym. J.* 96 (2017) 27–43. <https://doi.org/10.1016/j.eurpolymj.2017.08.054>.
- [445] M. Neufurth, X. Wang, E. Tolba, B. Dorweiler, H.C. Schröder, T. Link, B. Diehl-Seifert, W.E.G. Müller, Modular small diameter vascular grafts with bioactive functionalities, *PLoS One.* 10 (2015). <https://doi.org/10.1371/JOURNAL.PONE.0133632>.
- [446] A. Abdal-hay, M. Bartnikowski, S. Hamlet, S. Ivanovski, Electrospun biphasic tubular scaffold with enhanced mechanical properties for vascular tissue engineering, *Mater. Sci. Eng. C.* 82 (2018) 10–18.

References

- <https://doi.org/https://doi.org/10.1016/j.msec.2017.08.041>.
- [447] Z. Macek Jilkova, J. Lisowska, S. Manet, C. Verdier, V. Deplano, C. Geindreau, E. Faurobert, C. Albigès-Rizo, A. Duperray, CCM proteins control endothelial $\beta 1$ integrin dependent response to shear stress, *Biol. Open.* 3 (2014) 1228–1235. <https://doi.org/10.1242/bio.201410132>.
- [448] P. Baranska, H. Jerczynska, Z. Pawlowska, W. Koziolkiewicz, C.S. Cierniewski, Expression of integrins and adhesive properties of human endothelial cell line EA. hy 926, *Cancer Genomics Proteomics.* 2 (2005) 265–269.
- [449] Y. Fang, T. Zhang, L. Zhang, W. Gong, W. Sun, Biomimetic design and fabrication of scaffolds integrating oriented micro-pores with branched channel networks for myocardial tissue engineering, *Biofabrication.* 11 (2019) 35004. <https://doi.org/10.1088/1758-5090/ab0fd3>.
- [450] D. Sharma, D. Ross, G. Wang, W. Jia, S.J. Kirkpatrick, F. Zhao, Upgrading prevascularization in tissue engineering: A review of strategies for promoting highly organized microvascular network formation, *Acta Biomater.* 95 (2019) 112–130. <https://doi.org/10.1016/J.ACTBIO.2019.03.016>.
- [451] D.J. Medina-Leyte, M. Domínguez-Pérez, I. Mercado, M.T. Villarreal-Molina, L. Jacobo-Albavera, Use of human umbilical vein endothelial cells (HUVEC) as a model to study cardiovascular disease: A review, *Appl. Sci.* 10 (2020) 938. <https://doi.org/10.3390/app10030938>.
- [452] G. Gstraunthaler, Alternatives to the use of fetal bovine serum: serum-free cell culture, *ALTEX-Alternatives to Anim. Exp.* 20 (2003) 275–281.
- [453] A.A. Ucuzian, A.A. Gassman, A.T. East, H.P. Greisler, Molecular mediators of angiogenesis, *J. Burn Care Res.* 31 (2010) 158–175. <https://doi.org/10.1097/BCR.0b013e3181c7ed82>.
- [454] D. Gospodarowicz, H. Bialecki, T.K. Thakral, The angiogenic activity of the fibroblast and epidermal growth factor, *Exp. Eye Res.* 28 (1979) 501–514. [https://doi.org/10.1016/0014-4835\(79\)90038-1](https://doi.org/10.1016/0014-4835(79)90038-1).
- [455] N.Y.C. Lin, K.A. Homan, S.S. Robinson, D.B. Kolesky, N. Duarte, A. Moisan, J.A. Lewis, H. John, A. Paulson, Renal reabsorption in 3D vascularized proximal tubule models, *Proc. Natl. Acad. Sci. U. S. A.* 116 (2019) 5399–5404. <https://doi.org/10.1073/pnas.1815208116>.
- [456] R.E. Unger, A. Sartoris, K. Peters, A. Motta, C. Migliaresi, M. Kunkel, U. Bulnheim, J. Rychly, C. James Kirkpatrick, Tissue-like self-assembly in cocultures of endothelial cells and osteoblasts and the formation of microcapillary-like structures on three-dimensional porous biomaterials, *Biomaterials.* 28 (2007) 3965–3976. <https://doi.org/10.1016/J.BIOMATERIALS.2007.05.032>.
- [457] Shun Zhang, Zhengpeng Wan, R. D. Kamm, Vascularized organoids on a

- chip: strategies for engineering organoids with functional vasculature, *Lab Chip*. 21 (2021) 473–488. <https://doi.org/10.1039/D0LC01186J>.
- [458] K.A. Homan, D.B. Kolesky, M.A. Skylar-Scott, J. Herrmann, H. Obuobi, A. Moisan, J.A. Lewis, Bioprinting of 3D Convoluted Renal Proximal Tubules on Perfusable Chips, *Sci. Rep.* 6 (2016) 1–13. <https://doi.org/10.1038/srep34845>.
- [459] D.B. Kolesky, K.A. Homan, M.A. Skylar-Scott, J.A. Lewis, Three-dimensional bioprinting of thick vascularized tissues, *Proc. Natl. Acad. Sci. U. S. A.* 113 (2016) 3179–3184. <https://doi.org/10.1073/pnas.1521342113>.
- [460] N. V Goncharov, A.D. Nadeev, R.O. Jenkins, P. V Avdonin, Markers and biomarkers of endothelium: when something is rotten in the state, *Oxid. Med. Cell. Longev.* 2017 (2017). <https://doi.org/10.1155/2017/9759735>.
- [461] P. Lertkiatmongkol, D. Liao, H. Mei, Y. Hu, P.J. Newman, Endothelial functions of platelet/endothelial cell adhesion molecule-1 (CD31), *Curr. Opin. Hematol.* 23 (2016) 253–259. <https://doi.org/10.1097/MOH.0000000000000239>.
- [462] L.-I. Larsson, *Immunocytochemistry: theory and practice*, CRC press, 1988.
- [463] M.C. Jamur, C. Oliver, Permeabilization of Cell Membranes, *Methods Mol. Biol.* 588 (2010) 63–66. https://doi.org/10.1007/978-1-59745-324-0_9.
- [464] R.W. Burry, Controls for immunocytochemistry: an update, *J. Histochem. Cytochem.* 59 (2011) 6–12. <https://doi.org/10.1369/jhc.2010.956920>.
- [465] I. Vollert, M. Seiffert, J. Bachmair, M. Sander, A. Eder, L. Conradi, A. Vogelsang, T. Schulze, J. Uebeler, W. Holthöner, H. Redl, H. Reichenspurner, A. Hansen, T. Eschenhagen, In vitro perfusion of engineered heart tissue through endothelialized channels, *Tissue Eng. - Part A*. 20 (2014) 854–863. <https://doi.org/10.1089/ten.tea.2013.0214>.
- [466] G. Altay, S. Tosi, M. García-Díaz, E. Martínez, Imaging the cell morphological response to 3D topography and curvature in engineered intestinal tissues, *Front. Bioeng. Biotechnol.* 8 (2020) 294. <https://doi.org/10.3389/fbioe.2020.00294>.
- [467] T.F. Watson, A. Azzopardi, M. Etman, P.C. Cheng, S.K. Sidhu, Confocal and multi-photon microscopy of dental hard tissues and biomaterials, *Am. J. Dent.* 13 (2000) 19D-24D. <http://europepmc.org/abstract/MED/11763913>.
- [468] M. Harling, P. Breeding, T. Haysley, M. Chesley, M. Mason, K. Tilbury, Multiphoton Microscopy for the Characterization of Cellular Behavior on Naturally Derived Polysaccharide Tissue Constructs With Irregular Surfaces for the Development of Platform Biomaterials, *Front. Bioeng.*

References

- Biotechnol. 0 (2020) 802. <https://doi.org/10.3389/FBIOE.2020.00802>.
- [469] W.L. Rice, S. Firdous, S. Gupta, M. Hunter, C.W.P. Foo, Y. Wang, H.J. Kim, D.L. Kaplan, I. Georgakoudi, Non-invasive characterization of structure and morphology of silk fibroin biomaterials using non-linear microscopy, *Biomaterials*. 29 (2008) 2015. <https://doi.org/10.1016/J.BIOMATERIALS.2007.12.049>.
- [470] M. Rubart, Two-Photon Microscopy of Cells and Tissue, *Circ. Res.* 95 (2004) 1154–1166. <https://doi.org/10.1161/01.RES.0000150593.30324.42>.
- [471] R.K.P. Benninger, D.W. Piston, Two-Photon Excitation Microscopy for the Study of Living Cells and Tissues, *Curr. Protoc. Cell Biol.* 59 (2013) 4.11.1-4.11.24. <https://doi.org/10.1002/0471143030.CB0411S59>.
- [472] K.W. Dunn, R.M. Sandoval, K.J. Kelly, P.C. Dagher, G.A. Tanner, S.J. Atkinson, R.L. Bacallao, B.A. Molitoris, Functional studies of the kidney of living animals using multicolor two-photon microscopy, <https://doi.org/10.1152/Ajpcell.00159.2002>. 283 (2002). <https://doi.org/10.1152/AJPCCELL.00159.2002>.
- [473] M. Drobizhev, N.S. Makarov, S.E. Tillo, T.E. Hughes, A. Rebane, Two-photon absorption properties of fluorescent proteins, *Nat. Methods*. 8 (2011) 393. <https://doi.org/10.1038/NMETH.1596>.
- [474] T. Betz, J. Teipel, D. Koch, W. Hartig, J.R. Guck, J. Käs, H.W. Giessen, Excitation beyond the monochromatic laser limit: simultaneous 3-D confocal and multiphoton microscopy with a tapered fiber as white-light laser source, *J. Biomed. Opt.* 10 (2005) 54009. <https://doi.org/10.1117/1.2114788>.
- [475] F. Bestvater, E. Spiess, G. Stobrawa, M. Hacker, T. Feurer, T. Porwol, U. Berchner-Pfannschmidt, C. Wotzlaw, H. Acker, Two-photon fluorescence absorption and emission spectra of dyes relevant for cell imaging, *J. Microsc.* 208 (2002) 108–115. <https://doi.org/10.1046/j.1365-2818.2002.01074.x>.
- [476] E.M.C. Hillman, V. Voleti, W. Li, H. Yu, Light-Sheet Microscopy in Neuroscience, *Annu. Rev. Neurosci.* 42 (2019) 295. <https://doi.org/10.1146/ANNUREV-NEURO-070918-050357>.
- [477] E.G. Reynaud, J. Peychl, J. Huisken, P. Tomancak, Guide to light-sheet microscopy for adventurous biologists, *Nat. Methods*. 12 (2015) 30–34. <https://doi.org/10.1038/nmeth.3222>.
- [478] R. Tomer, K. Khairy, P.J. Keller, Light sheet microscopy in cell biology, *Cell Imaging Tech.* (2012) 123–137. https://doi.org/10.1007/978-1-62703-056-4_7.
- [479] K. Chatterjee, F.W. Pratiwi, F.C.M. Wu, P. Chen, B.-C. Chen, Recent progress in light sheet microscopy for biological applications, *Appl. Spectrosc.* 72 (2018) 1137–1169.

<https://doi.org/10.1177/0003702818778851>.

- [480] J. Andilla, R. Jorand, O.E. Olarte, A.C. Dufour, M. Cazales, Y.L.E. Montagner, R. Ceolato, N. Riviere, J.-C. Olivo-Marin, P. Loza-Alvarez, C. Lorenzo, Imaging tissue-mimic with light sheet microscopy: A comparative guideline, *Sci. Rep.* 7 (2017) 1–14. <https://doi.org/10.1038/srep44939>.
- [481] M.D. Rocha, D.N. Düring, P. Bethge, F.F. Voigt, S. Hildebrand, F. Helmchen, A. Pfeifer, R.H.R. Hahnloser, M. Gahr, Tissue Clearing and Light Sheet Microscopy: Imaging the Unsectioned Adult Zebra Finch Brain at Cellular Resolution, *Front. Neuroanat.* 13 (2019). <https://doi.org/10.3389/FNANA.2019.00013>.
- [482] D.S. Richardson, J.W. Lichtman, Clarifying Tissue Clearing, *Cell.* 162 (2015) 246–257. <https://doi.org/10.1016/J.CELL.2015.06.067>.

Appendix A. LIST OF DISSEMINATION ACTIONS

EXHIBITIONS

DeLIVER Exhibition at Forskningsdagene, A virtual collection of pictures and stories from researchers and collaborators of DeLIVER, focused on the main topics of the project, organized by UiT The Arctic University of Norway (NO), First Ed.: Sept 2020, [link here](#).

OPEN TALKS

Microfluidics and Organ-on-a-chip: overcoming the limitations of traditional in vitro platforms, organized by MUSE Trento (IT) for the European Union's Horizon 2020 research and innovation programme ACDC (grant agreement No 824060), 29th Oct 2020, [link here](#).

Appendix B. LIST OF SECONDMENTS IN THE DeLIVER CONSORTIUM

Bielefeld University, Germany. 17 February – 1 March 2019.

Supervisor: Prof. Thomas Huser

Introduction to SR-SIM microscopy and preliminary tests on horizontal microfluidic design.

Birmingham University, IBR Wolfson Drive Medical School, UK. 2 – 23 July, 28 – 29 January 2020

Supervisor: Prof. Patricia Lalor

Isolation, culturing and imaging of primary LSECs on-chip.

Department of Biochemistry, University of Oxford, UK. 19 – 31 January 2020.

Supervisor : Prof. Lothar Schermelleh

SR-SIM imaging of fixed and living cells on microfluidic devices in a dish.

Appendix C. LIST OF CONFERENCE CONTRIBUTIONS

Alessandra Dellaquila, Aurélie Vigne, Thomas Huser, Sasha Cai Leshner-Pérez. **Design of microfluidic platforms for super resolution imaging of liver sinusoidal endothelial cell dynamics**, PD21, 45th International Conference on Micro and NanoEngineering (MNE 2019), Rhodes, Greece, 23-26 Sept 2019

Emma Thomee, Alexander McMillan, Alessandra Dellaquila, Alba Calatayud, Enrique Azuaje Hualde, Lourdes Basabe-Desmonts, Sasha Cai Leshner-Pérez. **Development of organ-on-chip barrier devices in new soft thermoplastics**, PD82, 45th International Conference on Micro and NanoEngineering (MNE 2019), Rhodes, Greece, 23-26 Sept 2019

Alexander H. McMillan, Emma K. Thomée, Alessandra Dellaquila and Sasha Cai Leshner-Pérez, **Fabrication and characterization of flexdym–polycarbonate devices: implementing new materials for organ-on-chip technologies**, M161.e, 23rd International Conference on Miniaturized Systems for Chemistry and Life Sciences (μ TAS 2019), Basel, Switzerland, 27 - 31 October 2019

Alessandra Dellaquila, Didier Letourneur and Teresa Simon-Yarza, **Vascularization and high-resolution imaging of 3D polysaccharide-based scaffolds as model of liver sinusoid**, 31st Conference of the European Society for Biomaterials (ESB 2021), 5 – 9 September 2021

Appendix D. LIST OF PUBLICATIONS ASSOCIATED WITH THE PROJECT

Alessandra Dellaquila, Emma K. Thomée, Alexander H. McMillan and Sasha C. Lesher-Pérez (2019). Lung-on-a-chip platforms for modeling disease pathogenesis. In PMI R&D, Philip Morris Products S.A. (Ed.), *Organ-on-a-chip: Engineered Microenvironments for Safety and Efficacy Testing* (pp. 133-180). Neuchâtel, Switzerland: Elsevier. <https://doi.org/10.1016/B978-0-12-817202-5.00004-8>

Alexander H. McMillan, Emma K. Thomée, Alessandra Dellaquila, Hussam Nassman, Tatiana Segura and Sasha C. Lesher-Pérez. Rapid Fabrication of Membrane-Integrated Thermoplastic Elastomer Microfluidic Devices, *Micromachines* **2020**, *11*(8), 731; <https://doi.org/10.3390/mi11080731>.

Alessandra Dellaquila, Chau Le Bao, Didier Letourneur and Teresa Simon-Yarza. In Vitro Strategies to Vascularize 3D Physiologically Relevant Models, *Advanced Science* **2021**, 2100798; [DOI: 10.1002/advs.202100798](https://doi.org/10.1002/advs.202100798)

